JAERI-M
88-060

EVALUATION REPORT ON SCTF CORE-III TESTS S3-14, S3-15 AND S3-16 (EFFECT OF RADIAL POWER PROFILE SHAPE ON TWO-DIMENSIONAL THERMAL-HYDRAULIC BEHAVIOR IN CORE)

March 1988

Takamichi IWAMURA, Tadashi IGUCHI, Hajime AKIMOTO
Tsutomu OKUBO, Akira OHNUKI, Isao SAKAKI
Hiromichi ADACHI, and Yoshio MURAO

日本原子力研究所
Japan Atomic Energy Research Institute

JAERI-Mレポートは，日本原子力研究所が不定期に公刊している研究報告書です。
入手の問合わせは，日本原子力研究所技術情報部情報資料課（〒319－11茨城県那珂郡東海村）あて，お申しこしください。なお，このほかに財団法人原子力弘済会資料センター（〒319-11茨城県那珂郡東海村日本原子力研究所内）で複写による実費頒布をおこなっております。

JAERI-M reports are issued irregularly.
Inquiries about availability of the reports should be addressed to Information Division, Department of Technical Information, Japan Atomic Energy Research Institute, Tokai-mura, Naka-gun, Ibaraki-ken 319-11, Japan.

編集兼発行　日本原子力研究所
印　　刷　日立高速印刷株式会社

Evaluation Report on SCTF Core-III Tests S3-14, S3-15 and S3-16 (Effect of Radial Power Profile Shape on Two-Dimensional Thermal-Hydraulic Behavior in Core)

Takamichi IWAMURA, Tadashi IGUCHI, Hajime AKIMOTO
Tsutomu OKUBO, Akira OHNUKI, Isao SAKAKI
Hiromichi ADACHI and Yoshio MURAO

Department of Reactor Safety Research
Tokai Research Establishment
Japan Atomic Energy Research Institute
Tokai-mura, Naka-gun, Ibaraki-ken

(Received February 5, 1988)

It was revealed from previous reflood tests using Slab Core Test Facility (SCTF) that the heat transfer was enhanced in high power bundles and degraded in low power bundles due to the radial power distribution. In the present study, the effects of local power ratio itself and the shape of radial power distribution were separately investigated by comparing three tests: S3-14 (flat power distribution), S3-15 (inclined power distribution) and S3-16 (steep power distribution). Those three tests were performed under the same boundary conditions, total power and initial stored energy. The emergency core cooling (ECC) water was injected into the lower plenum.

The test results indicated that the heat transfer enhancement and degradation was governed mainly by the bundlewise radial power ratio and less dependent on the shape of radial power distribution when the difference in power ratios between adjacent bundles is less than 0.44. The degree of heat transfer enhancement at high power bundles was increased with the radial peak power ratio. Even at an average power bundle, the

---

The work was performed under contract with the Atomic Energy Bureau of Science and Technology Agency of Japan.

heat transfer was enhanced in the non-uniform radial power distribution tests.

Keywords: LOCA, ECCS, Two-Dimensional Effect, Reflood, Reactor Safety, Heat Transfer, Quench, Two-Phase Flow, SCTF

ＳＣＴＦ第３次炉心試験Ｓ３－14，Ｓ３－15及びＳ３－16評価報告（半径方向出力分布形状が炉心内２次元熱水力学的挙動に及ぼす影響）

日本原子力研究所東海研究所原子炉安全工学部
岩村　公道・井口　正・秋本　肇・大久保　努
大貫　晃・榊　勲・安達　公道・村尾　良夫

（1988年２月５日受理）

平板炉心試験装置（ＳＣＴＦ）を用いた再冠水試験により，半径方向出力分布が存在すると，高出力バンドルでは熱伝達が促進され，低出力バンドルでは熱伝達が劣下することが既に明らかとなっている。本研究では，Ｓ３－14（平坦出力分布），Ｓ３－15（傾斜出力分布）及びＳ３－16（急峻出力分布）の３試験を比較することにより，局所出力比自体の効果と半径方向出力分布形状の効果を分離して評価した。以上の３試験は，同一の境界条件，総出力及び初期蓄積熱の条件下で実施した。また，緊急冷却（ＥＣＣ）水は下部プレナムに注入した。

試験結果により，熱伝達の促進及び劣化は，主としてバンドル出力比に強く依存し，隣接バンドル間の出力比の差が0.44 以下の場合は，半径方向出力分布の形状に，ほとんど依存しないことが明らかとなった。また，高出力バンドルにおける熱伝達促進の程度は，最大出力比と共に増大した。不均一半径方向出力分布試験では，平均出力バンドルにおいても，熱伝達の促進が認められた。

本報告書は，電源開発促進対策特別会計法に基づき，科学技術庁からの受託によって行った研究の成果である。

東海研究所：〒319-11 茨城県那珂郡東海村白方字白根２－４

Contents

1. INTRODUCTION 1
2. TEST DESCRIPTION 2
2.1 Test Facility 2
2.2 Test Condition 3
2.3 Test Procedure 3
3. TEST RESULTS 5
3.1 Measured Boundary Conditions 5
3.2 Overall Fluid Behavior 5
3.2.1 Fluid Behavior in Upper Plenum and around End Box Tie Plate 5
3.2.2 Water Accumulation Behavior in Core and Downcomer 6
3.2.3 Steam Generation Rate and Steam Outflow Rate 6
3.2.4 Fluid Behavior in Primary Loops 7
3.3 Two-Dimensional Fluid Behavior in Core 7
3.3.1 Horizontal Differential Pressures and Pressure Distribution 7
3.3.2 Void Fraction Distribution 8
3.3.3 Froth Level Distribution 8
3.4 Two-Dimensional Thermal Behavior 9
4. DISCUSSIONS 10
4.1 Effect of Radial Power Distribution on Heat Transfer Coefficient 10
4.2 Effect of Radial Peak Power Ratio on Heat Transfer Coefficient 11
5. CONCLUSION 12
Acknowledgment 12
References 12
Appendix A Slab Core Test Facility Core-III 56
Appendix B Froth Level Detector in SCTF-III 106
Appendix C Selected Data of Test S3-14 112
Appendix D Selected Data of Test S3-15 125
Appendix E Selected Data of Test S3-16 138

目　　次

1. 序論 …… 1
2. 試験 …… 2
2.1 試験装置 …… 2
2.2 試験条件 …… 3
2.3 試験方法 …… 3
3. 試験結果 …… 5
3.1 境界条件測定値 …… 5
3.2 全体的な流体挙動 …… 5
3.2.1 上部プレナム内及びエンドボックスタイプレート周辺の流体挙動 …… 5
3.2.2 炉心及びダウンカマ内の蓄水挙動 …… 6
3.2.3 蒸気発生率及び蒸気流出率 …… 6
3.2.4 一次系内流体挙動 …… 7
3.3 炉心内二次元流体挙動 …… 7
3.3.1 水平方向差圧及び圧力分布 …… 7
3.3.2 ボイド率分布 …… 8
3.3.3 フロスレベル分布 …… 8
3.4 二次元熱的挙動 …… 9
4. 考察 …… 10
4.1 半径方向出力分布が熱伝達率に及ぼす影響 …… 10
4.2 ピーク出力比が熱伝達率に及ぼす影響 …… 11
5. 結論 …… 12
謝　辞 …… 12
参考文献 …… 12
付録A 平板炉心試験装置（ＳＣＴＦ）第3次炉心 …… 56
付録B ＳＣＴＦ第3次炉心内フロスレベル検出器 …… 106
付録C 試験Ｓ3－14のデータ …… 112
付録D 試験Ｓ3－15のデータ …… 125
付録E 試験Ｓ3－16のデータ …… 138

List of Tables

Table 2.1 Test conditions for Tests S3-14, S3-15, and S3-16
Table 3.1 Chronology of major events

List of Figures

Fig. 2.1 Schematic diagram of SCTF
Fig. 2.2 Pressure vessel of SCTF Core-III
Fig. 2.3 Radial power distributions for Tests S3-14, S3-15, S3-16, S2-18, and C2-5
Fig. 2.4 Test sequence of Test S3-14
Fig. 2.5 Test sequence of Test S3-15
Fig. 2.6 Test sequence of Test S3-16
Fig. 3.1 ECC injection rates into lower plenum
Fig. 3.2 Comparison of mass flow rates at core inlet obtained by mass balance method
Fig. 3.3 Comparison of water temperatures at core inlet
Fig. 3.4 Comparison of core heating power
Fig. 3.5 Comparison of pressures at core center
Fig. 3.6 Comparison of pressures at the top of containment tank-II
Fig. 3.7 Comparison of collapsed liquid levels in upper plenum
Fig. 3.8 Comparison of differential pressures across end box tie plate
Fig. 3.9 Comparison of differential pressures across core full height
Fig. 3.10 Comparison of collapsed liquid levels in downcomer
Fig. 3.11 Comparison of steam generation rates calculated from heat balance method
Fig. 3.12 Comparison of steam outflow rates from pressure vessel obtained by mass balance method
Fig. 3.13 Comparison of differential pressures across hot leg
Fig. 3.14 Comparison of differential pressures across intact cold leg
Fig. 3.15 Comparison of differential pressures across broken cold leg pressure vessel side

Fig. 3.16 Comparison of differential pressures across broken cold leg steam/water separator side
Fig. 3.17 Comparison of horizontal differential pressures in core at 1.365 m
Fig. 3.18 Comparison of horizontal differential pressures in core at 1.905 m
Fig. 3.19(a) Comparison of equal pressure lines and bottom quench front distribution (50s after BOCREC)
Fig. 3.19(b) Comparison of equal pressure lines and bottom quench front distribution (100s after BOCREC)
Fig. 3.19(c) Comparison of equal pressure lines and bottom quench front distrituion (200s after BOCREC)
Fig. 3.19(d) Comparison of equal pressure lines and bottom quench front distrituion (300s after BOCREC)
Fig. 3.19(e) Comparison of equal pressure lines and bottom quench front distrituion (400s after BOCREC)
Fig. 3.20 Comparison of void fractions in core
Fig. 3.21 Output signals from froth level detector for Test S3-16
Fig. 3.22 Comparison of cladding temperatures at bundles with the same power ratio at 1.905 m
Fig. 3.23 Comparison of heat transfer coefficients at bundles with the same power ratio at 1.905 m
Fig. 3.24 Comparison of quench front propagation profile
Fig. 4.1 Difference in heat transfer coefficients between Tests S3-15 and S3-14 vs. distance from bottom quench front
Fig. 4.2 Difference in heat transfer coefficients between Tests S3-16 and S3-14 vs. distance from bottom quench front
Fig. 4.3 Effect of bundlewise power ratio and power distribution shape on heat transfer coefficient (Elevation 1.905 m)
Fig. 4.4 Effect of bundlewise power ratio and power distribution shape on heat transfer coefficient (Elevation 2.33 m)
Fig. 4.5 Effect of peak power ratio on heat transfer enhancement due to radial power distribution

1. INTRODUCTION

The Slab Core Test Facility (SCTF) test program is a part of the large scale reflood test program performed under contract with Atomic Energy Bureau of Science and Technology Agency of Japan, together with the Cylindrical Core Test Facility (CCTF) test program. The SCTF test program is one of the research activities based on the trilateral agreement among Japan Atomic Energy Research Institute (JAERI), the United States Nuclear regulatory Commission (USNRC) and the Federal Minister for Research and Technology (BMFT) of the Federal Republic of Germany (FRG).

One of the major objectives of the SCTF program is to investigate the effects of radial power distribution on the two-dimensional thermal-hydraulic behavior in the core during the reflood phase of a loss-of-coolant accident (LOCA) of a pressurized water reactor (PWR). The previous SCTF Core-I and Core-II tests revealed that the heat transfer above the quench front was enhanced in high power bundles and degraded in low power bundles due to a two-dimensional flow induced by the radial power distribution[1],[2].

However, it has not been clarified yet whether the two-dimensional heat transfer behavior depends only on the local power ratio itself or the location of high power bundle also affects the heat transfer enhancement. In the present study, the effects of local power ratio itself and the shape of radial power distribution on the two-dimensional heat transfer behavior are separately investigated by comparing three SCTF Core-III tests under different radial power distributions. Those tests are; Test S3-14 (flat power distribution), S3-15(inclined power distribution) and S3-16(steep power distribution). In addition, the effect of the difference in the power ratios between adjacent bundles on the heat transfer characteristics is discussed by comparing with the results of SCTF Core-II Test S2-18[3] and CCTF Core-II Test C2-05[4].

A brief description of the SCTF Core-III is presented in Appendix A. A froth level detector system installed in the SCTF Core-III is explained in Appendix B. Some selected data obtained from Tests S3-14, S3-15 and S3-16 are presented in Appendixes C, D and E, respectively.

2. TEST DESCRIPTION

2.1 Test Facility

A schematic diagram of SCTF is shown in Fig. 2.1 The primary coolant loops consist of a hot leg equivalent to four actual hot legs, a steam/water separator corresponding to four actual steam generators, an intact cold leg equivalent to three intact cold legs, a broken cold leg on the pressure vessel side, and a broken cold leg on the steam/water separator side. These two broken cold legs are connected to two containment tanks one by one which are connected to each other by a pressure equalizing pipe.

The flow area scaling ratio is 1/21 of a 1,100 MWe class Westinghouse-type PWR, whereas the heights of each component are preserved.

The ECC injection port in the gravity feed tests for a Westinghouse-type (US/J-type) PWR was the lower plenum as shown in Fig. 2.1

Figure 2.2 shows a vertical cross section of the pressure vessel. The pressure vessel includes a simulated core, an upper plenum with internals, a lower plenum, a core baffle and a downcomer. The configurations of the upper plenum structure and the end box simulate those of a 1,300 MWe class German-type PWR (GPWR) as practically as possible because the major purpose of the SCTF Core-III test series is to investigate the effectiveness of the combined-injection-type ECCS for a GPWR.

The simulated core consists of 8 bundles arranged in a row with full radial width. Bundle 1 corresponds to the center bundle and Bundle 8 to the peripheral bundle of a PWR. Each bundle consists of 236 heated rods and 20 non-heated rods arranged in a 16 x 16 array. The outer diameter and the heated length of the heated rod are 10.7 mm and 3,613 mm, respectively. The arrangement pitch of the rods is 14.3 mm.

The core and the upper plenumn are enveloped by honeycomb thermal insulators with wall plates to minimize the wall thermal effects.

The SCTF Core-III is described more in detail in reference (5) and a brief description is presented in Appendix A.

In Test S3-16, a froth level detector was used to measure the horizontal distribution of froth level, which is defined as the

boundary between continuous liquid phase and dispersed liquid phase. The froth level detector system is decribed in Appendix B.

2.2 Test Condition

The SCTF tests discussed in this report are Tests S3-14, S3-15, and S3-16, Major test conditions for these three tests are listed in Table 2.1

The radial power distributions are shown in Fig. 2.3. The radial power distribution is flat for Test S3-14, inclined for Test S3-15 and steep for Test S3-16 under the same total power and initial stored energy. The boundary conditions are also set to be the same for these three tests.

The maximum and minimum power ratios are based on those used at CCTF Test C2-5[4]. The radial power distribution in Test C2-5 was also simulated in SCTF Core-II Test S2-18[3]. The radial power distributions for Tests S2-18 and C2-5 are also shown in Fig. 2.3. In Tests S3-15, the power ratio was changed gradually bundle by bundle, while it was changed largely between Bundles 4 and 5 in Test S2-18. The peak power ratio was in Bundle 1 for Test S3-15 and in Bundle 4 for Test S3-16. The power ratios were corresponding to each other for these two tests as shown in Fig. 2.3.

The maximum cladding temperatures at the reflood initiation were determined to preserve the initial stored energy the same for Tests S3-14, S3-15 and S3-16.

2.3 Test Procedure

Figures 2.4, 2.5 and 2.6 show the test sequences for Tests S3-14, S3-15 and S3-16, respectively.

The core heating was initiated at time "zero" under the specified power distribution for each of these three tests with the total power of 7.12 MW. When four cladding temperatures exceeded a specified temperature, ECC injection into the lower plenum was initiated. When the water level in the lower plenum reached the bottom of core, the core power decay started, simulating the reactor time from 40 s after shutdown. This time is called BOCREC (Bottom of core recovery).
The decay curve was based on the 1.02x (ANS standard + Actinides).

As shown in Figs. 2.4, 2.5 and 2.6, the heating power was decreased to an extreamly low value followed by the drain of core water at about 600s after the BOCREC. Then the core power was increased again and ECC water injection into the lower plenum and the upper plenum was initiated. This phase of test (Phase 2) aimed to investigate the effect of ECC water injection condition on the flow direction in the core. However, the test results of this phase are not discussed in the present report.

3. TEST RESULTS

3.1 Measured Boundary Conditions

As compared in Fig. 3.1, the ECC injection rates into the lower plenum are exactly the same for Tests S3-14, S3-15, and S3-16. The core inlet mass flow rate is estimated by the following mass balance equation.

$$W_{in} = W_{ECC}+W_{IC}-W_{BC}-W_{LP}-W_{BF}-W_{DC} \qquad (1)$$

where, W_{in} = mass flow rate at core inlet
W_{ECC} = ECC injection rate
W_{IC} = mass flow rate through intact cold leg
W_{BC} = mass out-flow rate through broken cold leg
W_{LP} = mass accumulation rate in lower plenum
W_{BF} = mass accumulation rate in core baffle region
W_{DC} = mass accumulation rate in downcomer

The estimated mass flow rates at the core inlet are shown in Fig. 3.2. The core inlet mass flow rate during the initial 80s is much lower than the ECC injection rate because a large part of the injected water flows into the downcomer during this period as indicated in Fig. 3.10. Anyway, the core inlet mass flow rates are also in good agreement with each other for these three tests.

Figure 3.3 shows the comparison of water temperatures at the bottom of core heated part. The difference in the core inlet water temperatures is within 4K for these three tests.

Figure 3.4 shows the core heating powers at each bundle for Tests S3-14, S3-15, and S3-16. The initial power, power decay curve and radial power distribution are correctly established as specified.

The pressures at the core center and the top of containment tank-II are compared in Figs. 3.5 and 3.6, respectively. Those pressure histories for Tests S3-14, S3-15 and S3-16 are well agreed.

3.2 Overall Fluid Behavior

3.2.1 Fluid Behavior in Upper Plenum and around End Box Tie Plate

Figure 3.7 shows the collapsed liquid levels in the upper plenum for Tests S3-14, S3-15 and S3-16. The liquid levels are lower than

0.05m before 380s and then increase rapidly. The radial power distribution has no effect on the liquid level distribution in the upper plenum. The difference in the liquid levels among bundles is not as much clear as observed in the SCTF Core-II tests [6], probably due to the large difference in the upper plenum structure design[5].

The differential pressures across the end box tie plate above Bundles 1, 3, 5, 7 and 8 are compared in Fig. 3.8 for Tests S3-14, S3-15 and S3-16. Although a large difference in the differential pressures is observed among bundles even in the flat power distribution test (S3-14), no clear effect of the radial power distribution is recognized on the radial distibution of the differential pressures across the end box tie plate.

3.2.2 Water Accumulation Behavior in Core and Downcomer

The differential pressures across the core full height and the collapsed liquid levels in the downcomer are compared in Figs. 3.9 and 3.10, respectively. No significant effect of radial power distribution is observed on the water accumulation behavior in the core and the downcomer.

As shown in Fig. 3.10, the downcomer liquid level increases up to 4.5 m until 80s, indicating that a large amount of the lower plenum injection water flows into the downcomer during the initial 80s. After that time, the liquid level is kept constant at 4.5 m level. The downcomer overflow did not occur because the nozzle of broken cold leg is attached at 6.6 m elevation.

3.2.3 Steam Generation Rate and Steam Outflow Rate

Figures 3.11 and 3.12 show the comparisons of the steam generation rates in the core and the steam outflow rates from the pressure vessel, respectively. The steam generation rate is obtained from a heat balance method and the steam outflow rate from a mass balance method[6]. As shown in Fig. 3.11, the radial power distribution has no significant effect on the total steam generation rate because the total power and the initial stored energy were set to be identical for Tests S3-14, S3-15 and S3-16. The steam outflow rate is slightly lower in Test S3-14, while no difference is observed between the other two tests.

It is indicated by comparing these two figures that the steam generation rate is larger than the steam outflow rate especially during the initial 60s. One of the reasons of this discrepancy is considered to be the fact that a fraction of the generated steam contributes to the pressurization of the pressure vessel.

3.2.4 Fluid Behavior in Primary Loops

Figures 3.13 through 3.16 show the comparisons of differential pressures across the hot leg, the intact cold leg, the broken cold leg pressure vessel side, and the broken cold leg steam/water separator side.

As shown in these figures, the behaviors of the differential pressures in the primary loops are approximately agreed to each other among Tests S3-14, S3-15, and S3-16. However, the differential pressures in the broken cold legs are slightly larger in Test S3-16 and smaller in Test S3-14.

3.3 Two-Dimensional Fluid Behavior in Core

3.3.1 Horizontal Differential Pressures and Pressure Distribution

Figures 3.17 and 3.18 show the comparisons of horizontal differential pressures in the core at elevations of 1.365 and 1.905 m, respectively. The possitive differential pressure means that the pressure is higher at the Bundle 1 side than the Bundle 8 side.

Above the bottom quench front, the pressure at Bundle 4 is the highest in Test S3-16 (steep power distribution), while the pressure at the Bundle 1 side is higher than the pressure at the Bundle 8 side in Test S3-15 (inclined power distribution). On the other hand, the horizontal differential pressures are negliegibly small in Test S3-14 (flat power distribution). It is therefore indicated that the two-dimensional flow behavior is corresponding to the radial power distribution. That is, the cross flow direction above the quench front is always from the higher power bundle to the lower power bundle.

The above-mentioned two-dimensional flow behavior is clearly seen in the equal pressure lines shown in Figs. 3.19 (a) through (e) at 50, 100, 200, 300 and 400s after the BOCREC, respectively. These equal pressure lines were obtained by vertical interpolations of absolute

pressures at various points. The absolute pressures were obtained by combining the measured absolute pressure with the measured horizontal and vertical differential pressures. The distribution of bottom quench front is also shown in these figures.

It is suggested from Fig. 3.19 that the flow circulation type is a single mode in Test S3-15 and a dual mode in Test S3-16, correspoinding to the inclined and steep radial power distributions, respectively.

3.3.2 Void Fraction Distribution

Figure 3.20 shows the comparisons of void fractions in Bundles 2, 4 and 8 at elevation between 2.03 and 2.57 m. The void fractions were calculated from the measured vertical differential pressures by neglecting the effects of frictional and accelerational pressure drops.

As shown in Fig. 3.20, the void fraction is the lowest in Bundle 2 before 250s in Test S3-15. On the other hand, the void fraction is the lowest in Bundle 4 during the period between 60 and 270s in Test S3-16. The void fraction is the highest in Bundle 8 during the major period before quenching in Tests S3-15 and S3-16. Therefore, it is indicated that the liquid fraction (1 - void fraction) tends to be higher in higher power bundles above the quench front. After the bottom quench front reaches the measurement span, the void fraction in Bundle 8 becomes the lowest in Test S3-15 and S3-16 because the quench front propagation velocity is the highest and the steam generation rate is the lowest in the lowest power bundle.

3.3.3 Froth Level Distribution

The froth level detector has been developed and installed in SCTF Core-III to detect the froth level distribution above the quench front. Two-phase mixture was extracted through 4 nozzles located in Bundles 2, 4, 6 and 8 at elevation of 1.905 m. The absorption of light in the extracted two-phase mixture is measured with a laser through-beam photoelectric sensor to detect the time when water reaches the nozzle elevation. The froth level detector system is described in Appendix B.

Figure 3.21 shows the output signal of the froth level detector for Test S3-16. The water phase apears at first in Bundle 4 followed

by Bundles 6 and 2. The water phase are not clearly seen in Bundle 8 during the initial 50s. The timing of the first detection of water is exactly in the same order as the radial power ratio. However, the distribution of froth level, which is defined as the boundary between continuous liquid phase and dispersed liquid phase, was not clearly detected, because the output signal changed gradually after the first detection of liquid phase.

3.4 Two-Dimensional Thermal Behavior

Figure 3.22 shows the comparisons of heater rod temperatures at 1.905 m in the bundles with the same power ratio for Tests S3-15 and S3-16. The heat transfer coefficients corresponding to the temperature histories in Fig. 3.22 are shown in Fig. 3.23. The heat transfer coefficients were calculated with the SCTF heat transfer calculation code "HEATT"[7]

The histories of rod temperatures and heat transfer coefficient under the same power ratio are fairly well agreed with each other between these two tests especially in the bundles with the power ratio of 1.0. However, the rod temperature in Test S3-15 is slightly larger in the bundle with the power ratio of 1.2 and slightly smaller in the bundle with the power ratio of 0.81. Correspondingly, the heat transfer coefficient in Test S3-15 is slightly lower in the higher power ratio bundle and higher in the lower power ratio bundle.

Figure 3.24 shows the quench envelopes in Bundles 1 through 8 for Tests S3-14, S3-15 and S3-16. The radial distributions of the bottom quench front are shown in Figs 3.19 (a) through (e). The quench front propagation speed in the highest power bundle is the lowest among all bundles both in Tests S3-15 and S3-16. On the other hand, the quench front proceeds uniformly in the flat power distribution test (S3-14). At the later period, however, the quench front propagation tends to be delayed in the Bundle 8 side commonly in these three tests. Since no significant difference is observed in the distribution of liquid level in the upper plenum before the quench of whole core, the delay of quench front propagation in the Bundle 8 side is considered to be due to the asymmetric flow resulted from the fact that the hot leg nozzle is attached to the Bundle 8 side.

4. DISCUSSIONS

4.1 Effect of Radial Power Distribution on Heat Transfer Coefficient

The effects of the radial power ratio and the shape of radial power distribution on the two-dimensional heat transfer behavior are separately investigated by comparing the heat transfer coefficients in Test S3-15 (inclined power distribution) and Test S3-16 (steep power disbrituion).

Since the quench front propagation speed depends on the power distribution as shown in Figs. 3.19 and 3.24, the two-dimensional heat transfer characteristics are more adequately compared with respect to the distance from the bottom quench front than the time after flood. At elevations of 1.905 m and 2.33 m, the differences between the heat transfer coefficient at each bundle in Test S3-15 and that averaged over all bundles in Test S3-14 are plotted against the distance from the bottom quench front in Fig. 4.1. Here, in order to eliminate the effects of large oscillation and rapid increase of heat transfer coefficient, the data obtained when the quench front was below 0.05 m from the bottom of heated part or within 0.15 m from the thermocouple elevation were not used in the plots. The differences in the heat transfer coefficients between Tests S3-16 and S3-14 are also plotted against the distance from the bottom quench front in Fig. 4.2. It should be noted in Figs. 4.1 and 4.2 that the time proceeds from the right side to the left side. As shown in these figures, the heat transfer in the inclined or steep power distribution tests is enhanced not only in the high power bundles but also in the average power bundle.

In order to have a quantitative understanding of the relation between the radial power ratio and the increase or decrease of heat transfer coefficient, the averages and standard deviations of the differences in the heat transfer coefficients at elevations of 1.905 m and 2.33 m are plotted against the radial power ratios in Figs. 4.3 and 4.4, respectively. The standard deviations in these figures are relatively large because the differences in the heat transfer coefficients are not constant but depend on the distance from the bottom quench front. As shown in Figs. 4.3 and 4.4, the relation between the differences in the heat transfer coefficients and the radial power ratio are approximately the same for Tests S3-15 and S3-16.

In order to investigate the effect of the difference in the radial power ratios between adjacent bundles, the data from SCTF Core-II Test S2-18[3] and CCTF Test C2-05[4] are also shown in Fig. 4.3. The CCTF has a cylindrical core with 0.343 m radius. As shown in Fig. 2.3, the maximum and minimum power ratios are 1.36 and 0.76, respectively, for Tests S3-15, S3-16, S2-18 and C2-05. However, the maximum difference in power ratios between adjacent bundles is 0.44 in Tests S2-18 and C2-05, while that in Tests S3-15 and S3-16 is 0.16. As shown in Fig. 4.3, no significant difference can be recognized among these four tests in spite of the difference in radial power distribution and the difference in horizontal length of the core.

Therefore, it is concluded that, when the difference in power ratios between adjacent bundles is less than 0.44 and the core radius is more than 0.343 m, the heat transfer enhancement or degradation due to radial power distribution is governed mainly by the bundlewise radial power ratio and less dependent on the shape of radial power distribution and the length of core radius.

It is also indicated from Figs. 4.3 and 4.4 that the difference in elevations between 1.905 and 2.33 m has little effect on this relation.

4.2 Effect of Radial Peak Power Ratio on Heat Transfer Coefficient

Since the radial peak power ratio of 1.36 is the same for Tests S3-15, S3-16, S2-18 and C2-05, the effect of radial peak power ratio cannot be discussed in the previous section. This effect is investigated by comparing the test results under different peak power ratio.

The effect of peak power ratio on the heat transfer enhancement or degradation due to the radial power distribution is shown in Fig. 4.5. As noted from this figure, the degree of heat transfer enhancement at the high power bundle is increased with the peak power ratio. For example, even at the average power bundle (power ratio = 1.0), the heat transfer coefficient is increased by about 12 $W/m^2.K$ for Tests S3-15 and S3-16 (peak power ratio = 1.36), 6 $W/m^2.K$ for Test S2-12 (1.2) and 1 $W/m^2.K$ for Test S2-SH1 (1.065). Therefore, it is concluded that the heat transfer enhancement due to the radial power distribution is determined not only by the bundlewise power ratio itself but also by the magnitude of the radial peak power ratio.

5. CONCLUSION

(1) The heat transfer enhancement and degradation due to a radial power distribution was governed mainly by the bundlewise radial power ratio and less dependent on the shape of radial power distribution when the difference in power ratios between adjacent bundles is less than 0.44.

(2) The degree of heat transfer enhancement at high power bundles was increased with the radial peak power ratio.

(3) Even at an average power bundle, the heat transfer was enhanced in the non-uniform radial power distribution tests.

ACKNOWLEGMENT

The authors would like to express their appreciation to Mr. W. Pointner, a regident engineer from Federal Republic of Germany, for his useful discussions.

REFERENCES

(1) T. Iwamura et al., Effects of Radial Core Power Profile on Core Thermo-Hydraulic Behavior during Reflood Phase in PWR-LOCAs, J. Nucl. Sci. Tech., Vol. 20, No. 9, pp. 743-751, (1983).

(2) T. Iwamura et al., Experimental Study of Two-Dimensional Thermal-Hydraulic Behavior in Core during Reflood Phase of PWR LOCA, J. Nucl. Sci. Tech., Vol. 23, No. 2, pp. 123-135, (1986).

(3) T. Okubo et al., Analysis of SCTF/CCTF Counterpart Test Results, JAERI-M to be published.

(4) T. Iguchi, et al., Quick-look Report on CCTF Core-II Reflood Test C2-5 (Run 63) - Investigation of the Reflood Phenomena under Low Power Condition -, private communication.

5. CONCLUSION

(1) The heat transfer enhancement and degradation due to a radial power distribution was governed mainly by the bundlewise radial power ratio and less dependent on the shape of radial power distribution when the difference in power ratios between adjacent bundles is less than 0.44.

(2) The degree of heat transfer enhancement at high power bundles was increased with the radial peak power ratio.

(3) Even at an average power bundle, the heat transfer was enhanced in the non-uniform radial power distribution tests.

ACKNOWLEGMENT

The authors would like to express their appreciation to Mr. W. Pointner, a regident engineer from Federal Republic of Germany, for his useful discussions.

REFERENCES

(1) T. Iwamura et al., Effects of Radial Core Power Profile on Core Thermo-Hydraulic Behavior during Reflood Phase in PWR-LOCAs, J. Nucl. Sci. Tech., Vol. 20, No. 9, pp. 743-751, (1983).

(2) T. Iwamura et al., Experimental Study of Two-Dimensional Thermal-Hydraulic Behavior in Core during Reflood Phase of PWR LOCA, J. Nucl. Sci. Tech., Vol. 23, No. 2, pp. 123-135, (1986).

(3) T. Okubo et al., Analysis of SCTF/CCTF Counterpart Test Results, JAERI-M to be published.

(4) T. Iguchi, et al., Quick-look Report on CCTF Core-II Reflood Test C2-5 (Run 63) - Investigation of the Reflood Phenomena under Low Power Condition -, private communication.

5. CONCLUSION

(1) The heat transfer enhancement and degradation due to a radial power distribution was governed mainly by the bundlewise radial power ratio and less dependent on the shape of radial power distribution when the difference in power ratios between adjacent bundles is less than 0.44.

(2) The degree of heat transfer enhancement at high power bundles was increased with the radial peak power ratio.

(3) Even at an average power bundle, the heat transfer was enhanced in the non-uniform radial power distribution tests.

ACKNOWLEGMENT

The authors would like to express their appreciation to Mr. W. Pointner, a regident engineer from Federal Republic of Germany, for his useful discussions.

REFERENCES

(1) T. Iwamura et al., Effects of Radial Core Power Profile on Core Thermo-Hydraulic Behavior during Reflood Phase in PWR-LOCAs, J. Nucl. Sci. Tech., Vol. 20, No. 9, pp. 743-751, (1983).

(2) T. Iwamura et al., Experimental Study of Two-Dimensional Thermal-Hydraulic Behavior in Core during Reflood Phase of PWR LOCA, J. Nucl. Sci. Tech., Vol. 23, No. 2, pp. 123-135, (1986).

(3) T. Okubo et al., Analysis of SCTF/CCTF Counterpart Test Results, JAERI-M to be published.

(4) T. Iguchi, et al., Quick-look Report on CCTF Core-II Reflood Test C2-5 (Run 63) - Investigation of the Reflood Phenomena under Low Power Condition -, private communication.

(5) H. Adachi, et al., Design of Slab Core Test Facility (SCTF) in Large Scale Reflood Test Program, Part III: Core-III, private communication.

(6) T. Iwamura, et al., Two-Dimensional Thermal-Hydraulic Behavior in Core in SCTF Core-II Cold Leg Injection Tests (Radial Power Profile Test Results), JAERI-M 85-106, (1985).

(7) M. Osakabe and Y. Sudo., Heat Transfer Calculation of Simulated Heater Rods throughout Reflood Phase in Postulated PWR-LOCA Experiments, J. Nucl. Sci. Tech vol. 20, No. 7, pp 559-570 (1983).

Table 2.1 Test conditions for Tests S3-14, S3-15 and S3-16

(1) Common test condition

	Nominal	Measured
System pressure	0.2 Mpa	(Fig. 3.6)
Initial total power	7.12 MW	(Fig. 3.4)
ECC water injection rate		(Fig. 3.1)
Acc period (maximum)	37 kg/s	
LPCI period (after 100s)	3.75 kg/s	
ECC water temperature		(Fig. 3.3)
Acc period	353K	(Water temperature
LPCI period (after 28s)	393 K	at core inlet)
Decay curve	1.02 (ANS+Act.) after shut down	from 40S

(2) Different test condition

	S3-14	S3-15	S3-16
Radial power ratio			
Bundle 1	1.0	1.36	0.81
Bundle 2	1.0	1.2	0.91
Bundle 3	1.0	1.1	1.1
Bundle 4	1.0	1.0	1.36
Bundle 5	1.0	0.9	1.2
Bundle 6	1.0	0.86	1.0
Bundle 7	1.0	0.81	0.86
Bundle 8	1.0	0.76	0.76
Maximum cladding temperature at reflood initiation			
specified	922 K	1108 K	1108 K
measured	946 K	1151 K	1134 K

Table 3.1 Chronology of major events

(1) Test S3-14 (Run 718)

	Time after core power "ON"	Time after BOCREC
Core power "ON"	0 S	-115 S
ECC injection initiation	106.5	-8.5
Core power decay initiation	114	-1
BOCREC	115	0
Maximum pressure at the top of core (1059 K)	140	25
Maximum pressure at the center of core (0.254 Mpa)	149	34
Maximum core temperature (1059 K)	212	97
Whole core quenched	552.5	437.5

(2) Test S3-15 (Run 719)

	Time after core power "ON"	Time after BOCREC
Core power "ON"	0 S	-122 S
ECC injection initiation	114	-8
Core power decay initiation	122	0
BOCREC	122	0
Maximum core temperature (1183 K)	140	18
Maximum pressure at the top of containment tank-II (0.227 Mpa)	146	24
Maximum pressure at the ceter of core (0.258 Mpa)	155	33
Whole core quenched	574.5	452.5

Table 3.1 (continued)

(3) Test S3-16 (Run 720)

	Time after core power "ON"	Time after BOCREC
Core power "ON"	0 S	-123 S
ECC injection initiation	114	-9
Core power decay initiation	122	-1
BOCREC	123	0
Maximum pressure at the top of containment tank-II (0.228 Mpa)	147	24
Maximum pressure at the ceter of core (0.258 Mpa)	156	33
Maximum core temperature (1222 K)	198	75
Whole core quenched	567.5	444.5

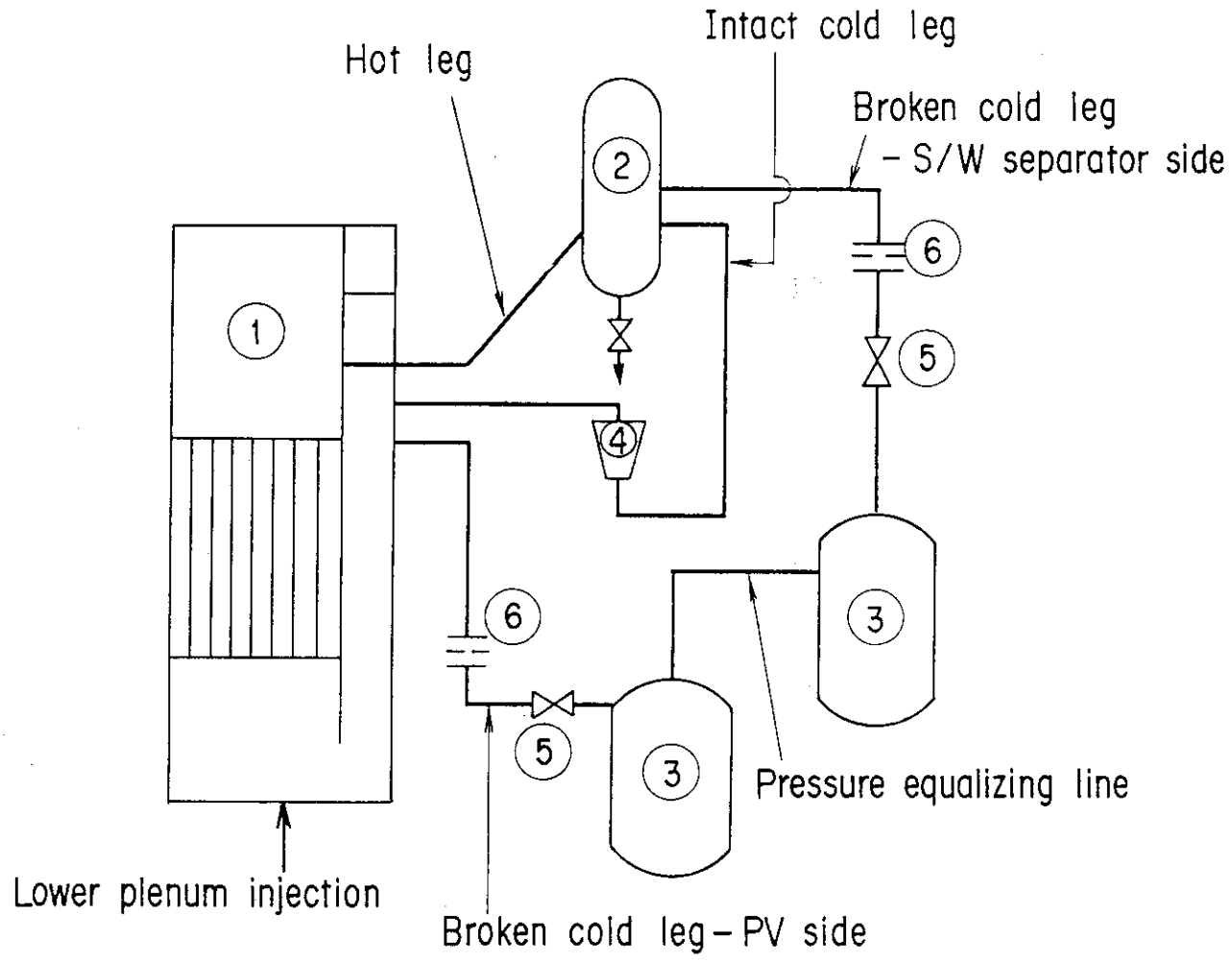

① Pressure vessel
② Steam / water separator
③ Containment tanks
④ Pump simulator
⑤ Break valves
⑥ Flow resistance simulators

Fig. 2.1 Schematic diagram of SCTF

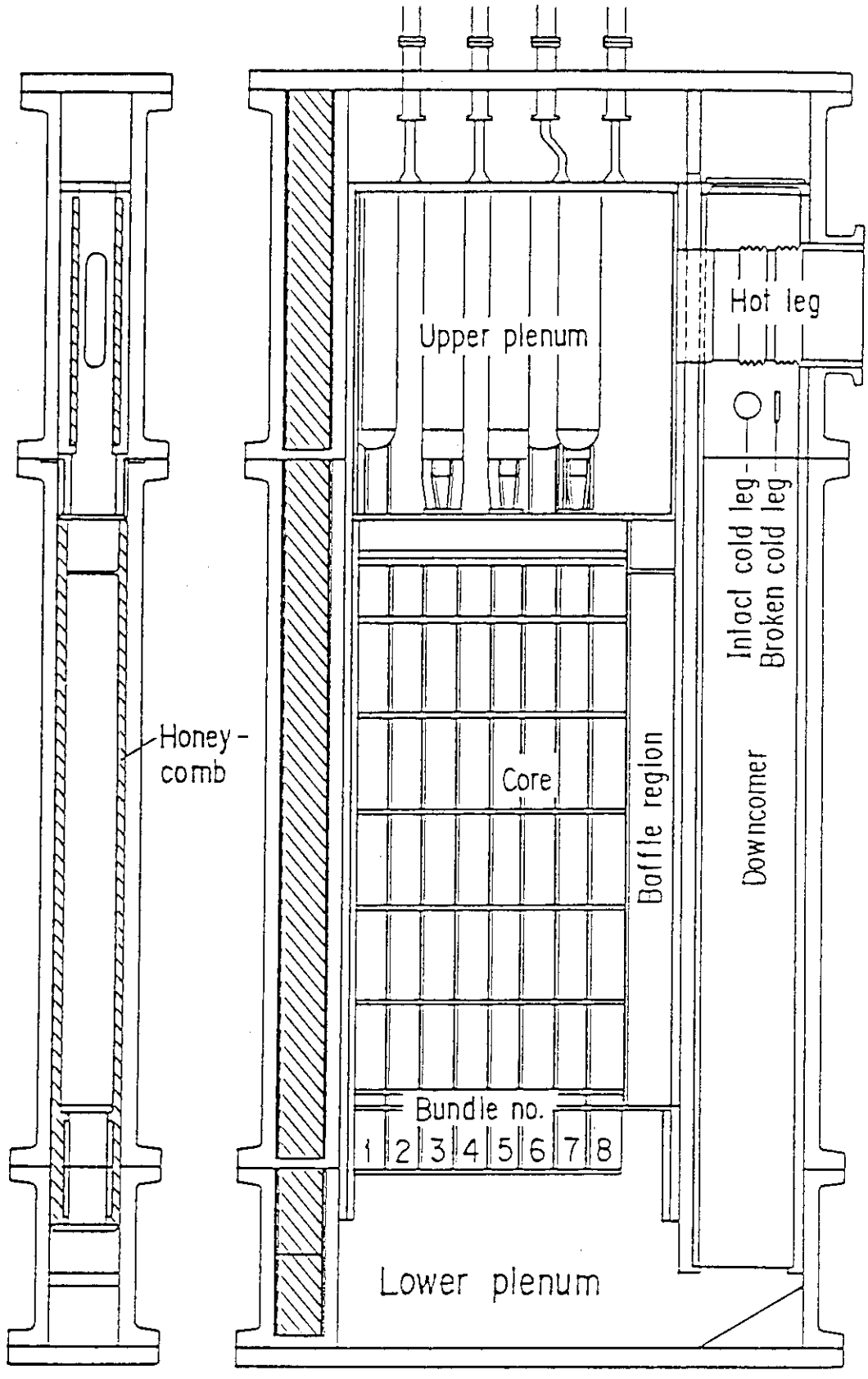

Fig. 2.2 Pressure vessel of SCTF Core-III

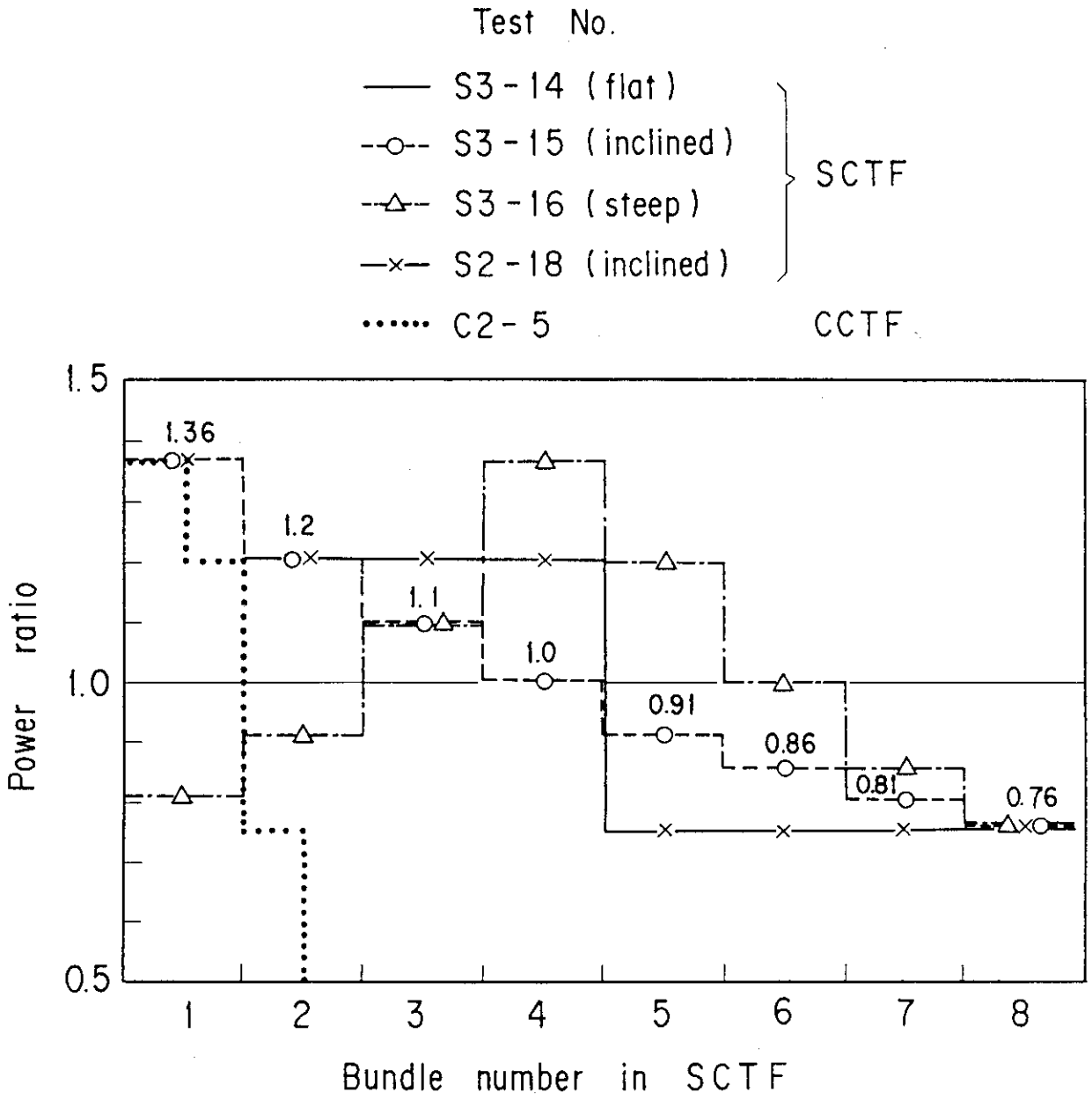

Fig. 2.3 Radial power distributions for Tests S3-14, S3-15, S3-16, S2-18, and C2-5

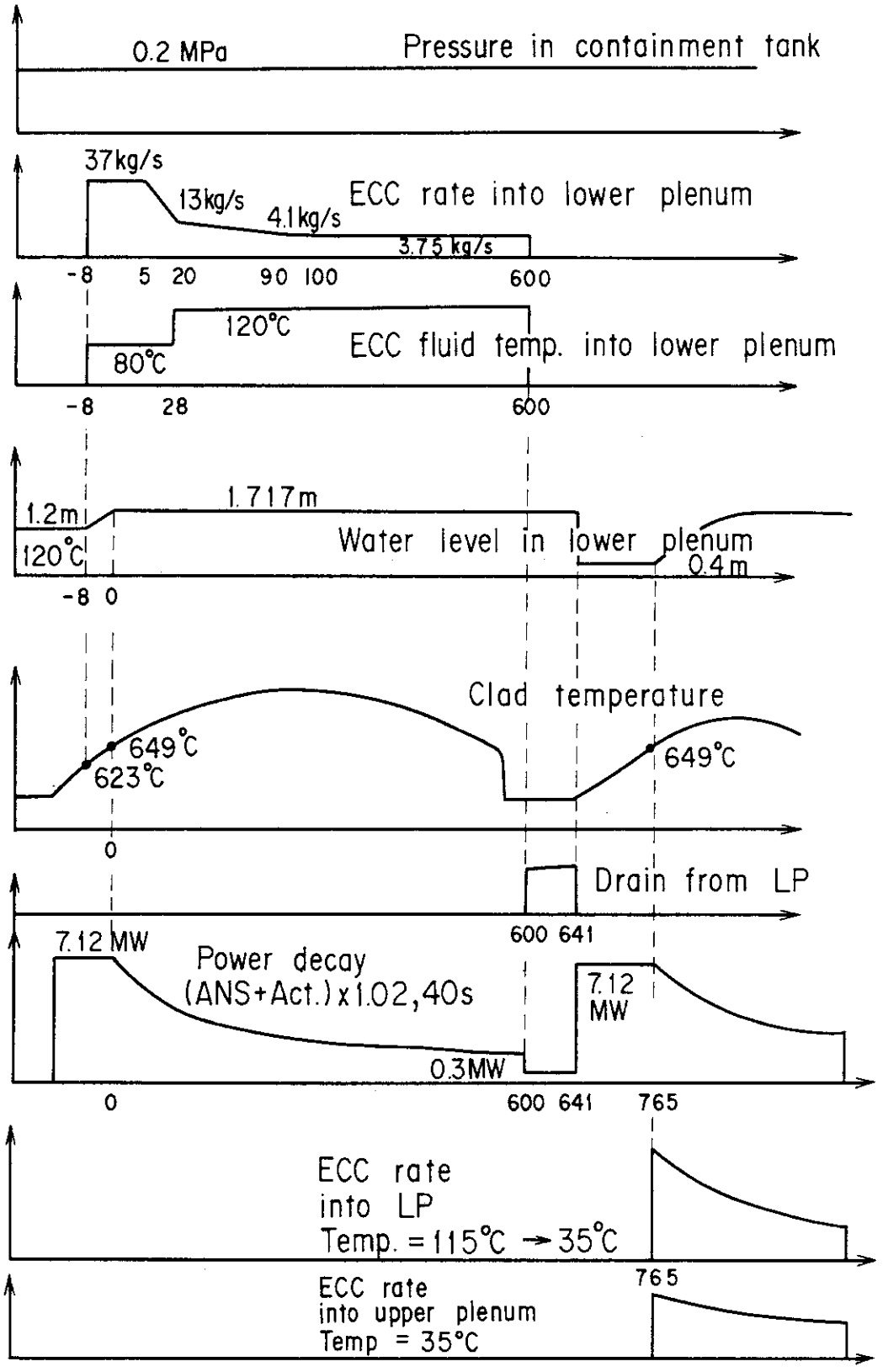

Fig. 2.4 Test sequence of Test S3-14

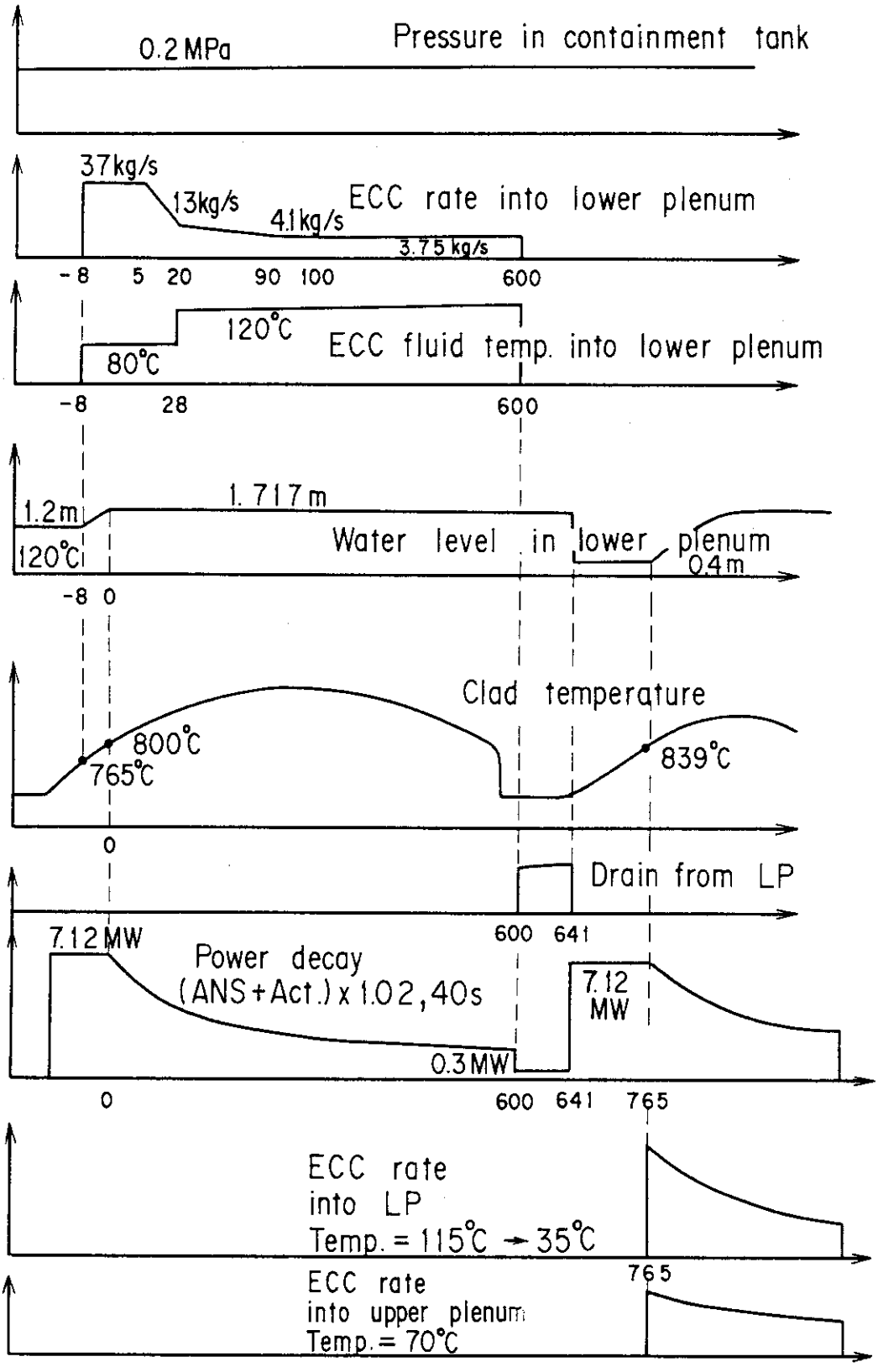

Fig. 2.5 Test sequence of Test S3-15

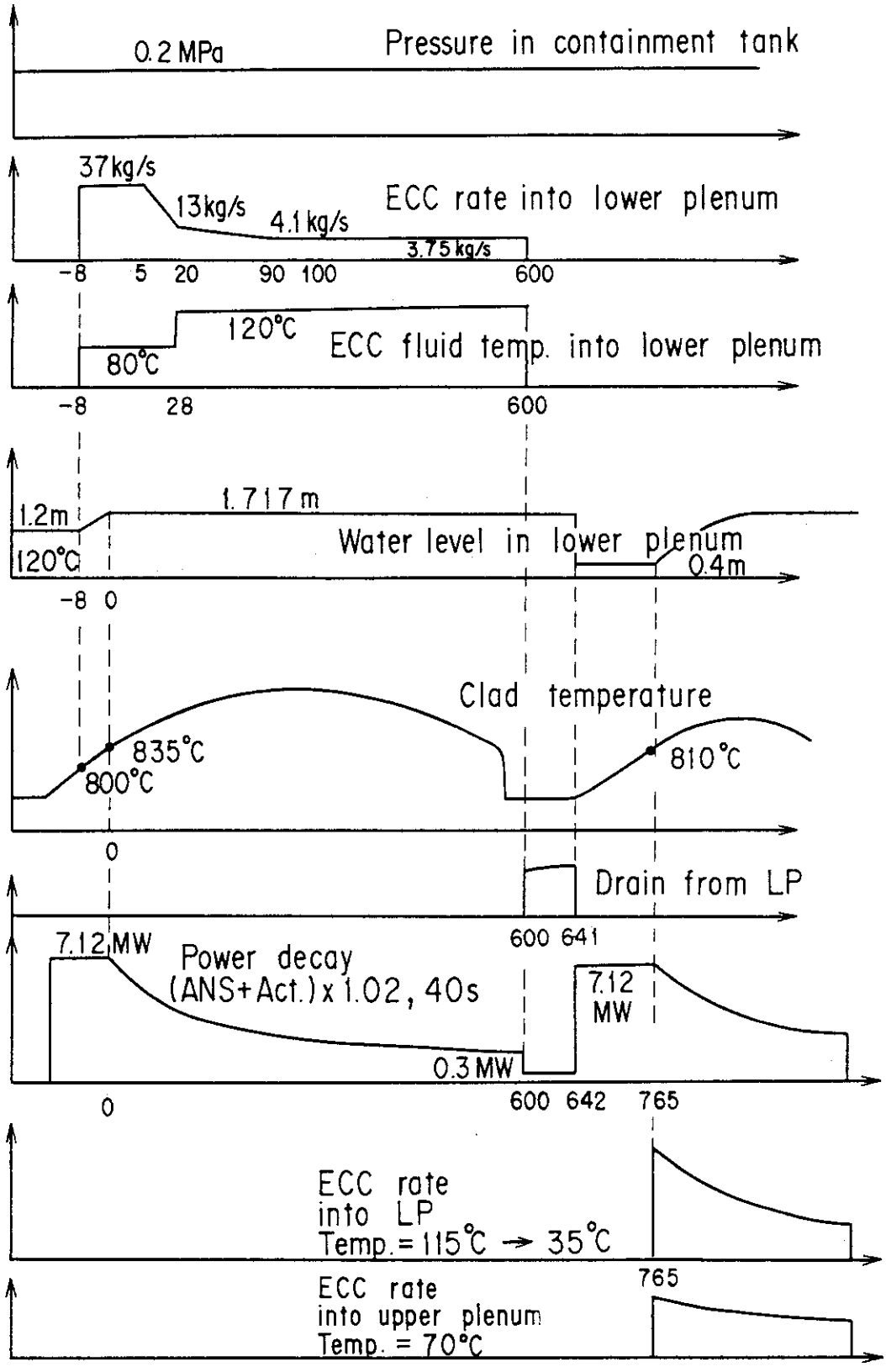

Fig. 2.6 Test sequence of Test S3-16

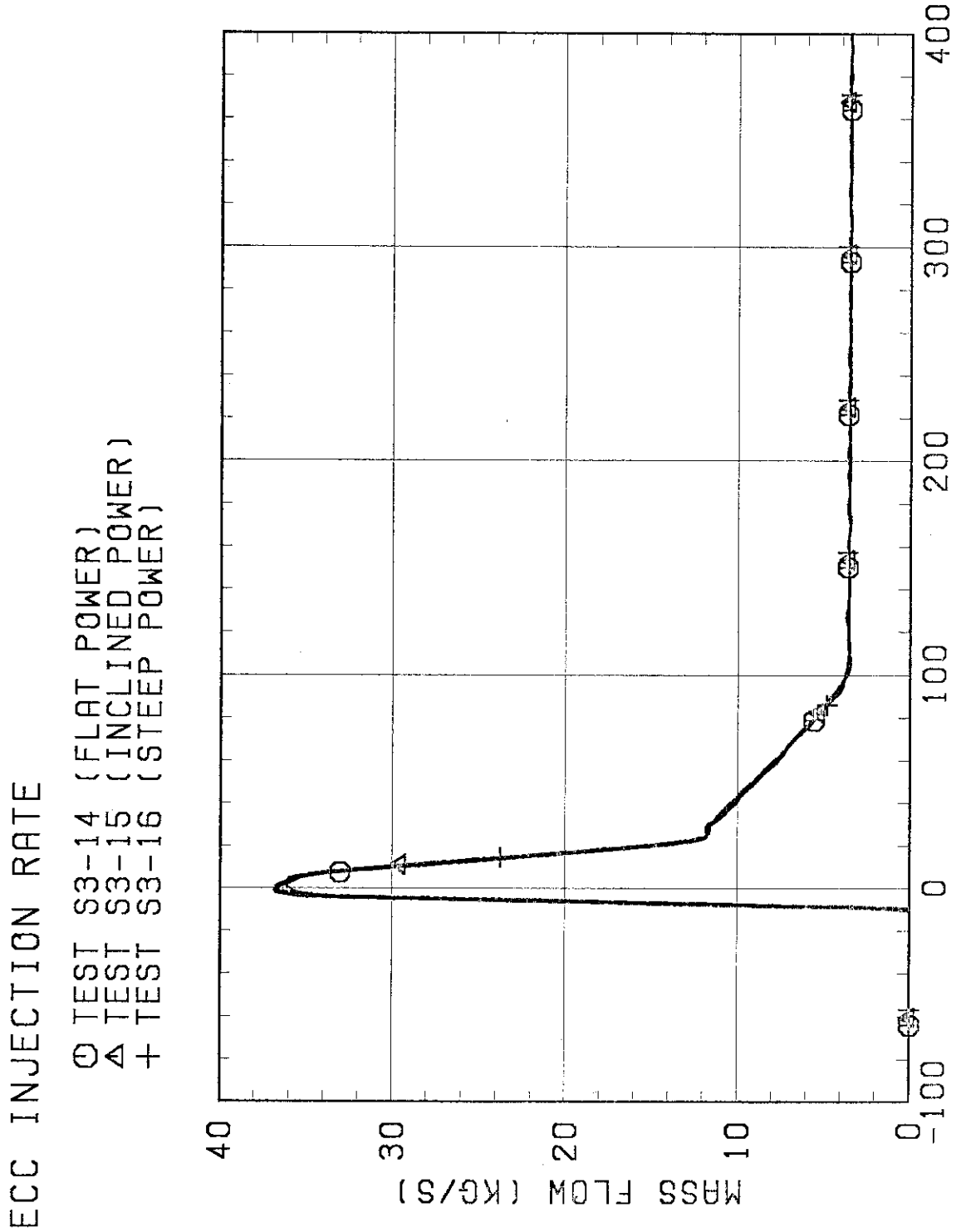

Fig. 3.1 ECC injection rates into lower plenum

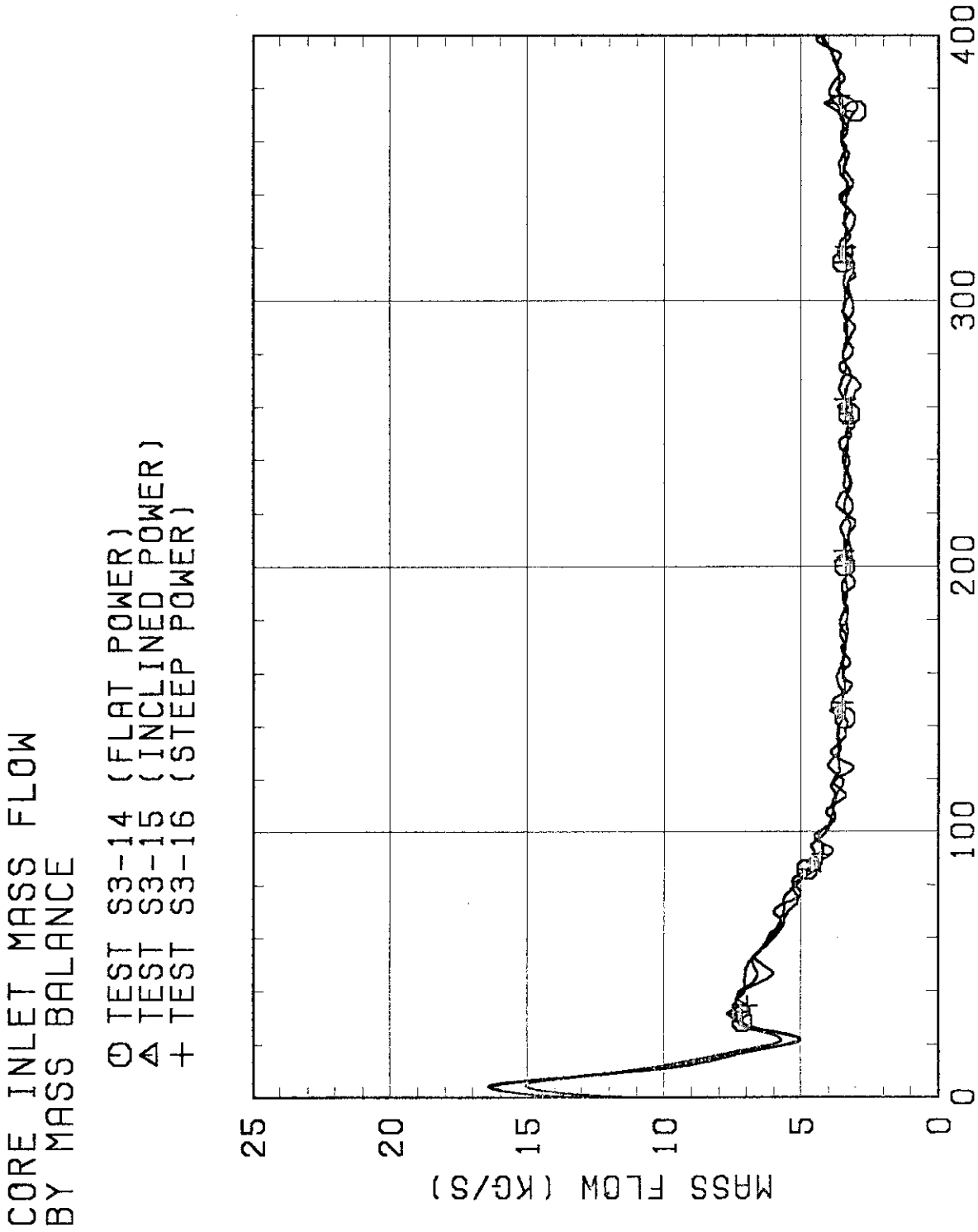

Fig. 3.2 Comparison of mass flow rates at core inlet obtained by mass balance method

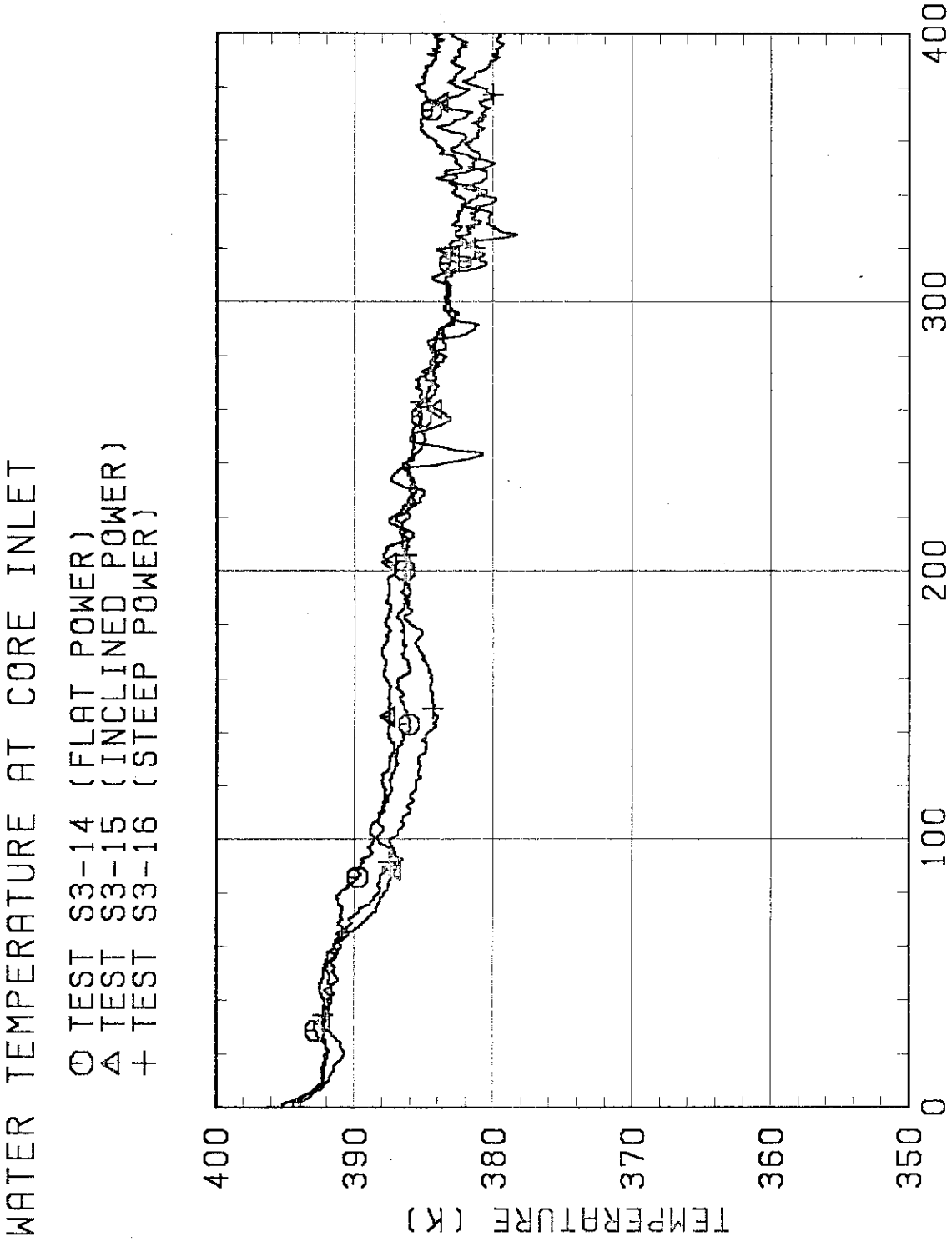

Fig. 3.3 Comparison of water temperatures at core inlet

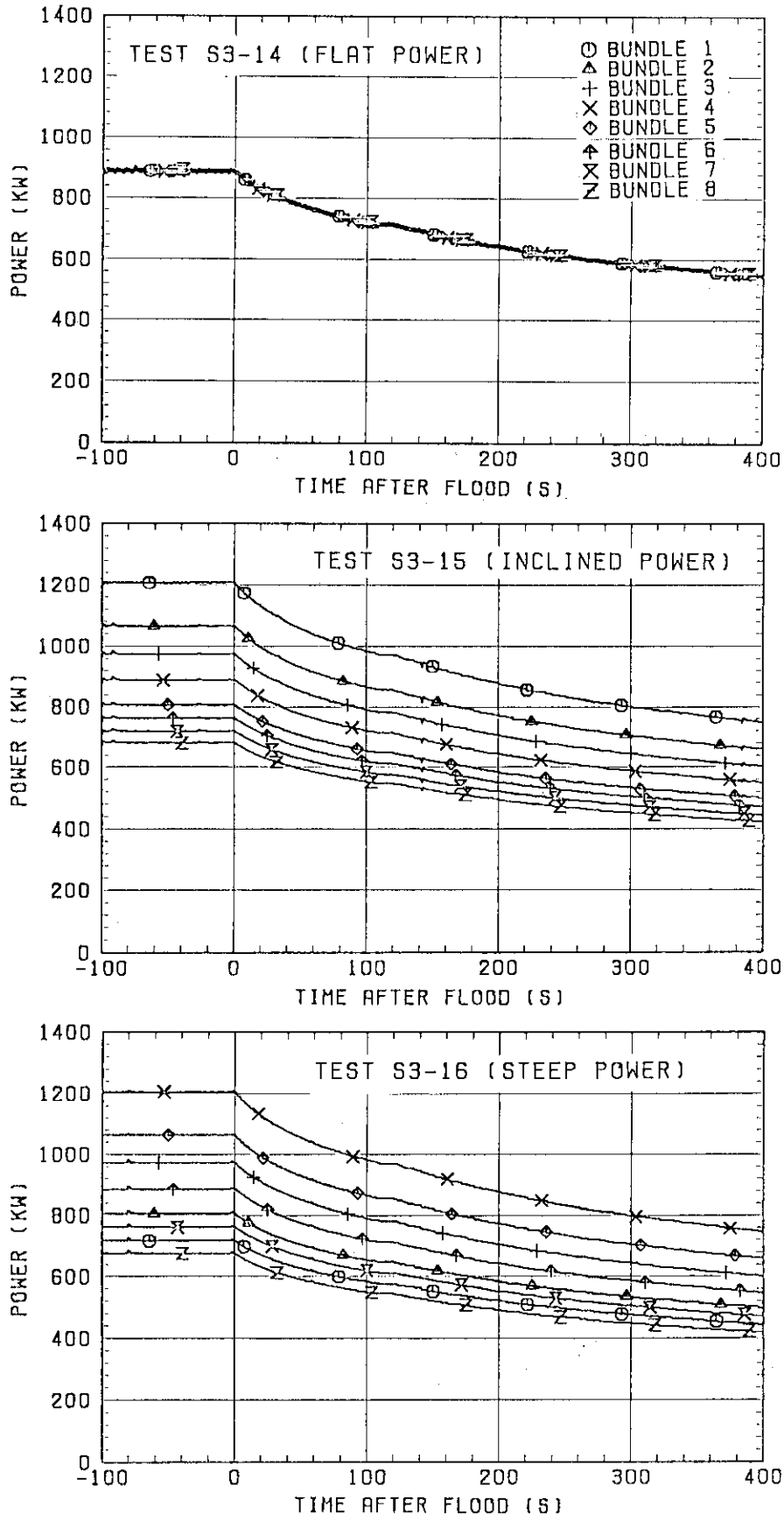

Fig. 3.4 Comparison of core heating power

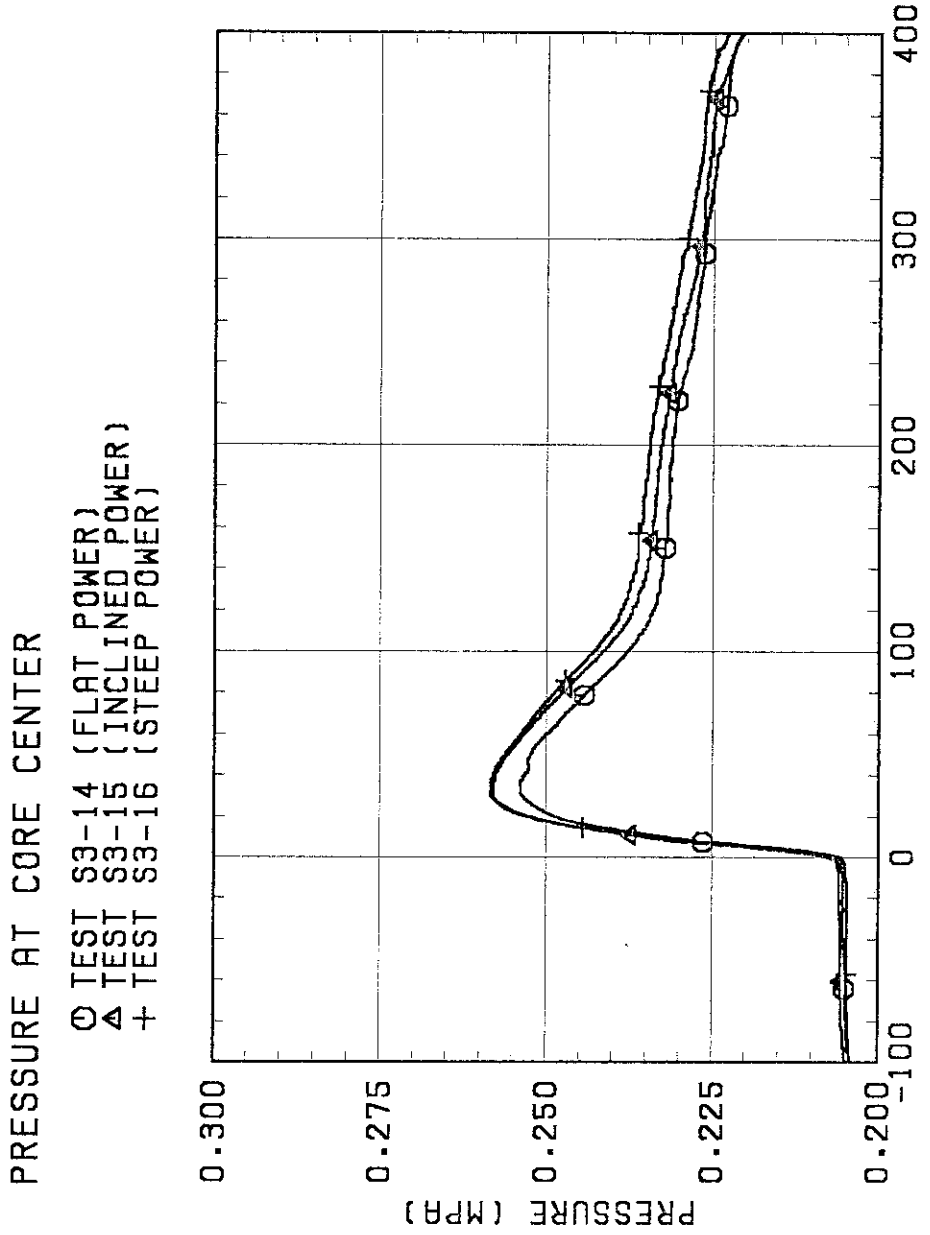

Fig. 3.5 Comparison of pressures at core center

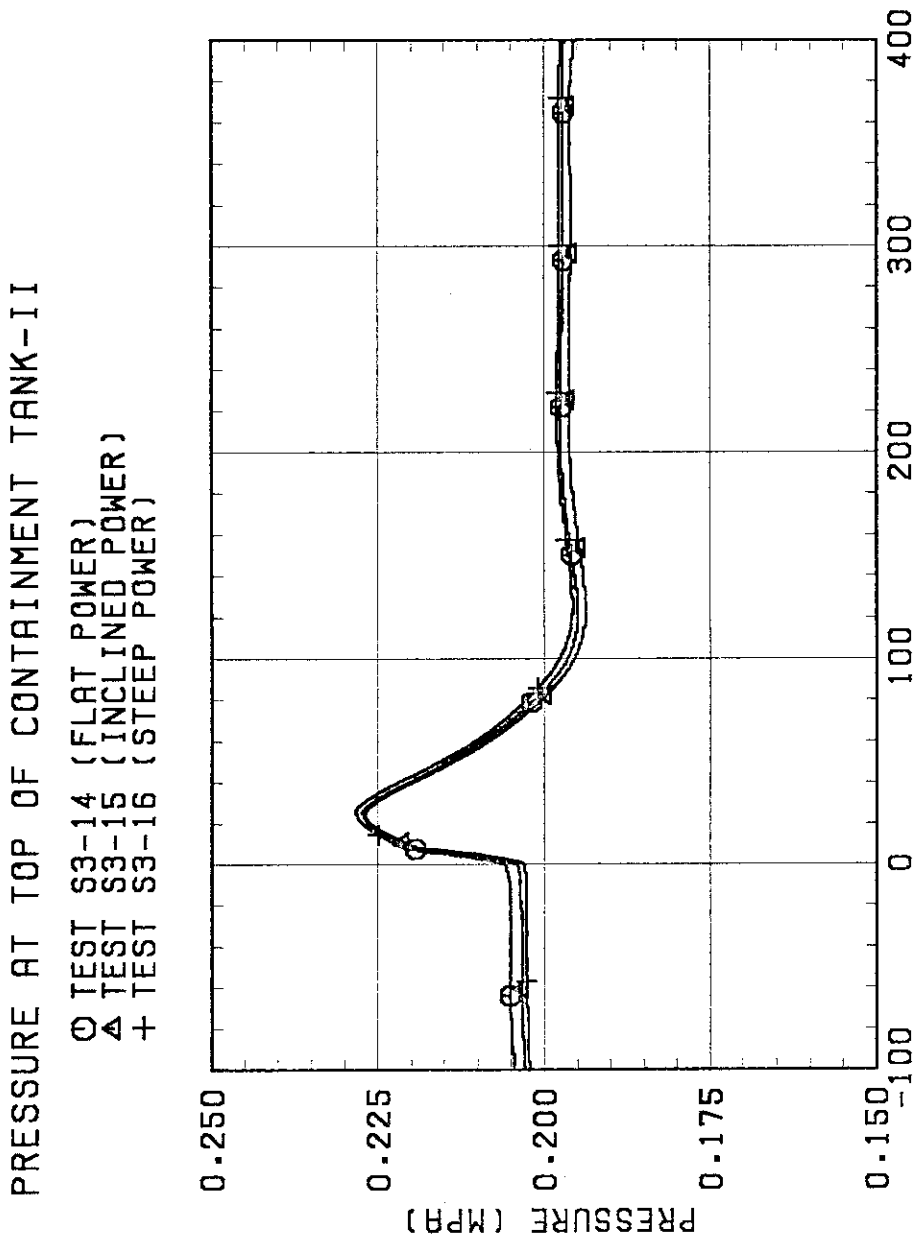

Fig. 3.6 Comparison of pressures at the top of containment tank-II

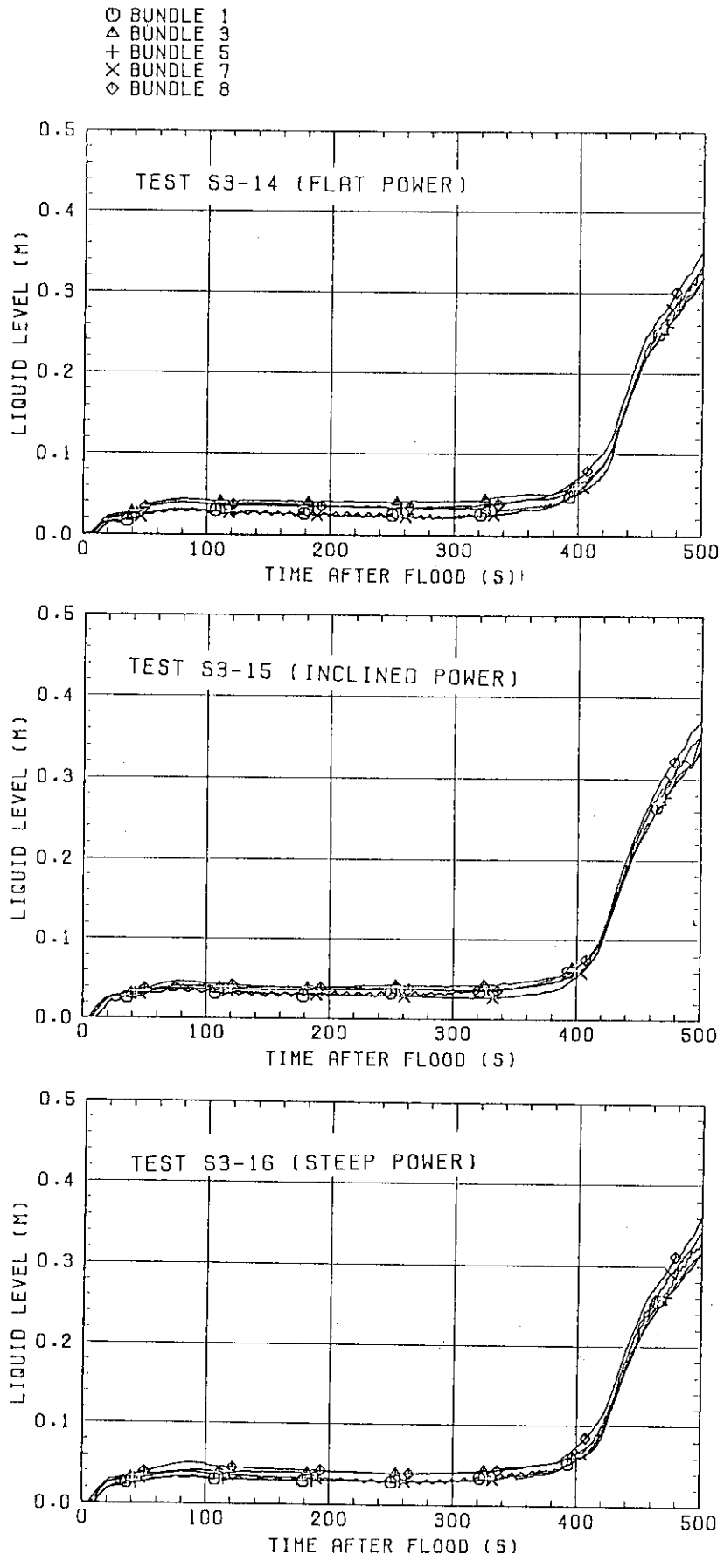

Fig. 3.7 Comparison of collapsed liquid levels in upper plenum

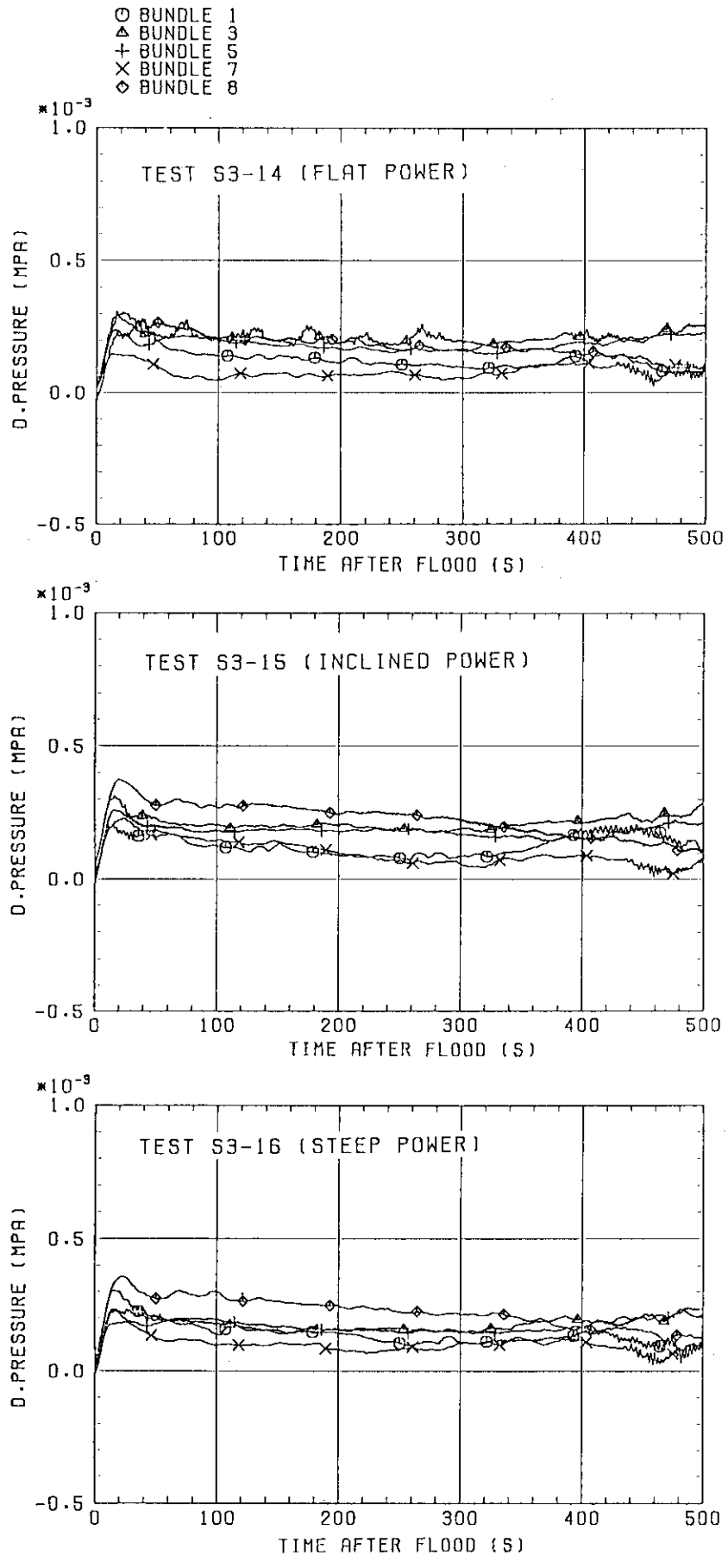

Fig. 3.8 Comparison of differential pressures across end box tie plate

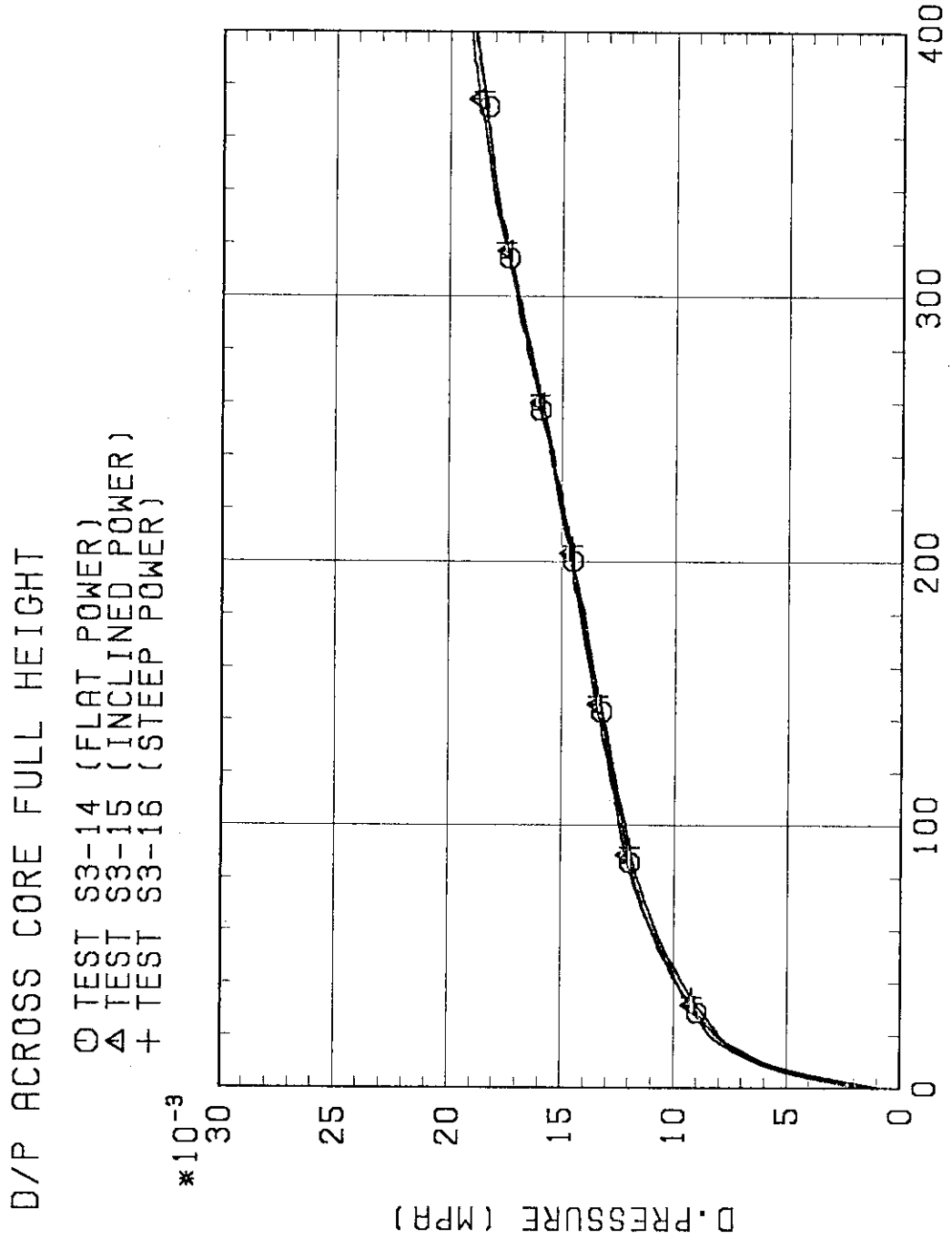

Fig. 3.9 Comparison of differential pressures across core full height

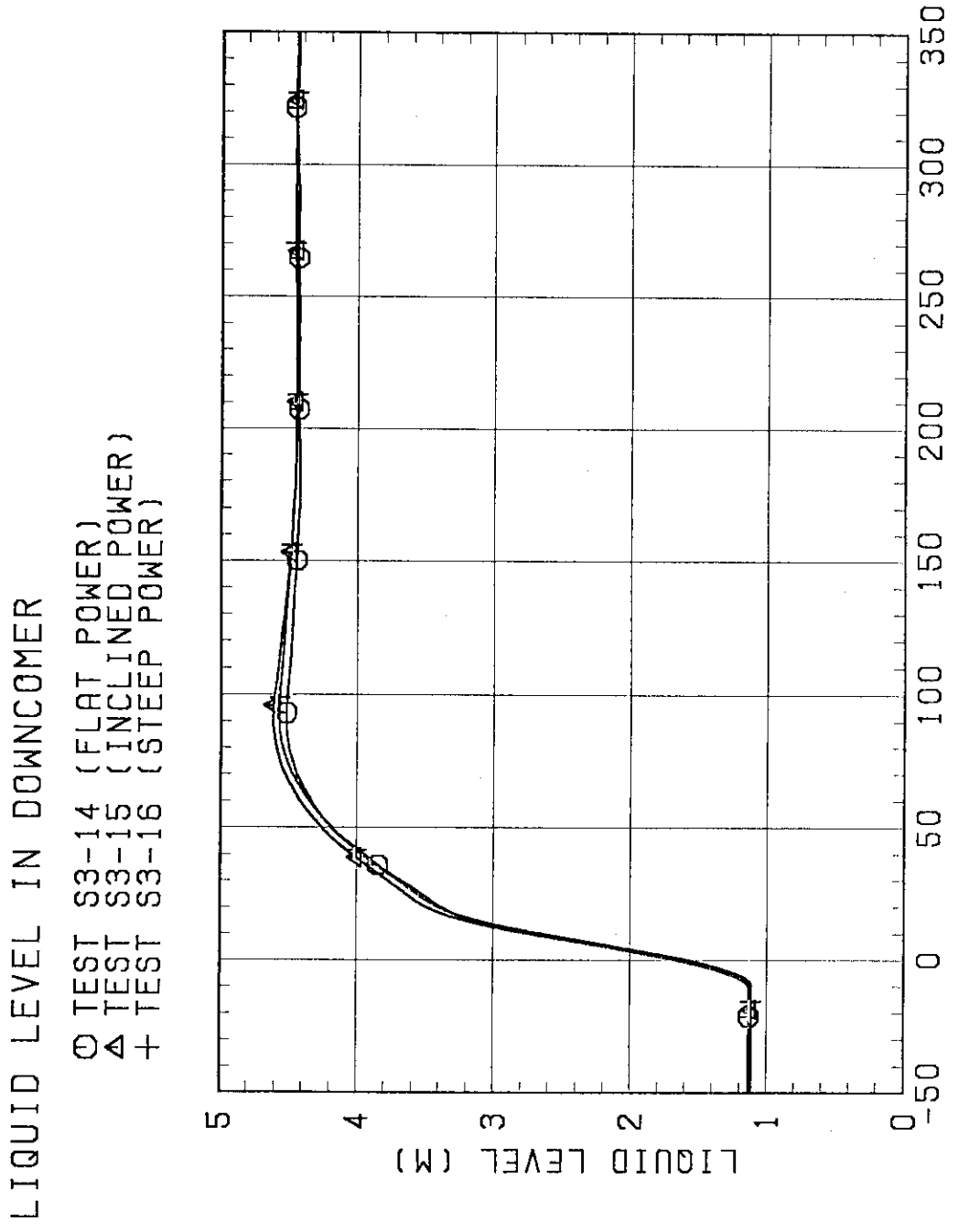

Fig. 3.10 Comparison of collapsed liquid levels in downcomer

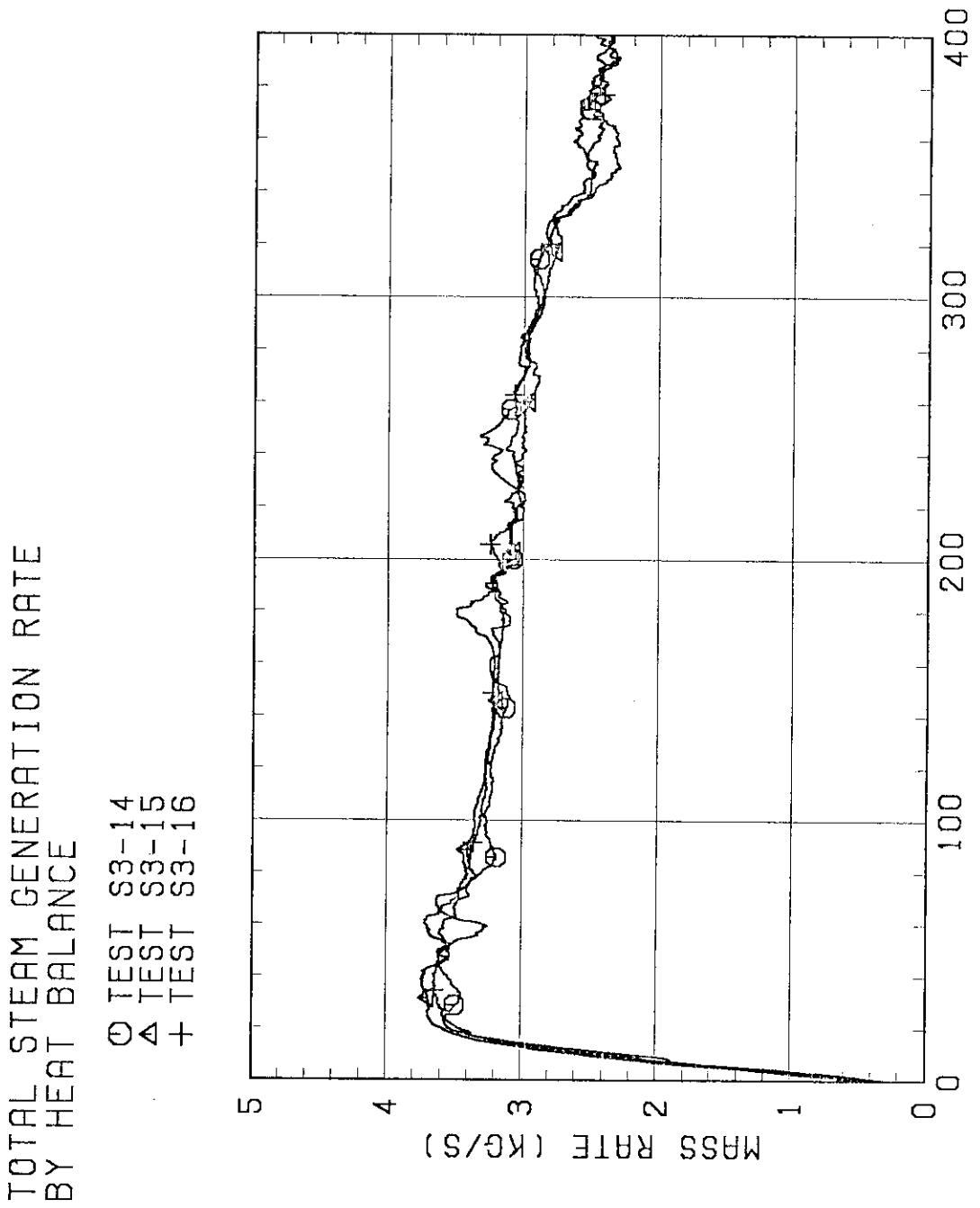

Fig. 3.11 Comparison of steam generation rates calculated from heat balance method

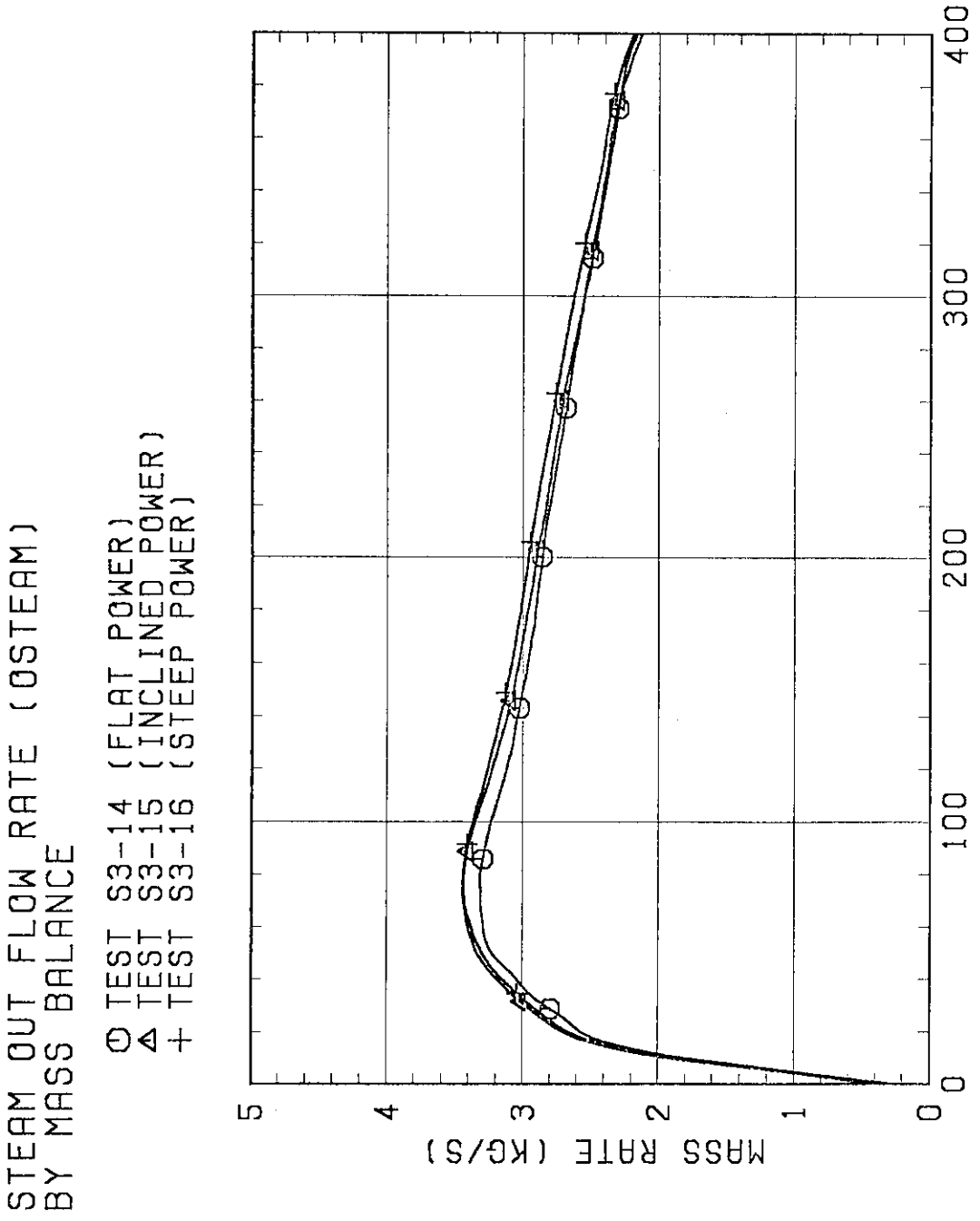

Fig. 3.12 Comparison of steam outflow rates from pressure vessel obtained by mass balance method

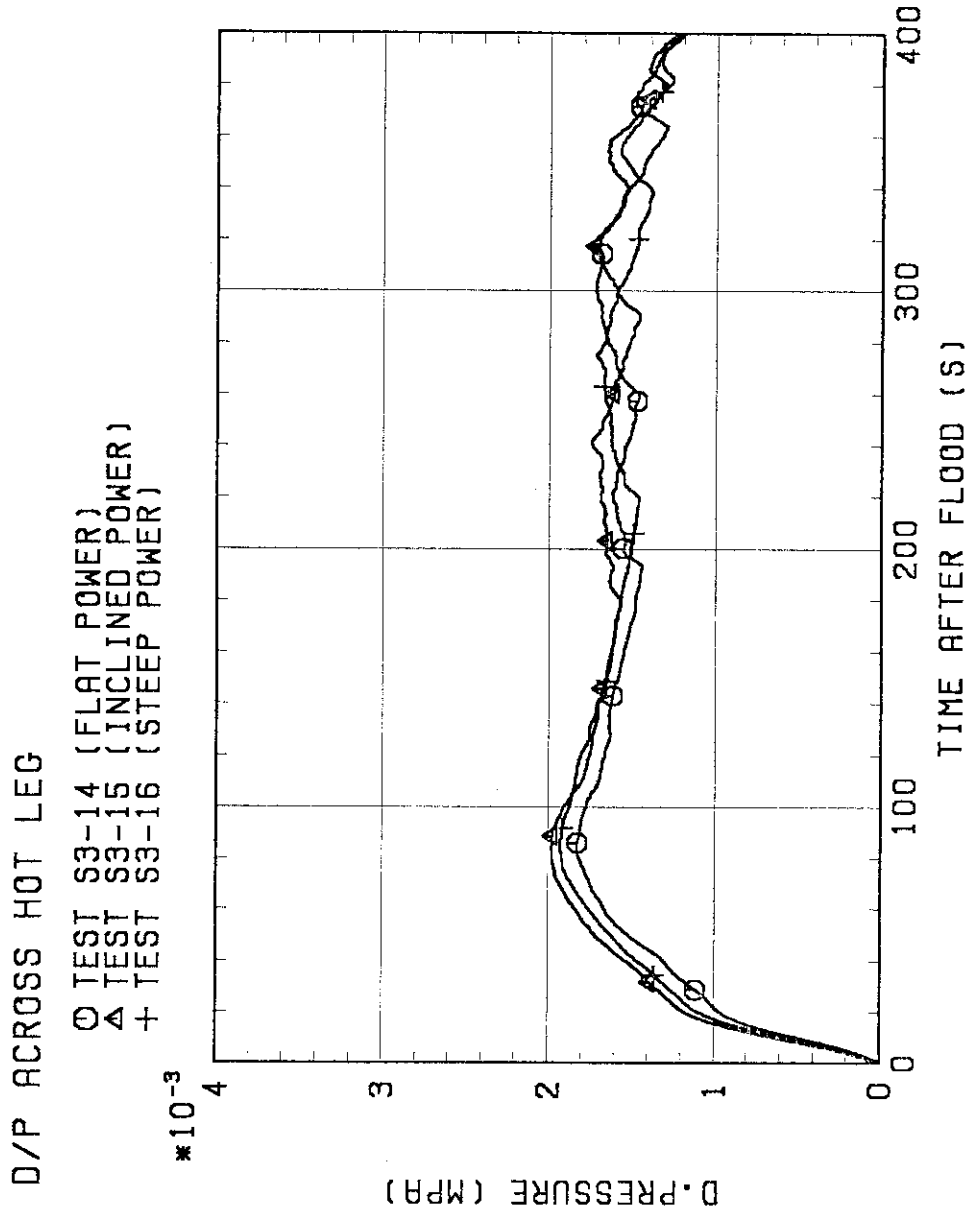

Fig. 3.13 Comparison of differential pressures across hot leg

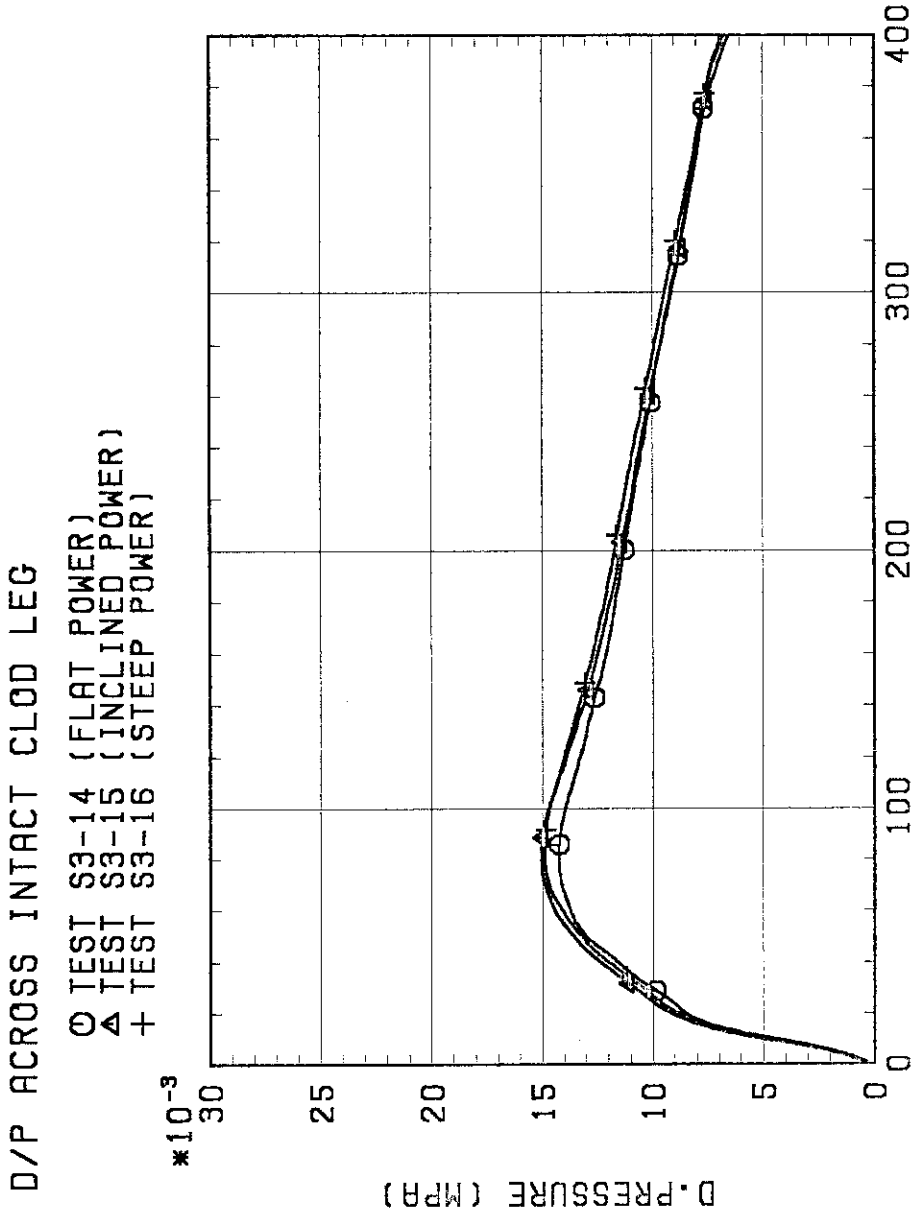

Fig. 3.14 Comparison of differential pressures across intact cold leg

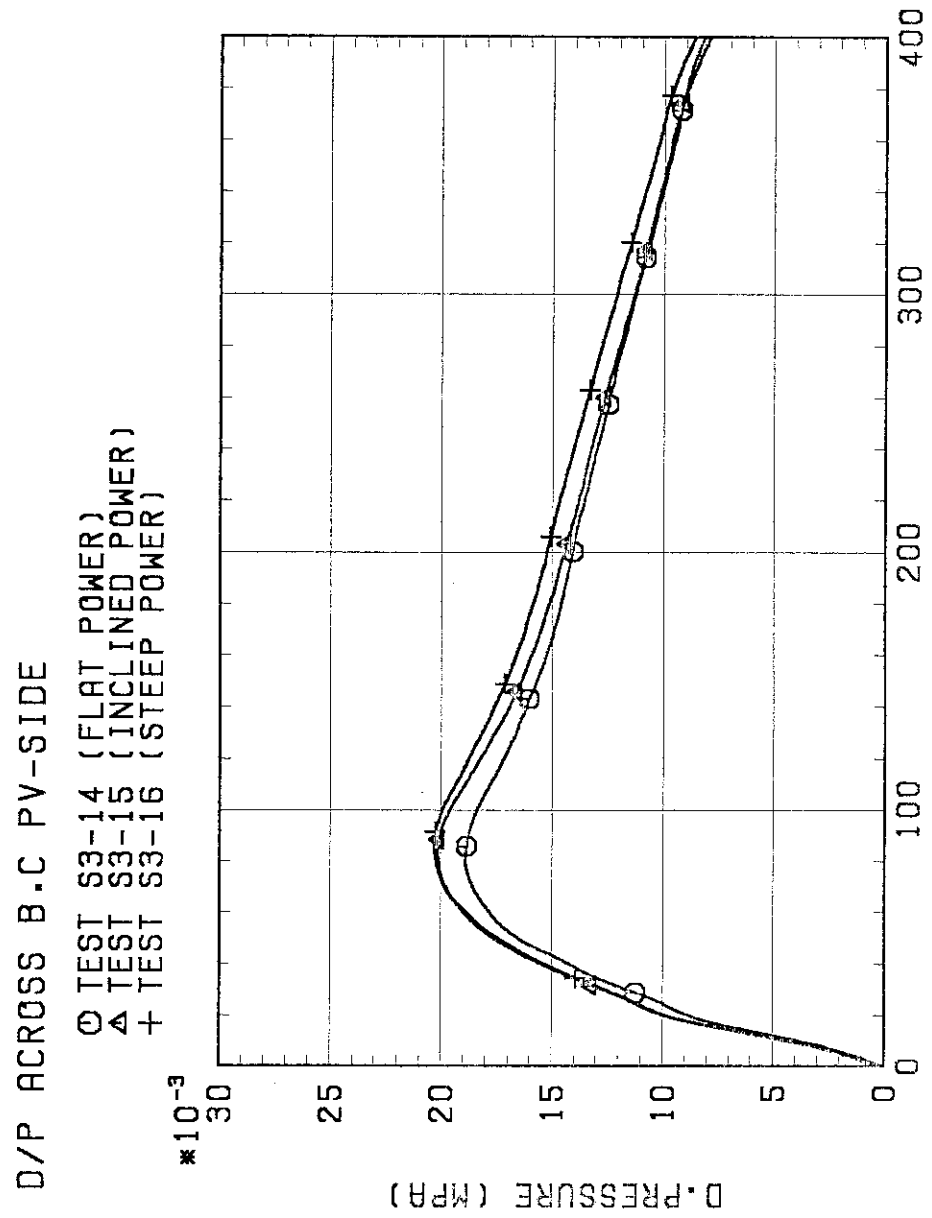

Fig. 3.15 Comparison of differential pressures across broken cold leg pressure vessel side

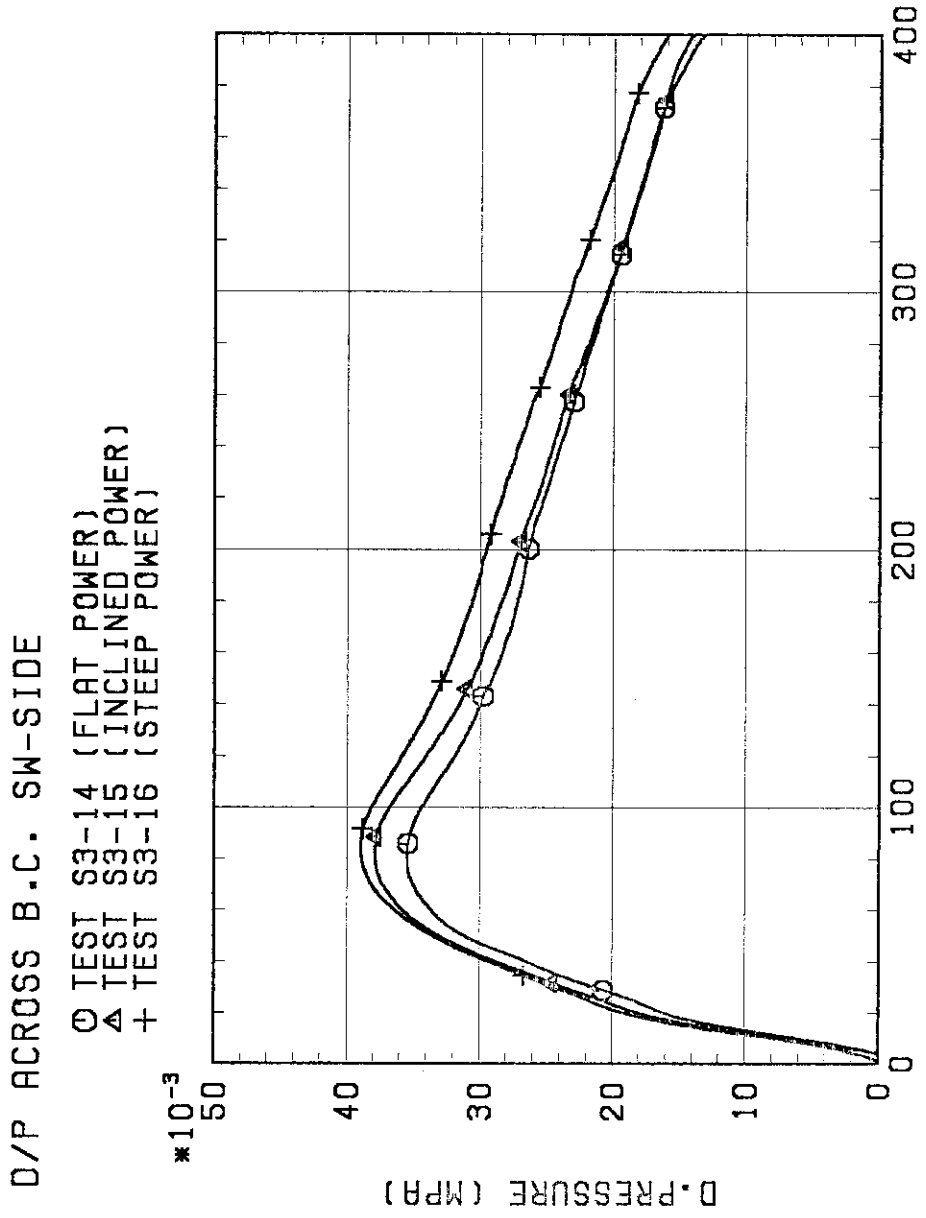

Fig. 3.16 Comparison of differential pressures across broken cold leg steam/water separator side

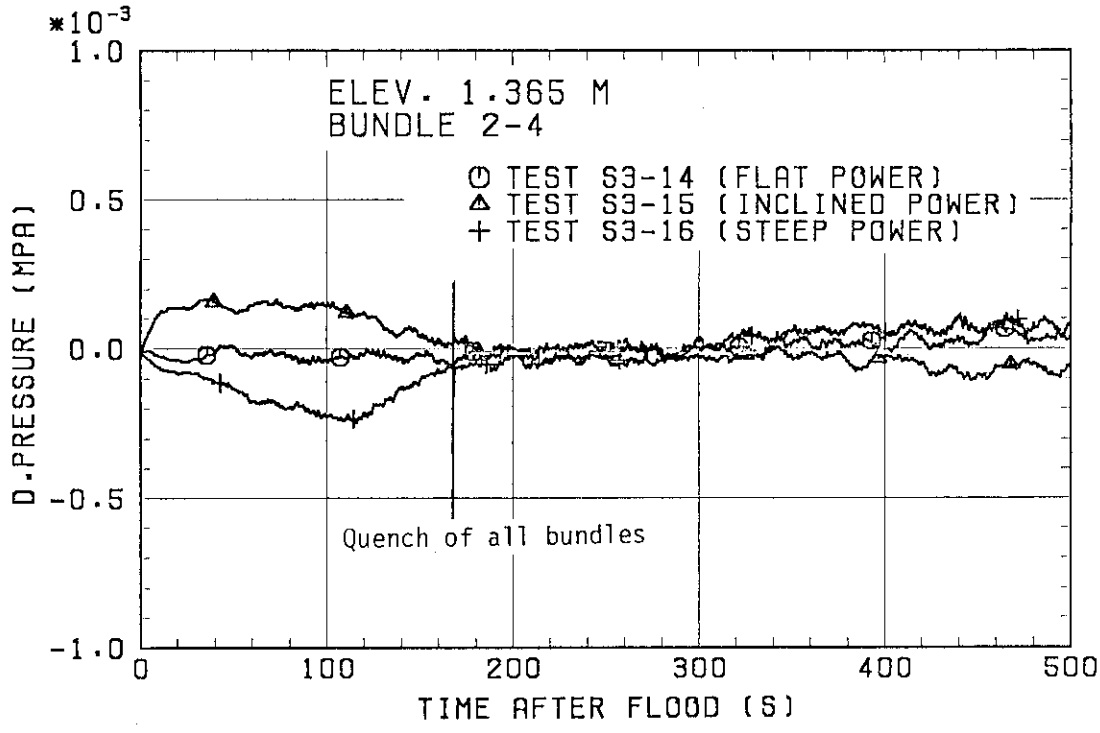

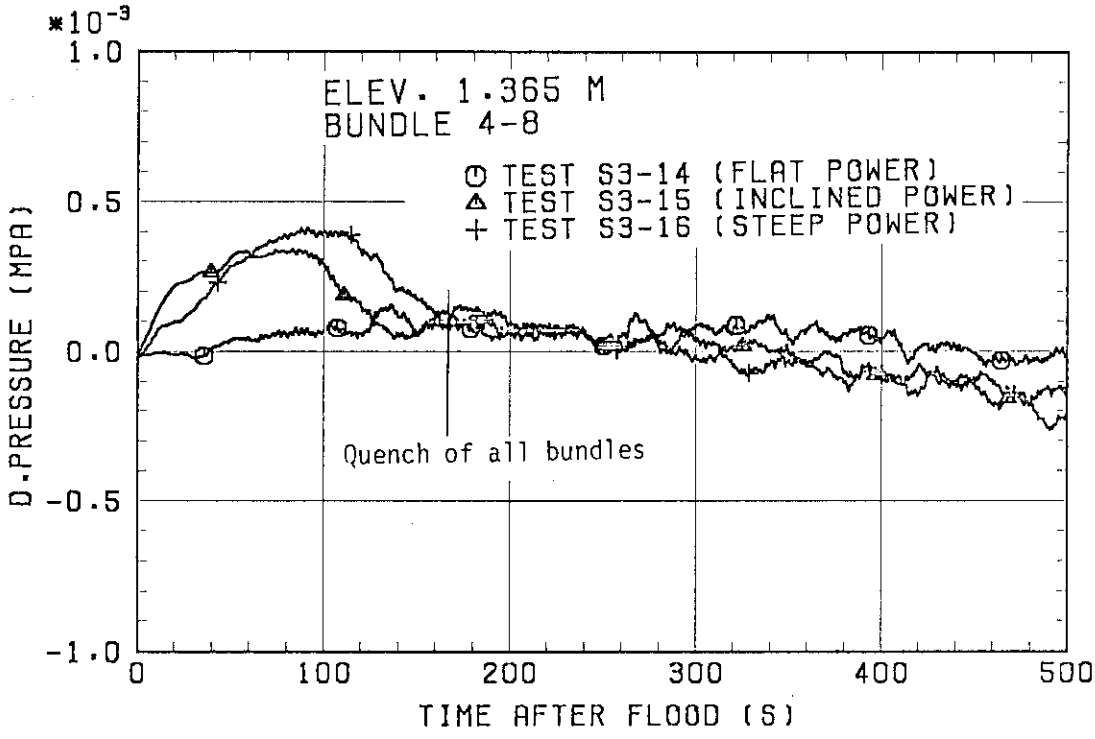

Fig. 3.17 Comparison of horizontal differential pressures in core at 1.365 m

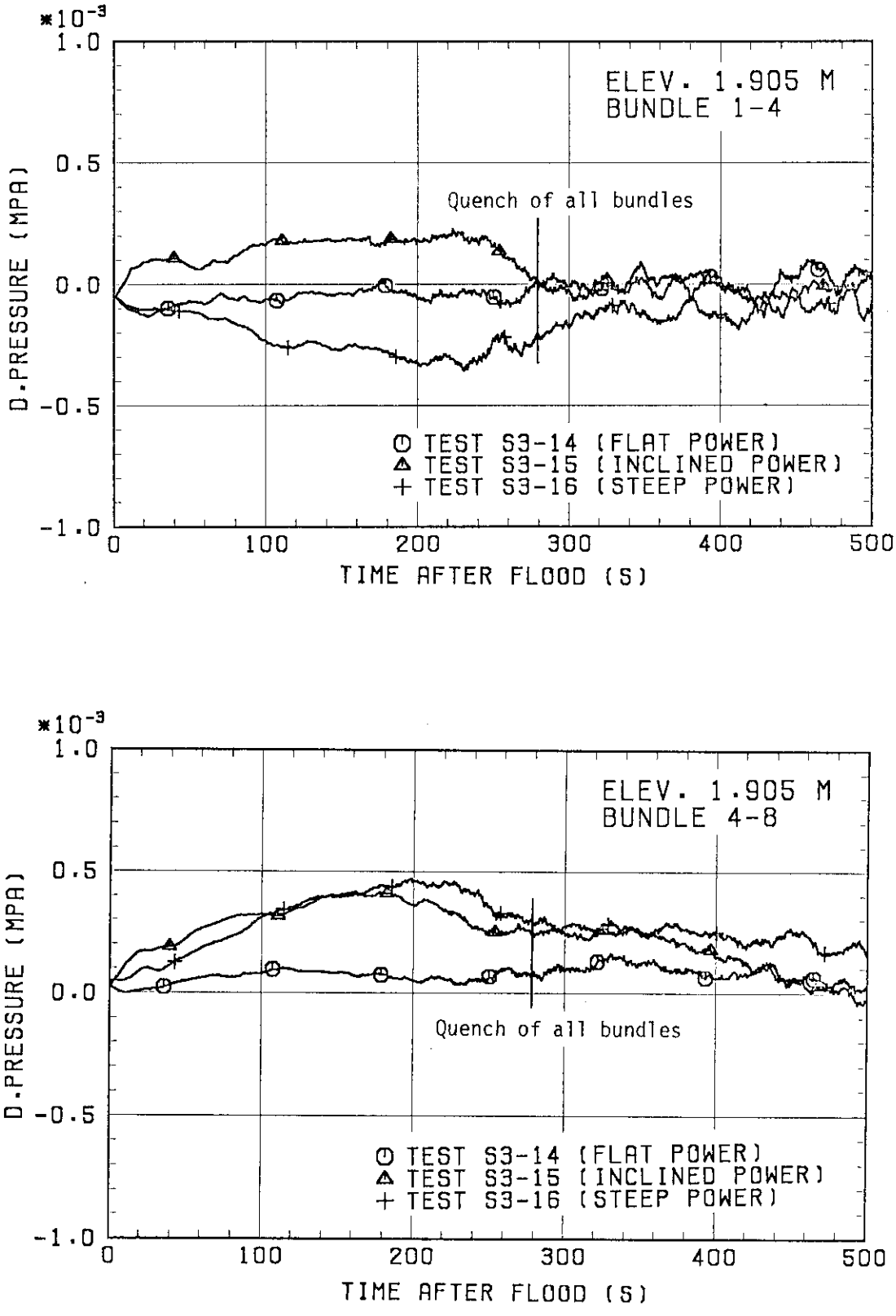

Fig. 3.18 Comparison of horizontal differential pressures in core at 1.905 m

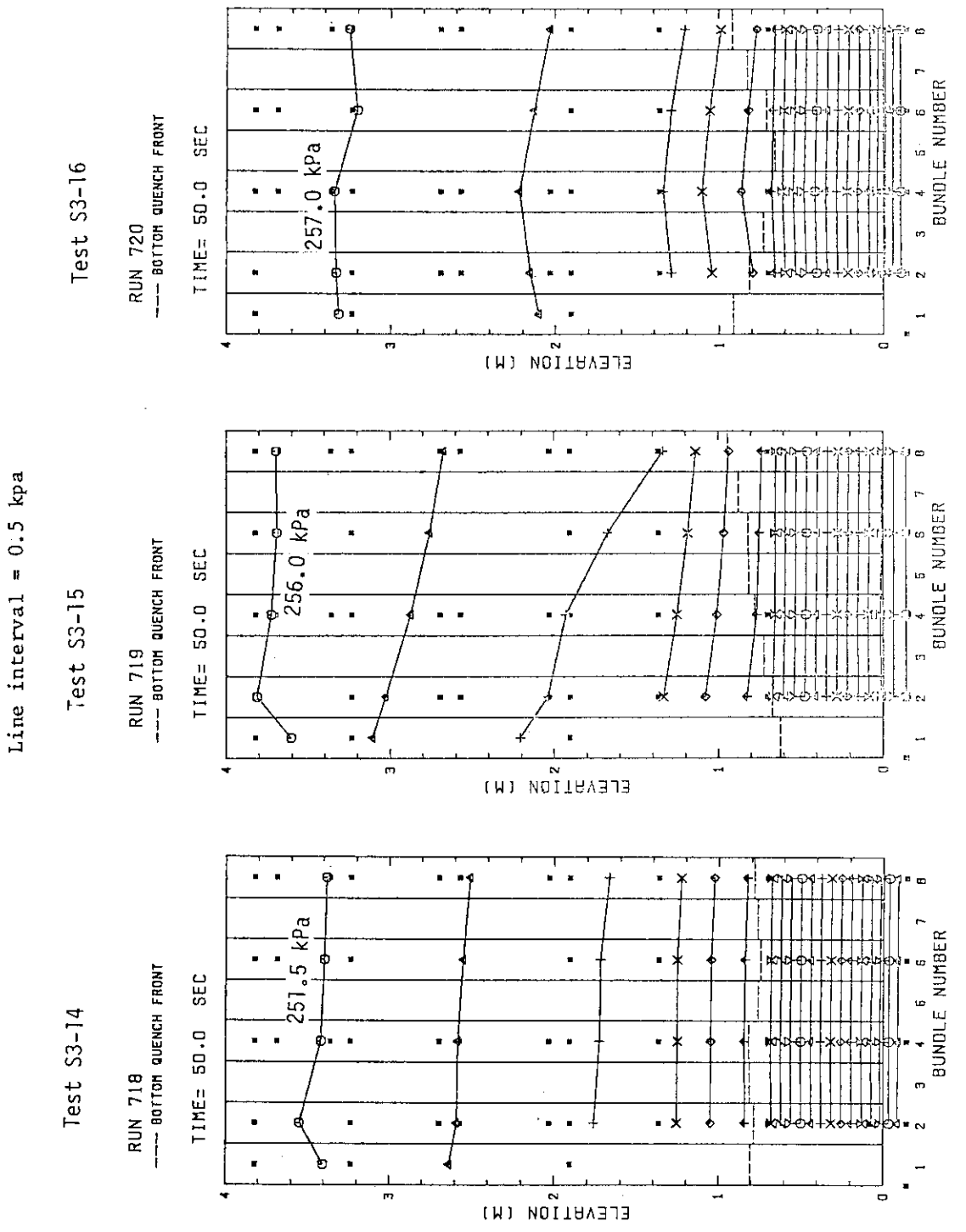

Fig. 3.19(a) Comparison of equal pressure lines and bottom quench front distribution (50s after BOCREC)

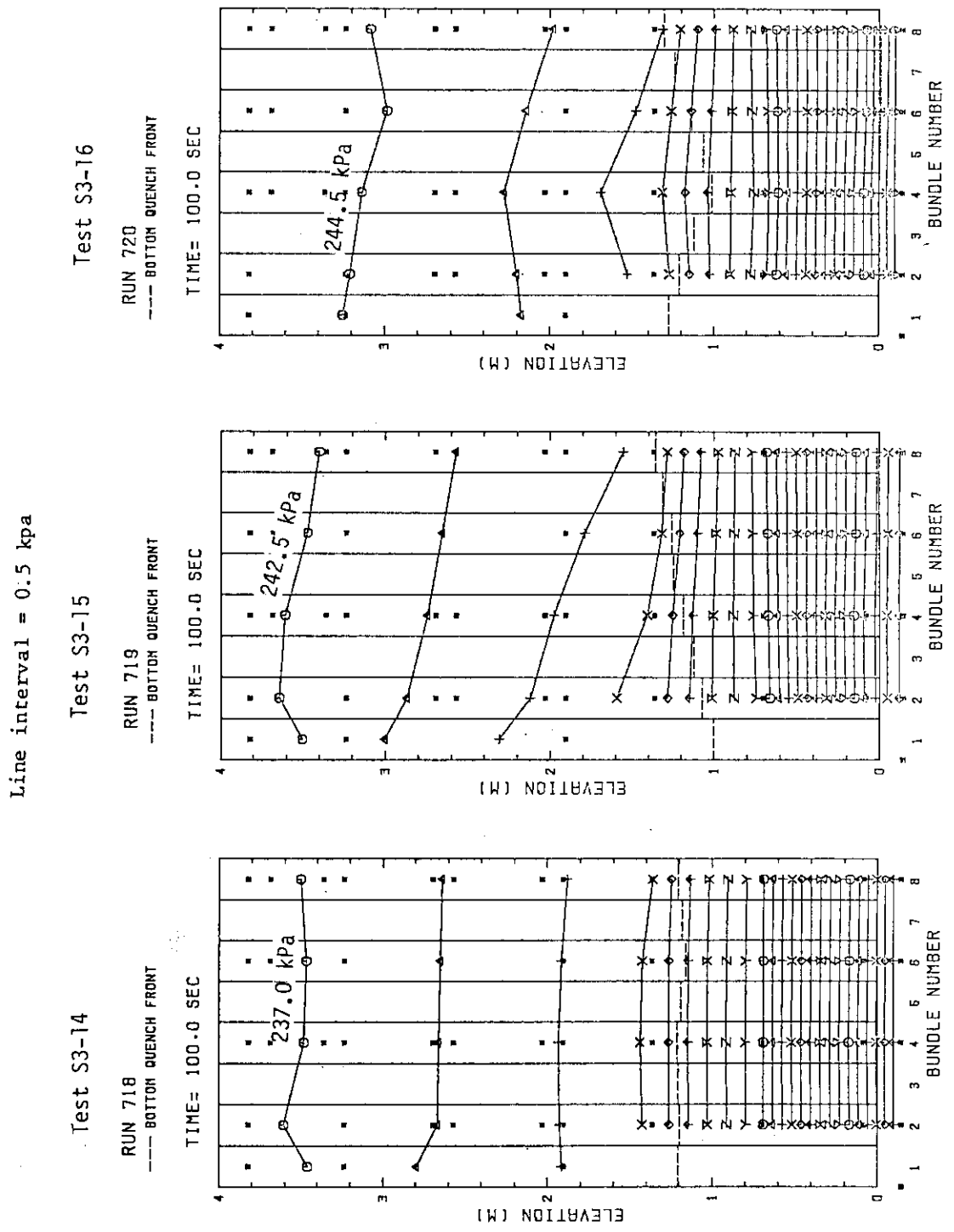

Fig. 3.19(b) Comparison of equal pressure lines and bottom quench front distribution (100s after BOCREC)

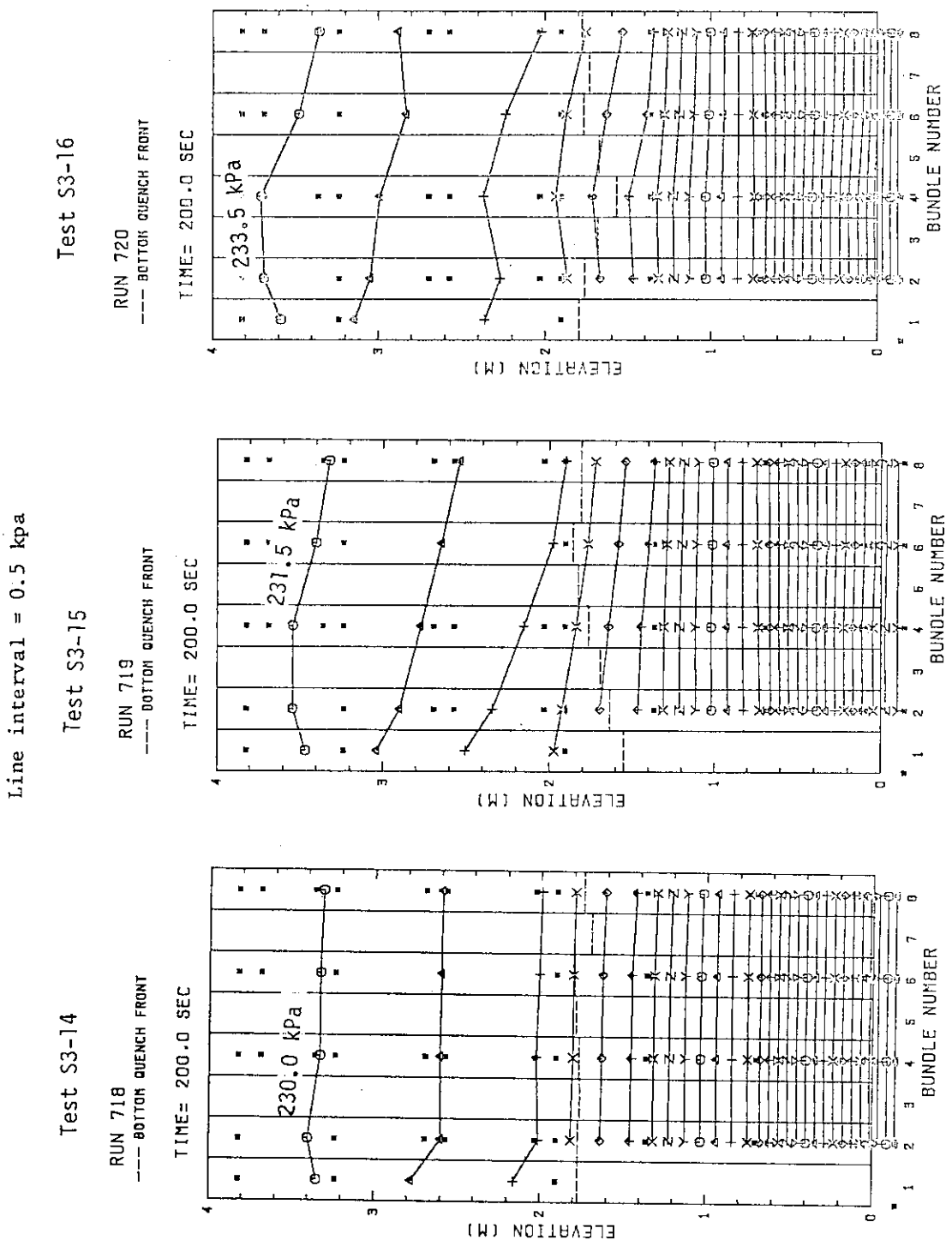

Fig. 3.19(c) Comparison of equal pressure lines and bottom quench front distrituion (200s after BOCREC)

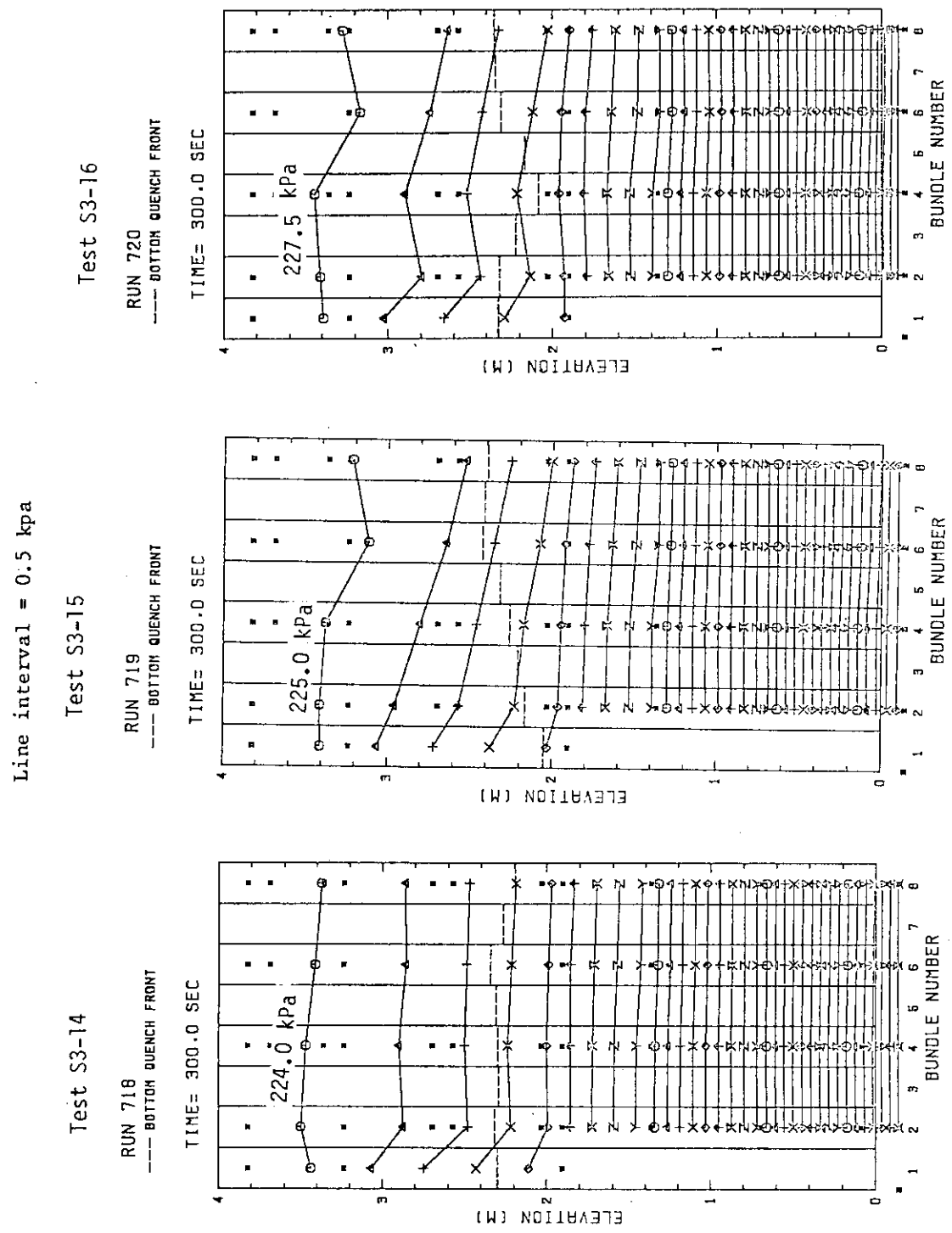

Fig. 3.19(d) Comparison of equal pressure lines and bottom quench front distrituion (300s after BOCREC)

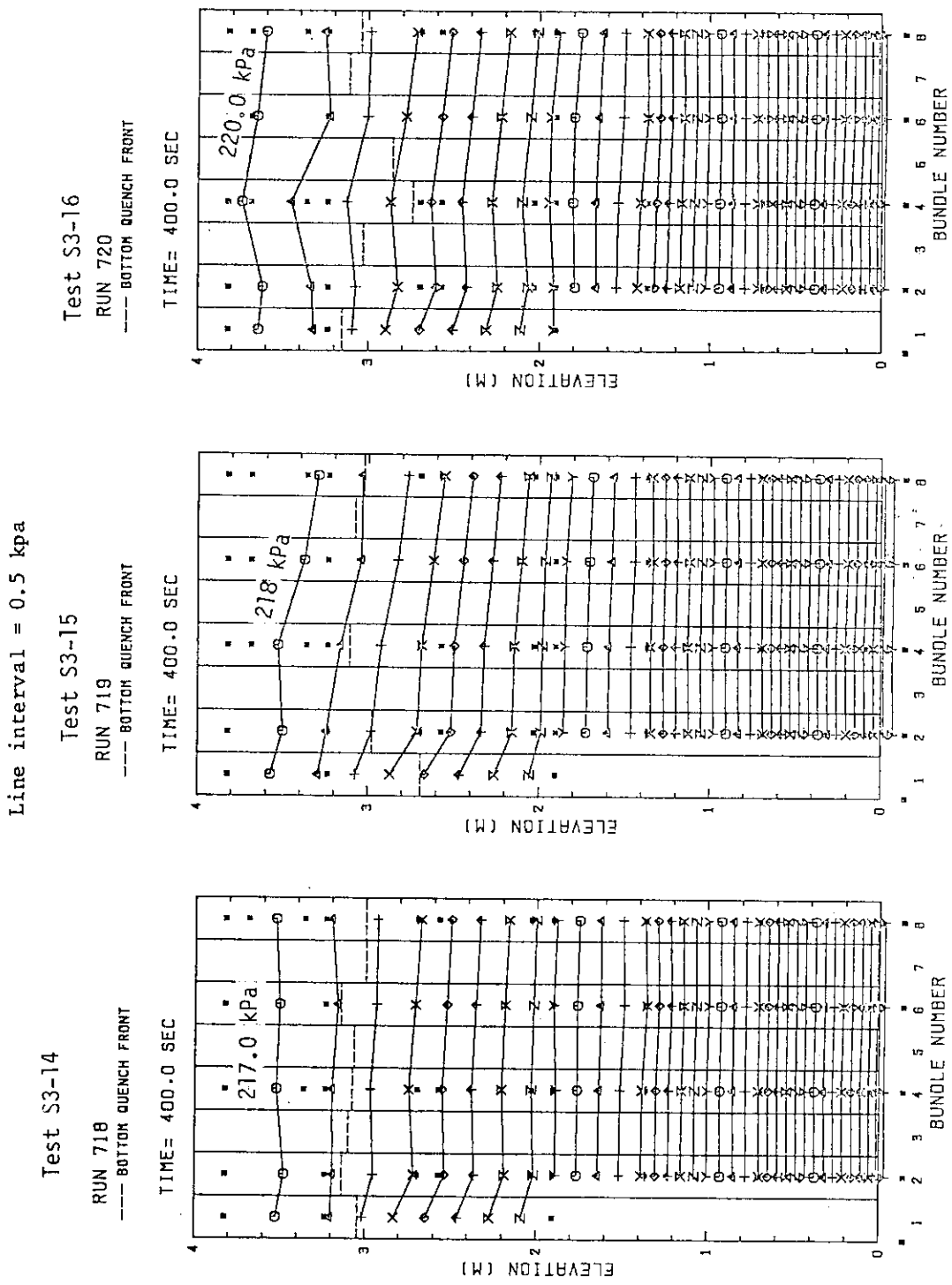

Fig. 3.19(e) Comparison of equal pressure lines and bottom quench front distrituion (400s after BOCREC)

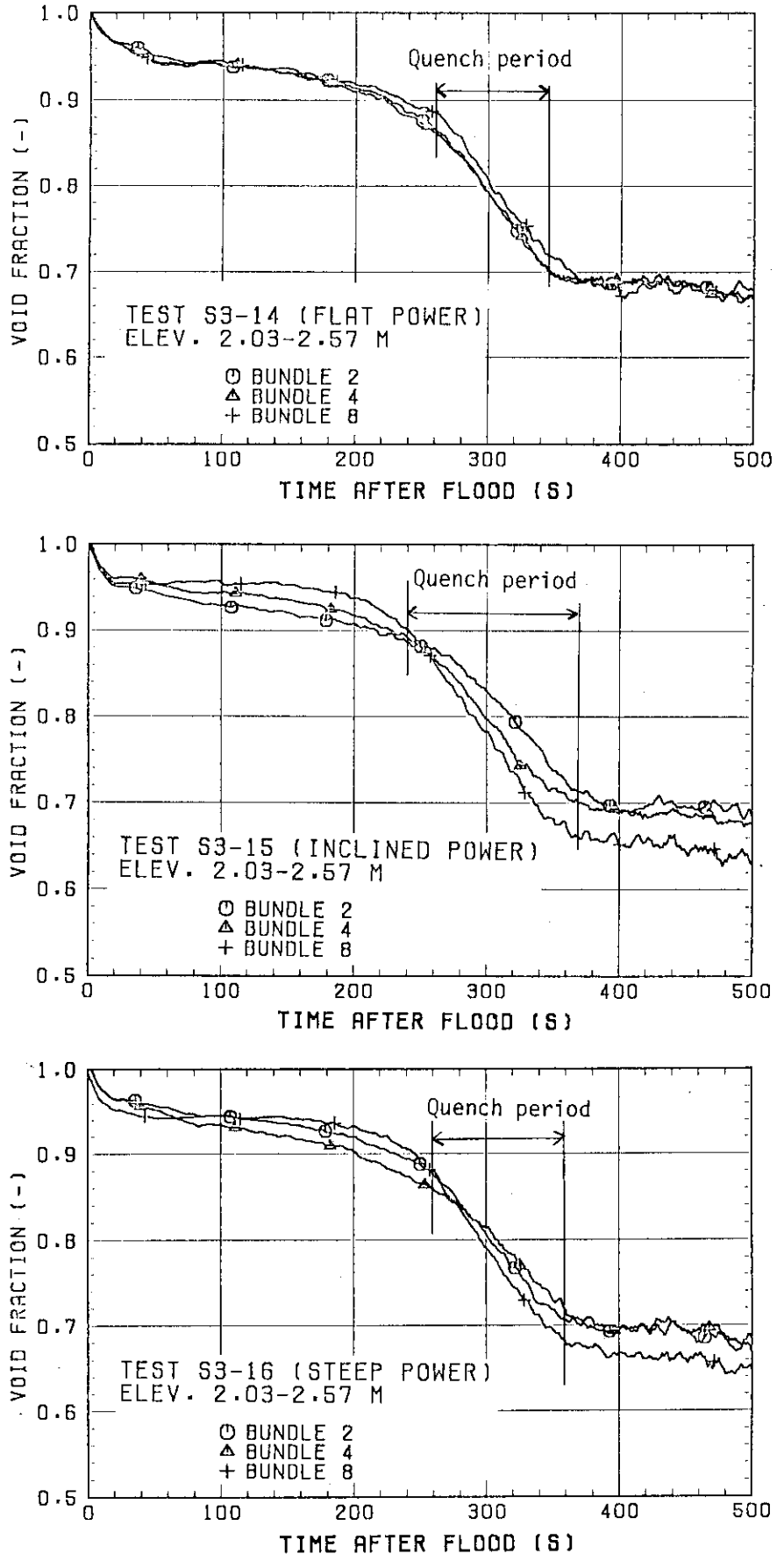

Fig. 3.20 Comparison of void fractions in core

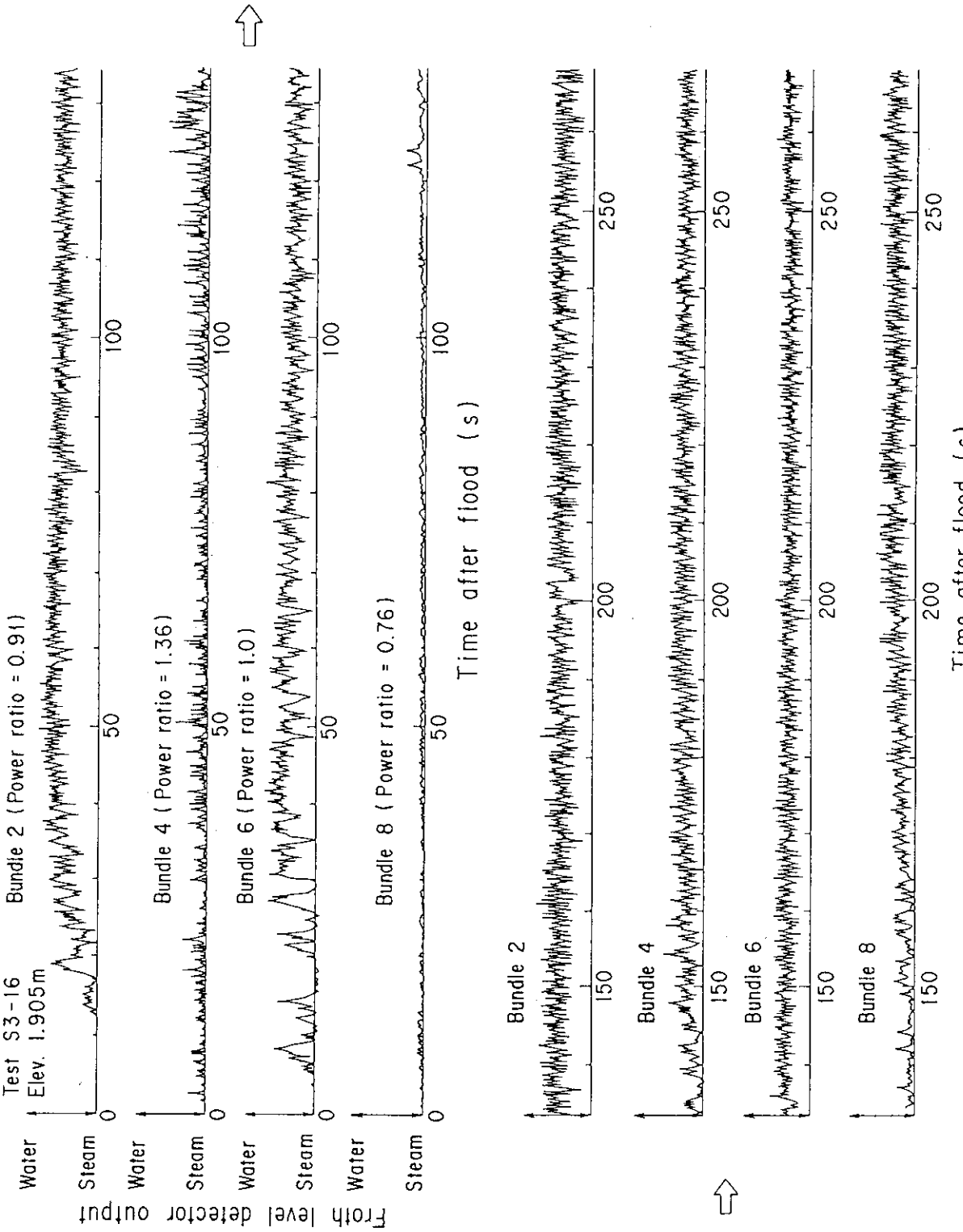

Fig. 3.21 Output signals from froth level detector for Test S3-16

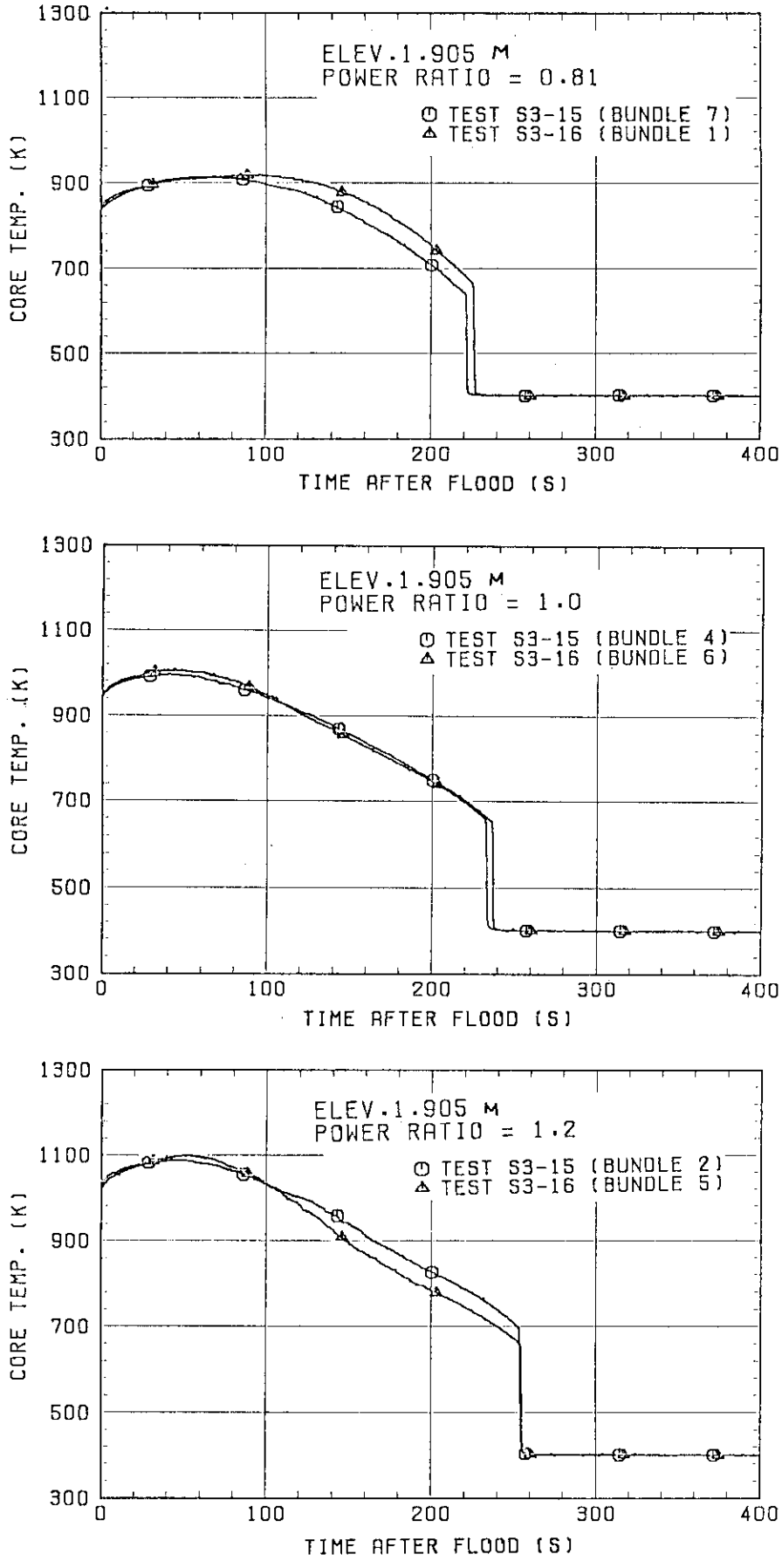

Fig. 3.22 Comparison of cladding temperatures at bundles with the same power ratio at 1.905 m

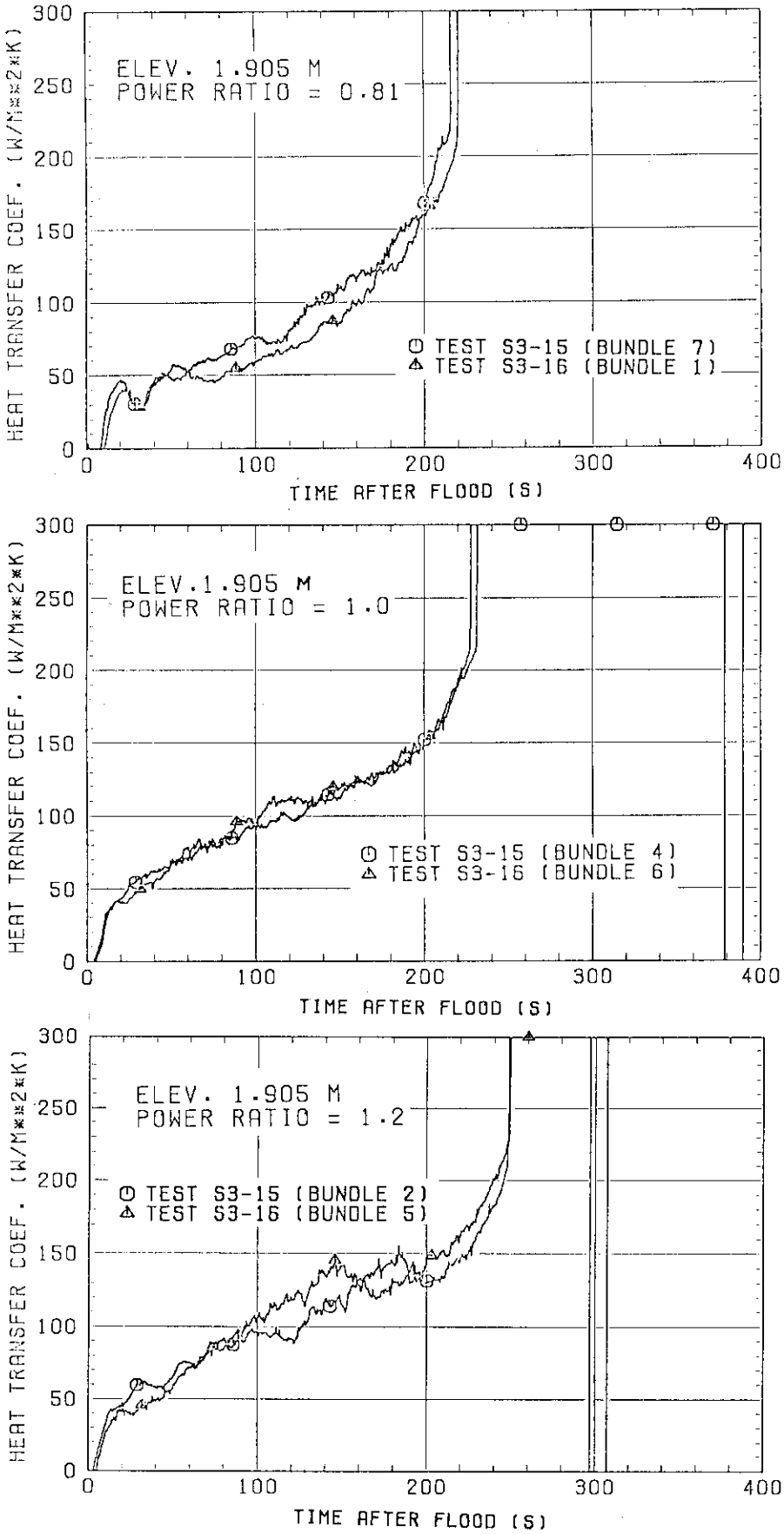

Fig. 3.23 Comparison of heat transfer coefficients at bundles with the same power ratio at 1.905 m

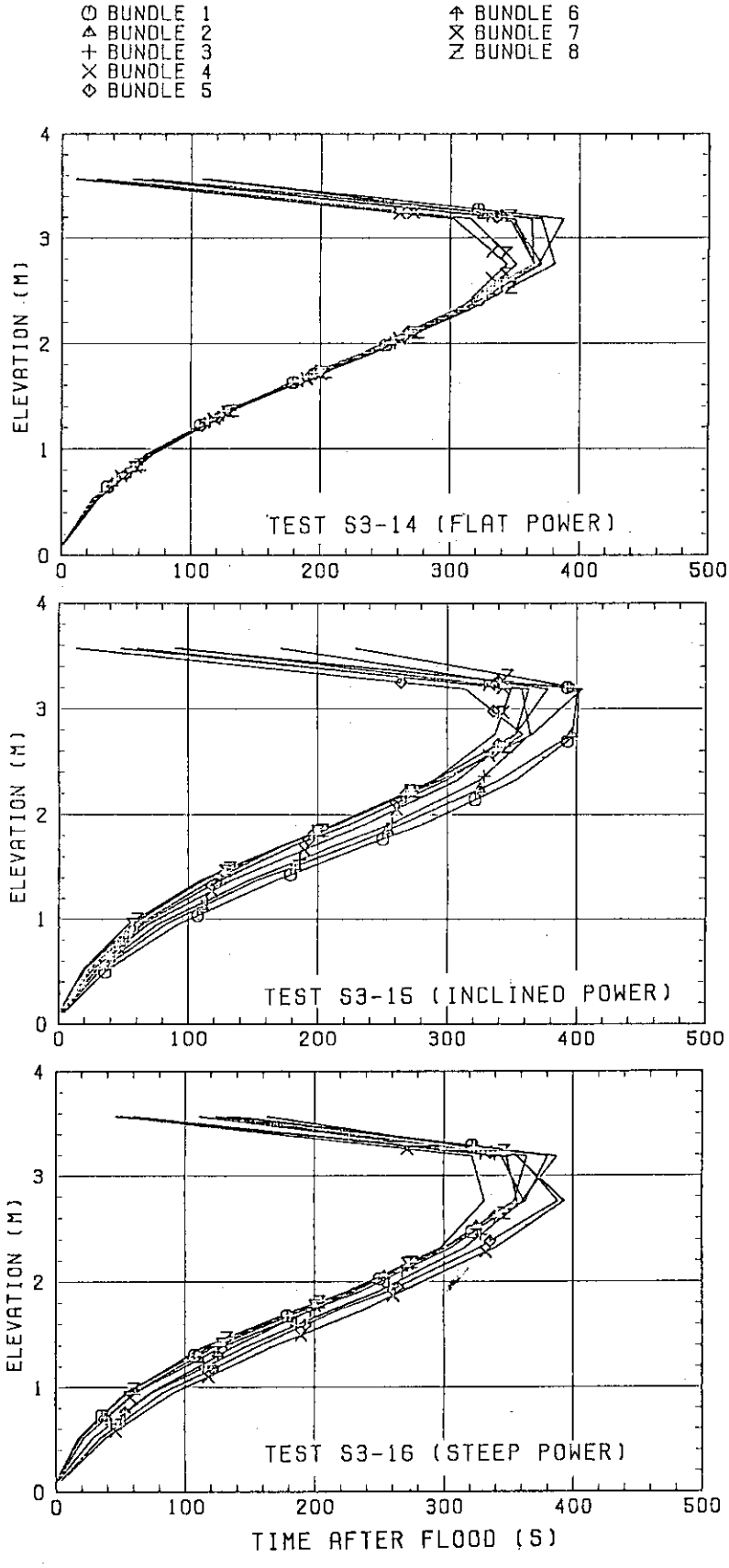

Fig. 3.24 Comparison of quench front propagation profile

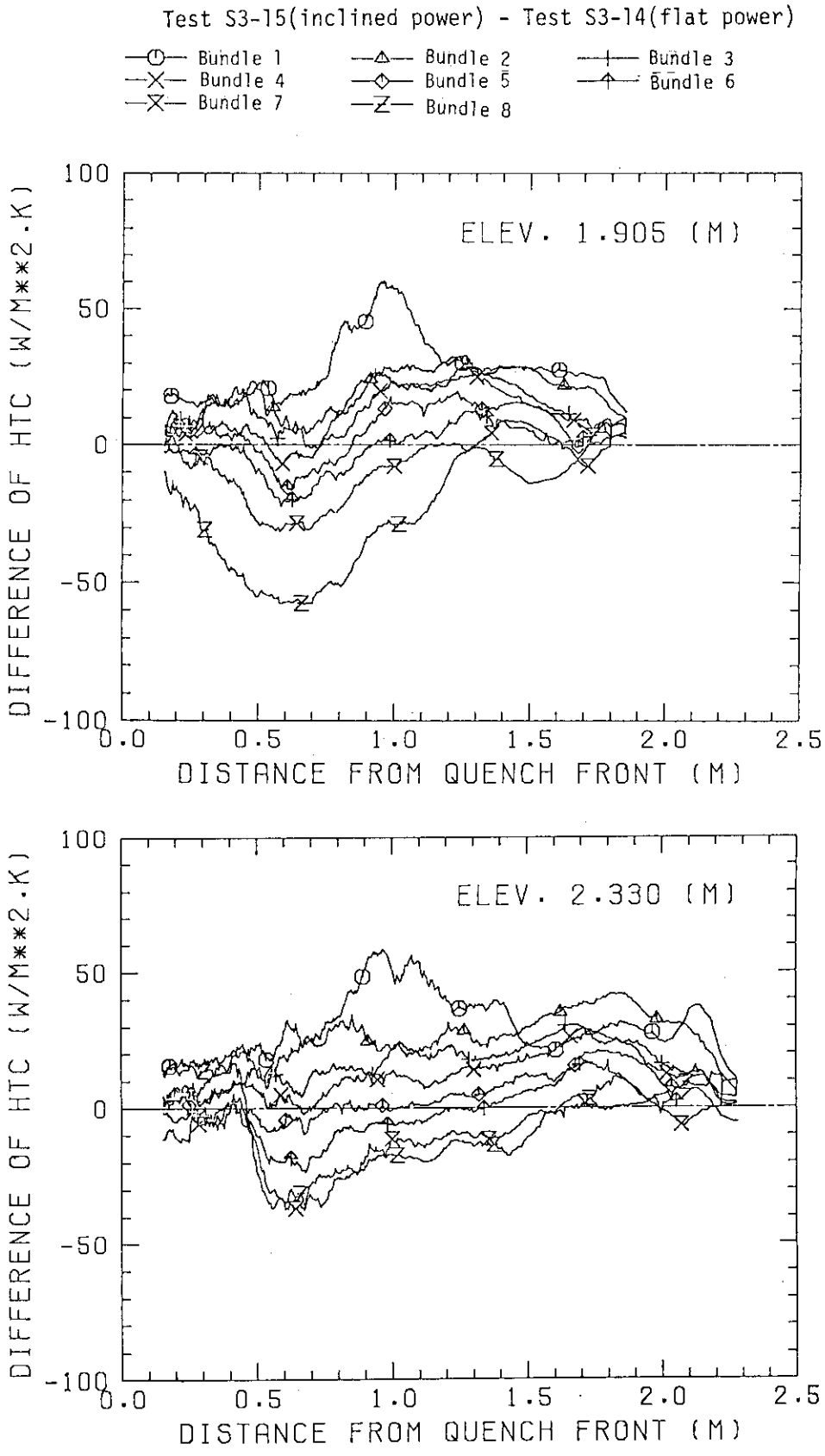

Fig. 4.1 Difference in heat transfer coefficients between Tests S3-15 and S3-14 vs. distance from bottom quench front

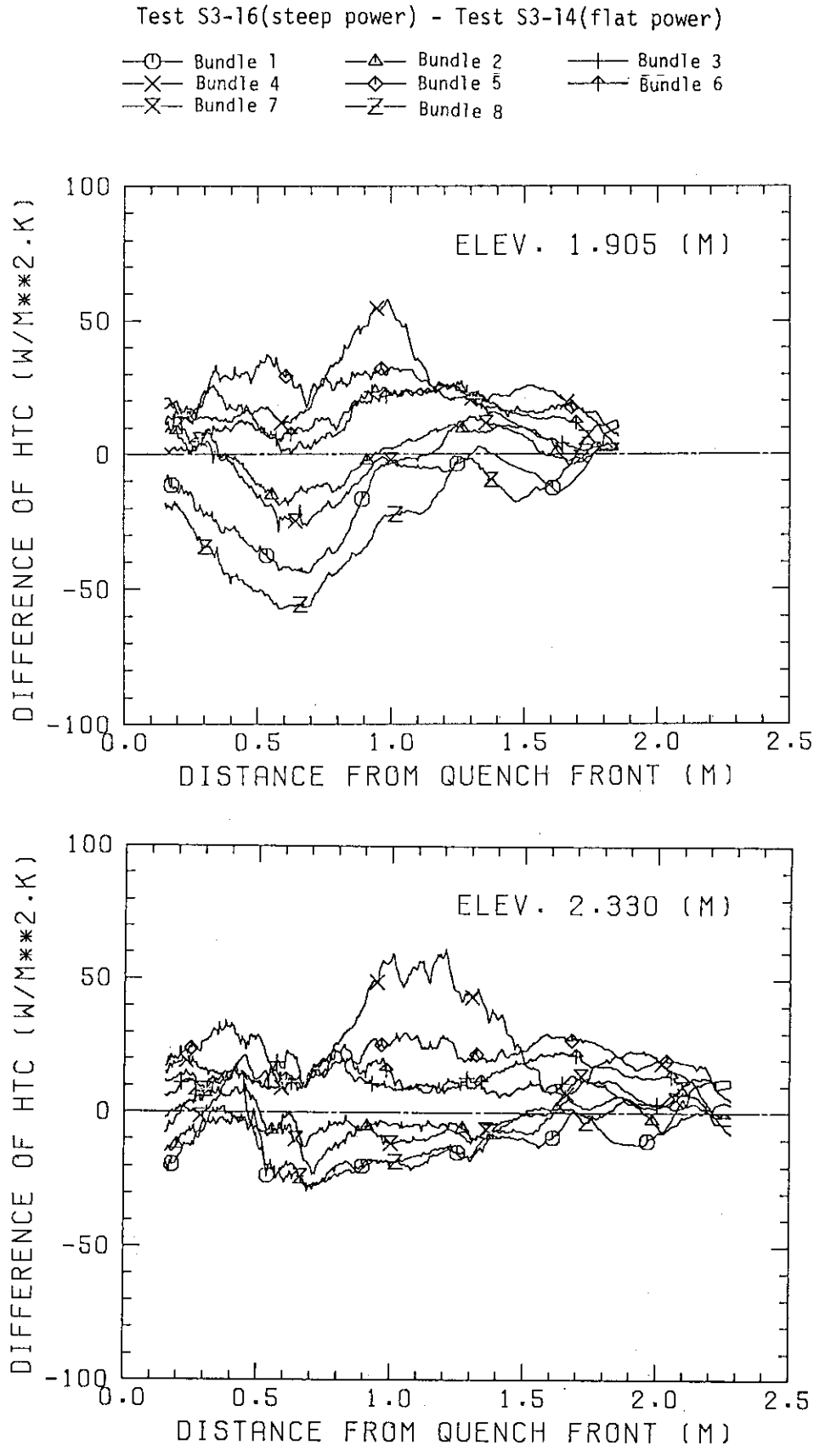

Fig. 4.2 Difference in heat transfer coefficients between Tests S3-16 and S3-14 vs. distance from bottom quench front

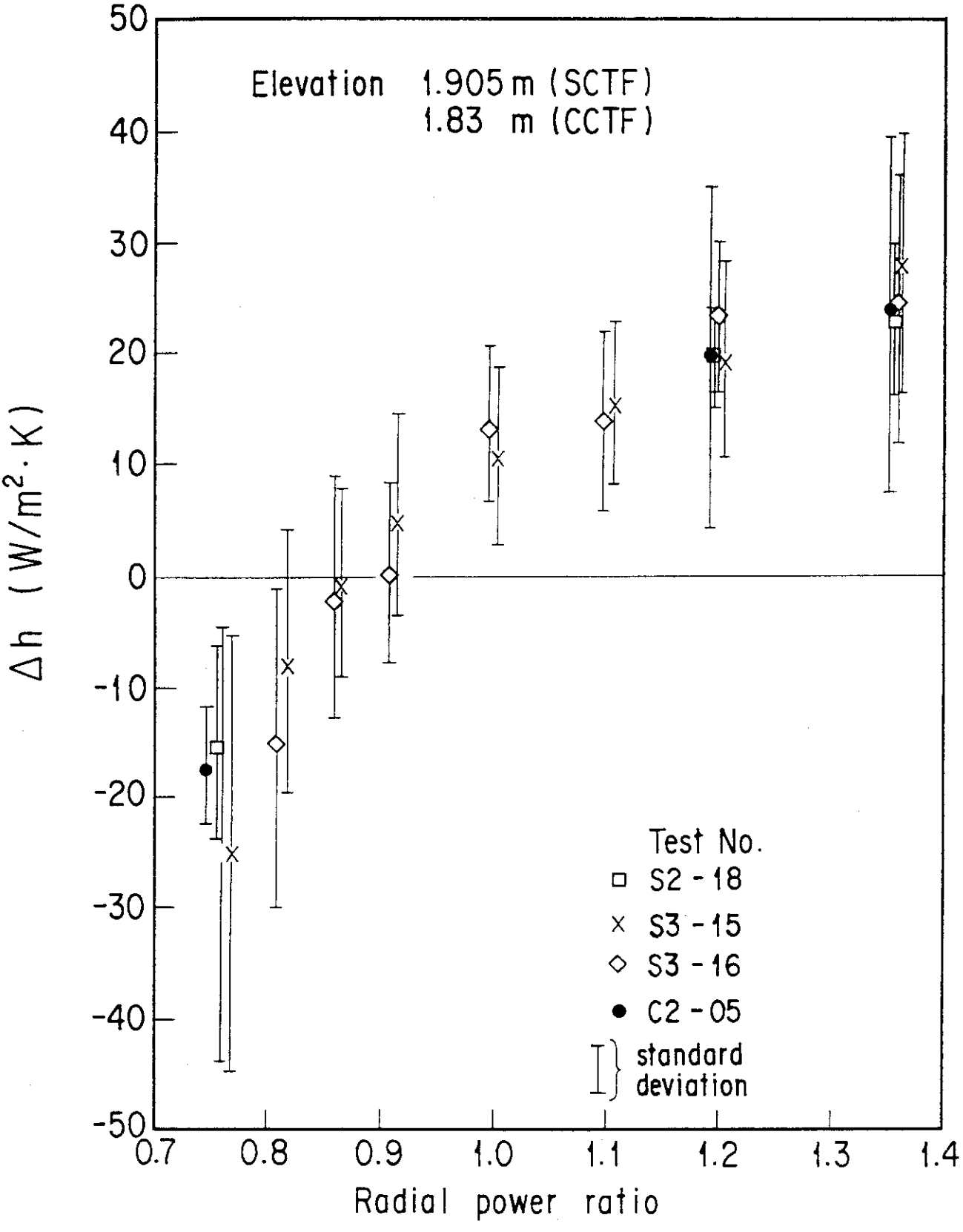

Fig. 4.3 Effect of bundlewise power ratio and power distribution shape on heat transfer coefficient (Elevation 1.905 m)

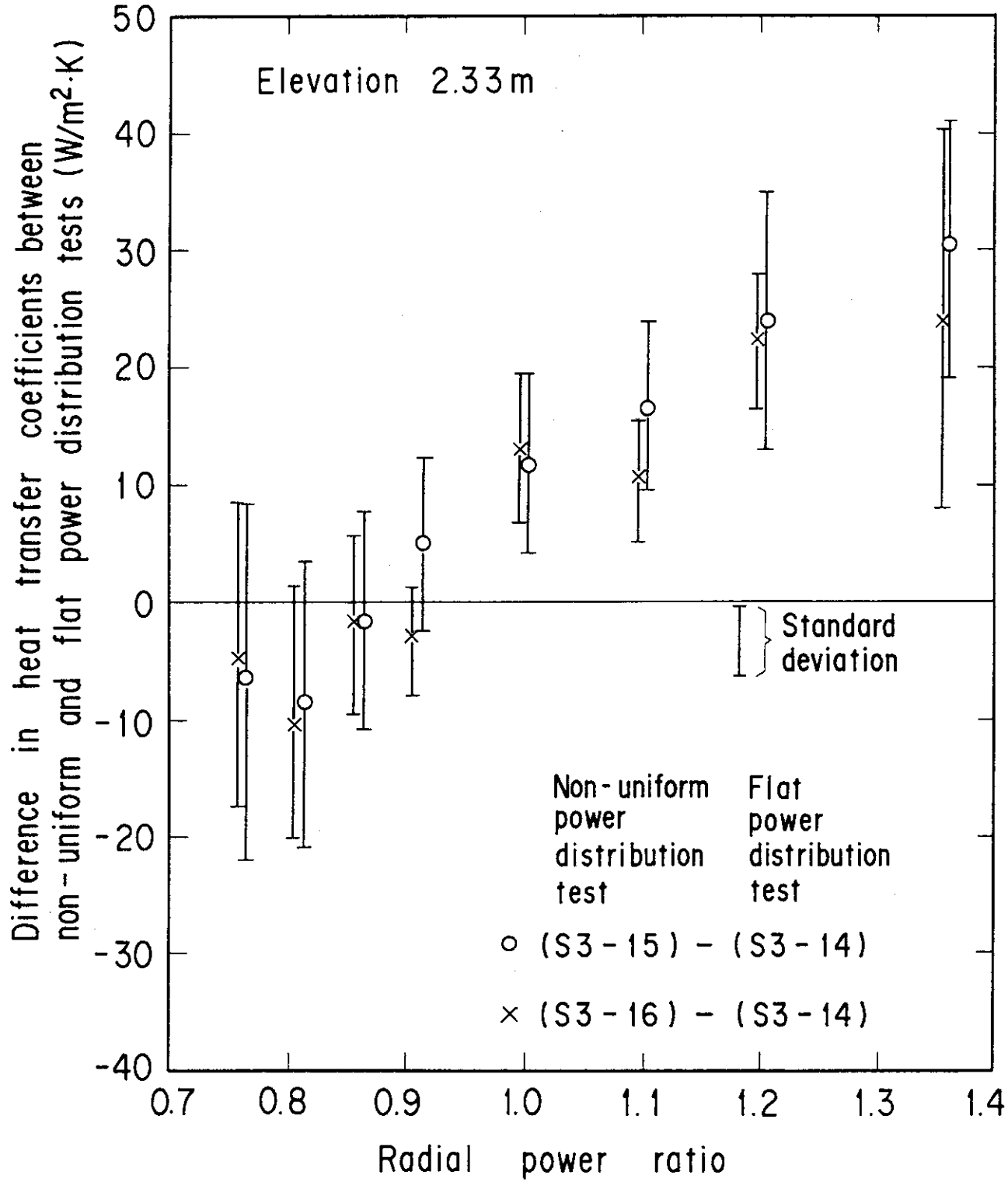

Fig. 4.4 Effect of bundlewise power ratio and power distribution shape on heat transfer coefficient (Elevation 2.33 m)

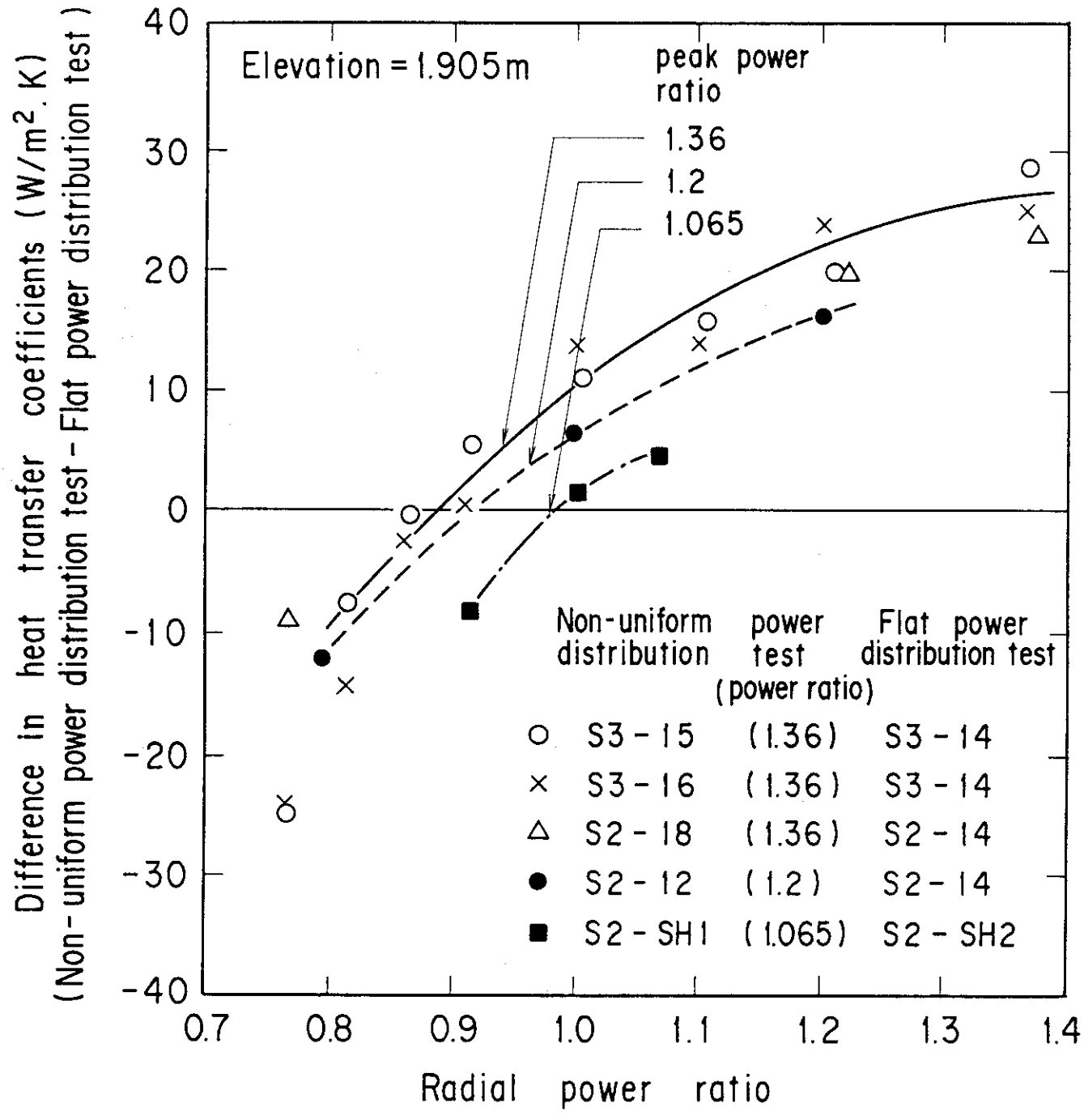

Fig. 4.5 Effect of peak power ratio on heat transfer enhancement due to radial power distribution

Appendix A Slab Core Test Facility (SCTF) Core-III

A.1 Test Facility

The overall schematic diagram of SCTF is shown in Fig. A-1. The principal dimensions of the facility is shown in Table A-1, and the comparison of dimensions between SCTF and the reference PWR is shown in Fig. A-2.

A.1.1 Pressure Vessel

The pressure vessel is of slab geometry as shown in Fig. A-3. The height of the components in the pressure vessel is almost the same as the reference reactor's, and the flow area and the fluid volume of each component are scaled down based on the nominal core flow area scaling, 1/21.

The core consists of 8 bundles arranged in a row and each bundle includes heater rods and non-heated rods with 16×16 array. The core is enveloped by the honeycomb thermal insulator which is attached on the back surface of core wall plate.

The downcomer is located at one end of the pressure vessel which corresponds to the periphery of the actual reactor pressure vessel. The core baffle region located between the core and the downcomer is isolated for Core-III to minimize uncertainty in actual core flow. The cross sections of the pressure vessel at the upper head, upper plenum, core and lower plenum are shown in Fig. A-4.

A.1.2 Interface between Core and Upper Plenum

The interface between the core and the upper plenum consists of upper core support plate (UCSP), end box and various structures in the end box such as control rod spider which is paired with the control rod guid assembly (CRGA) and its support column bottom and special baffle plate spider which is paired with the hold-down bridge. These structures are exactly the same as those for a German PWR except some minor modifications.

Figure A-5 shows arrangement of the UCSP, the end box and the top grid spacer. The configuration of the end box is shown in Fig. A-6.

Detail of the end boxes with drag transducer device and other internals is shown in Fig. A-7. The UCSP shown in Fig. A-8 has two kinds of holes, i.e., the square holes correspond to the end boxes with control rod spider and the circular holes correspond to the end boxes with special baffle plate spider.

A.1.3 Upper Plenum and Upper Head

The vertical and horizontal cross sections of the upper plenum are shown in Figs. A-9 and A-4, respectively. In the SCTF Core-III, the slab cut of the upper plenum of a German (KWU) PWR is simulated. The splitted and staggered arrangement of the CRGA support columns was chosen to make good simulation of horizontal flow in the upper plenum.

As shown in Fig. A-10, there are three kinds of CRGA support column. Support column-1 is installed above Bundles 3 and 5 and connected to the CRGA support column bottom with the transition cone. Cross section of the CRGA support calumn changes from a circle to a half circle in this transition cone. Support column 2 is installed above Bundles 6 and 7 and the bottom is closed with the half conical bottom seal plate with many flow holes. Support column 3 is essentially the same as support column 2 but the edge of one side is cut off in order to install above Bundle 1. Each CRGA support column has ten or eleven baffle plates with flow holes. Top flow paths to the upper head bottom and to the upper plenum top are also provided.

Figure A-11 shows vertical cross section of the bottom part of the upper plenum and the interface between the core and the upper plenum. There are eight side flow injection nozzles and eight side flow extraction nozzles just at the opposite side of the upper plenum bottom, corresponding to each bundle.

The upper plenum is separated from the upper head by an upper support plate. Four top injection nozzles penetrate the upper head and open the top of upper plenum as shown in Fig. A-12. Outlet part of the top injection nozzle has a rectangular cross section and double mesh screen with 45 degree cross angle is attached at the mouth.

A.1.4 Simulated Core

The simulated core for the SCTF Core-III consists of 8 heater rod bundles arranged in a row. Each bundle has 236 electrically heated rods and 20 non-heated rods. The arrangement of rods in a bundle is shown in Fig. A-13. The dimensions of the heater rods are based on 15×15 fuel rods bundle for a PWR and the heated length and the outer diameter of each heater rod are 3.613 m and 10.7 mm, respectively. A heater rod consists of a nichrome heater element, boron nitride (BN) or magnesium oxide (MgO) depending on elevation in the heated zone and Nichrofer 7216 (equivalent to Inconel 600) sheath. The sheath thickness is about 1.0 mm and is thicker than the actual fuel cladding because of the requirements for thermocouple installation. The heater element is a helical coil and has a 17 step chopped cosine axial power profile as shown in Fig. A-14. The peaking factor is 1.4.

Non-heated rods are either pipes or solid rods of stainless steel with 13.8 mm O.D. The heater rods and non-heated rods are fixed at the top of the core allowing downward expansion. In Fig. A-15, relative elevation of rods and spacers is shown.

For better simulation of flow resistance in the lower plenum, the simulated fuel rods end in the lower plenum and do not penetrate through the bottom plate of the lower plenum as shown in Fig. A-15.

A.1.5 Primary Loops

Primary loops consist of a hot leg equivalent to four hot legs in area, a steam/water separator for simulating single steam phase flow downstream of the steam generator and for measuring flow rate of carry over water, an intact cold leg equivalent to three intact loops, a broken cold leg on the pressure vessel side and a broken cold leg on the steam/water separator side. These two broken cold legs are connected to two containment tanks through break valves, respectively. The arrangement of the primary loops is shown in Fig. A-16. The flow area of each loop is scaled down based on the core flow area scaling, 1/21. It should be emphasized that the cross section of the hot leg is an elongated circle with an actual height to realize proper flow pattern in the hot leg. The steam/water separator has a steam generator inlet plenum simulator to correctly simulate the flow

characteristics of carryover water into the U-tubes. The cross section of the hot leg and the configuration of the steam genrator inlet plenum simulator are shown in Fig. A-17.

A pump simulator and a loop seal part are provided for the intact cold leg. The arangement of the intact cold leg is shown in Fig. A-18. The pump simulator consists of the casing and duct simulators and an orifice plate as shown in Fig. A-19. The loop resistance is adjusted with the orifice plates attached to the intact cold leg, the steam/water separator side and pressure vessel side broken cold legs and the pump simulator.

A.1.6 ECC Water Injection System

Three kinds of ECCSs are provided, i.e., the accumulator injection system (Acc), low pressure coolant injection system (LPCI) and combined injection system. Available injection locations for the former two are the intact and broken cold legs, the hot leg, the lower plenum and the downcomer. On the other hand, those for the last one are the top and bottom-side of the upper plenum and the intact and broken cold legs.

A.1.7 Containment Tanks and Auxiliary System

Two containment tanks are provided to SCTF. The containment tank-I is connected with the downcomer through the pressure vessel side broken cold leg and the containment tank-II is connected with the steam/water separator through the steam/water separator side broken cold leg. Especially in the containment tank-I, carryover water from the downcomer is measured by the differentiation of the liquid level. These containment tanks and auxiliary system such as a pressurizer for injecting water from the Acc tanks, etc. are shared with CCTF.

A.2 Instrumentation

The instrumentation in SCTF has been provided both by JAERI and USNRC. The JAERI-provided instrumentation includes the measurement of temperatures, pressures, differential pressures, liquid levels, flow velocities, and heating powers. USNRC has provided film probes, impedance probes, string probes, liquid level detectors (LLDs), fluid distribution grids (FDGs), turbine meters, drag disks, densitometers, spool pieces, drag bodies, break through detectors and video optical probes. Locations of the JAERI-provided instruments are shown in Figs. A-20 through A-43.

Table A-1 Principal Dimensions of the SCTF

1. Core Dimension		
(1) Quantity of Bundle	8 Bundles	
(2) Bundle Array	1 × 8	
(3) Bundle Pitch	230 mm	
(4) Rod Array in a Bundle	16 × 16	
(5) Rod Pitch in a Bundle	14.3 mm	
(6) Quantity of Heater Rod in a Bundle	236 rods	
(7) Quantity of Non-Heated Rod in a Bundle	20 rods	
(8) Total Quantity of Heater Rods	236×8=1,888	rods
(9) Total Quantity of Non-Heated Rods	20×8=160	rods
(10) Effective Heated Length of Heater Rod	3613 mm	
(11) Diameter of Heater Rod	10.7 mm	
(12) Diameter of Non-Heated Rod	13.8 mm	
2. Flow Area & Fluid Volume		
(1) Core Flow Area	0.25	m^2
(2) Core Fluid Volume	0.903	m^3
(3) Baffle Region Flow Area (isolated)	(0.096)	m^2
(4) Baffle Region Fluid Volume (nominal)	0.355	m^3
(5) Cross-Sectional Area of Core Additional Fluid Volumes Including Gap between Core Barrel and Pressure Vessel Wall and Various Penetration Holes	0.07 ~ 0.10	m^2 m^2
(6) Downcomer Flow Area	0.158	m^2
(7) Upper Annulus Flow Area	0.158	m^2
(8) Upper Plenum Horizontal Flow Area (max.)	0.541	m^2
(9) Upper Plenum Vertical Flow Area	0.525	m^2
(10) Upper Plenum Fluid Volume	1.156	m^3
(11) Upper Head Fluid Volume	0.86	m^3
(12) Lower Plenum Fluid Volume (excluding below downcomer)	1.305	m^3
(13) Steam Generator Inlet Plenum Simulator Flow Area	0.626	m^2
(14) Steam Generator Inlet Plenum Simulator Fluid Volume	0.931	m^3
(15) Steam Water Separator Fluid Volume	5.3	m^3
(16) Flow Area at the Top Plate of Steam Generator Inlet Plenum Simulator	0.195	m^2
(17) Hot Leg Flow Area	0.0826	m^2

Table A-1 (continue)

(18) Intact Cold Leg Flow Area (Diameter = 297.9 mm) Inverted U-Tube with 0.0314 m^2 Cross-Sectional Area (Diameter = 200 mm) and 10 m Height from the Top of Steam Generator Inlet Plenum Simulator Can Be Added As an Option.	0.0697	m^2
(19) Broken Cold Leg Flow Area (Diameter = 151.0 mm)	0.0197	m^2
(20) Containment Tank-I Fluid Volume	30	m^3
(21) Containment Tank-II Fluid Volume	50	m^3
(22) Flow Area of Exhausted Steam Line from Containment Tank-II to the Atmosphere	see Fig. 3-63	

3. Elevation & Height

(1) Top Surface of Upper Core Support Plate (UCSP)	0	mm
(2) Bottom Surface of UCSP	- 40	mm
(3) Top of the Effective Heated Length of Heater Rod	- 444	mm
(4) Bottom of the Effective Heated Length of Heater Rod	-4,057	mm
(5) Bottom of the Skirt in the Lower Plenum	-5,270	mm
(6) Bottom of Intact Cold Leg	+ 724	mm
(7) Bottom of Hot Leg	+1,050	mm
(8) Top of Upper Plenum	+2,200	mm
(9) Bottom of Steam Generator Inlet Plenum Simulator	+1,933	mm
(10) Centerline of Loop Seal Bottom	-2,281	mm
(11) Bottom Surface of End Box	- 263	mm
(12) Top of Upper Annulus of Downcomer	+2,234	mm
(13) Height of Steam Generator Inlet Plenum Simulator	1,595	mm
(14) Height of Loop Seal	3,140	mm
(15) Inner Height of Hot Leg Pipe	737	mm
(16) Bottom of Lower Plenum	-5,772	mm
(17) Top of Upper Head	+2,887	mm

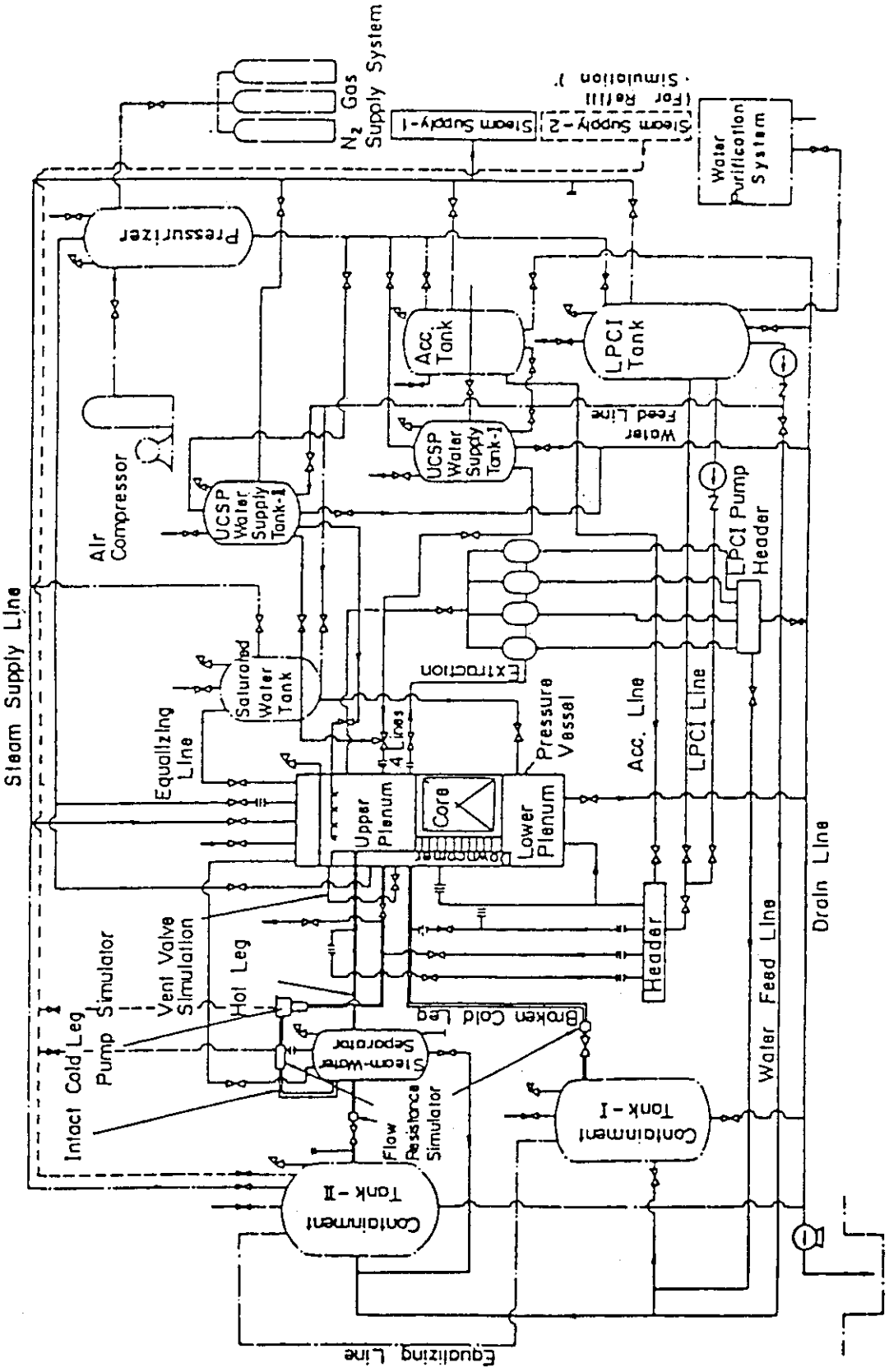

Fig. A-1 Schematic Diagram of Slab Core Test Facility

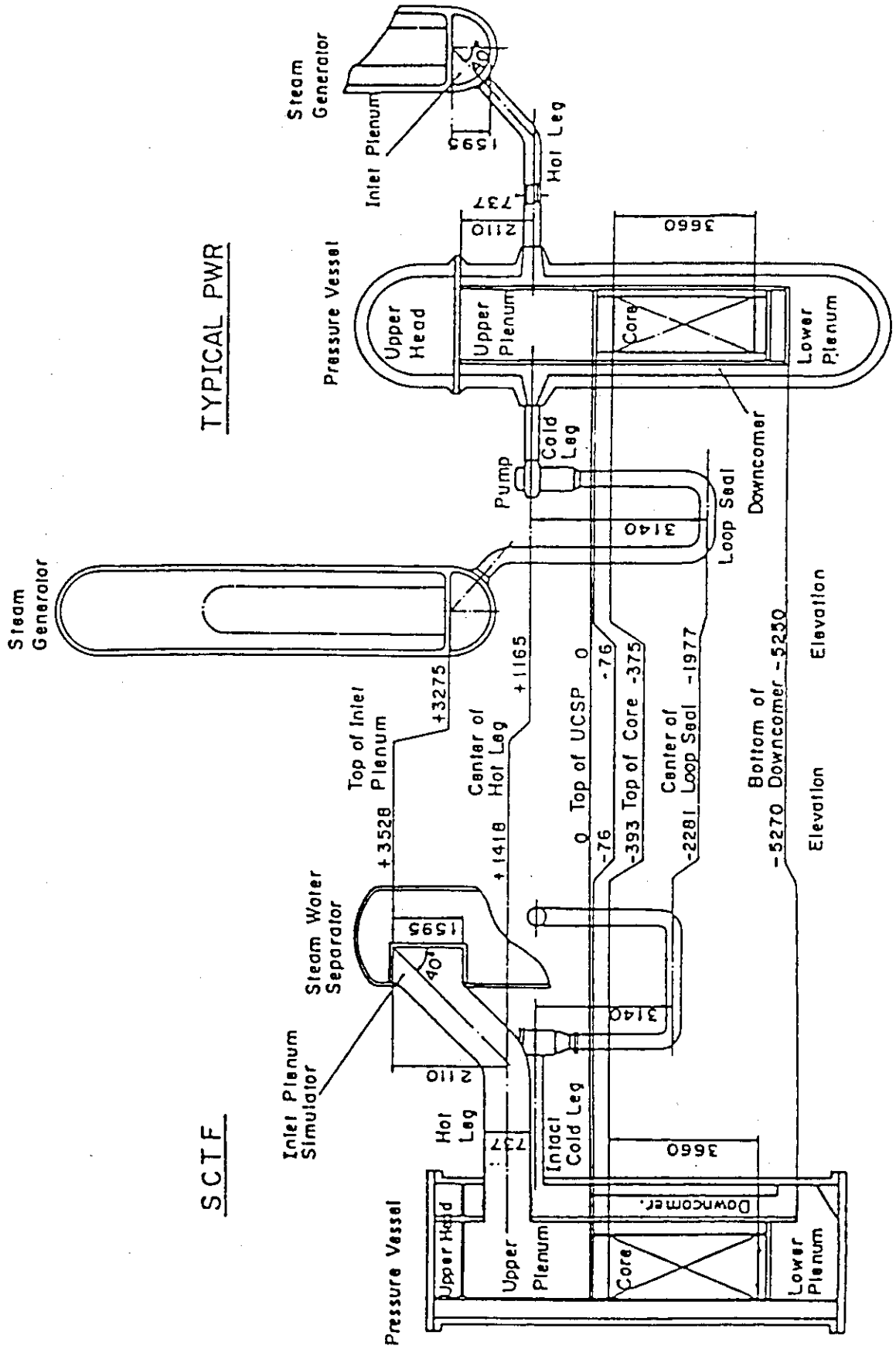

Fig. A-2 Comparison of Dimensions between SCTF and a Reference PWR

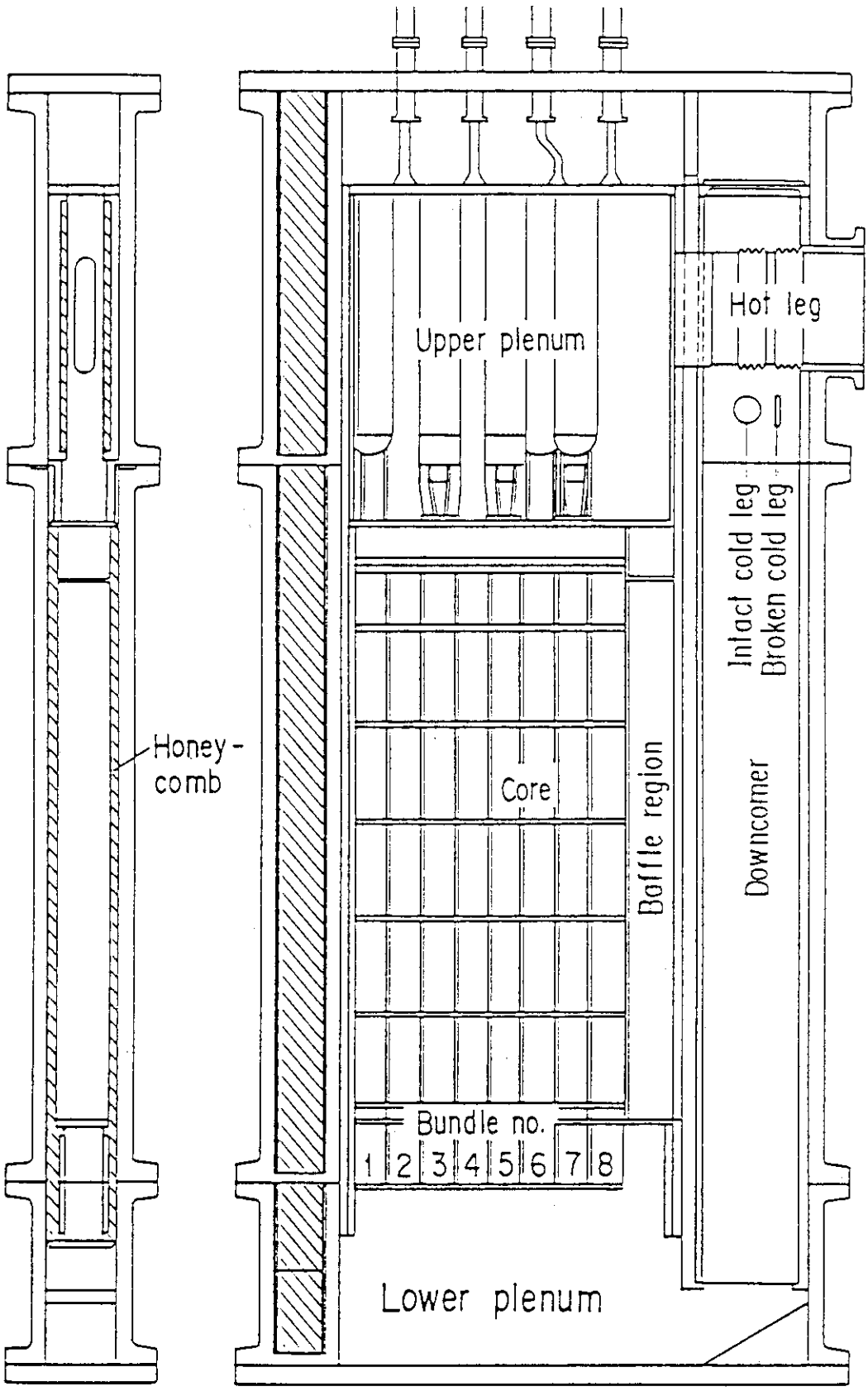

Fig. A-3 Vertical Cross Sections of Pressure Vessel

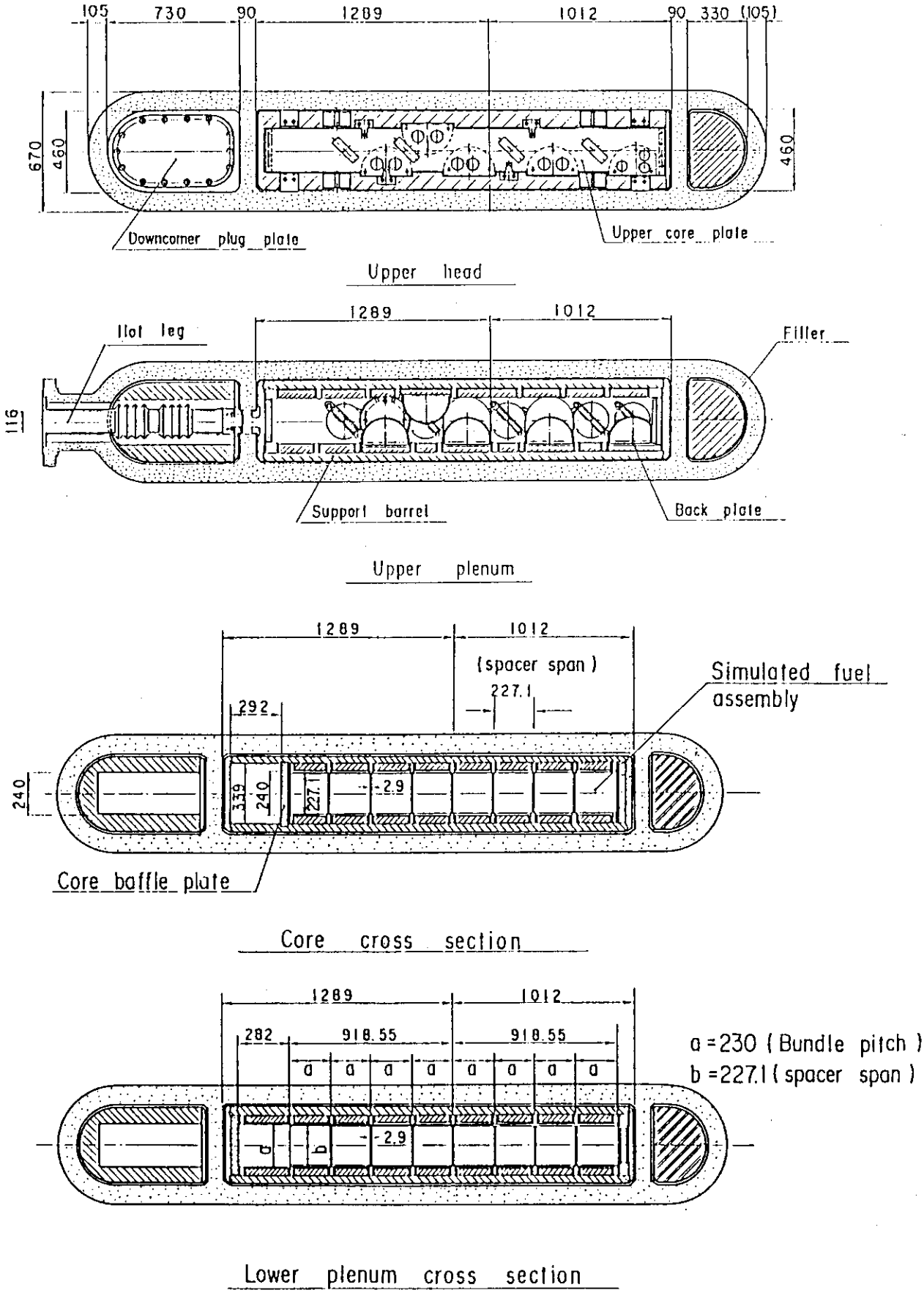

Fig. A-4 Horizontal Cross Sections of Pressure Vessel

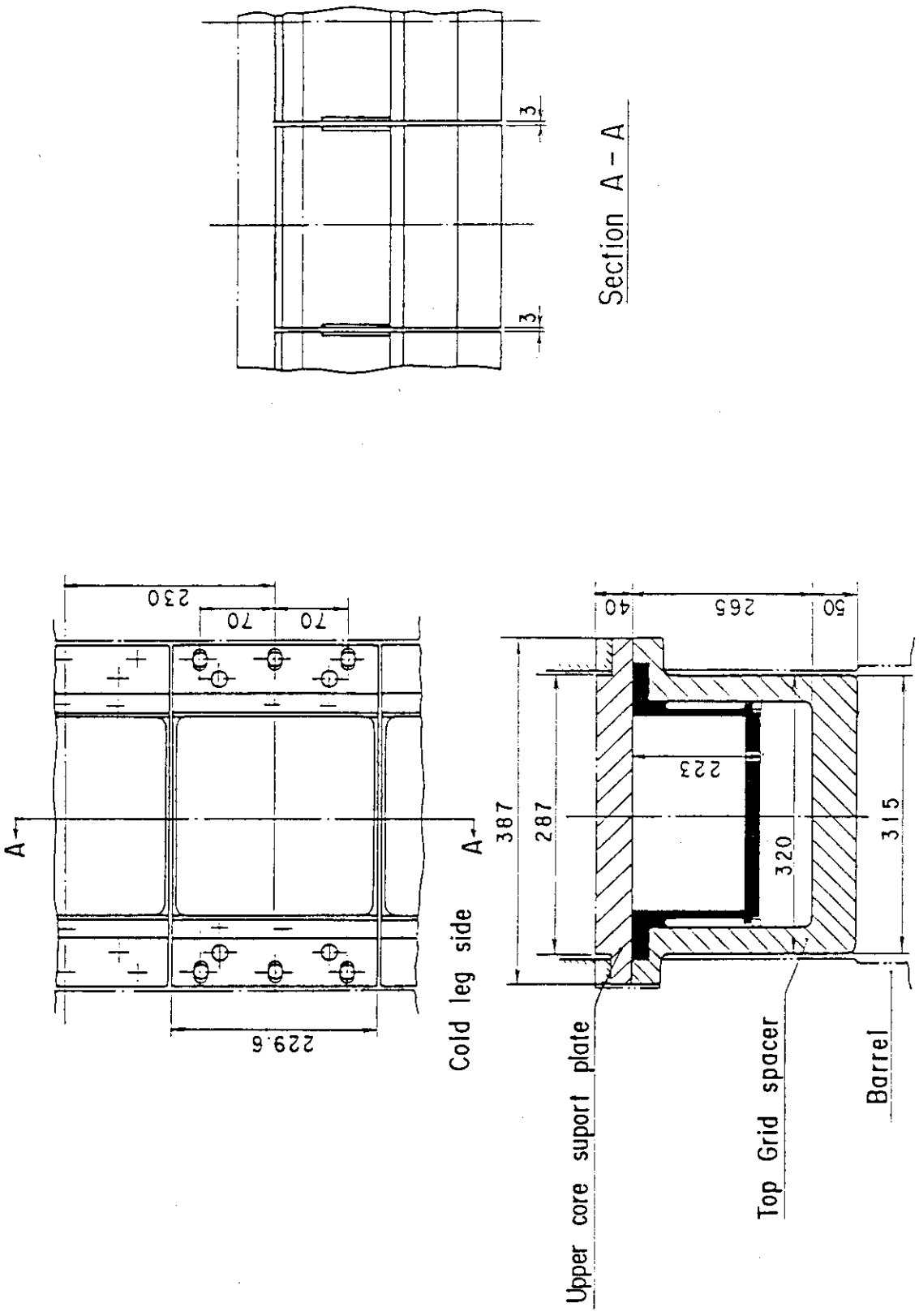

Fig. A-5 Arrangement and Principal Dimension of End Boxes and Top Grid Spacers

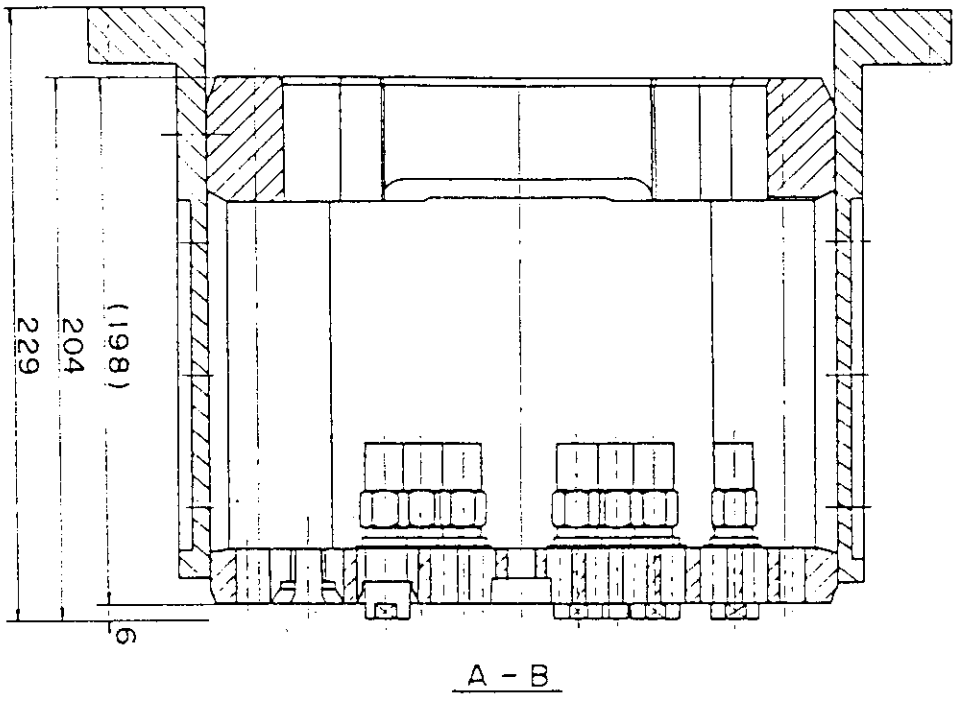

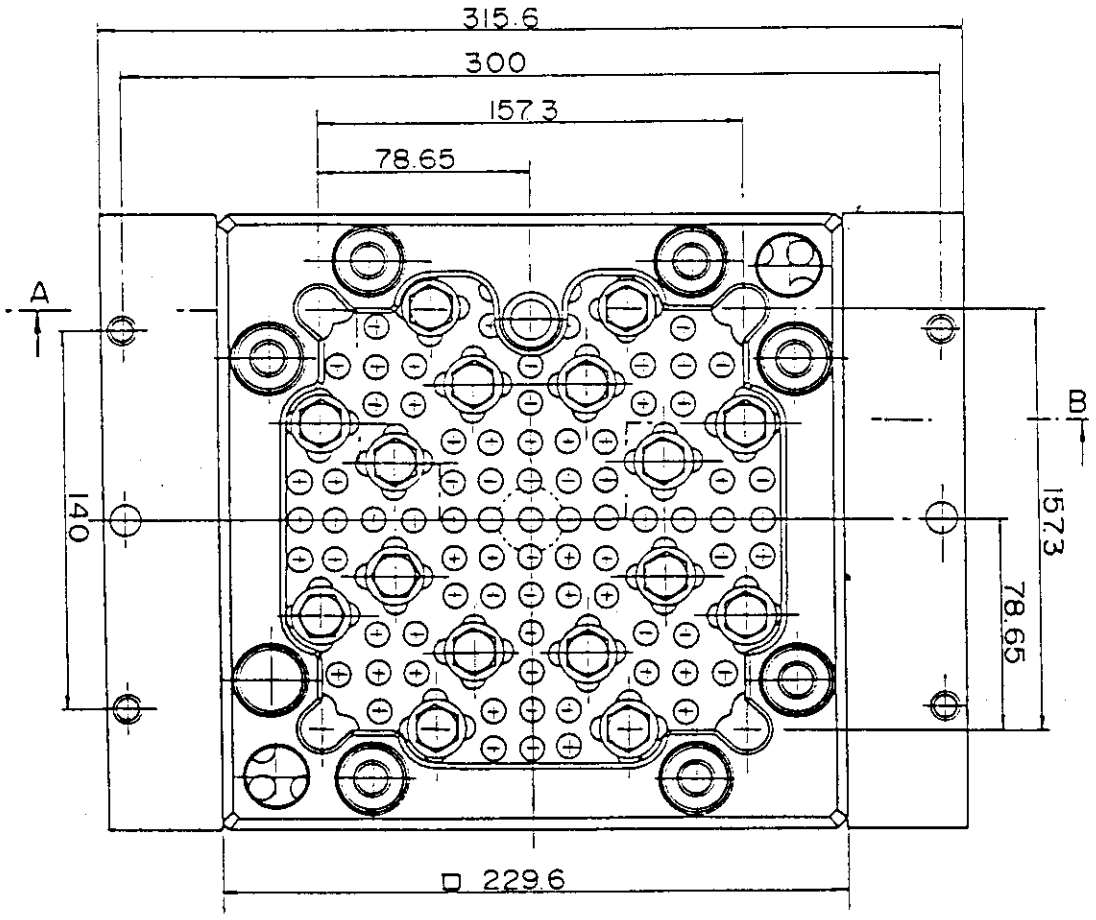

Fig. A-6 Configuration and Dimension of End Boxes

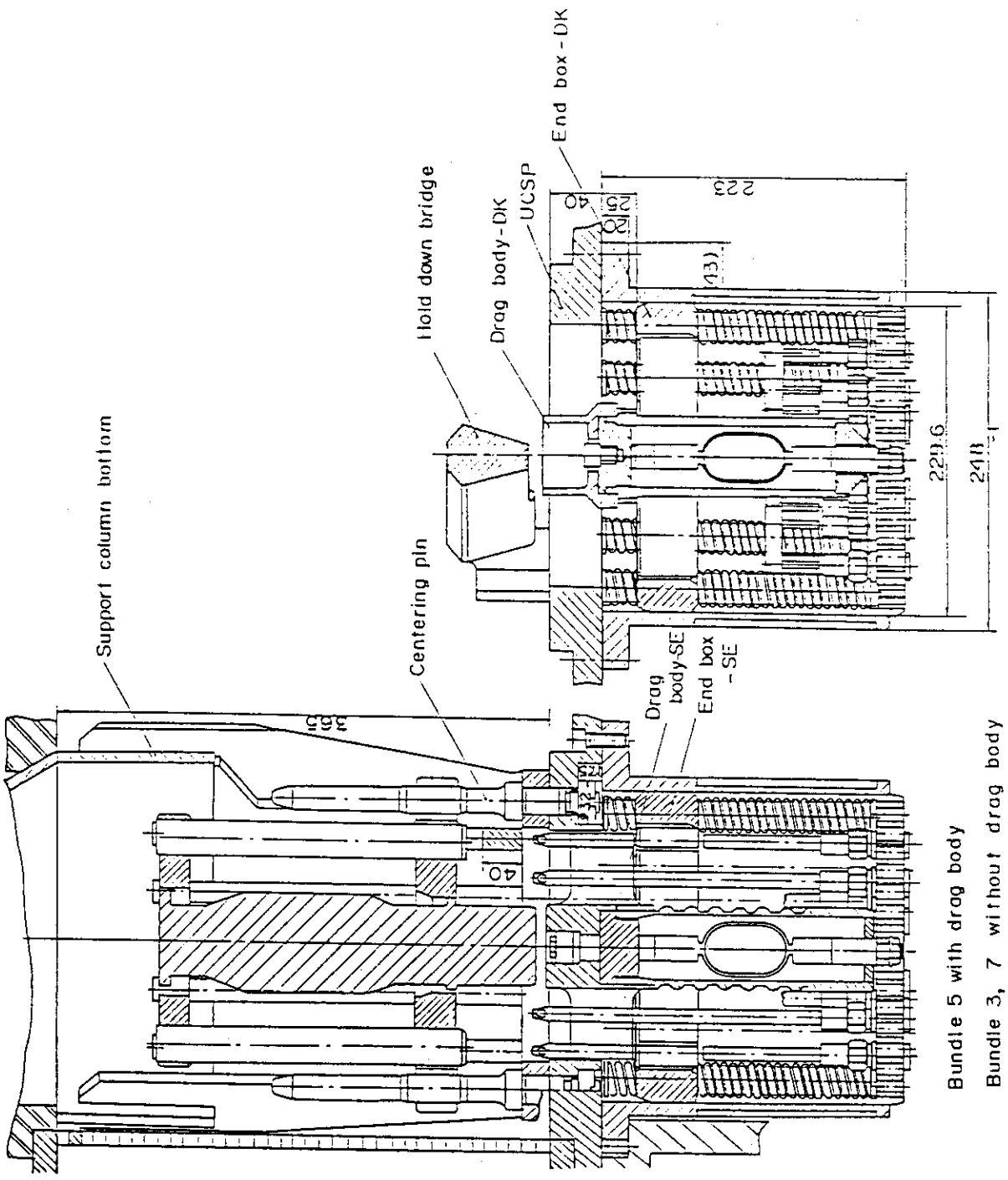

Fig. A-7 Detail of End Boxes with Drag Bodies

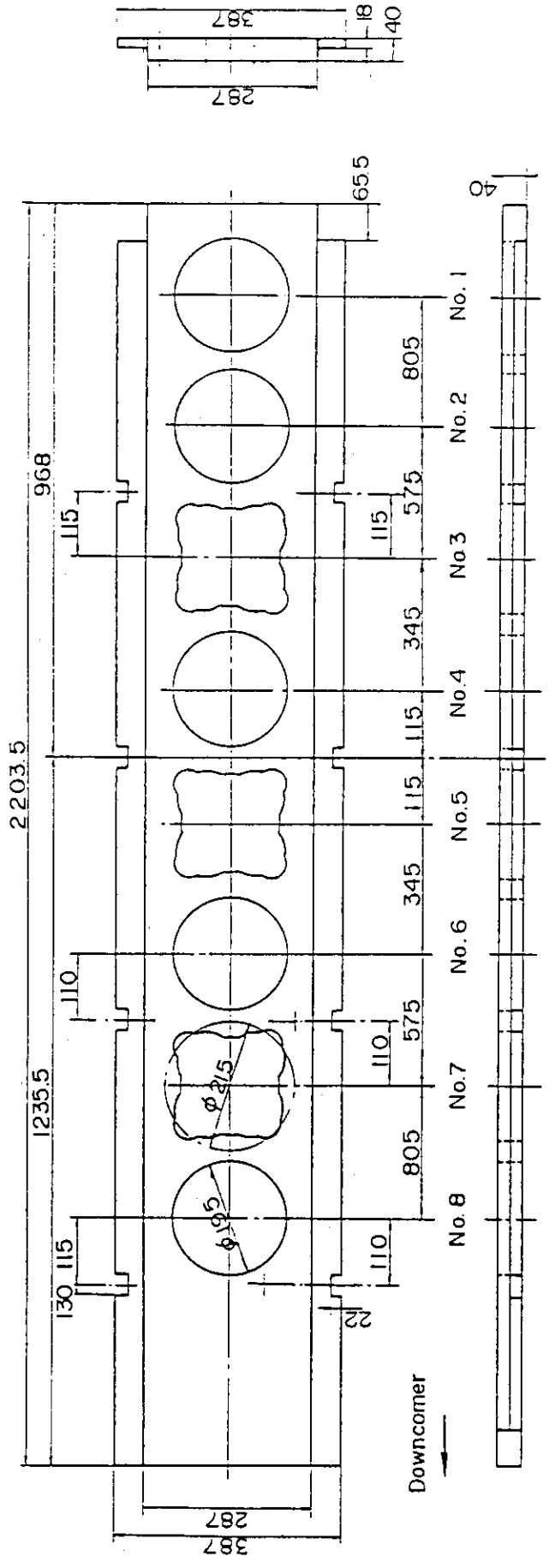

Fig. A-8 Dimension of Upper Core Support Plate

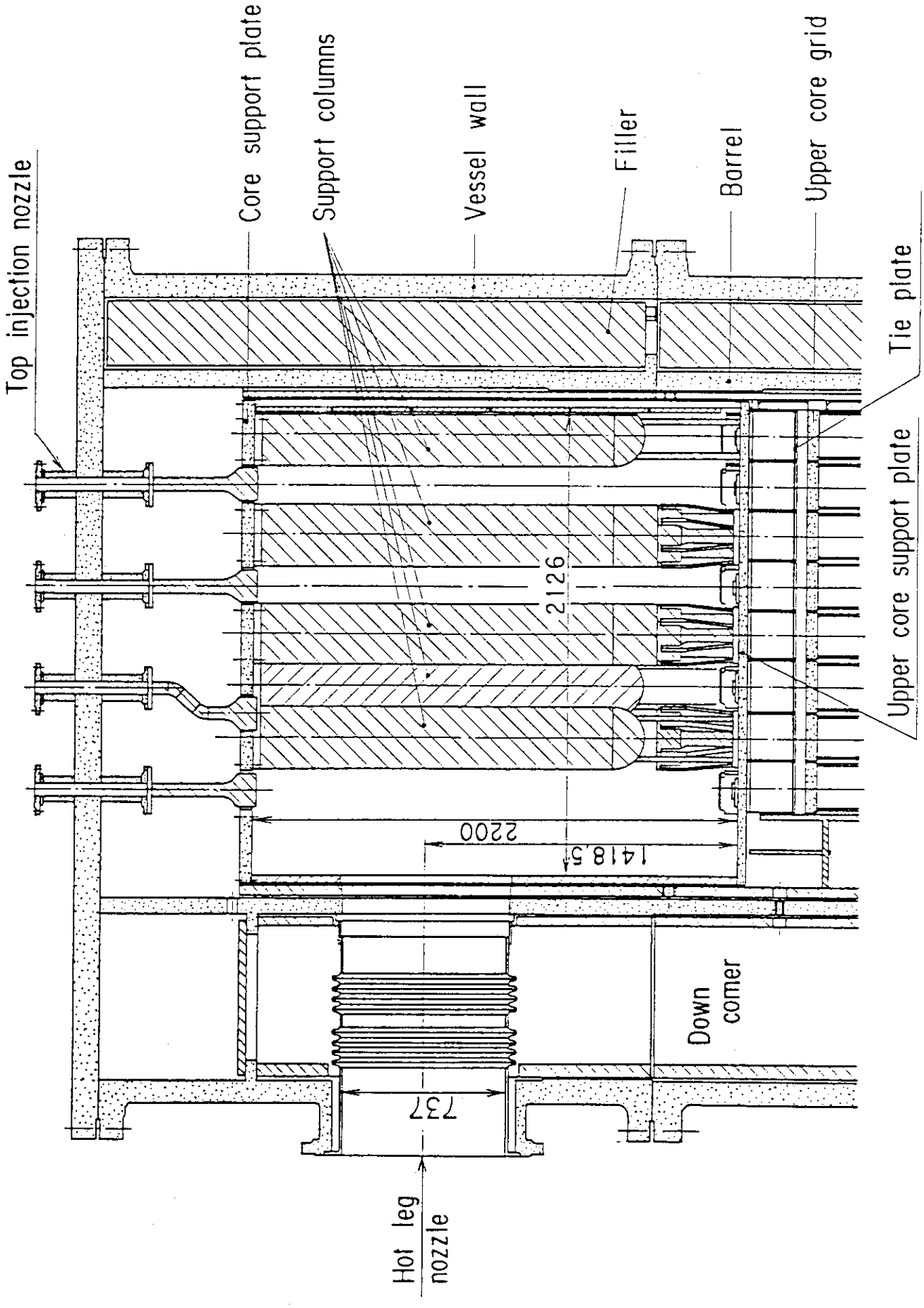

Fig. A-9 Vertical Cross Section of Upper Plenum Internals

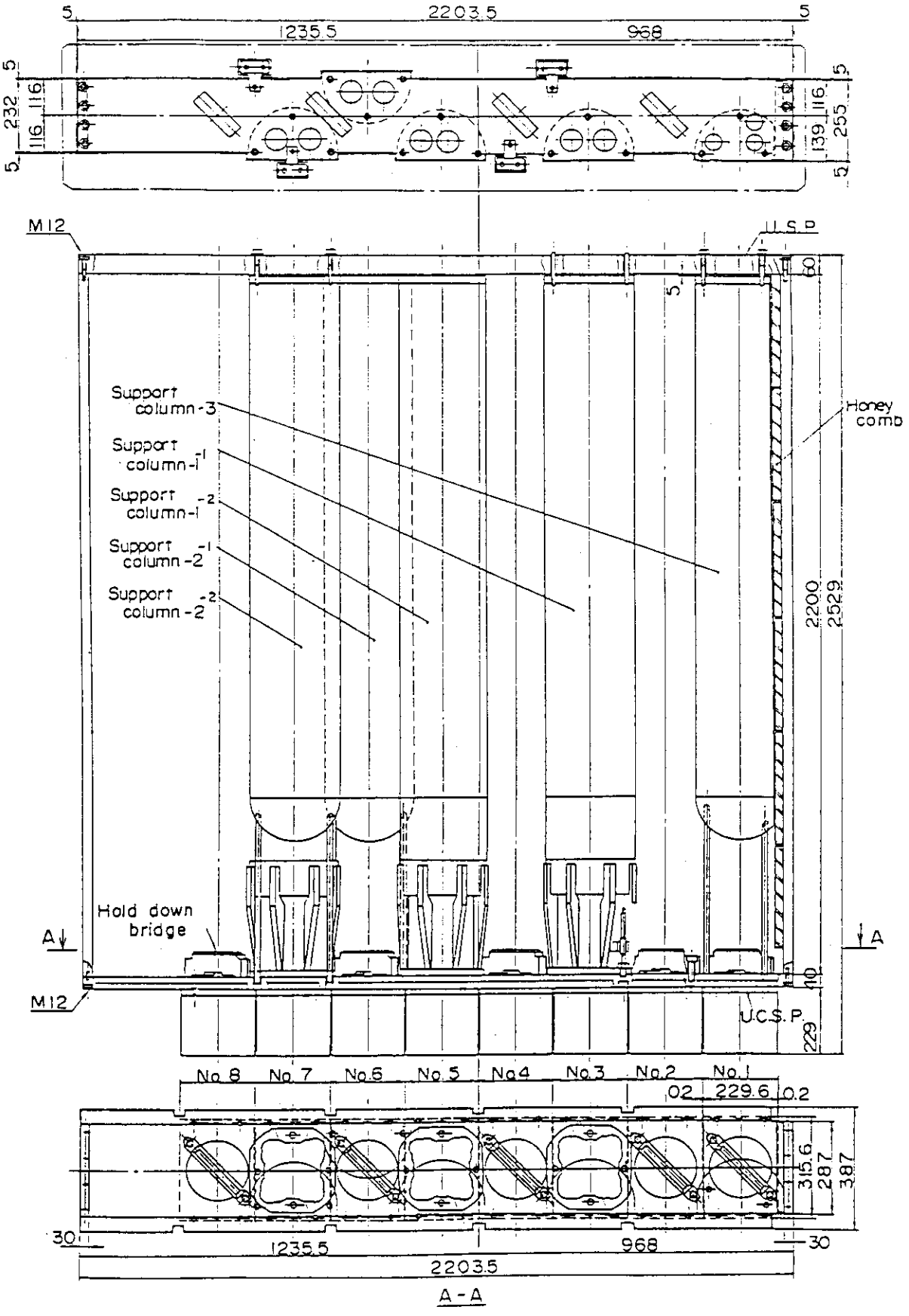

Fig. A-10 Three Kinds of CRGA Support Column

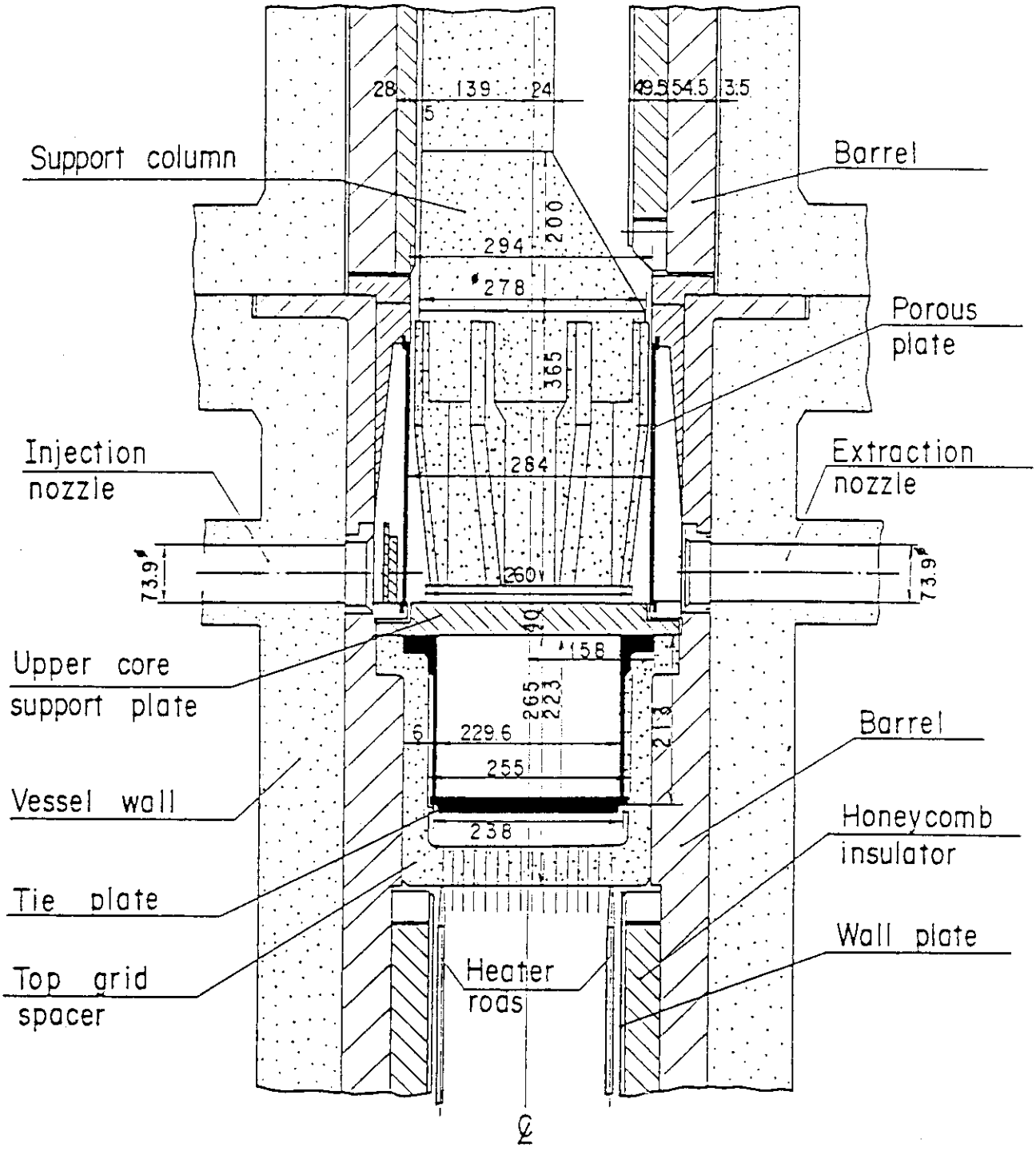

Fig. A-11 Vertical Cross Section of Interface between Core and Upper Plenum

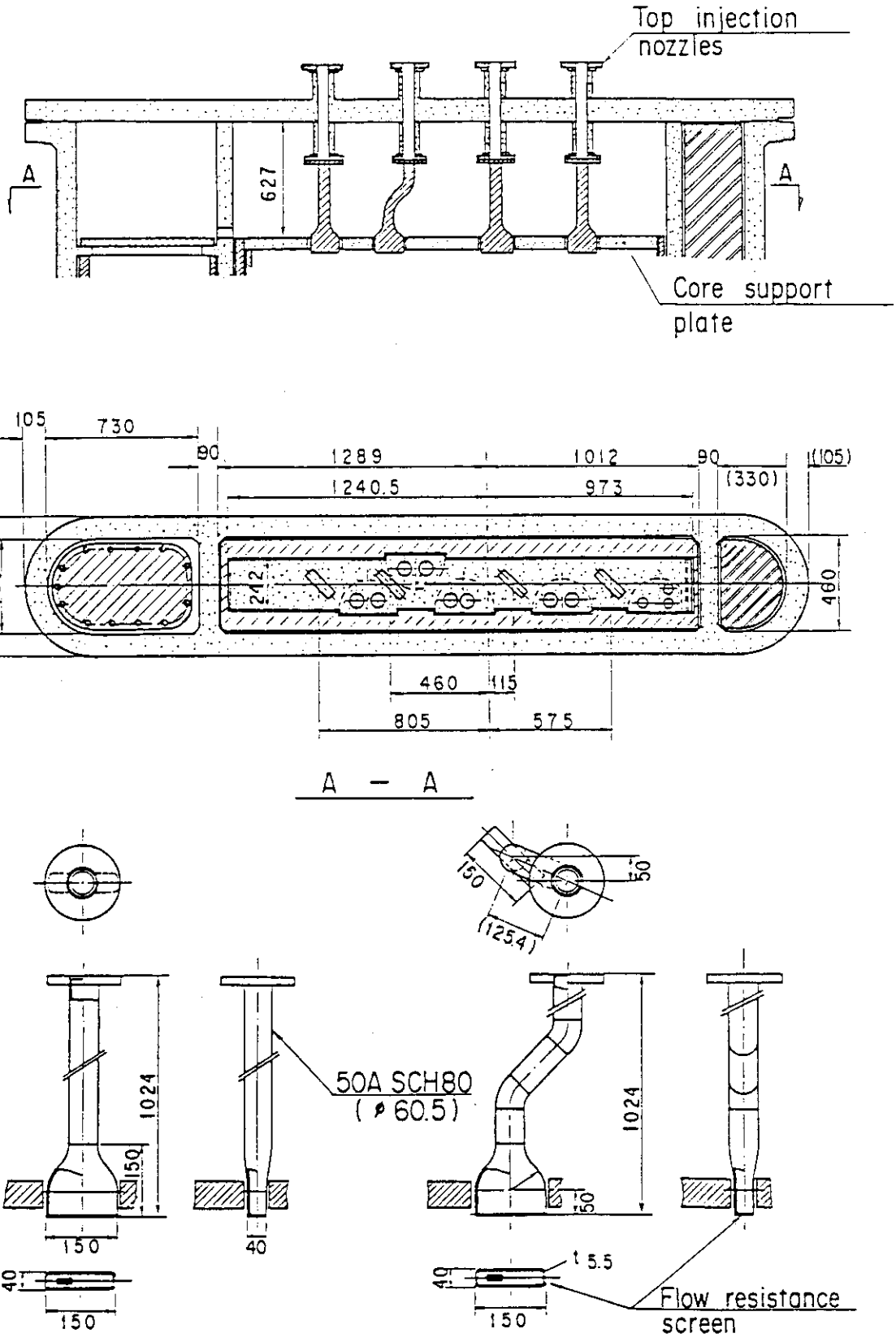

Fig. A-12 Schematic of Upper Head

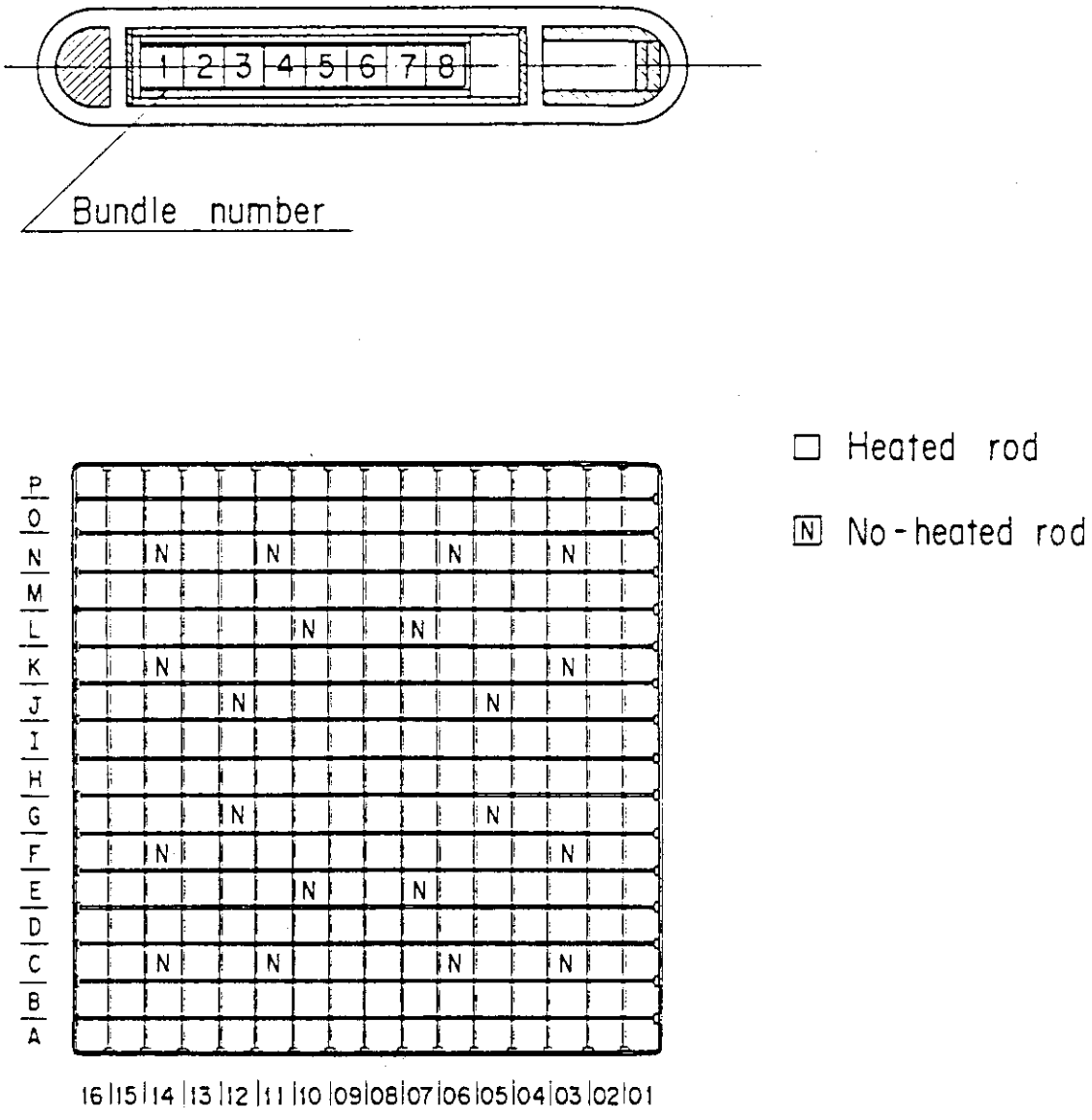

Fig. A-13 Arrangement of Heater Rod Bundles

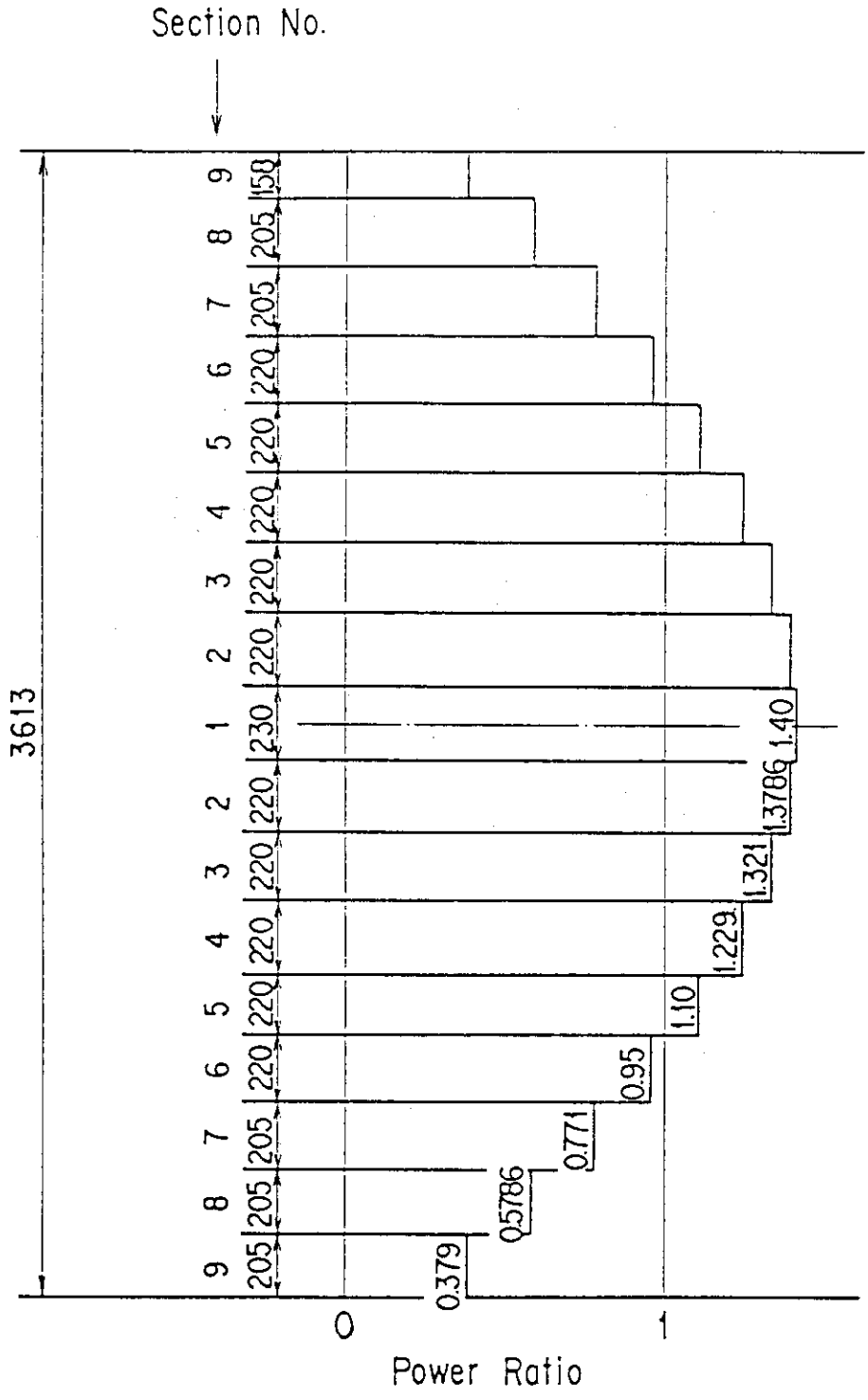

Fig. A-14 Axial Power Distribution of Heater Rods

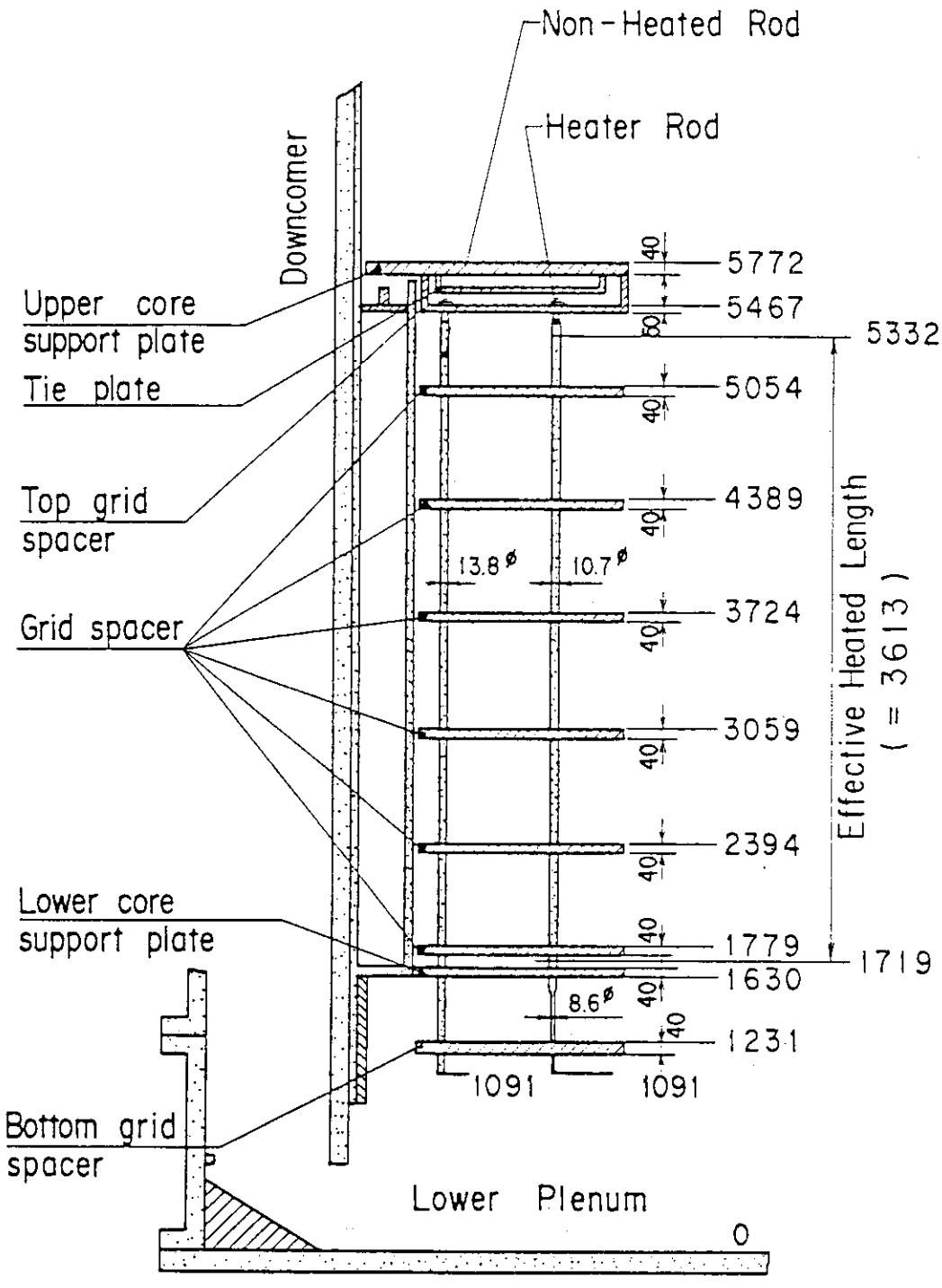

Fig. A-15 Relative Elevation and Dimension of Core

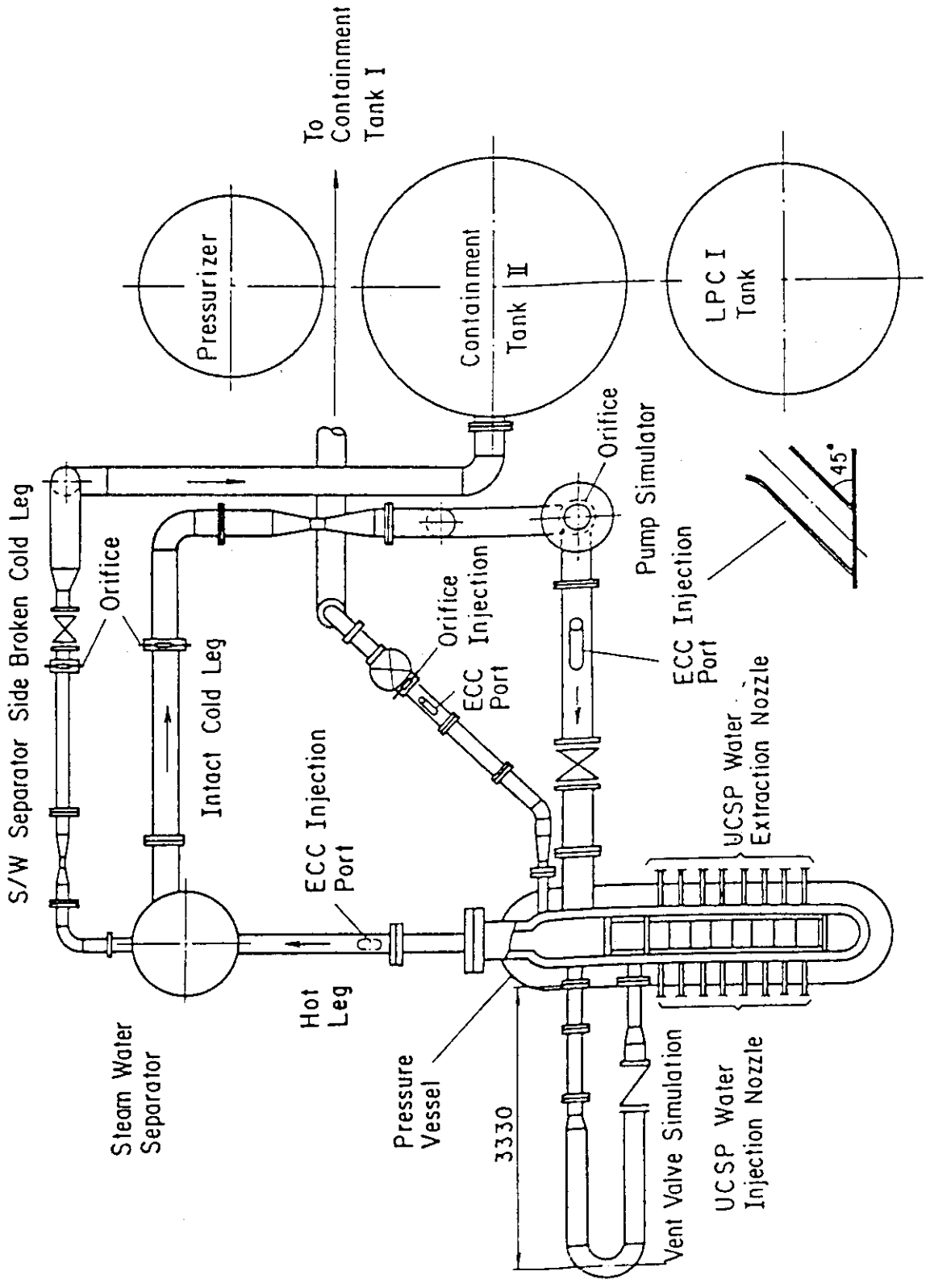

Fig. A-16 Overview of the Arrangements of SCTF

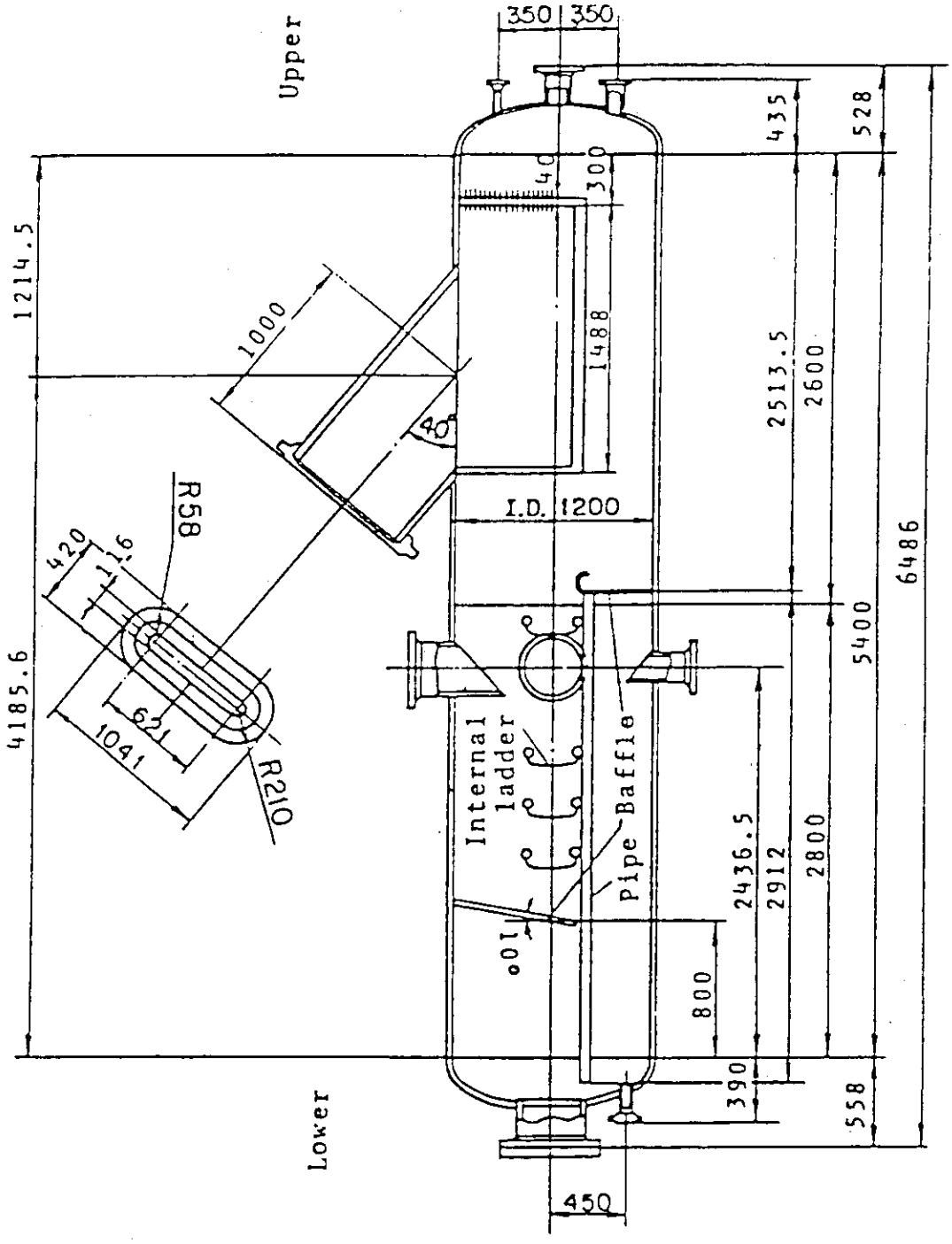

Fig. A-17 Steam/Water Separator

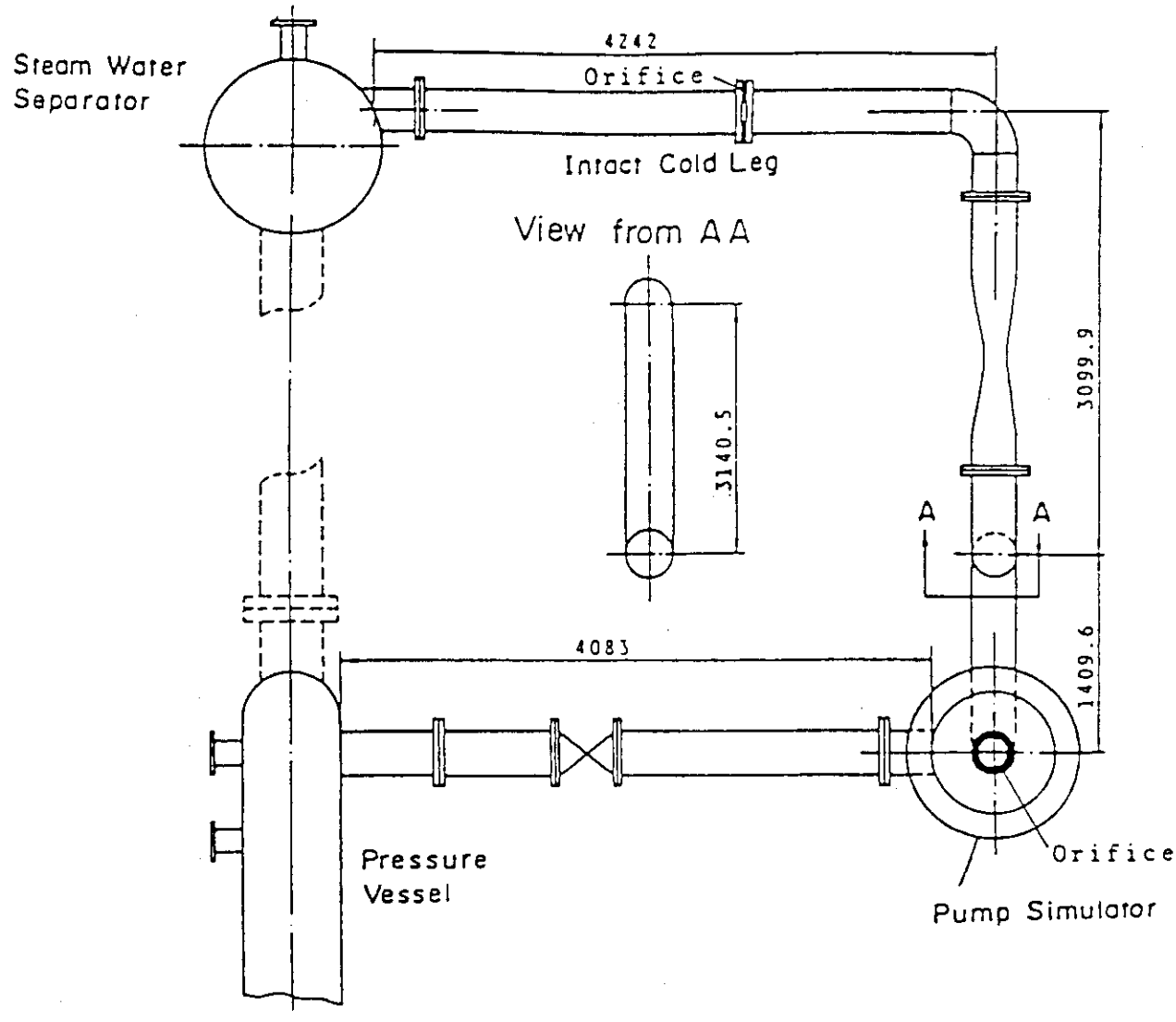

Fig. A-18 Arrangement of Intact Cold Leg

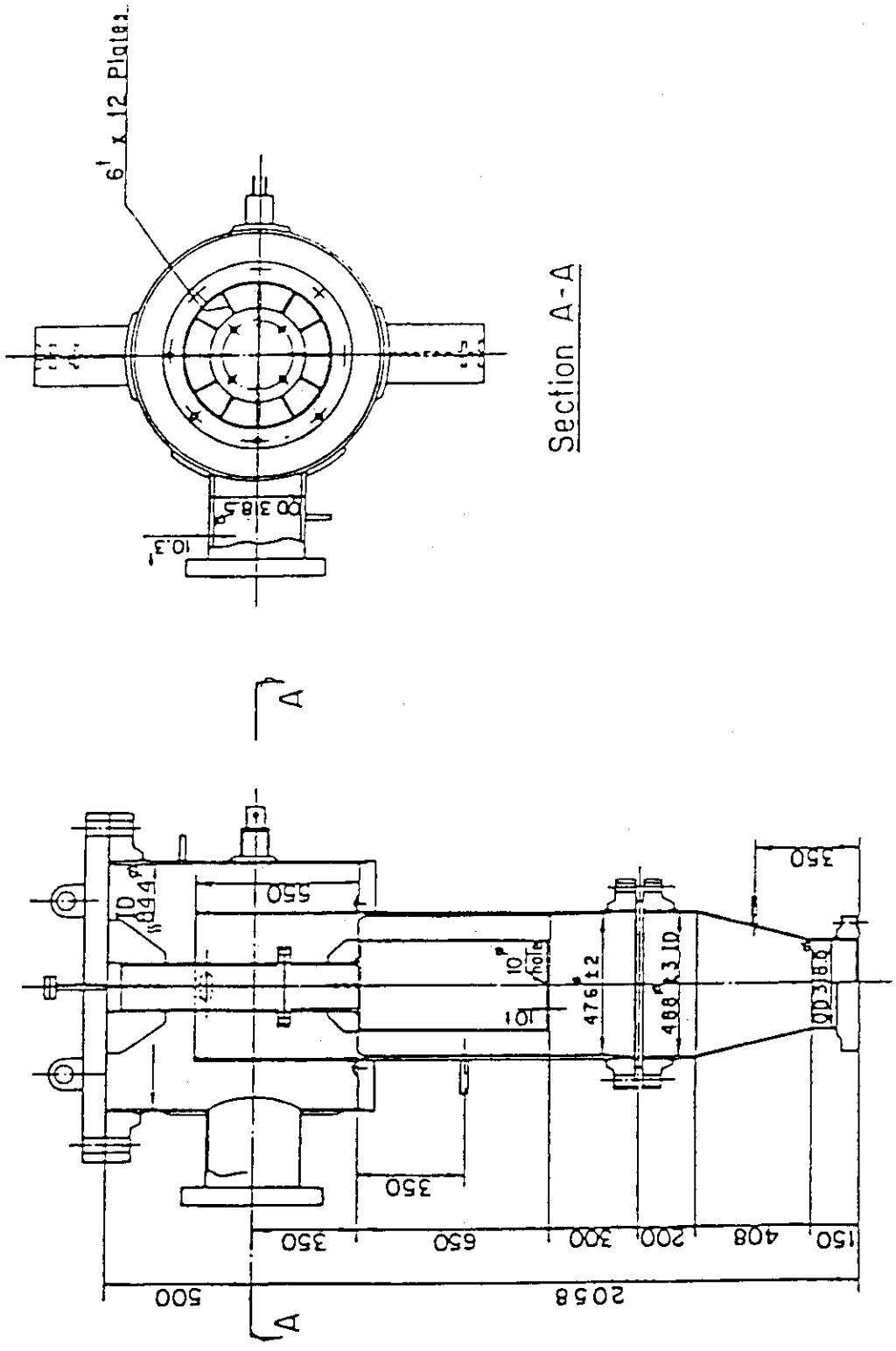

Fig. A-19 Configuration and Dimension of Pump Simulator

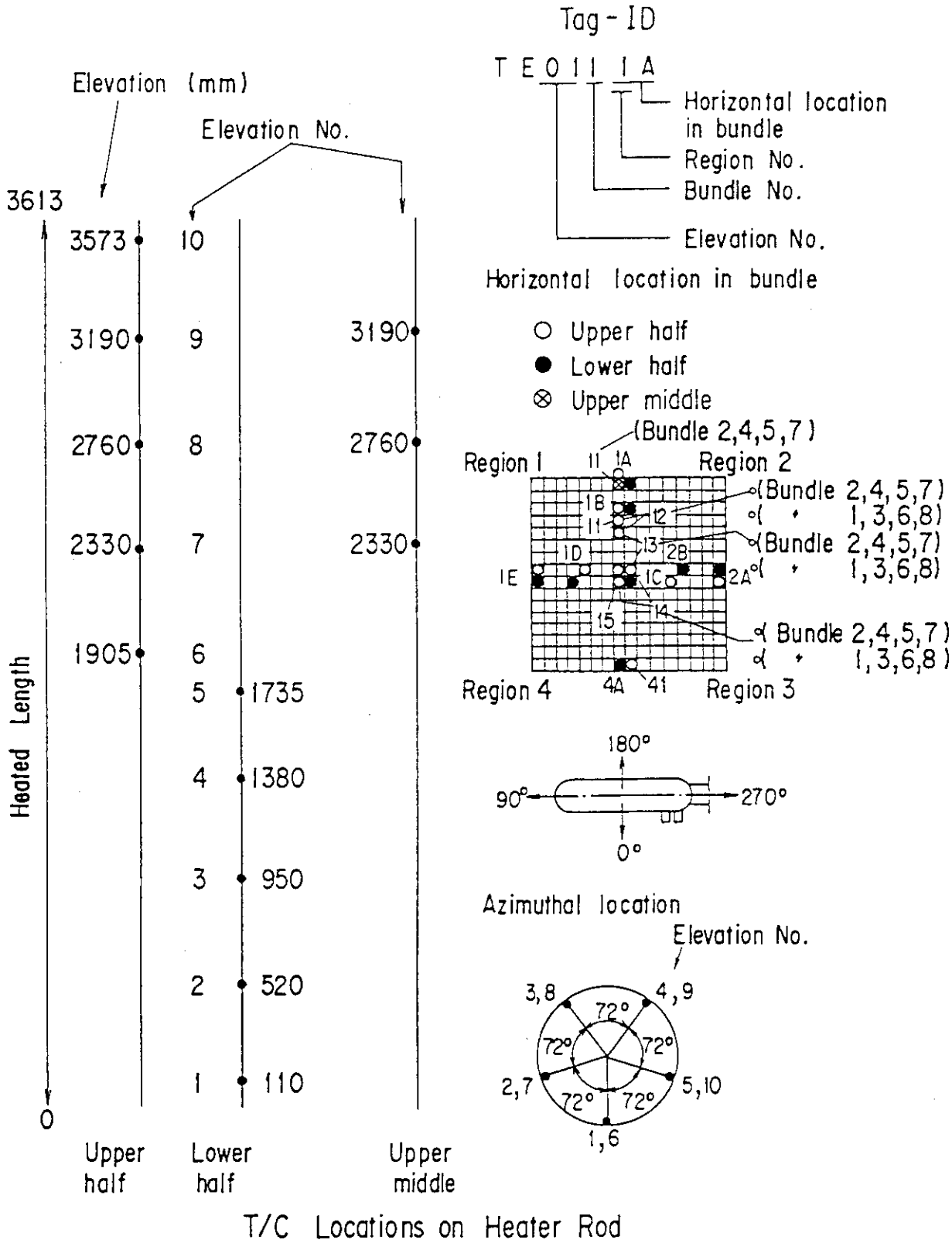

Fig. A-20 Thermocouple Locations of Heater Rod Surface Temperature Measurements

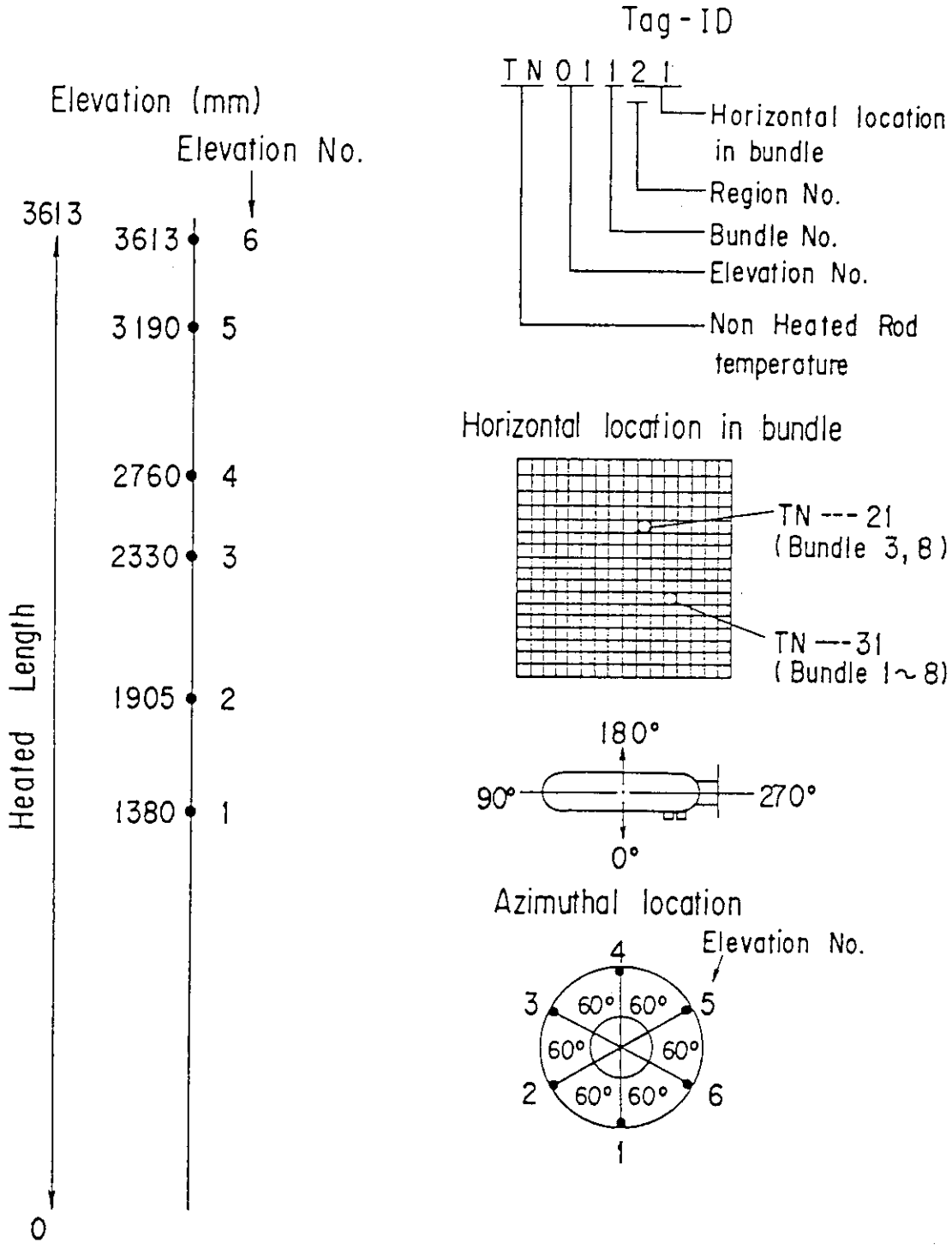

Fig. A-21 Thermocouple Locations of Non-Heated Rod Surface temperature Measurements

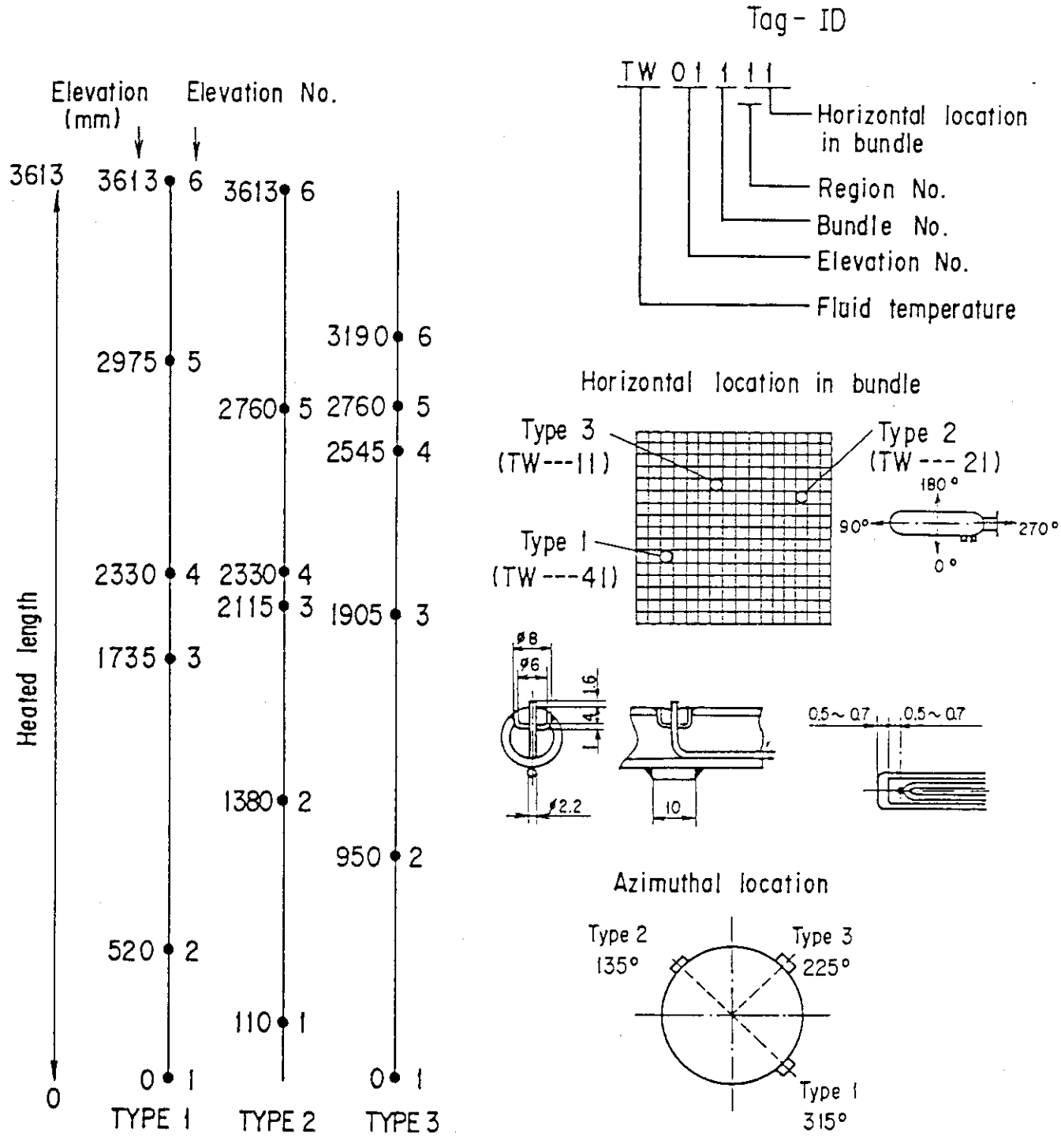

Fig. A-22 Thermocouple Locations of Fluid Temperature Measurements in Core

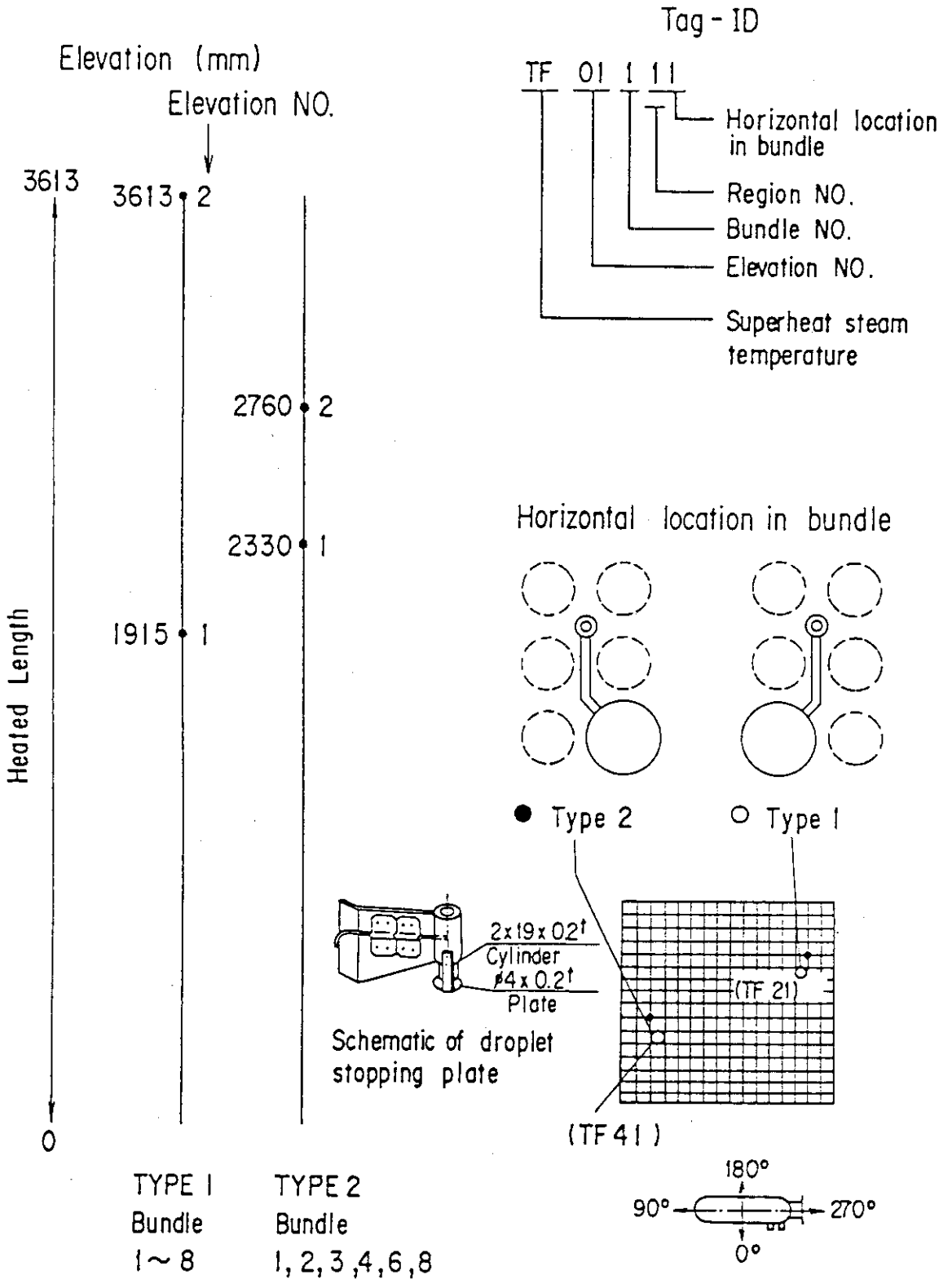

Fig. A-23 Thermocouple Locations of Steam Temperature Measurements in Core

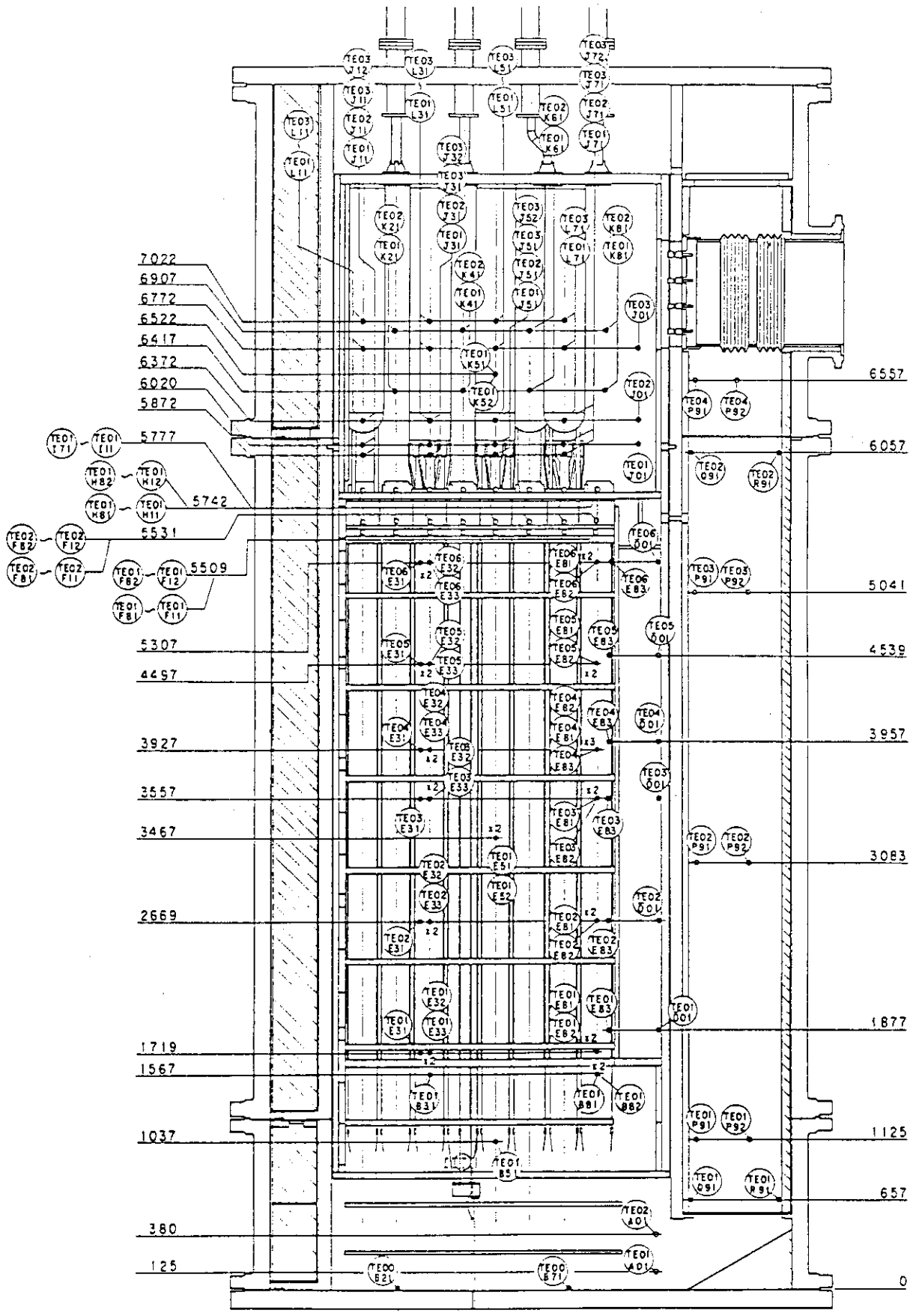

Fig. A-24 Thermocouple Locations of Temperature Measurements in Pressure Vessel except Core Region (Vertical View)

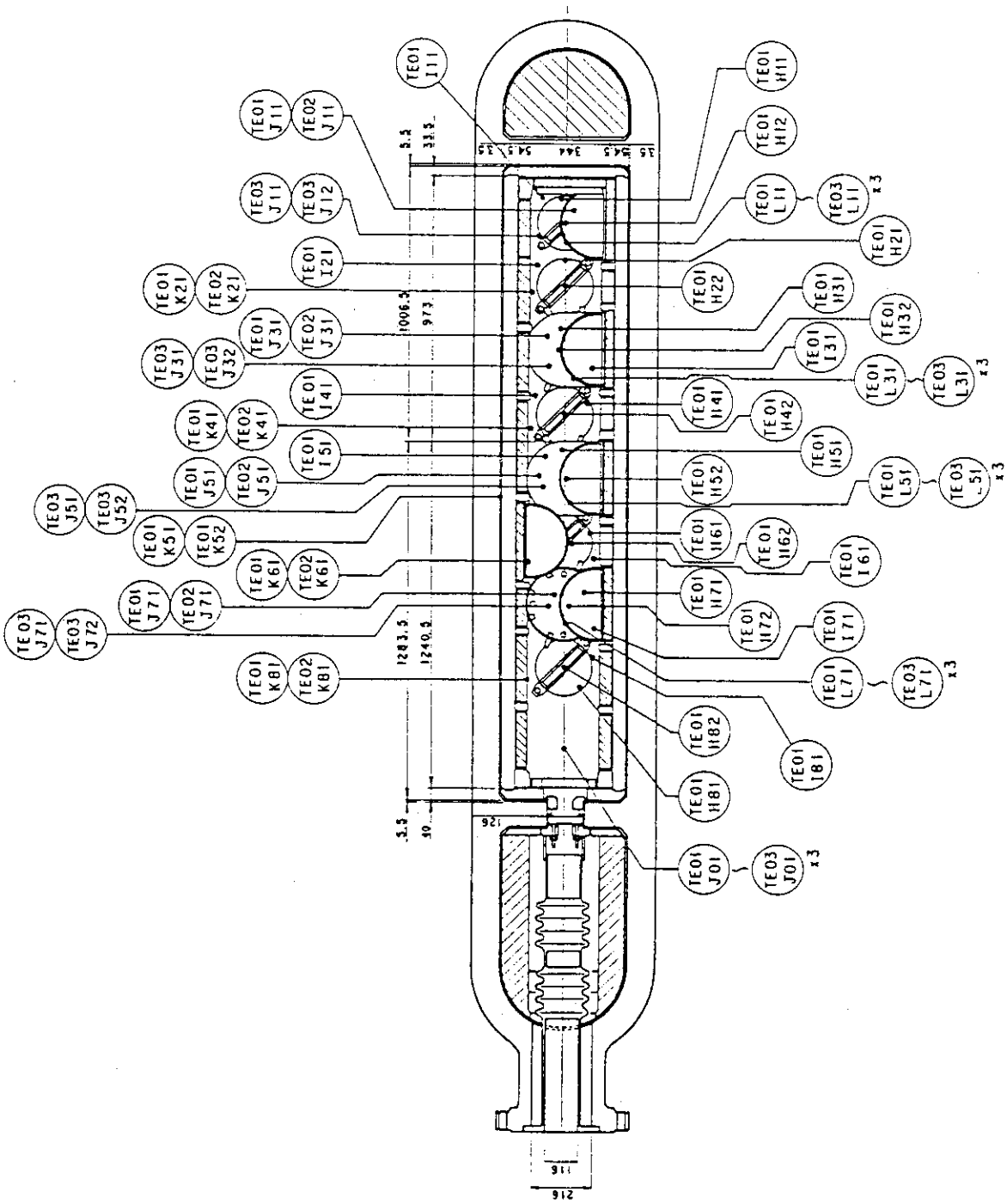

Fig. A-25 Thermocouple Locations of Temperature Measurements in Upper Plenum (Horizontal View)

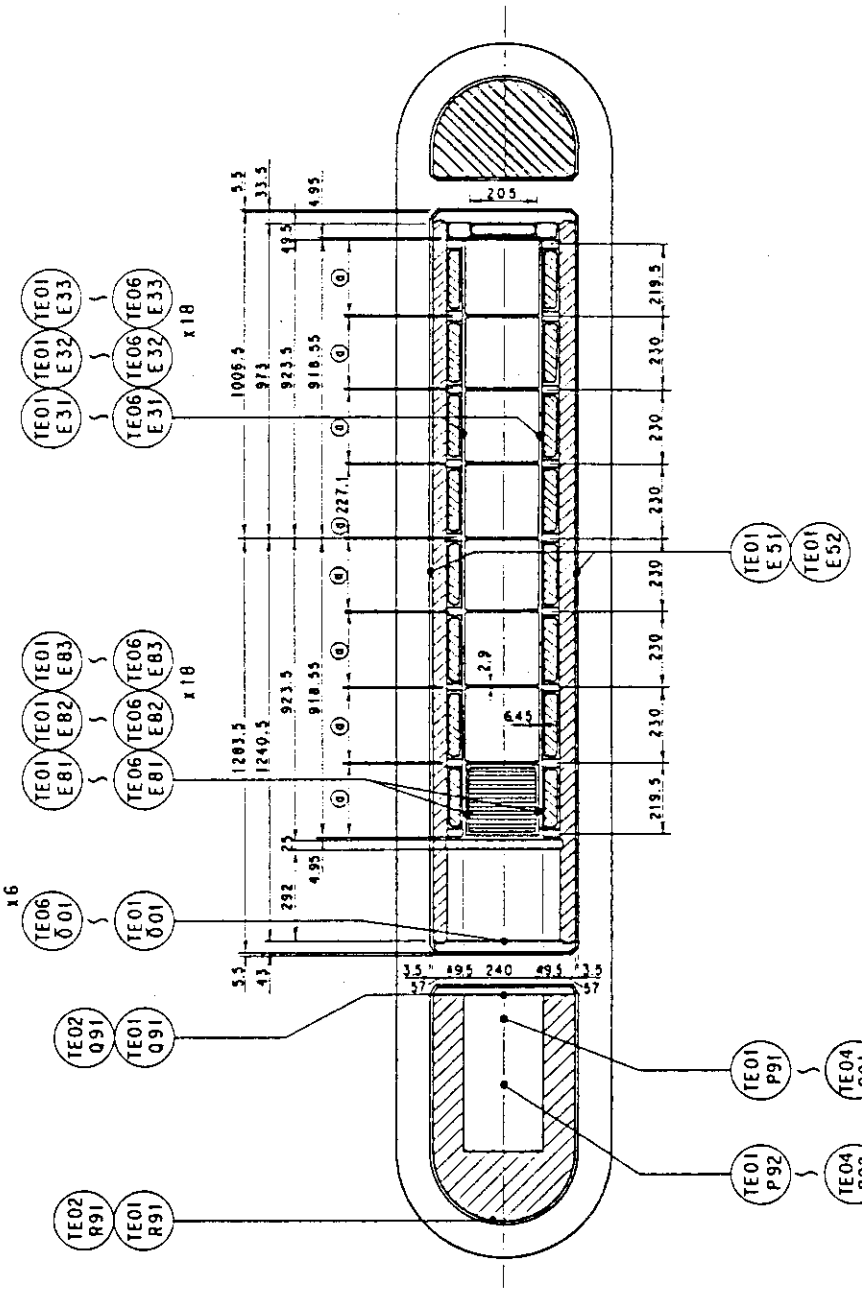

Fig. A-26 Thermocouple Locations of Temperature Measurements in Pressure Vessel except Upper Plenum (Horizontal View)

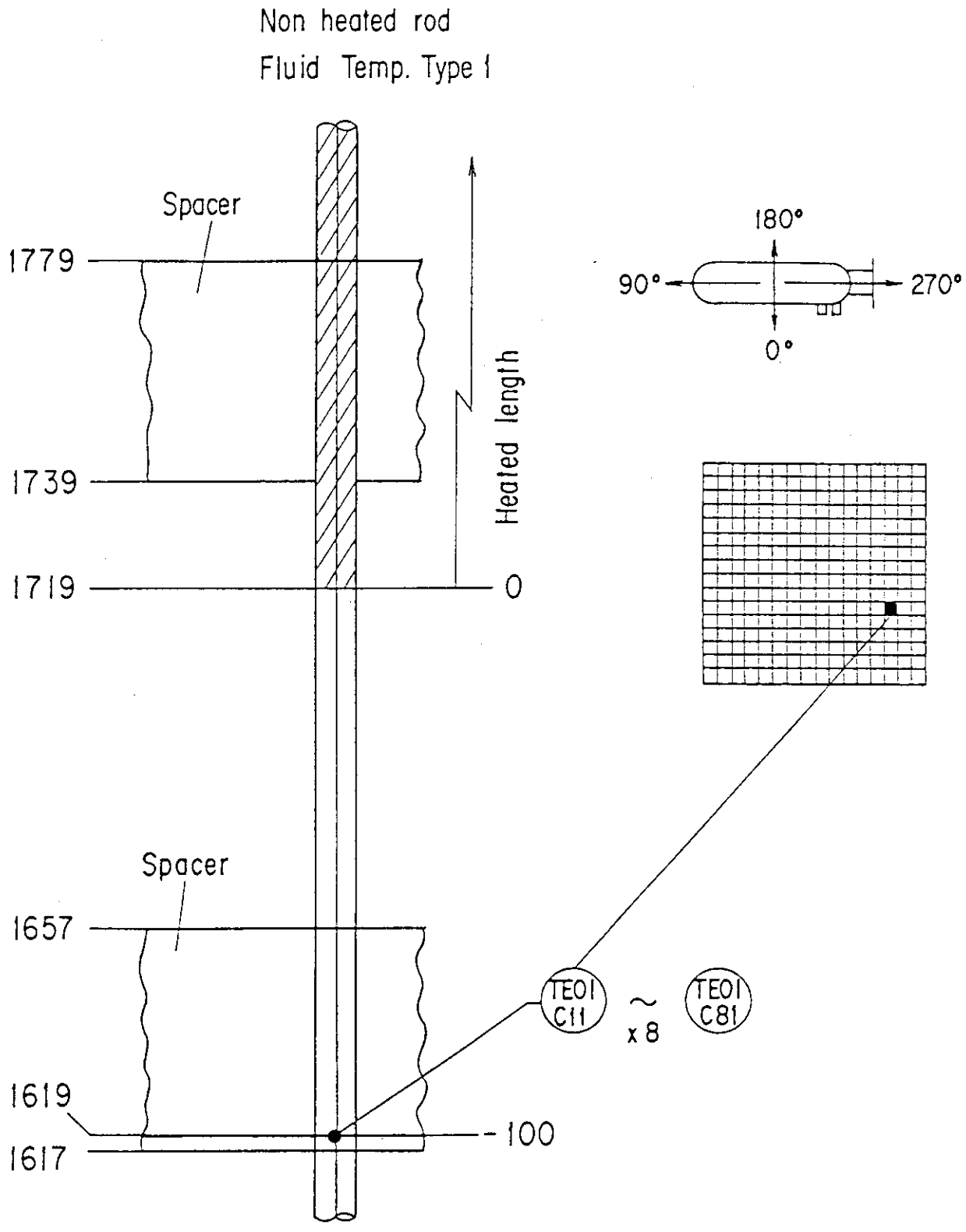

Fig. A-27 Thermocouple Locations of Fluid Temperature Measurements at Core Inlet

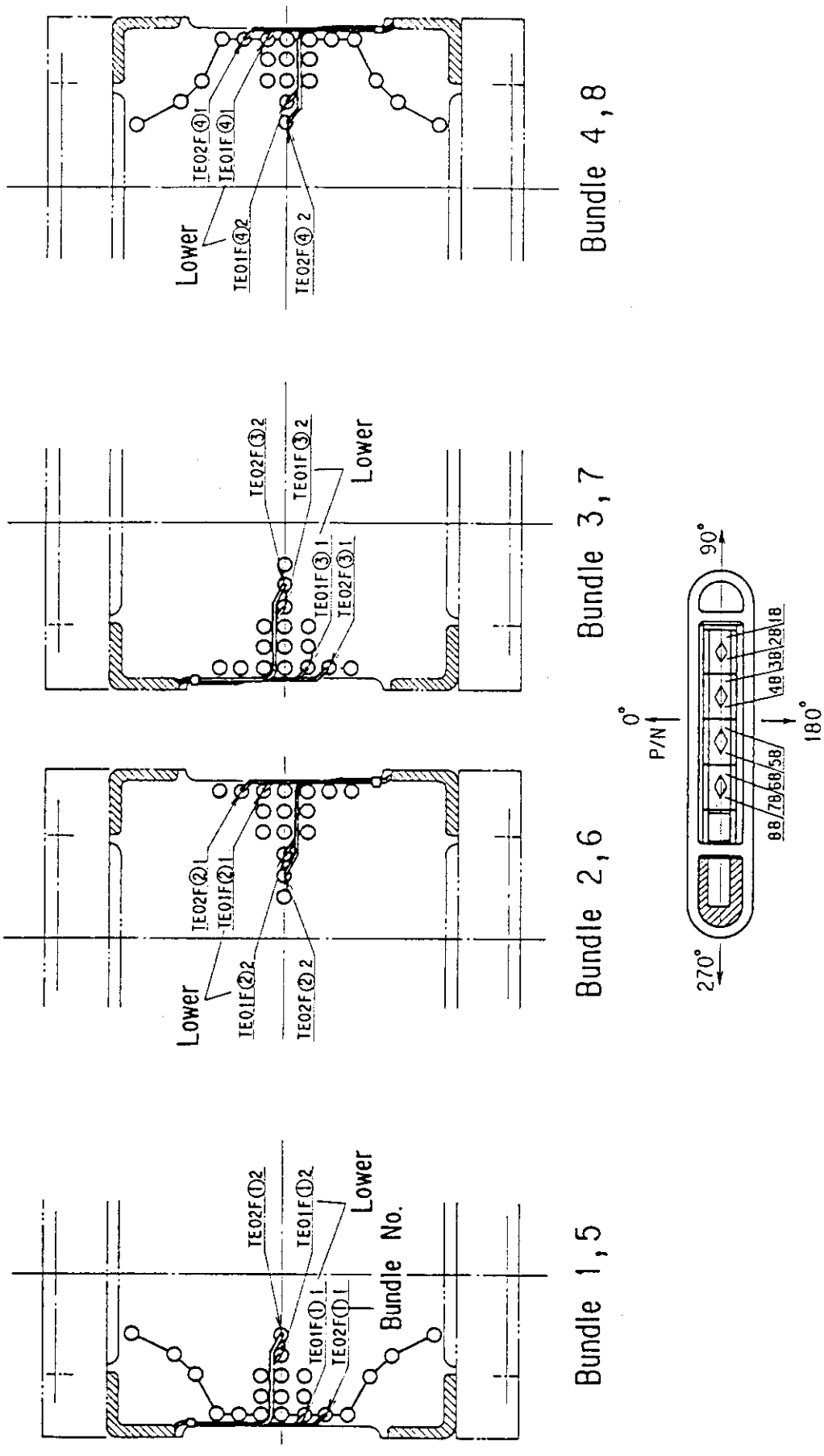

Fig. A-28 Thermocouple Locations of Fluid Temperature Measurements just above and below End Box Tie Plates

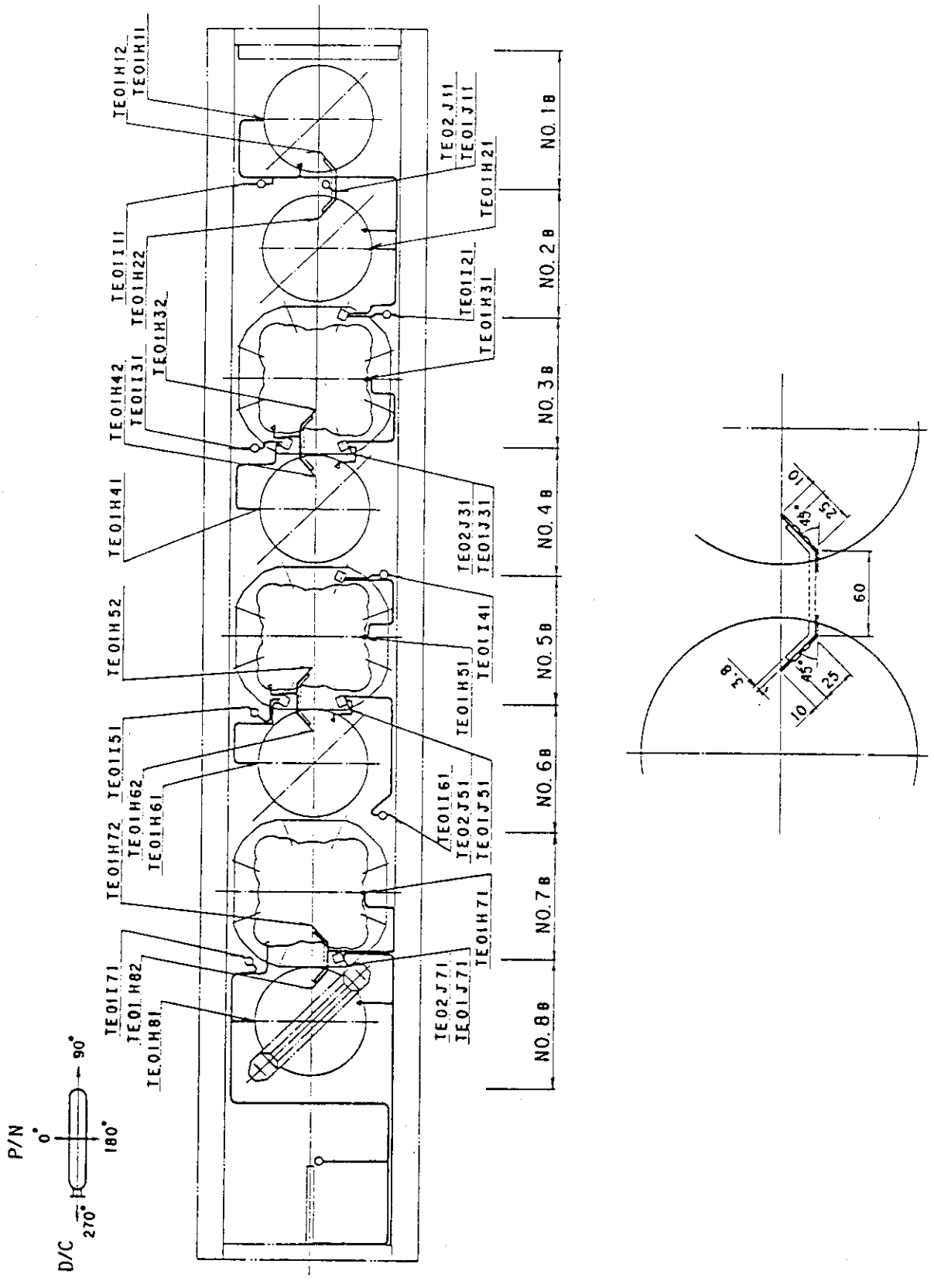

Fig. A-29 Thermocouple Locations of Fluid Temperature Measurements on UCSP and at Inside and Periphery of UCSP Holes

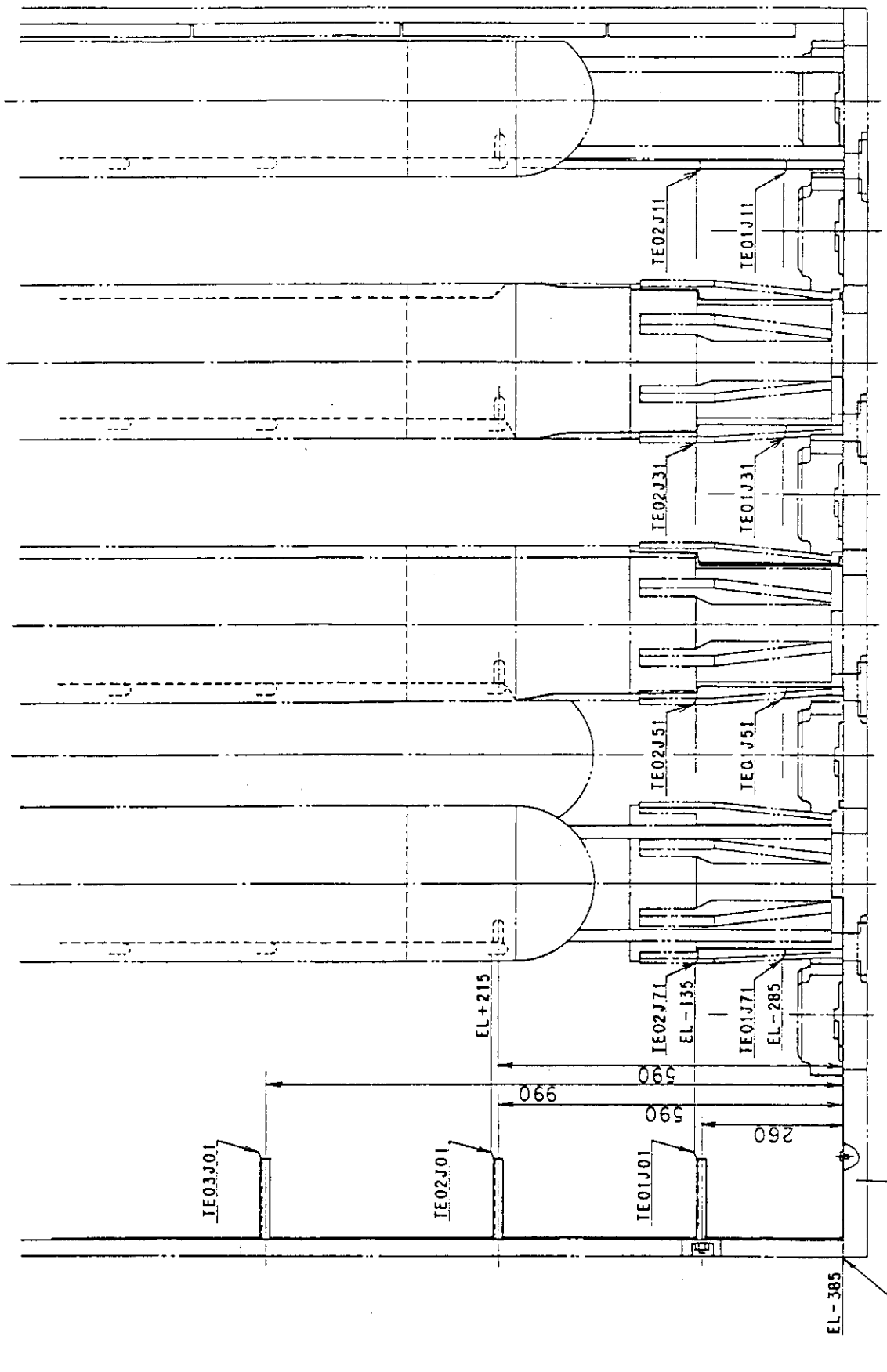

Fig. A-30 Thermocouple Locations of Fluid Temperature Measurements on and above UCSP

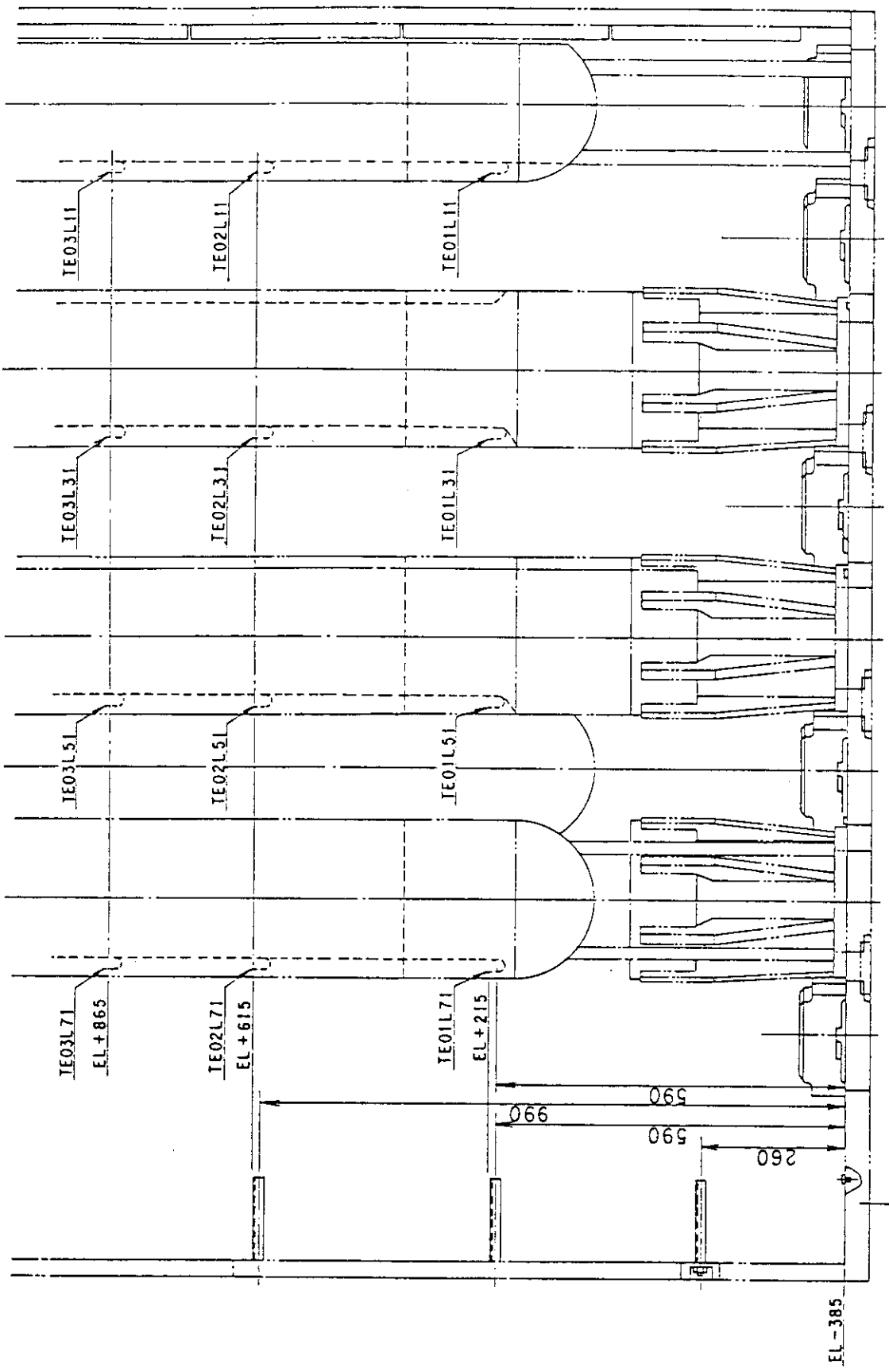

Fig. A-31 Thermocouple Locations of Surface Temperature Measurements of Upper Plenum Structures

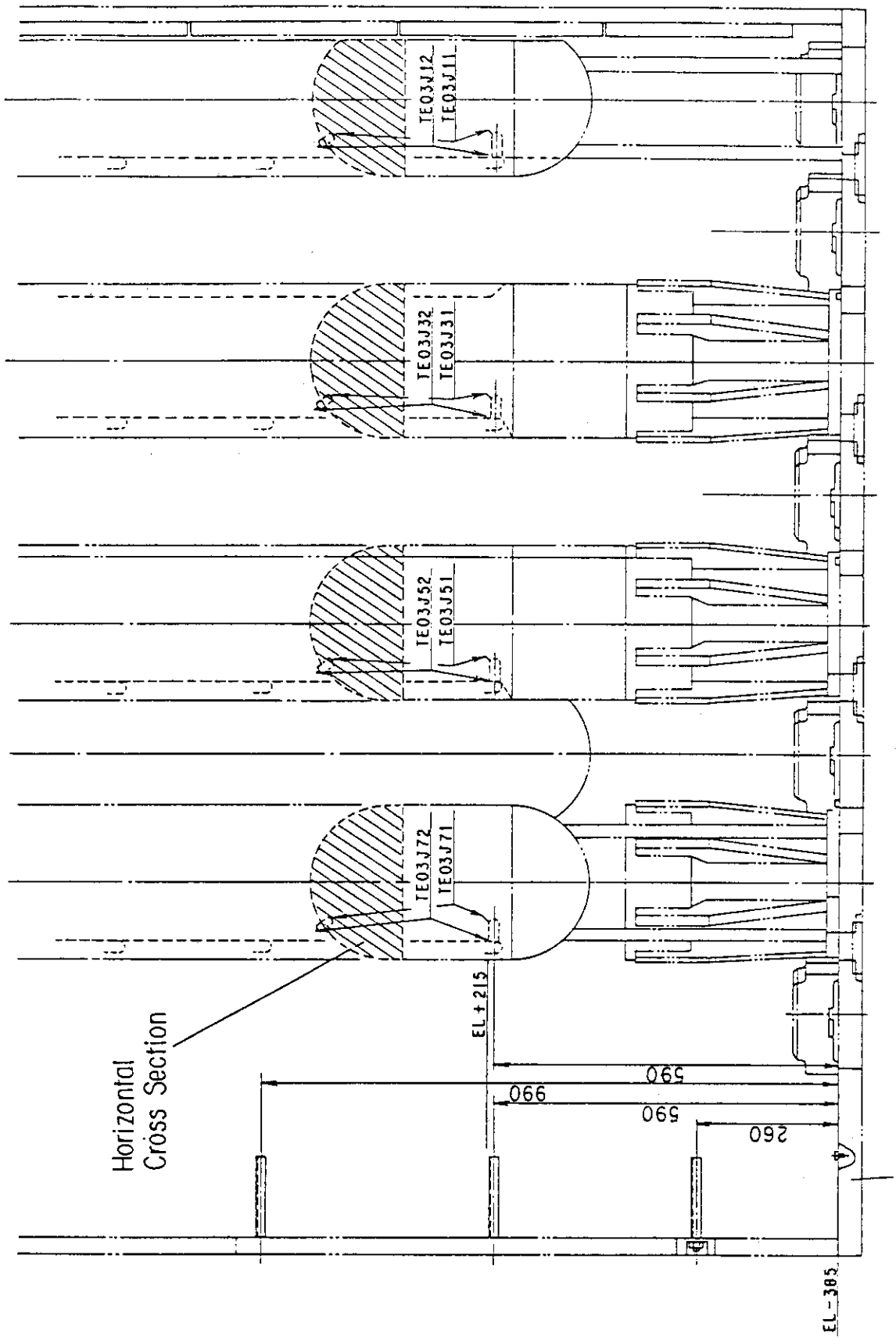

Fig. A-32 Thermocouple Locations of Steam Temperature Measurements above UCSP Holes

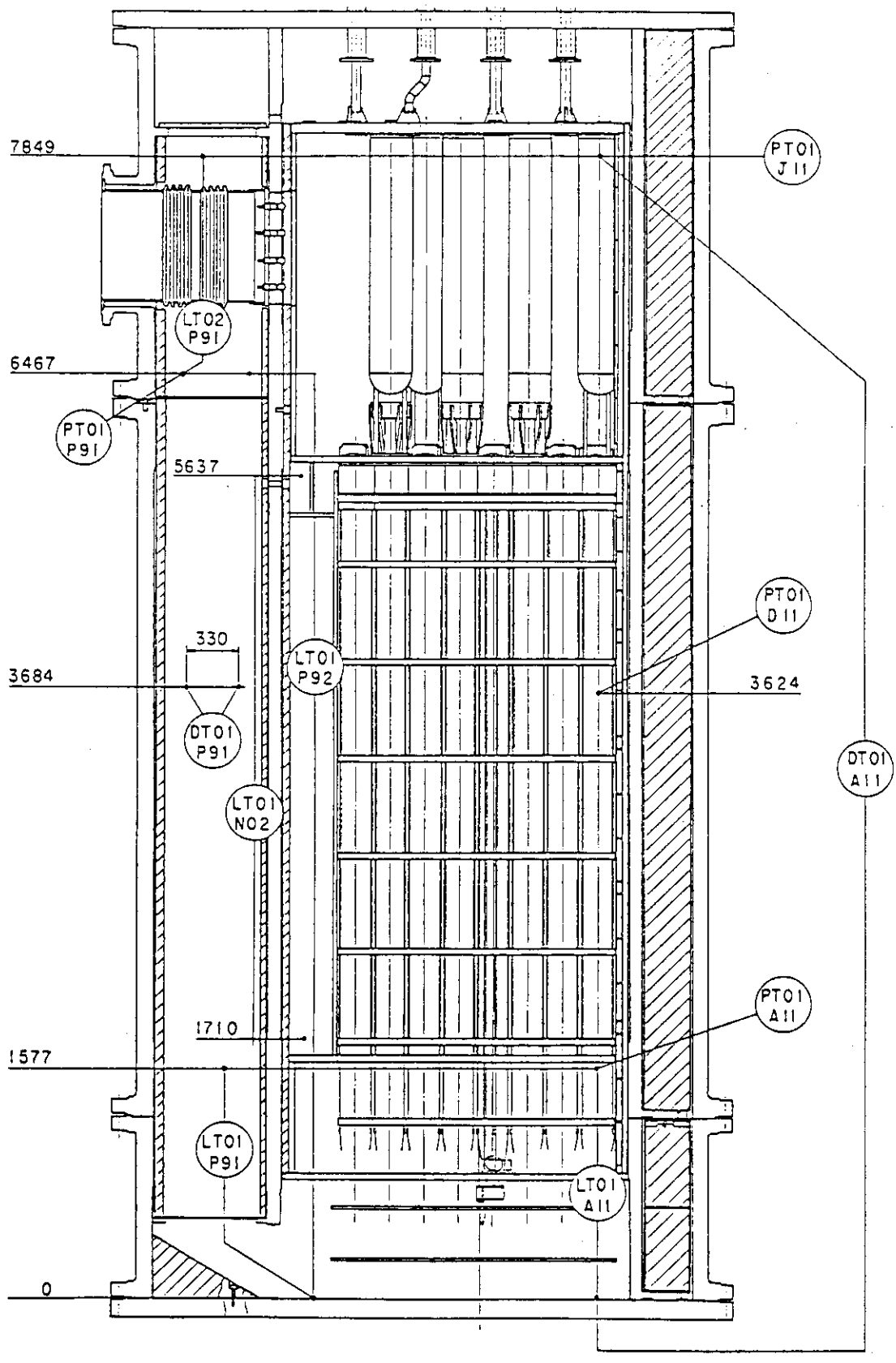

Fig. A-33 Locations of Pressure Measurements in Pressure Vessel, Differential Pressure Measurements between Upper and Lower Plenums and Liquid Level Measurements in Downcomer and Lower Plenum

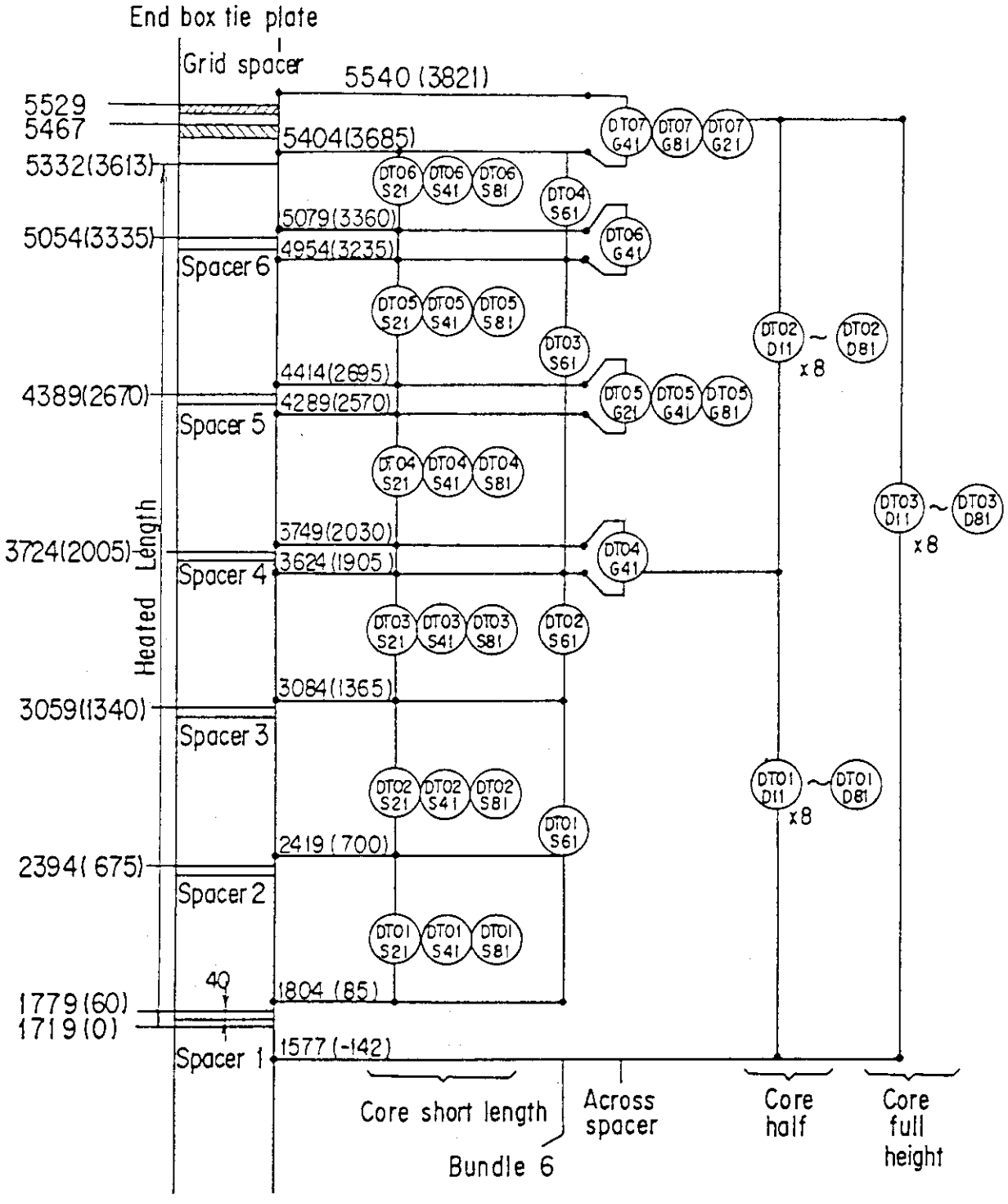

Fig. A-34 Locations of Vertical Differential Pressure Measurements in Core

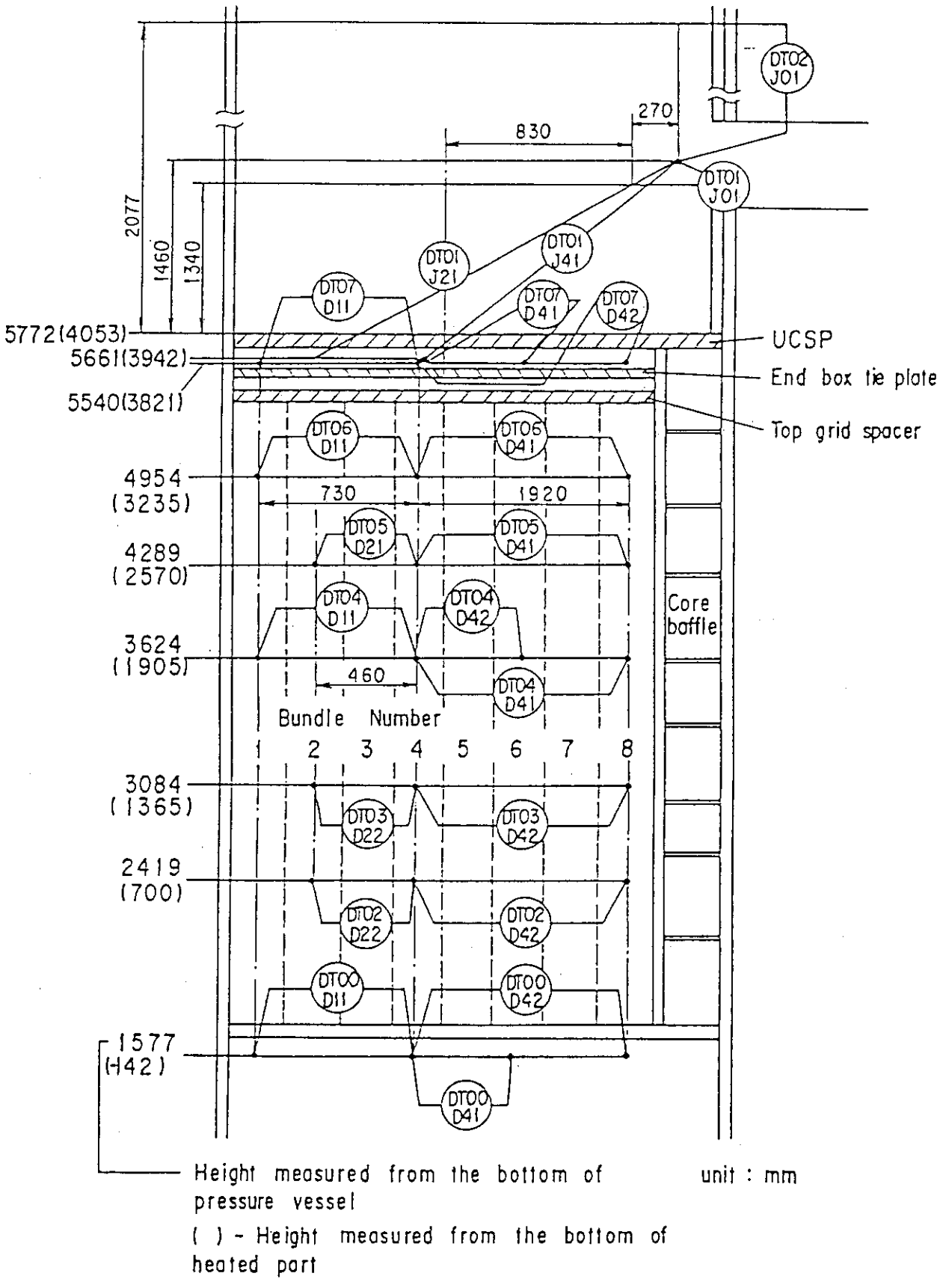

Fig. A-35 Locations of Horizontal Differential Pressure Measurements in Core and Differential Pressure Measurements between End Boxes and Inlet of Hot Leg

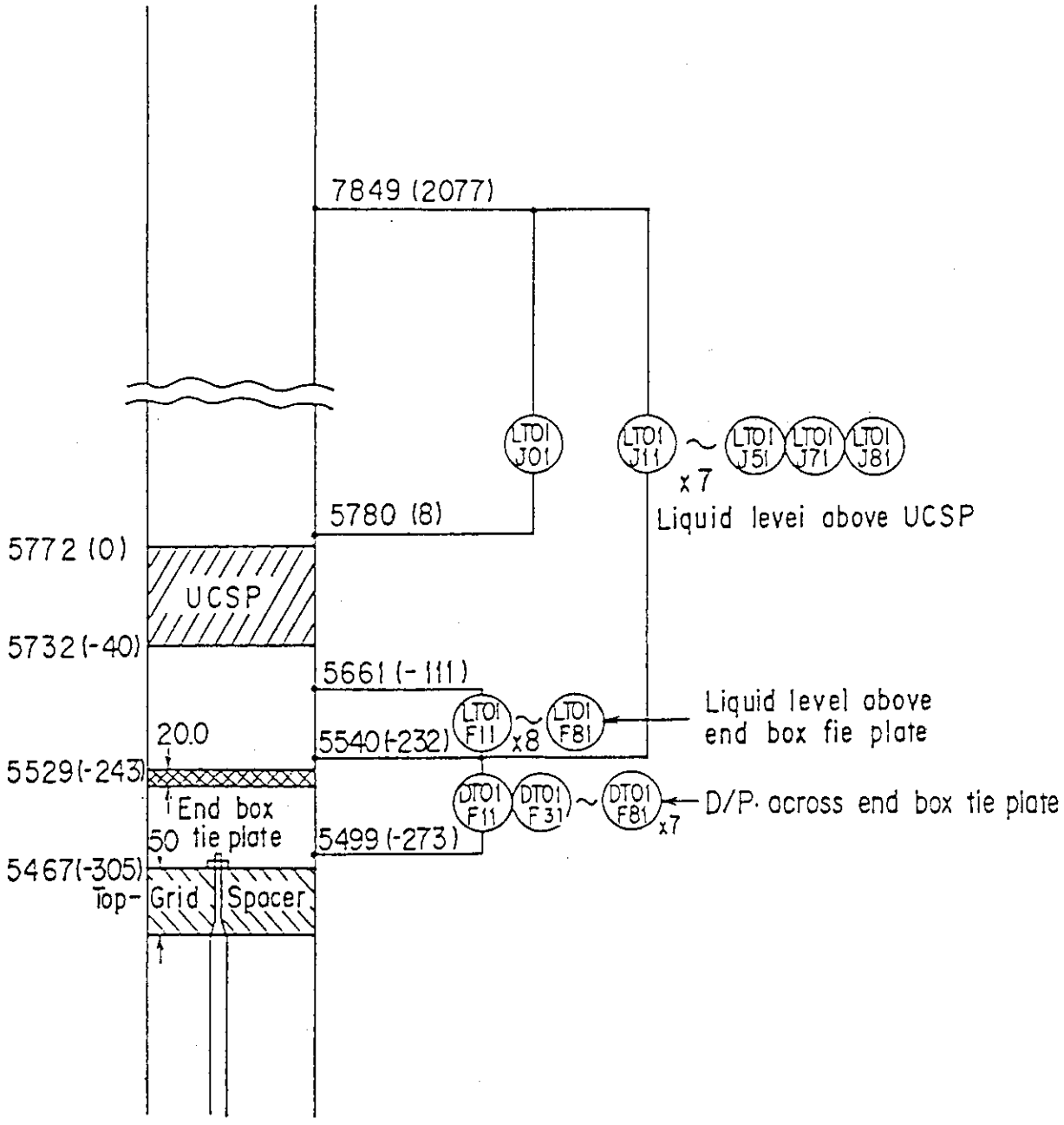

Fig. A-36 Locations of Differential Pressure Measurements across End Box Tie Plate

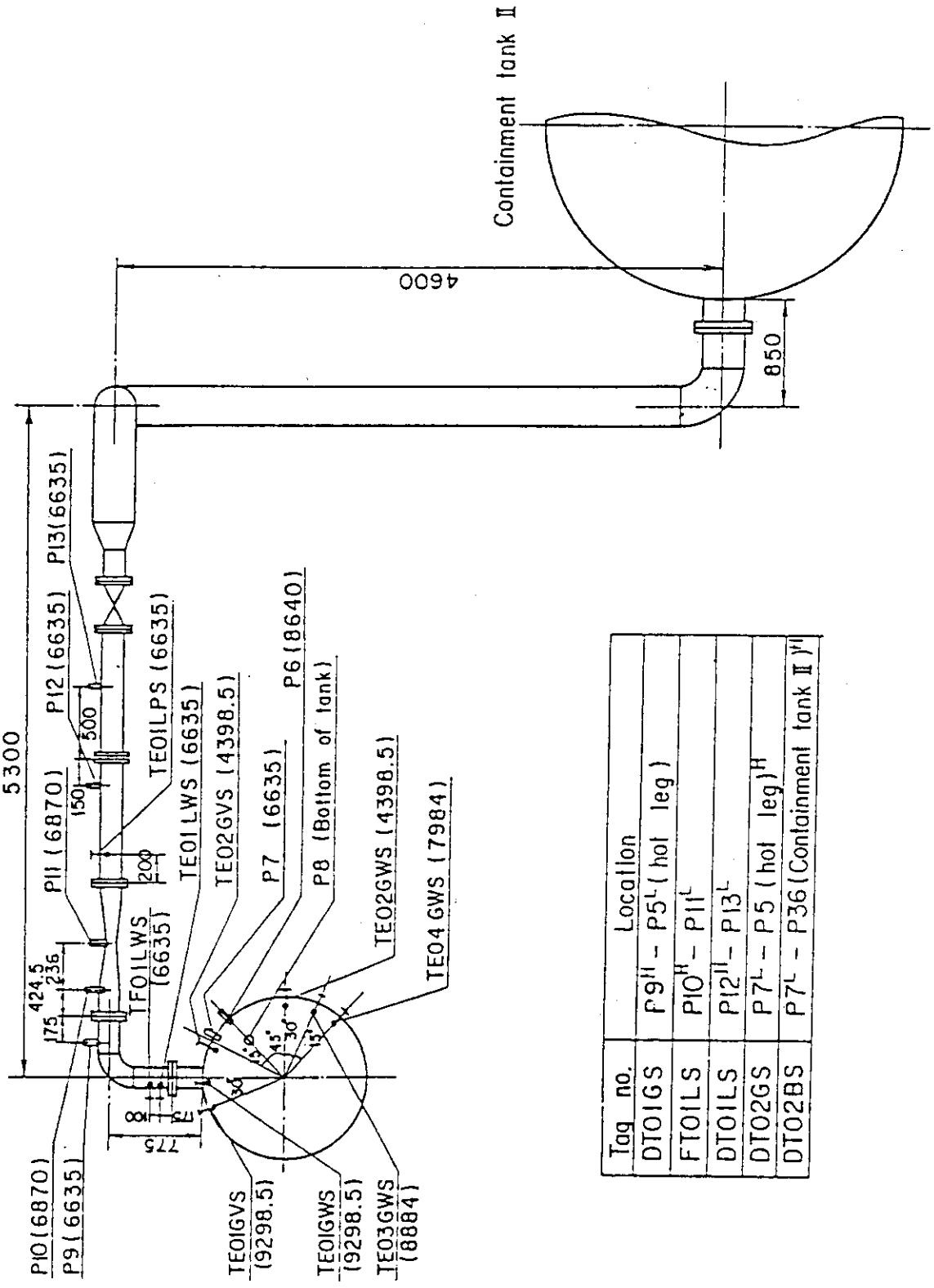

Tag no.	Location
DT01GS	$P9^{H} - P5^{L}$ (hot leg)
FT01LS	$P10^{H} - P11^{L}$
DT01LS	$P12^{H} - P13^{L}$
DT02GS	$P7^{L} - P5$ (hot leg)^{H}
DT02BS	$P7^{L} - P36$ (Containment tank II)^{H}

Fig. A-37 Locations of Broken Cold Leg Instruments (Steam-Water Separator Side)

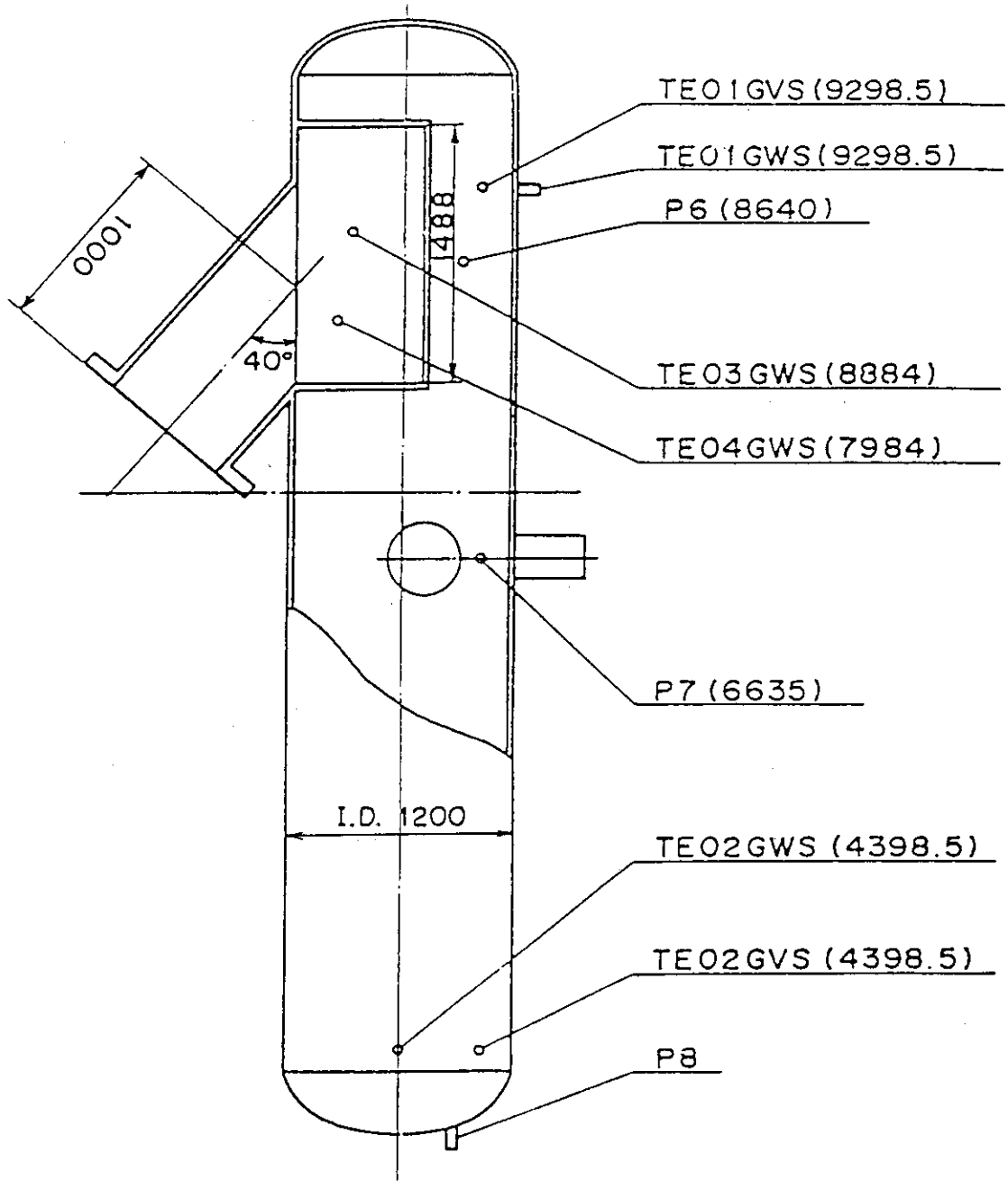

Fig. A-38 Locations of Steam-Water Separator Instruments

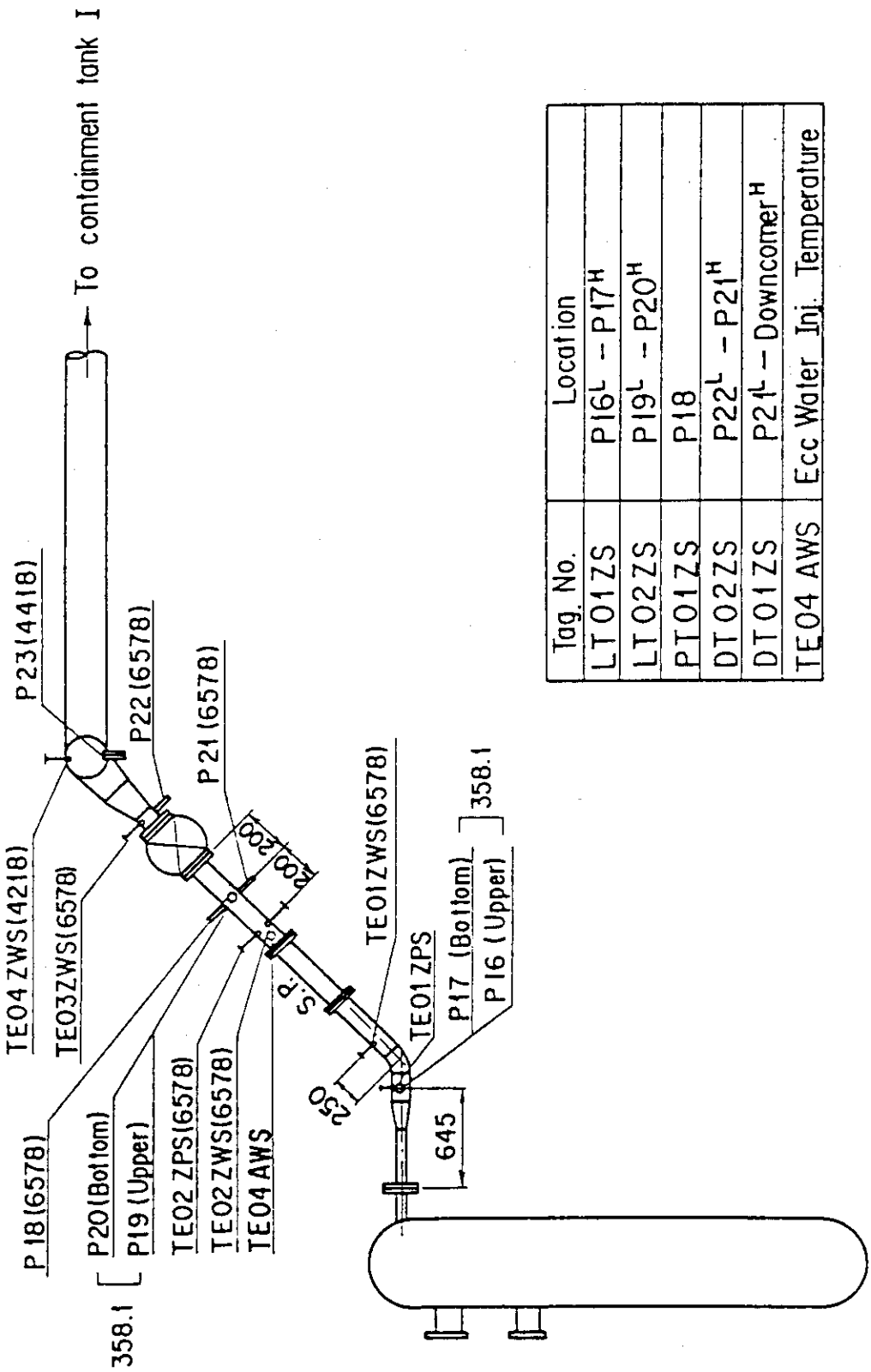

Fig. A-39 Locations of Broken Cold Leg Instruments
(Pressure Vessel Side)

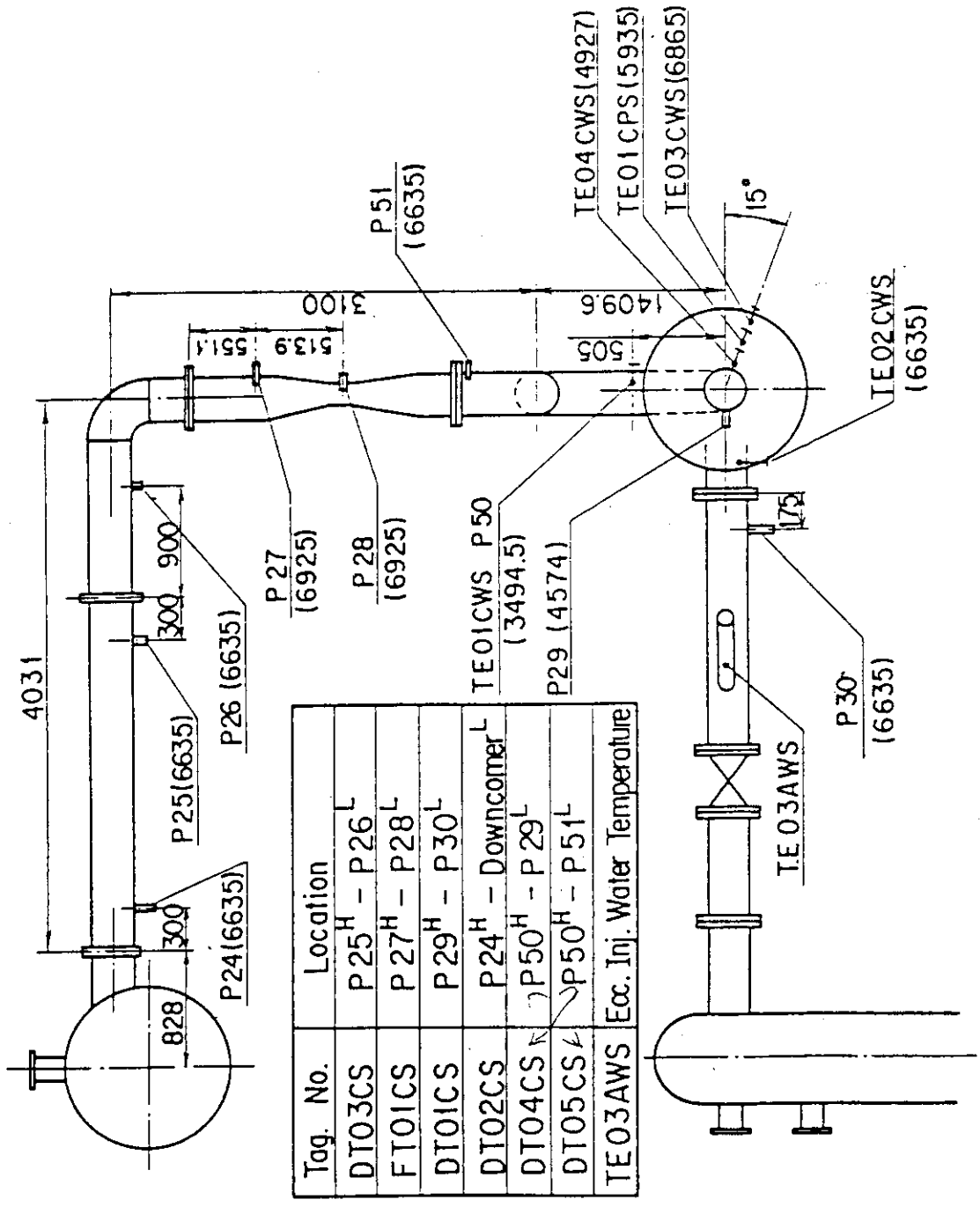

Fig. A-40 Locations of Intact Cold Leg Instruments

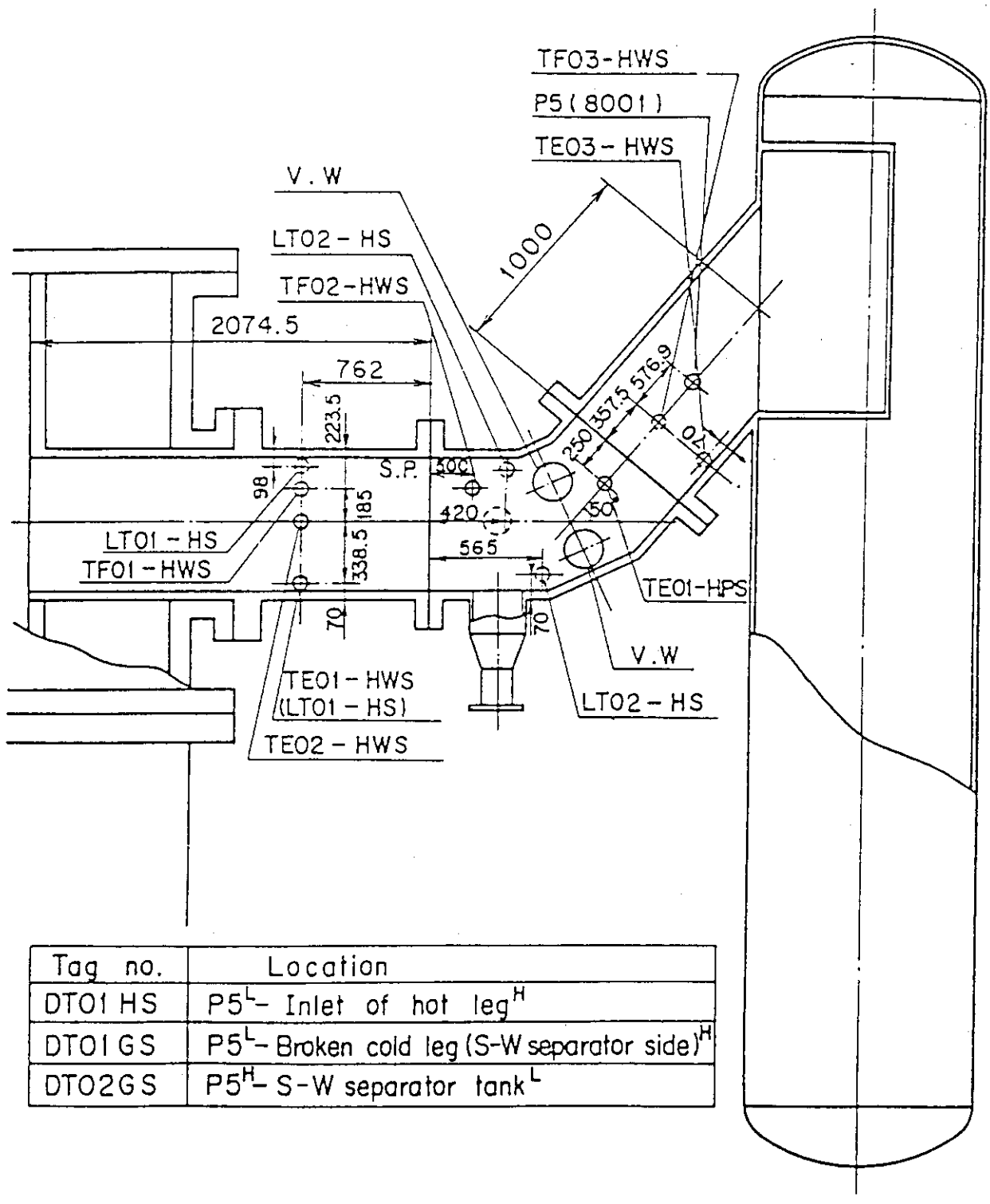

Tag no.	Location
DT01HS	$P5^{L}$- Inlet of hot leg^{H}
DT01GS	$P5^{L}$- Broken cold leg (S-W separator side)^{H}
DT02GS	$P5^{H}$- S-W separator tank^{L}

Fig. A-41 Locations of Hot Leg Instruments

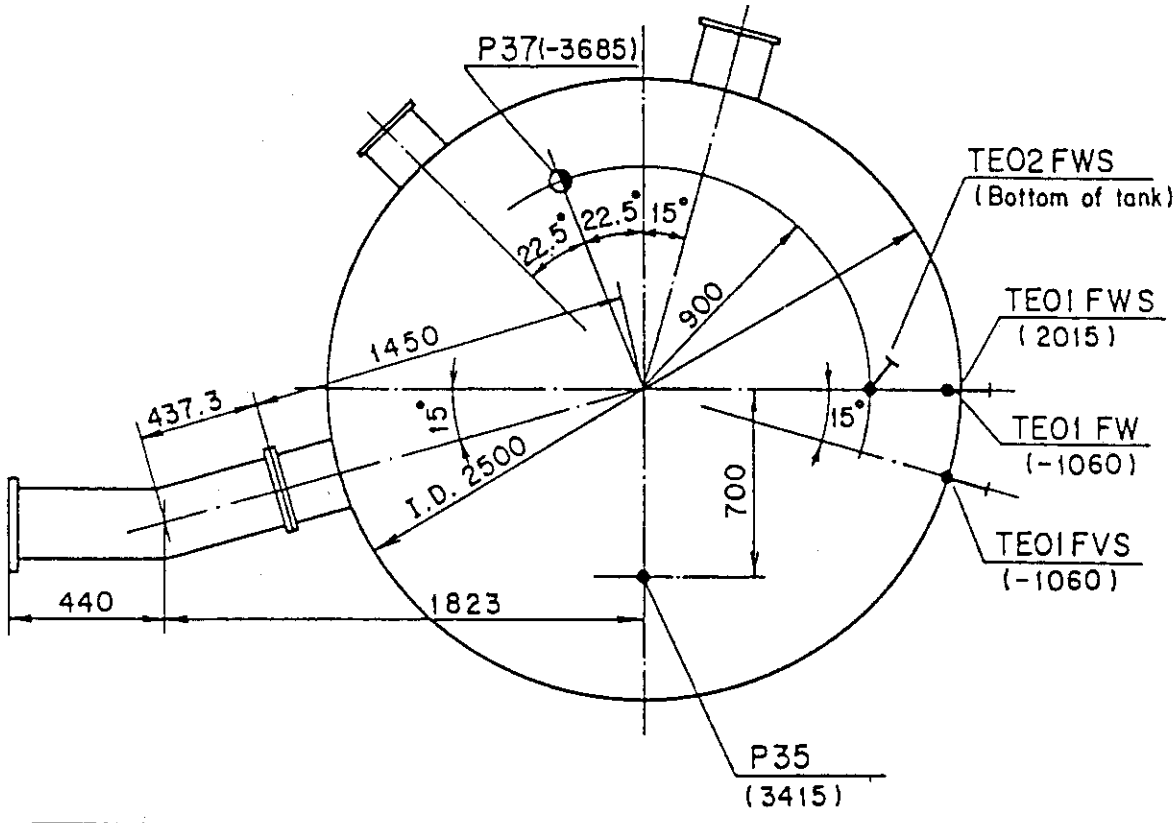

Tag. no.	Location
LT01FS	$P35^{L}$ – $P37^{H}$
DT01FS	$P35^{H}$ – $Downcomer^{L}$
DT01E	$P35^{L}$ – P36(C.T.II)^{H}
PT01F	P35

Fig. A-42 Locations of Containment Tank-I Instruments

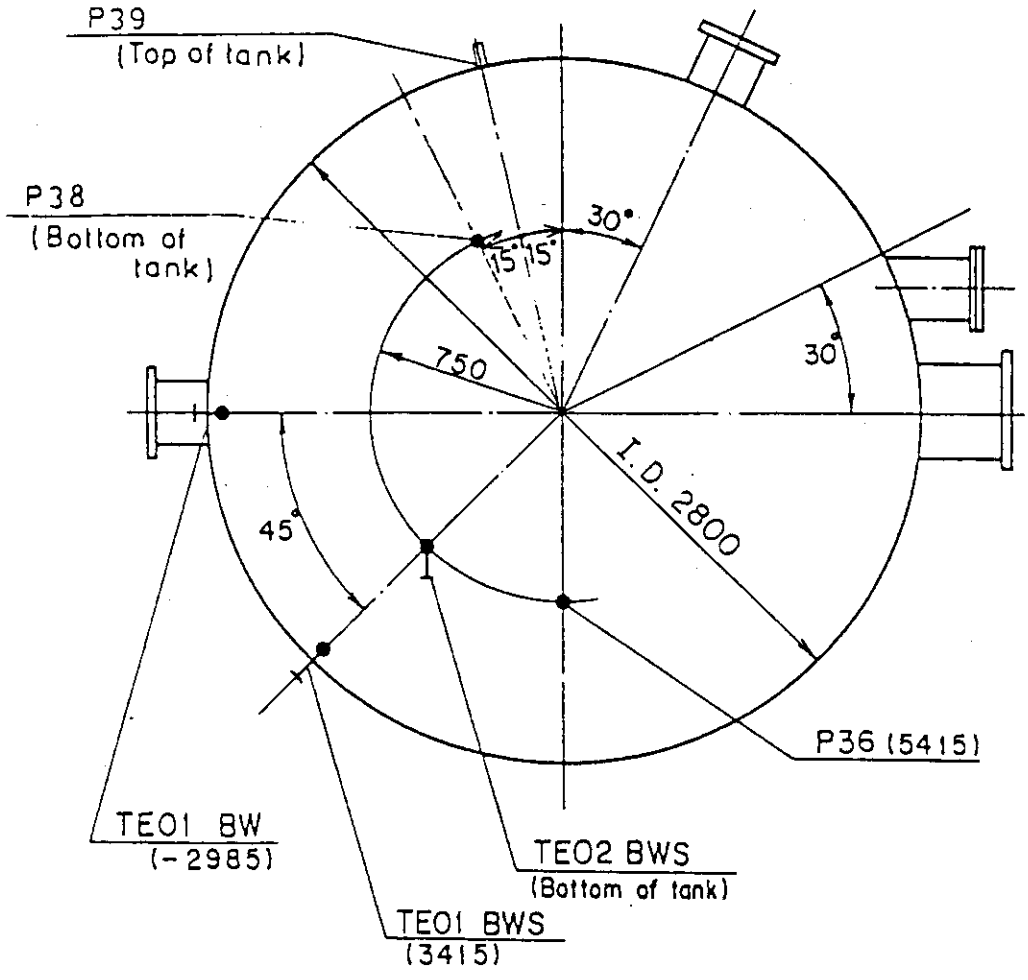

Tag no.	Location
DT01 BS	$P36^{H}$– Upper plenum^{L}
DT02 BS	$P36^{H}$– S-W Separator^{L}
DT01 E	$P36^{H}$– P35 (C.T.I)^{L}
PT01 B	P36
LT01 1B	$P38^{H}$– $P39^{L}$

Fig. A-43 Locations of Containment Tank-II Instruments

Appendix B Froth Level Detector in SCTF-III

B.1 Background

It was revealed from the SCTF tests that the heat transfer was enhanced in higher power bundles and degraded in lower power bundles. The radial power distribution may induce the two-dimensional flow in the core as schematically illustrated in Fig. B.1. Since the heat transfer coefficient is considered to be strongly affected by the two-dimensional flow behavior, it is important to measure the flow distribution in the core. A liquid froth level, which is defined as the boundary level between continuous liquid phase and dispersed liquid phase, provides important information on the two-dimensioanl flow behavior if the froth level really exists.

Some conventional and advanced instruments such as DP cells, γ-densitometers, and conductivity-type liquid level detectors (CLLD's) were installed to obtain the information on the two-dimensional fluid behavior. Some of the data from these instruments were used to investigate the two-dimensional fluid behavior. However, the froth level was not able to be clearly detected with these instruments because of the following problems:

(1) DP cell
- Measurement span is too long (540 mm).
- Effects of frictional and accelerational pressure drops are included

(2) γ-densitometer
- γ-beam was obstructed by the movement or bowing of rods during a test

(3) CLLD
- Some sensors do not work well

In order to directly detect the froth level above the quench front, a new instrument has been developed and installed in the SCTF Core-III.

B.2 Froth Level Detector System

The froth level detector system is shown in Fig. B.2. The steam/water mixture is extracted through four nozzles of the SCTF pressure vessel. As shown in Fig. B.3, these four nozzles are at the same elevation of 1.905 m and located in Bundles 2, 4, 6 and 8. A stainless steel pipe is inserted through each of these nozzles to extract the two-phase mixture. The outer diameter of this pipe is 3 mm. The extraction pipe is connected to an extraction tank. During a test, the drain value of the extraction tank is opened so as to give a large pressure difference for extraction. The absorption of light in the extracted two-phase mixture is measured with a laser through-beam photoelectric sensor at the measurement location. The configuration of this sensor is shown in Fig. B.4.

The laser beam emitted from a laser diode is made paralled by a lense. The diameter and length of the parallel laser beam are 10 and 300 mm, respectively. The extraction tube is connected to a glass tube in the measurement location. During a test, the change in the absorption rate due to the coming of liquid phase is converted to an analog output variable from 1 to 5 V.

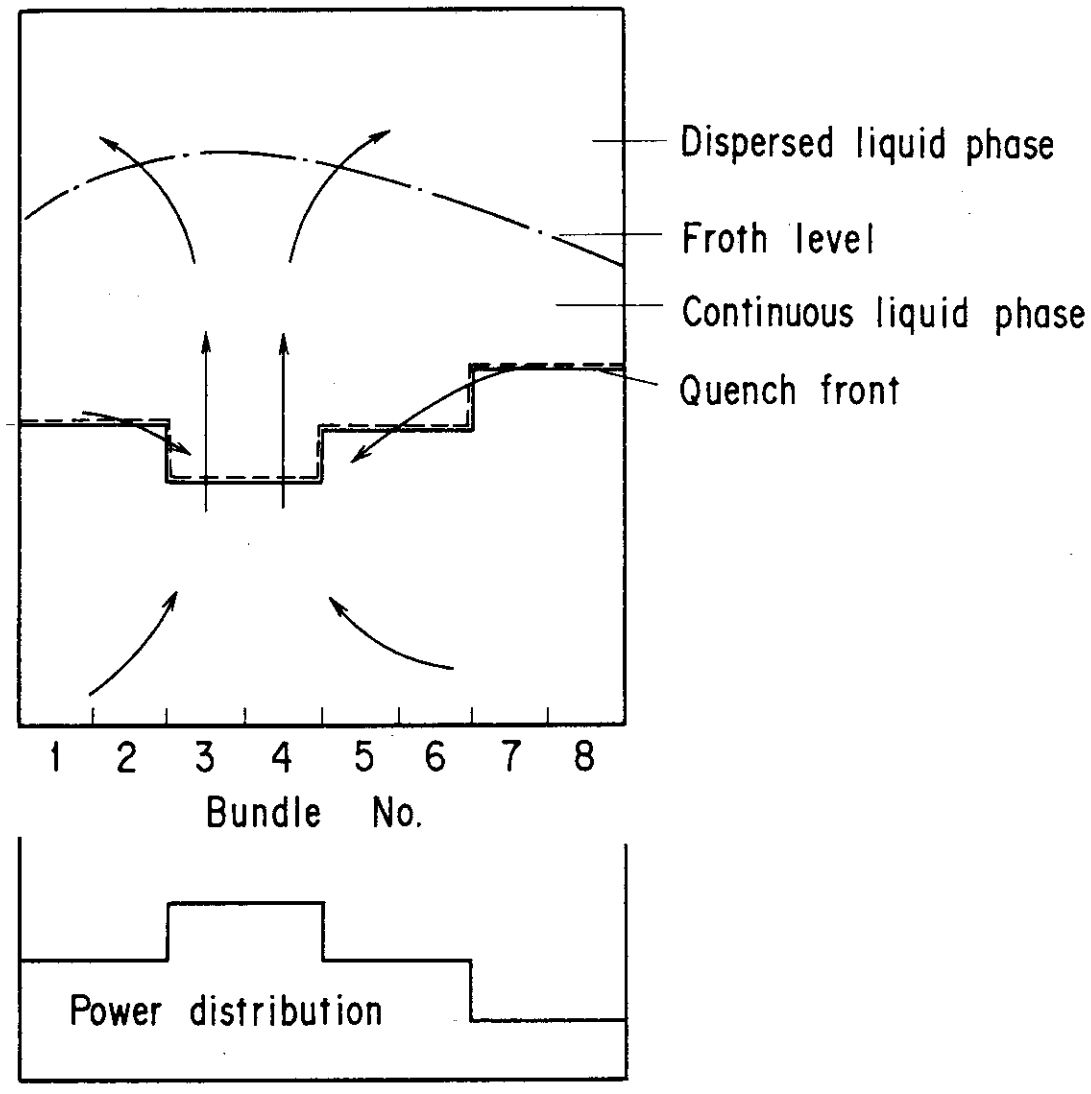

Fig. B.1 Concept of two-dimensional flow in core

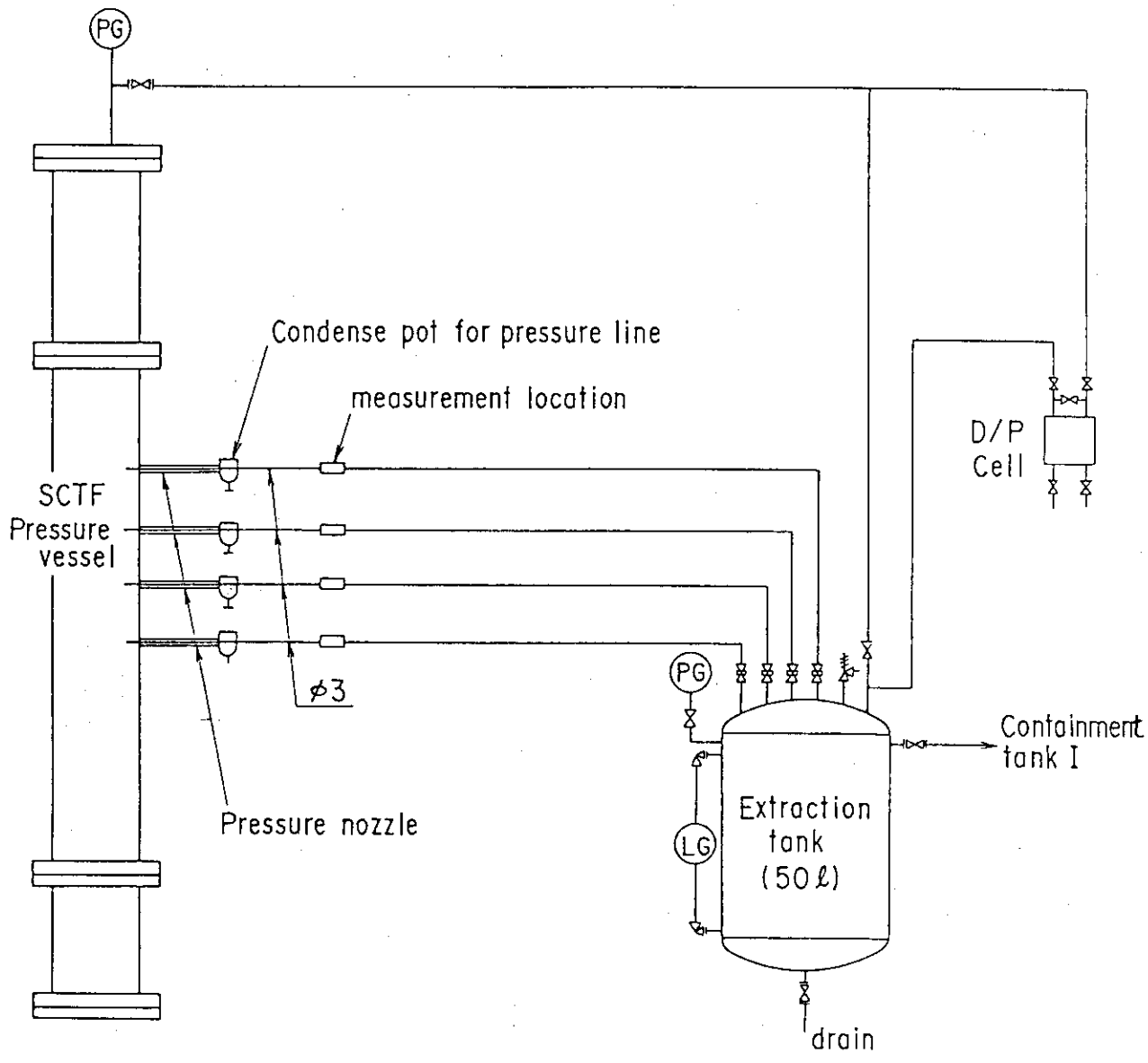

Fig. B.2 Froth level detector system in SCTF Core-III

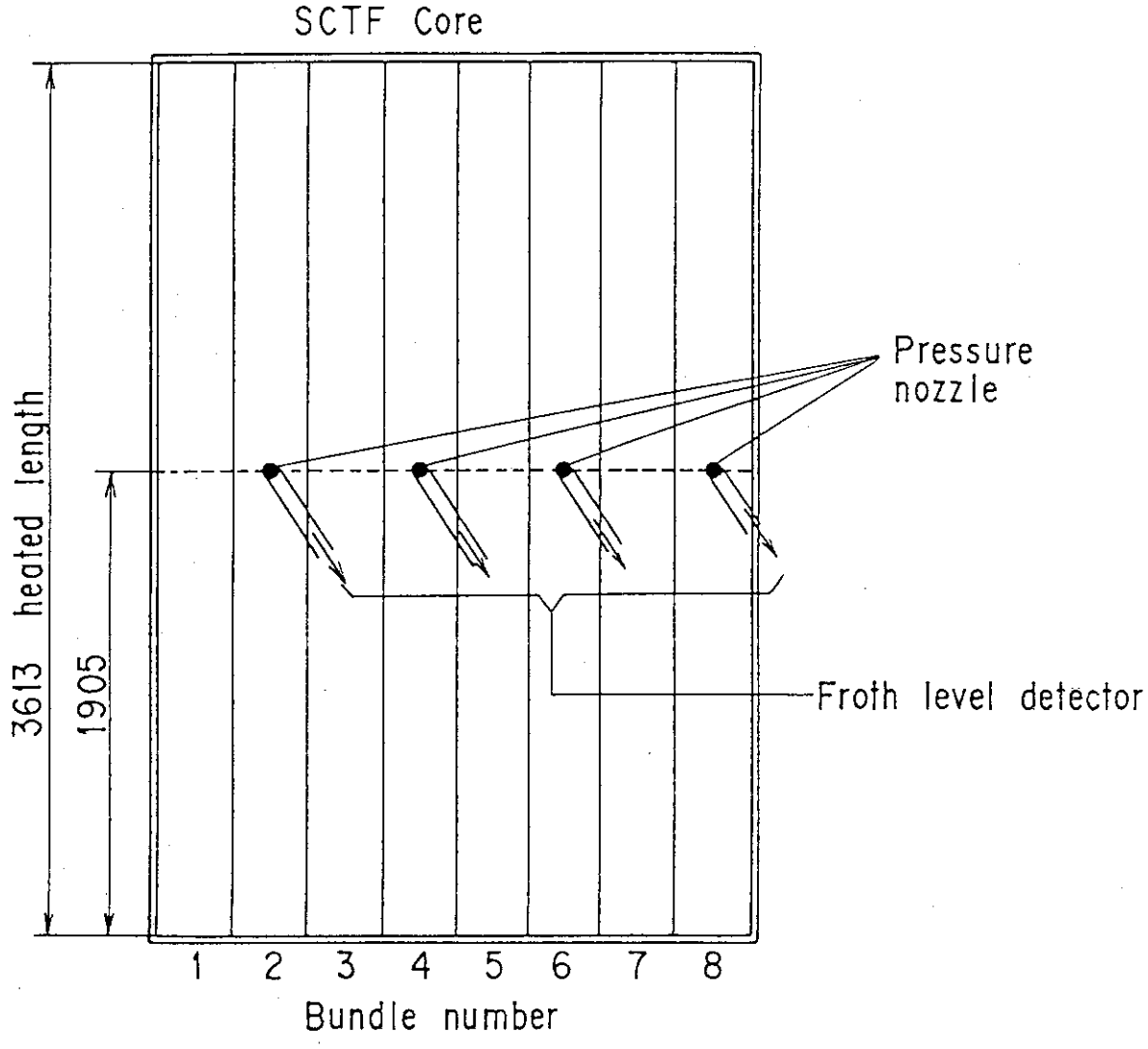

Fig. B.3 Location of froth level detector nozzle

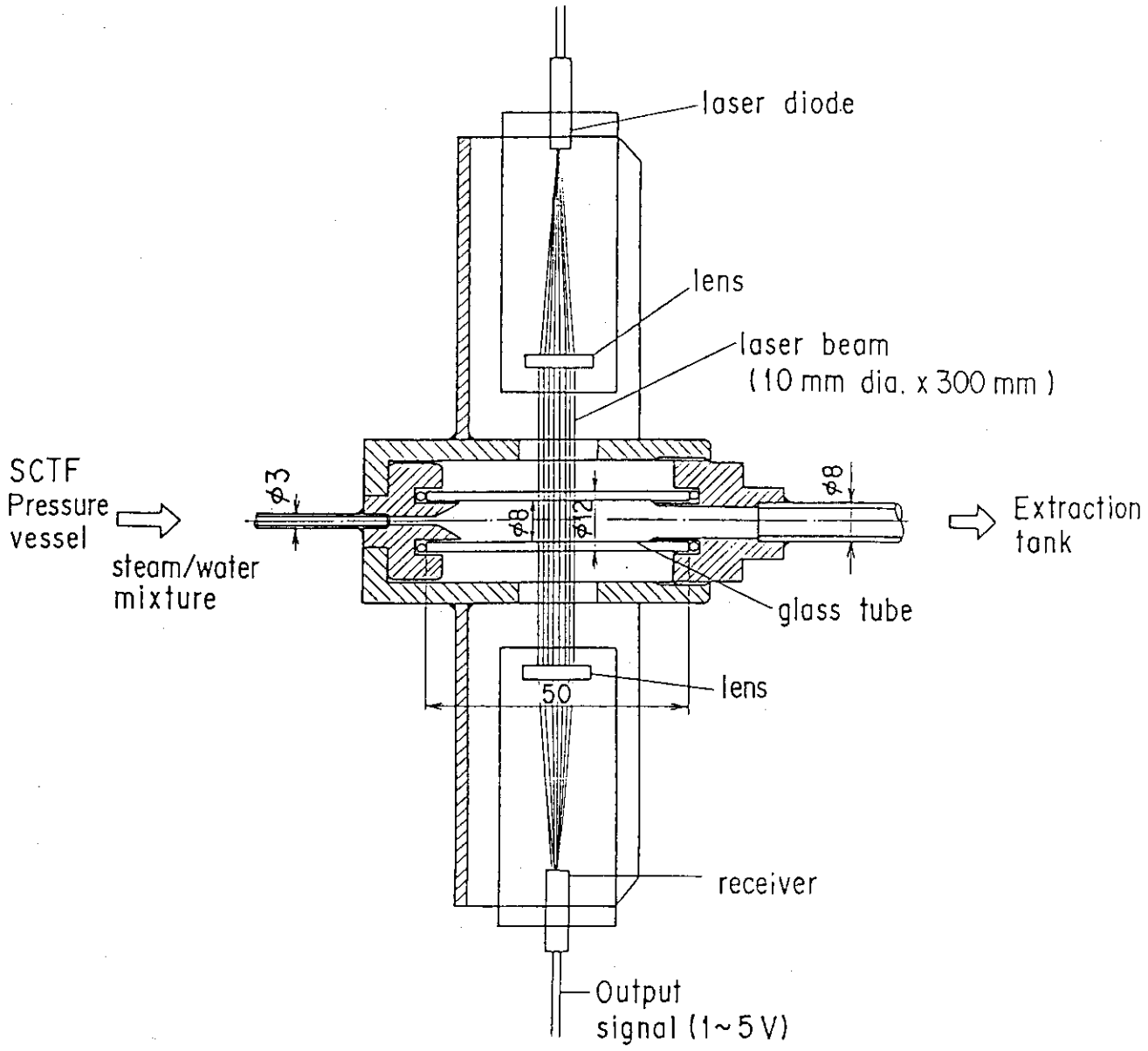

Fig. B.4 Laser through-beam photoelectric sensor

Appendix C Selected Data of Test S3-14

Fig. C- 1 C- 8	Heater rod temperatures
Fig. C- 9 C-12	Non-heated rod temperatures
Fig. C-13 C-16	Steam temperatures
Fig. C-17 C-18	Fluid temperatures just above end box tie plate
Fig. C-19 C-20	Fluid temperatures above UCSP
Fig. C-21 C-24	Fluid temperatures in core
Fig. C-25 C-26	Liquid levels above end box tie plate
Fig. C-27 C-28	Liquid levels above UCSP
Fig. C-29	Liquid levels in downcomer
Fig. C-30	Liquid level in lower plenum
Fig. C-31	Liquid levels in hot leg
Fig. C-32 C-33	Differential pressures across core full height
Fig. C-34 C-35	Differential Pressures across end box tie plate
Fig. C-36 C-38	Horizontal differential pressures in core
Fig. C-39 C-43	Differential pressures in primary loops
Fig. C-44 C-45	Pressures in pressure vessel and containment tanks
Fig. C-46 C-47	Bundle powers
Fig. C-48	Ecc flow rate

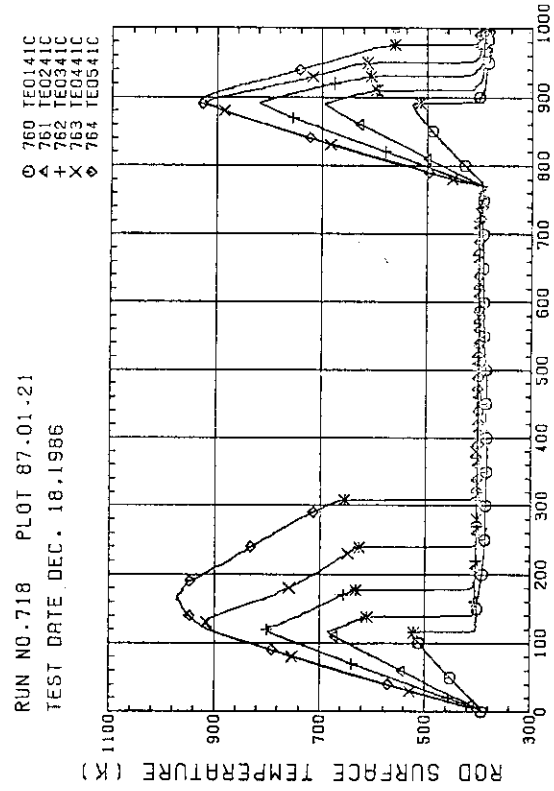

Fig. C-1 HEATER ROD TEMPERATURE (BUNDLE 2-1C, LOWER HALF)

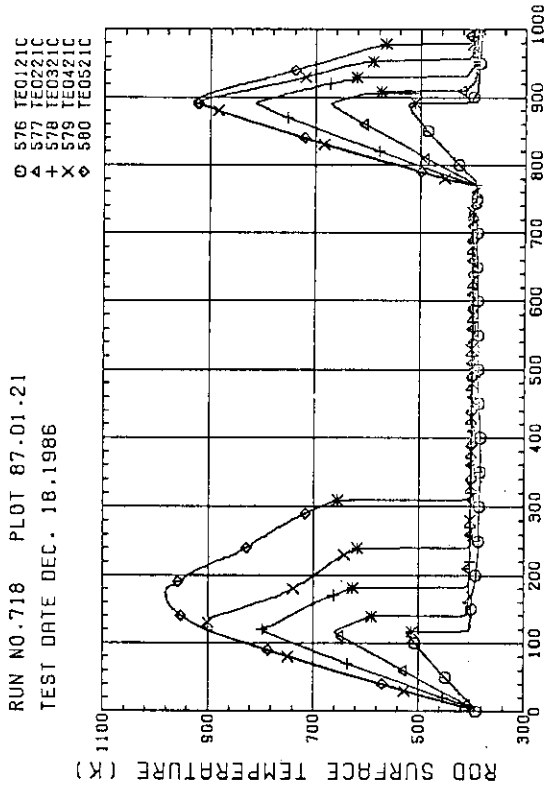

Fig. C-2 HEATER ROD TEMPERATURE (BUNDLE 2-1C, UPPER HALF)

Fig. C-3 HEATER ROD TEMPERATURE (BUNDLE 4-1C, LOWER HALF)

Fig. C-4 HEATER ROD TEMPERATURE (BUNDLE 4-1C, UPPER HALF)

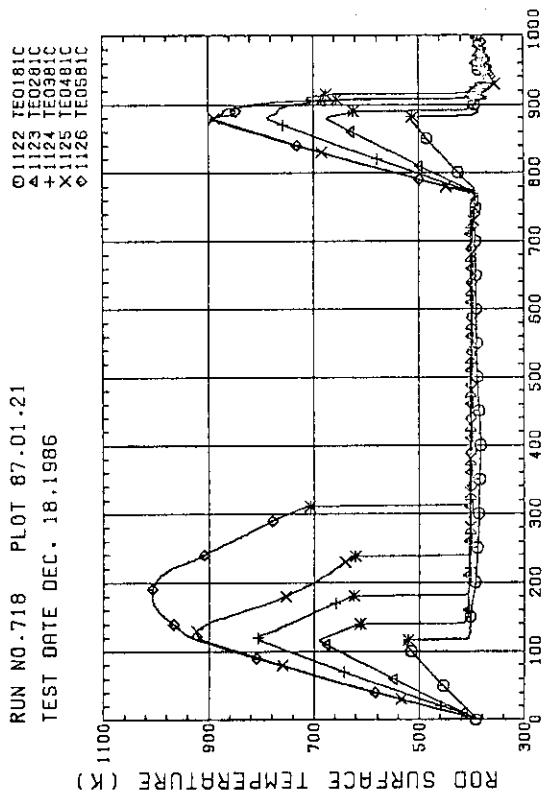

Fig. C-7 HEATER ROD TEMPERATURE (BUNDLE 8-1C, LOWER HALF)

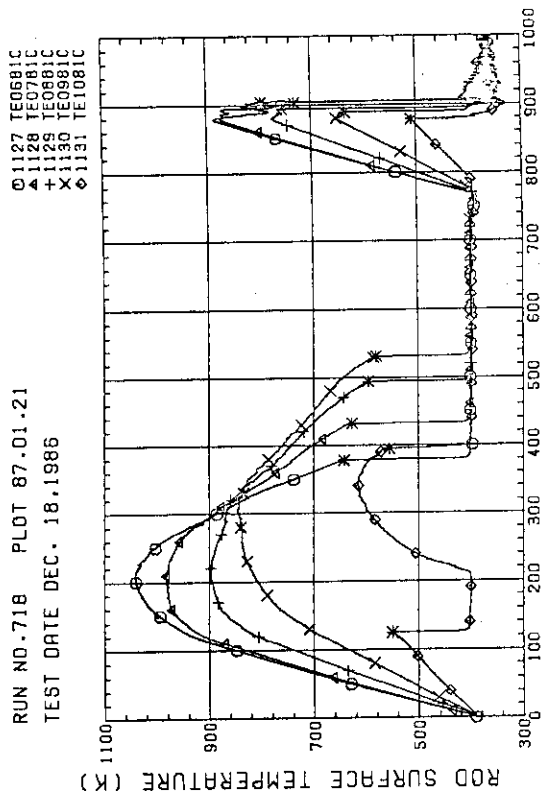

Fig. C-8 HEATER ROD TEMPERATURE (BUNDLE 8-1C, UPPER HALF)

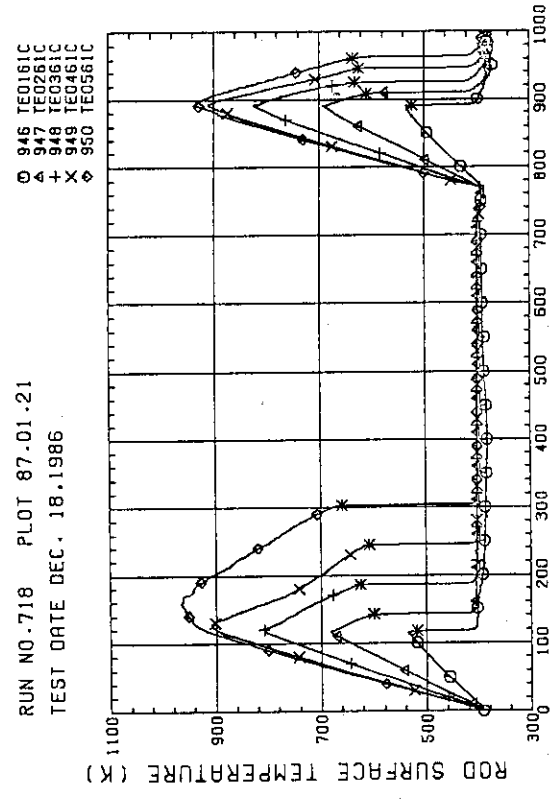

Fig. C-5 HEATER ROD TEMPERATURE (BUNDLE 6-1C, LOWER HALF)

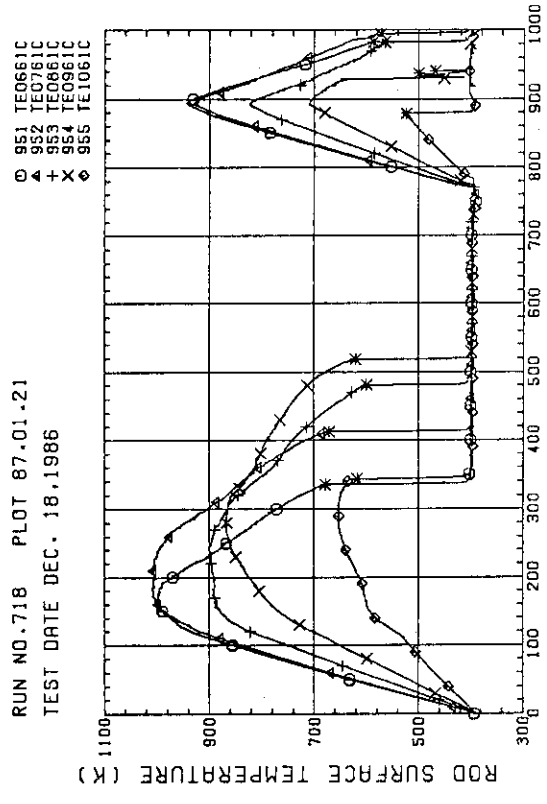

Fig. C-6 HEATER ROD TEMPERATURE (BUNDLE 6-1C, UPPER HALF)

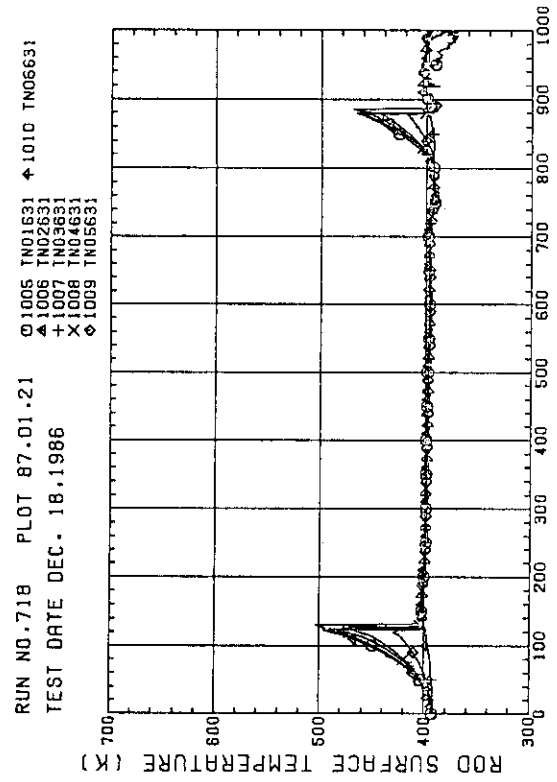

Fig. C-11 NON-HEATED ROD TEMPERATURE (BUNDLE 6-31)

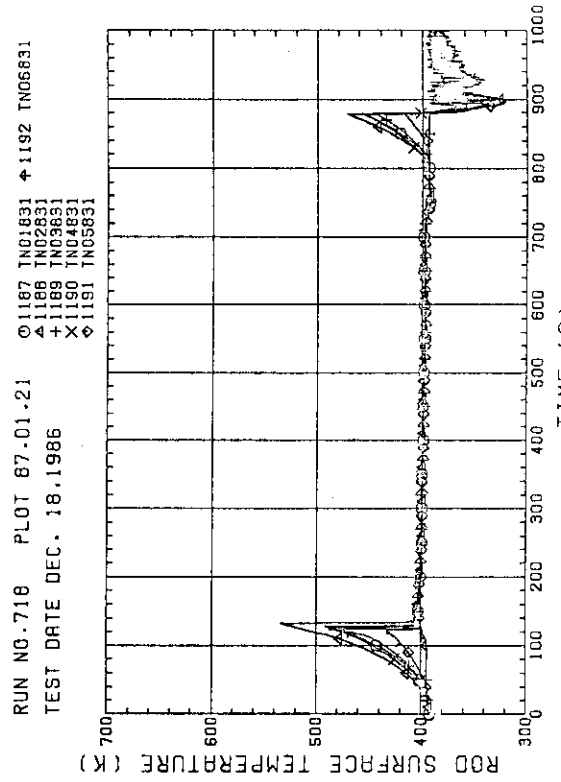

Fig. C-12 NON-HEATED ROD TEMPERATURE (BUNDLE 8-31)

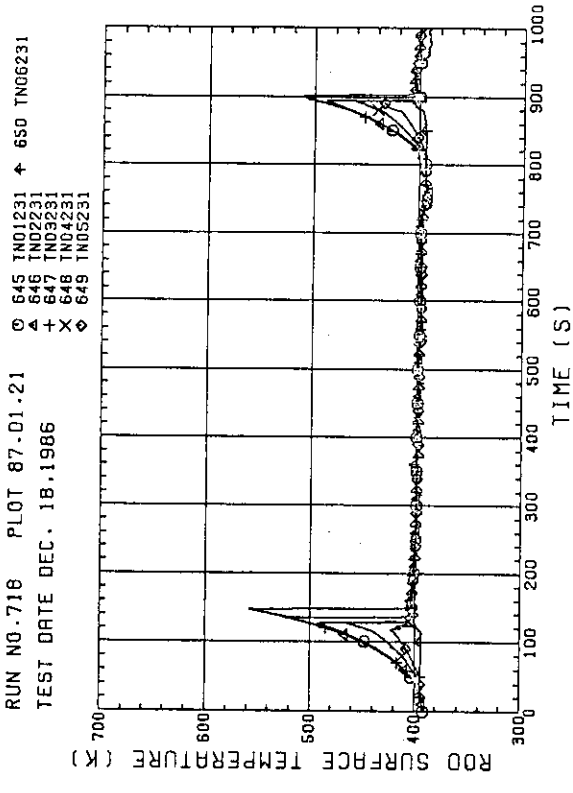

Fig. C-9 NON-HEATED ROD TEMPERATURE (BUNDLE 2-31)

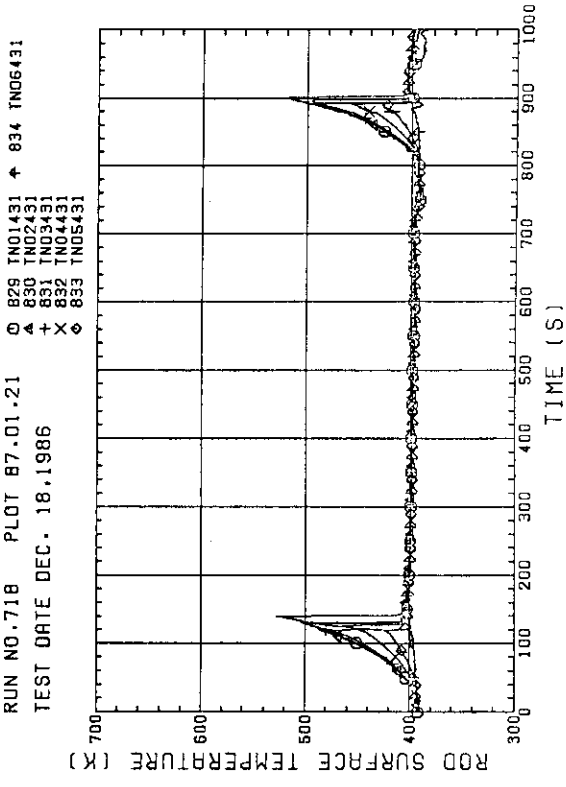

Fig. C-10 NON-HEATED ROD TEMPERATURE (BUNDLE 4-31)

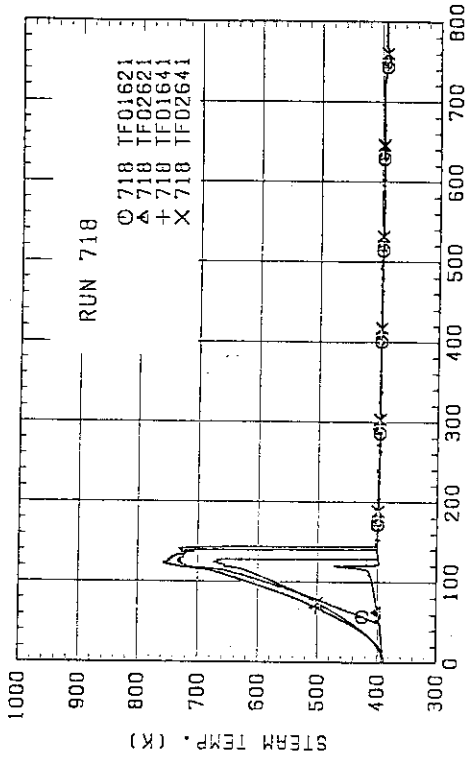

FIG. C-15 STEAM TEMPERATURE IN CORE, BUNDLE 6

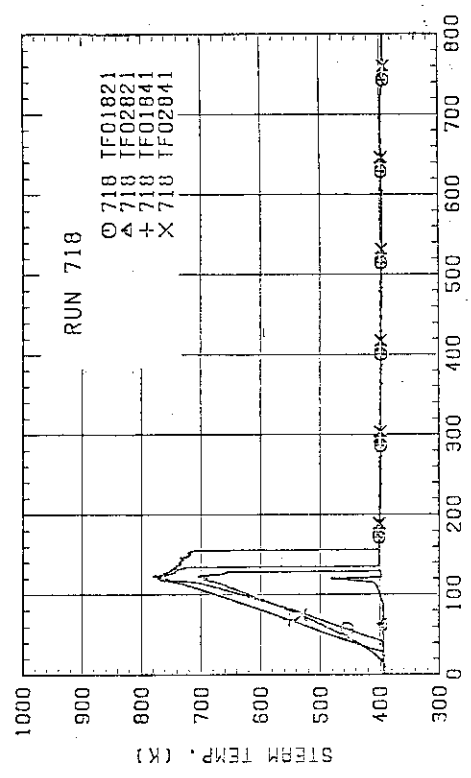

FIG. C-16 STEAM TEMPERATURE IN CORE, BUNDLE 8

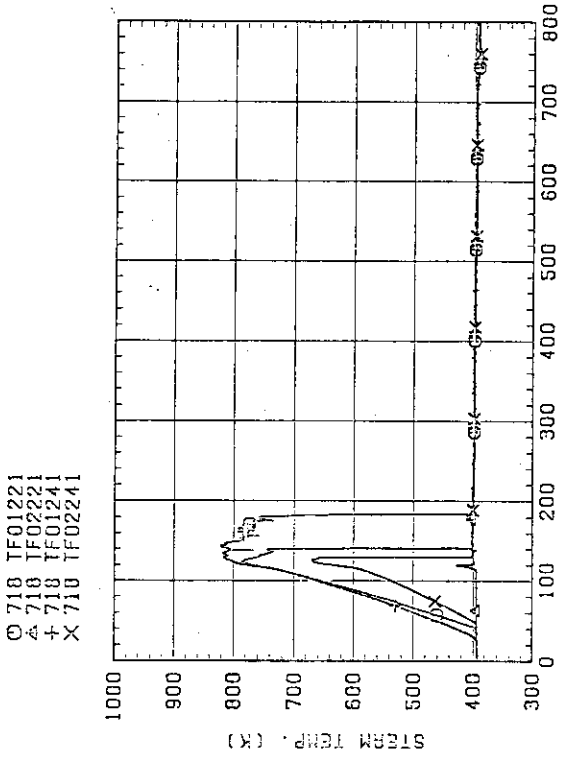

FIG. C-13 STEAM TEMPERATURE IN CORE, BUNDLE 2

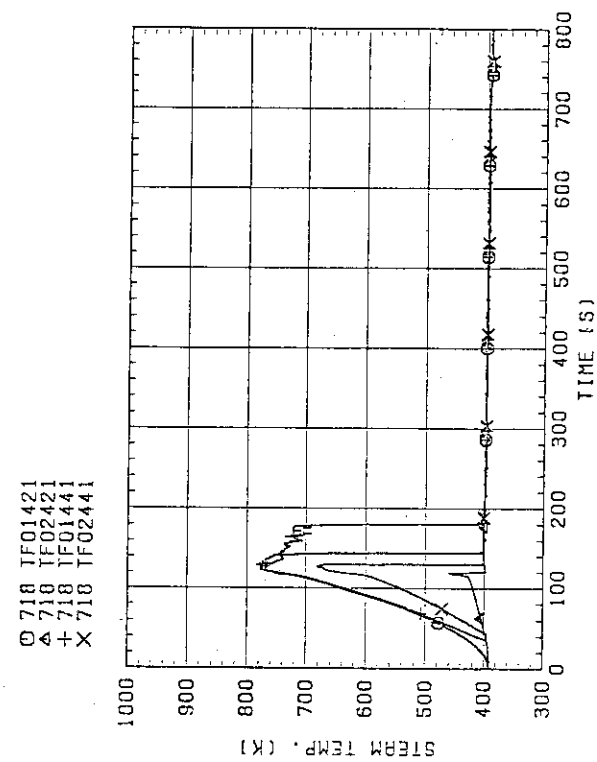

FIG. C-14 STEAM TEMPERATURE IN CORE, BUNDLE 4

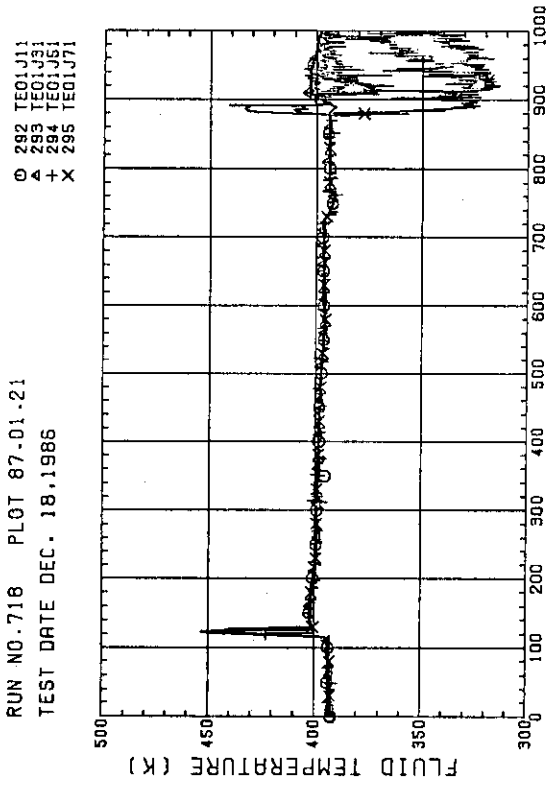

Fig. C-19 FLUID TEMPERATURE ABOVE UCSP (BUNDLE 1,3,5,7, 100MM ABOVE UCSP)

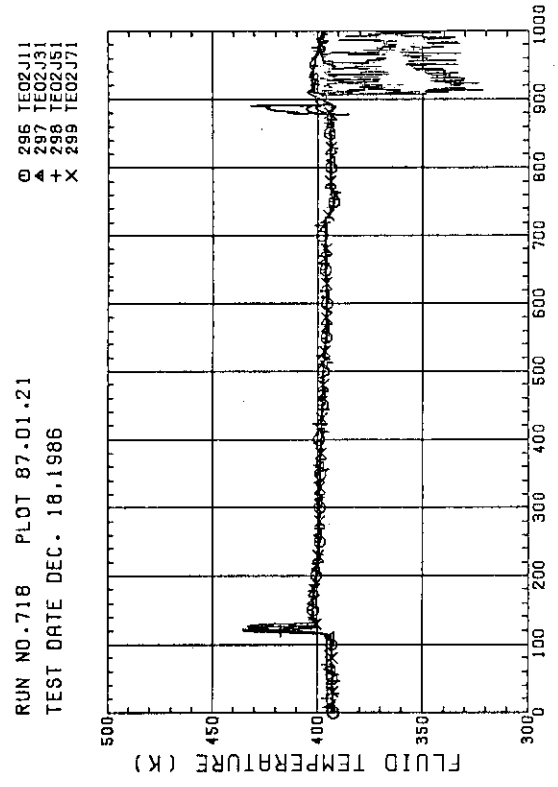

Fig. C-20 FLUID TEMPERATURE ABOVE UCSP (BUNDLE 1,3,5,7, 250MM ABOVE UCSP)

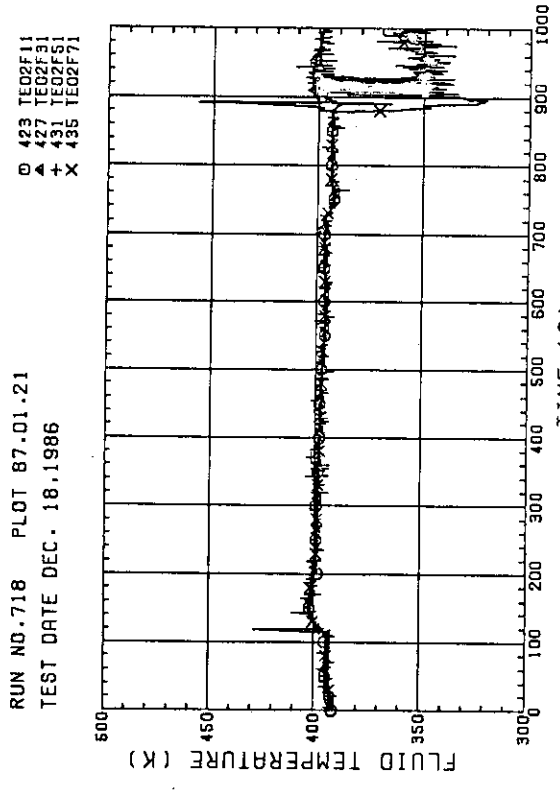

Fig. C-17 FLUID TEMPERATURE JUST ABOVE END BOX TIE PLATE (BUNDLE 1,3,5,7, OPPOSITE SIDE OF COLD LEG, OUTER)

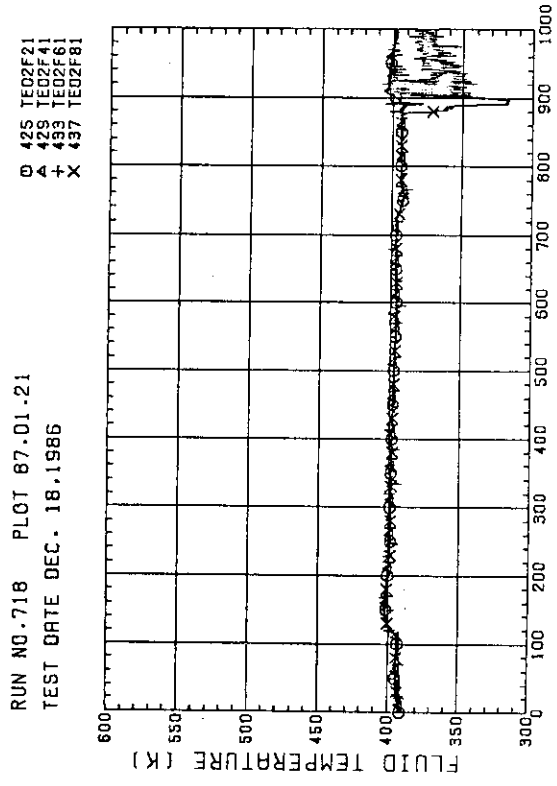

Fig. C-18 FLUID TEMPERATURE JUST ABOVE END BOX TIE PLATE (BUNDLE 2,4,6,8, COLD LEG SIDE, OUTER)

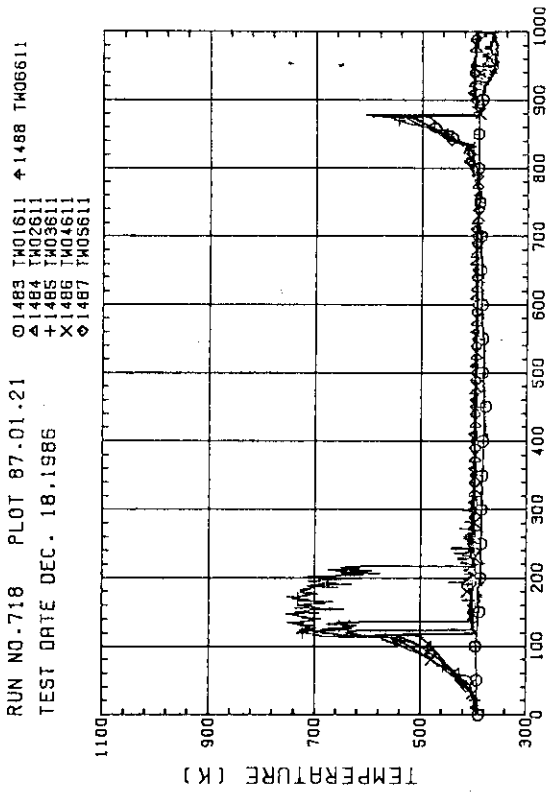

Fig. C-21 TEMPERATURE FOR SPUTTERING DETECTION
BUNDLE 2 , REGION 1 , TYPE 3

Fig. C-23 TEMPERATURE FOR SPUTTERING DETECTION
BUNDLE 6 , REGION 1 , TYPE 1 3

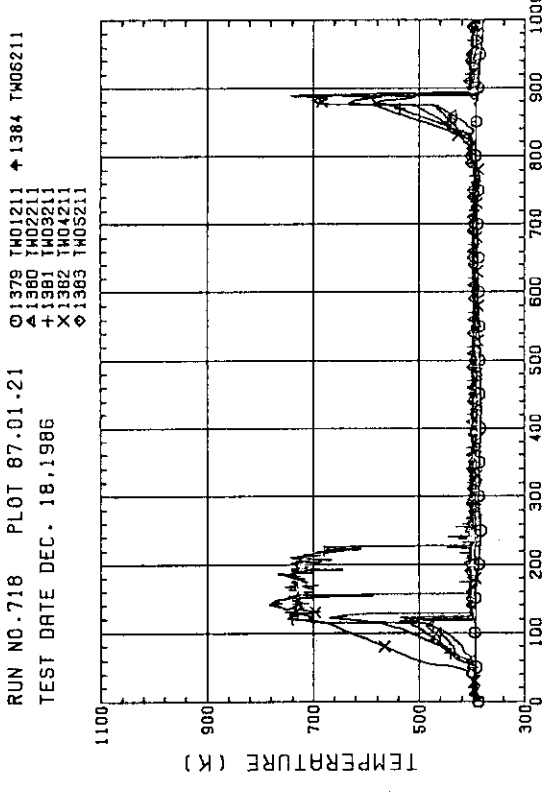

Fig. C-22 TEMPERATURE FOR SPUTTERING DETECTION
BUNDLE 4 , REGION 1 , TYPE 3

Fig. C-24 TEMPERATURE FOR SPUTTERING DETECTION
BUNDLE 8 , REGION 1 , TYPE 3

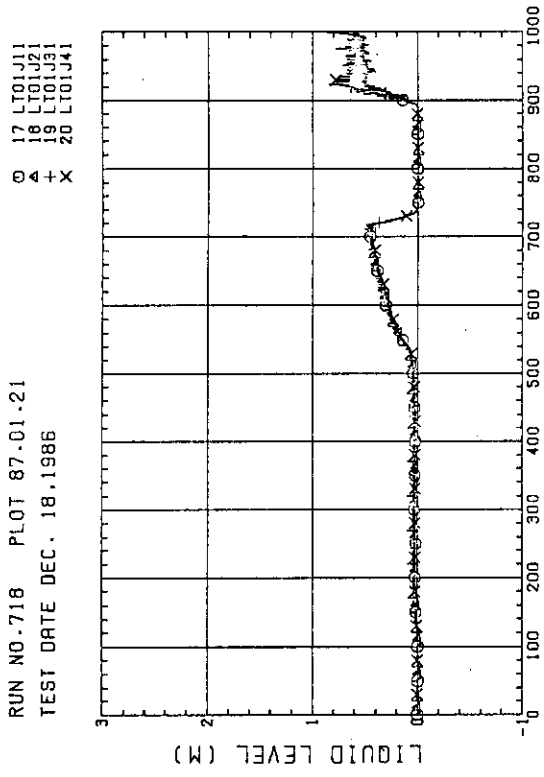

Fig. C-27 LIQUID LEVEL ABOVE UCSP (BUNDLE 1,2,3,4)

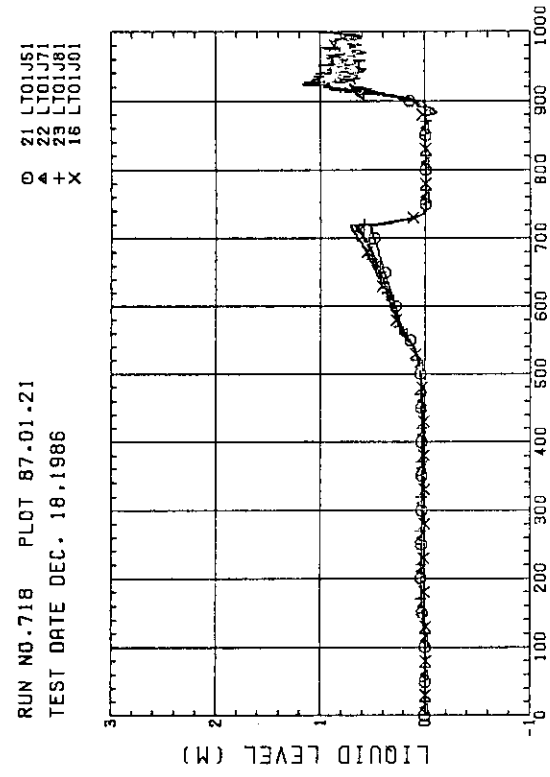

Fig. C-28 LIQUID LEVEL ABOVE UCSP (BUNDLE 5,6,7,8 AND CORE BAFFLE)

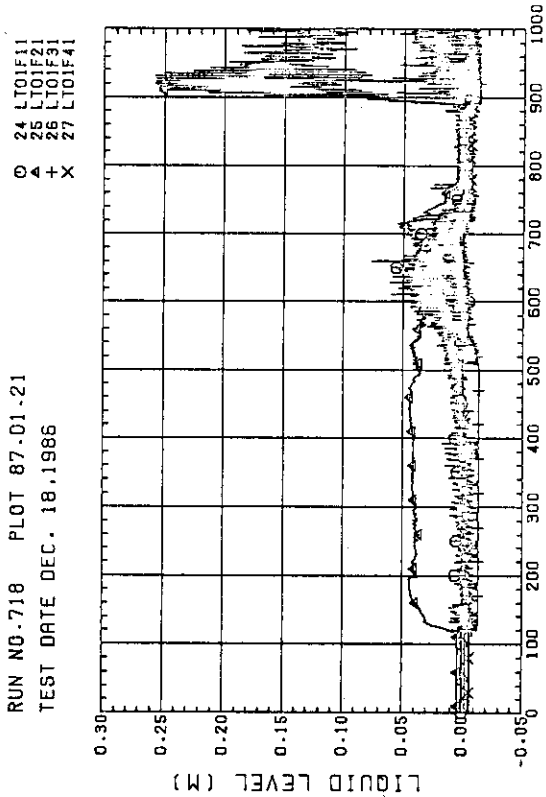

Fig. C-25 LIQUID LEVEL ABOVE END BOX TIE PLATE (BUNDLE 1,2,3,4)

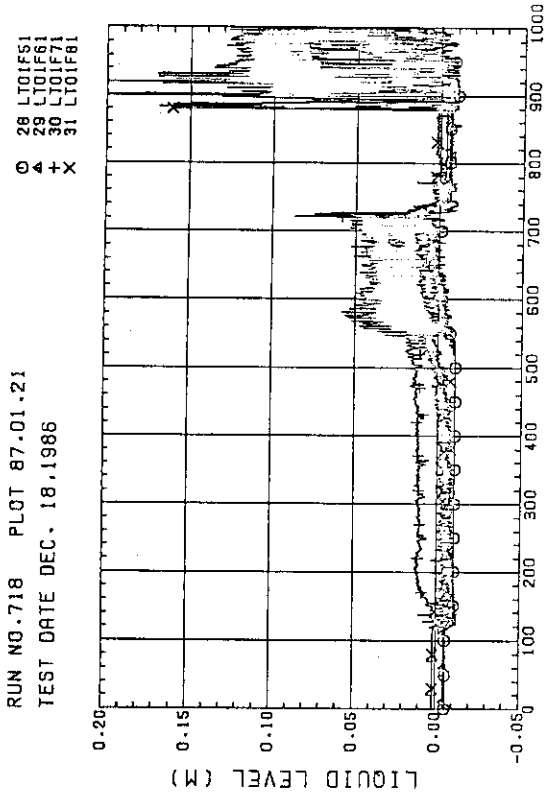

Fig. C-26 LIQUID LEVEL ABOVE END BOX TIE PLATE (BUNDLE 5,6,7,8)

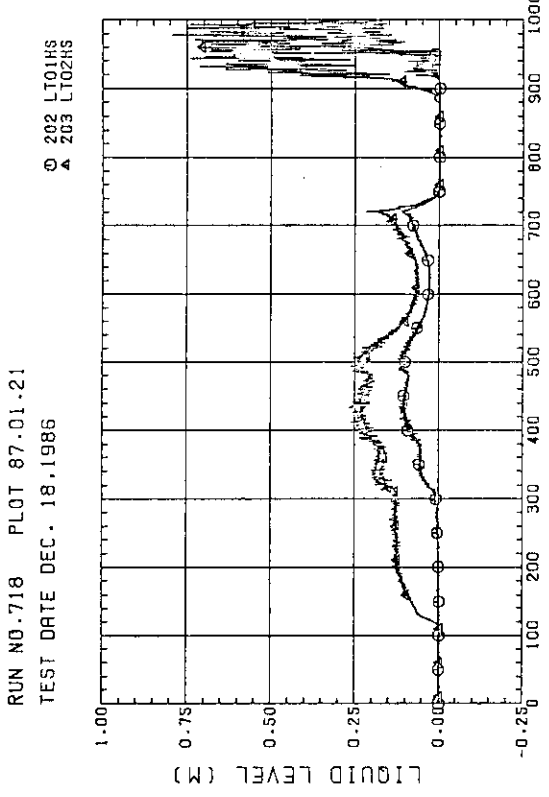

Fig. C-31 LIQUID LEVEL IN HOT LEG
(O1HS - PV SIDE, O2HS - STEAM/WATER SEPARATOR SIDE)

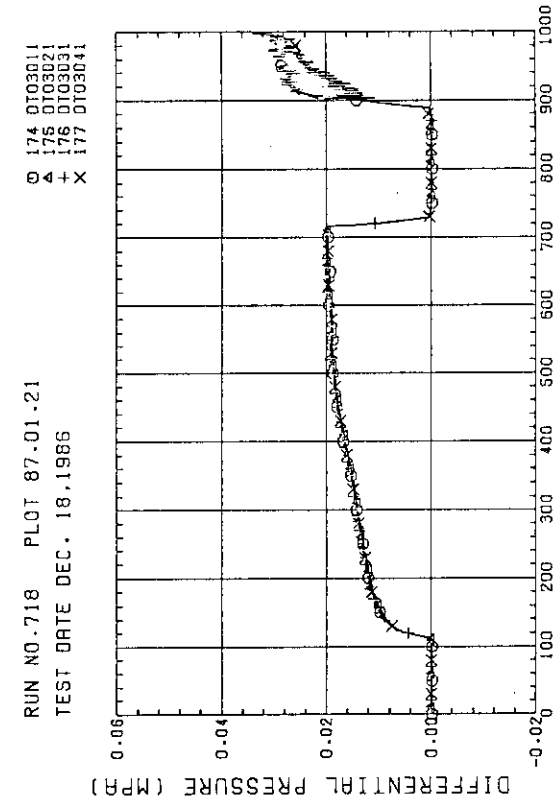

Fig. C-32 DIFFERENTIAL PRESSURE OF CORE FULL HIGHT
(BUNDLE 1,2,3,4)

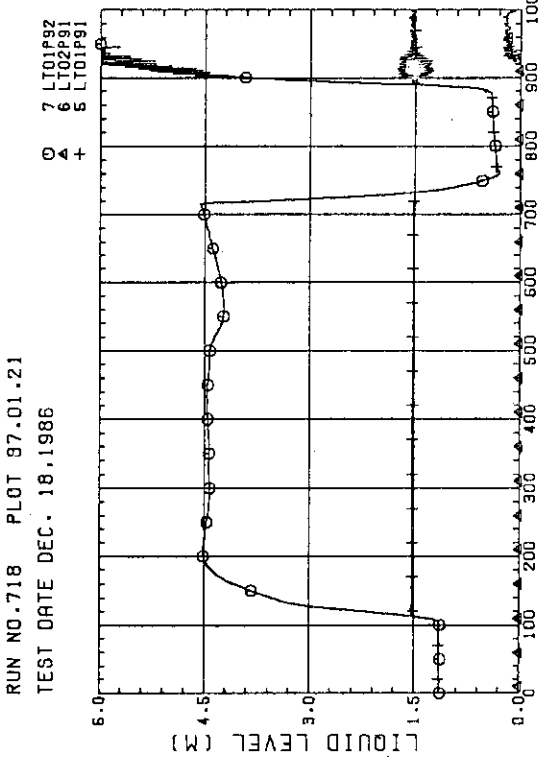

Fig. C-29 LIQUID LEVEL IN DOWNCOMER (O1P91-ABOVE BLOCKING PLATE,
O1P92-ACROSS BLOCKING PLATE, O2P91-C.L. TO TOP OF PV)

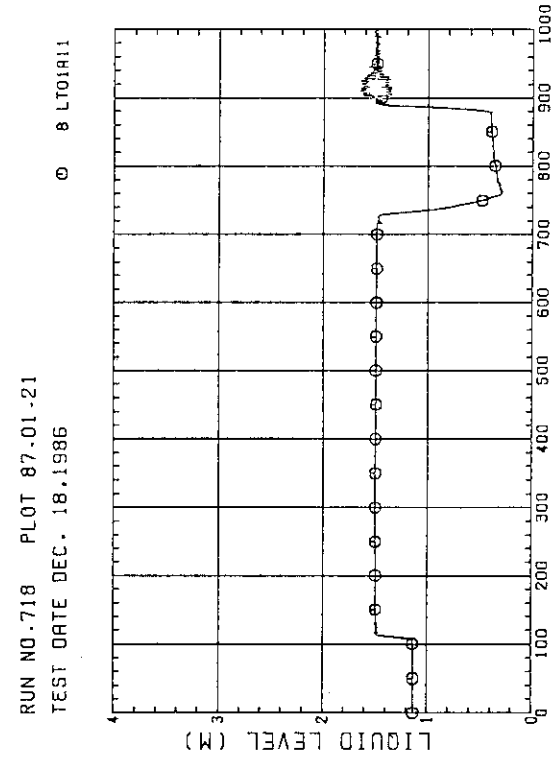

Fig. C-30 LIQUID LEVEL IN LOWER PLENUM

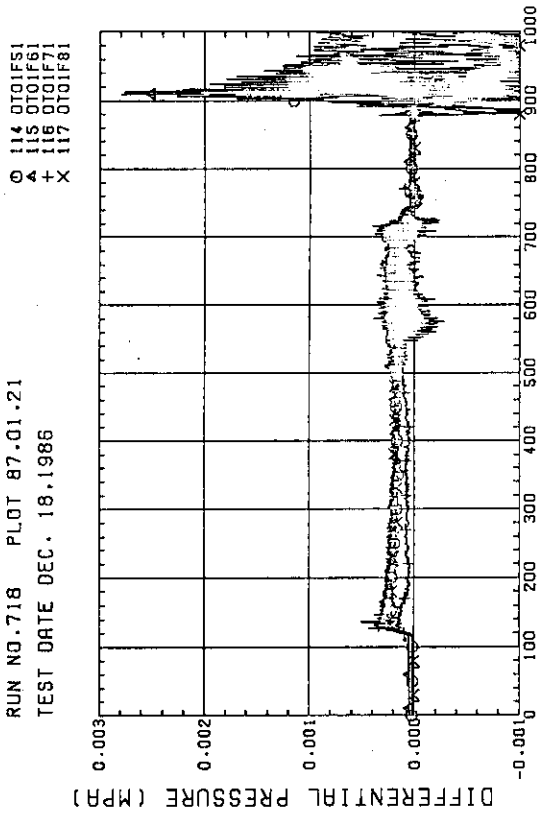

Fig. C-33 DIFFERENTIAL PRESSURE OF CORE FULL HEIGHT (BUNDLE 5,6,7,8)

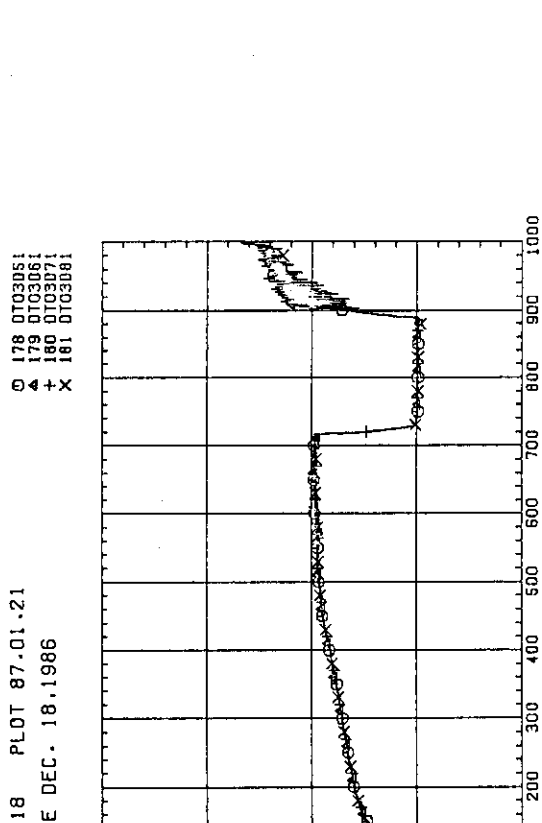

Fig. C-35 DIFFERENTIAL PRESSURE ACROSS END BOX TIE PLATE (BUNDLE 5,6,7,8)

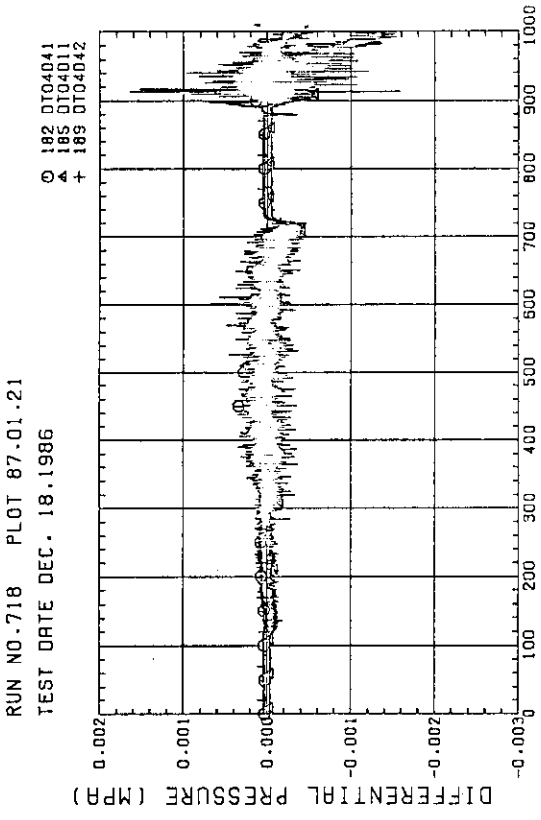

Fig. C-36 DIFFERENTIAL PRESSURE, HORIZONTAL AT 1905 MM (11-BUNDLE 1-4, 41-BUNDLE 4-8, 42-BUNDLE 4-6)

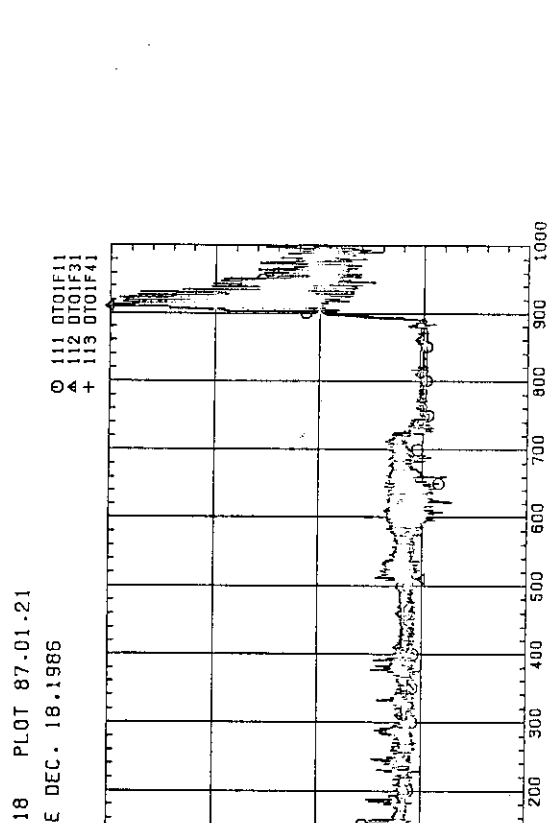

Fig. C-34 DIFFERENTIAL PRESSURE ACROSS END BOX TIE PLATE (BUNDLE 1,3,4)

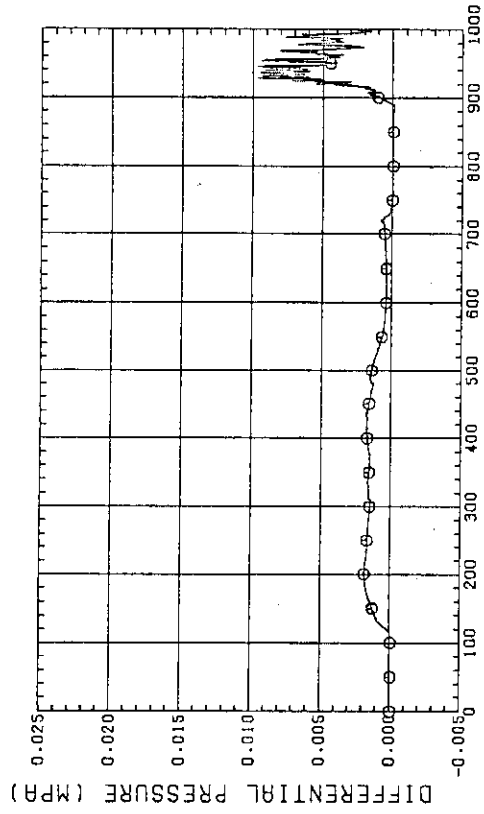

Fig. C-39 DIFFERENTIAL PRESSURE OF HOT LEG, HOT LEG INLET - STEAM/WATER SEPARATOR INLET

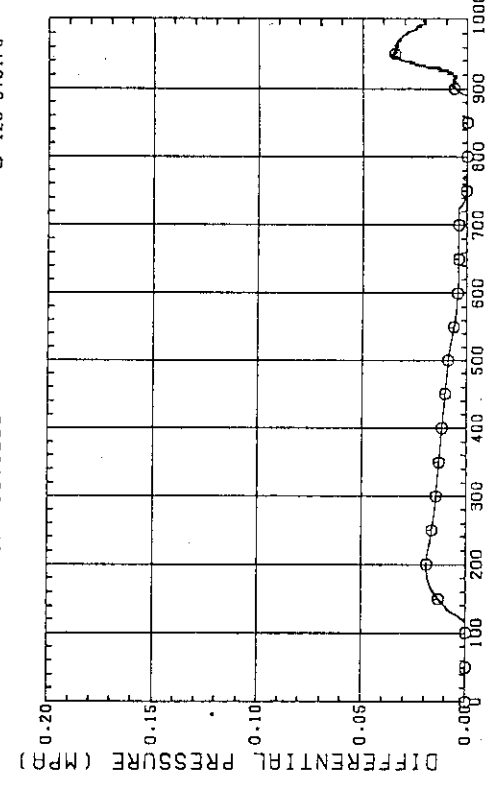

Fig. C-40 DIFFERENTIAL PRESSURE OF BROKEN COLD LEG - PV SIDE, DOWNCOMER - CONTAINMENT TANK-1

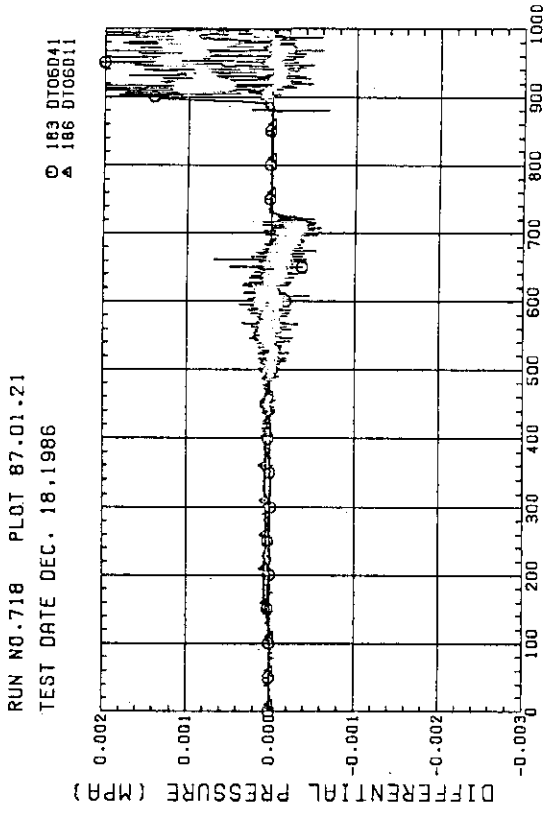

Fig. C-37 DIFFERENTIAL PRESSURE, HORIZONTAL AT 3235 MM (11-BUNDLE 1-4, 41-BUNDLE 4-8)

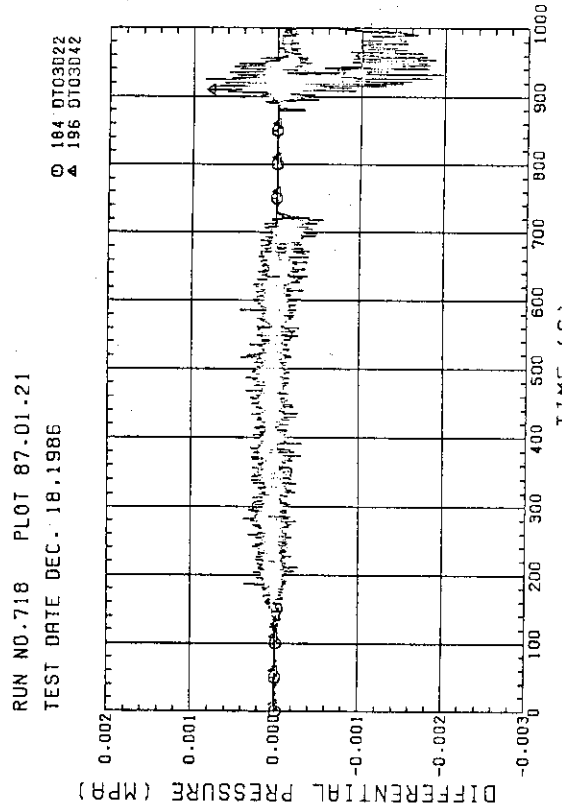

Fig. C-38 DIFFERENTIAL PREESURE, HORIZONTAL AT 1365 MM (22-BUNDLE 2-4, 42-BUNDLE 4-8)

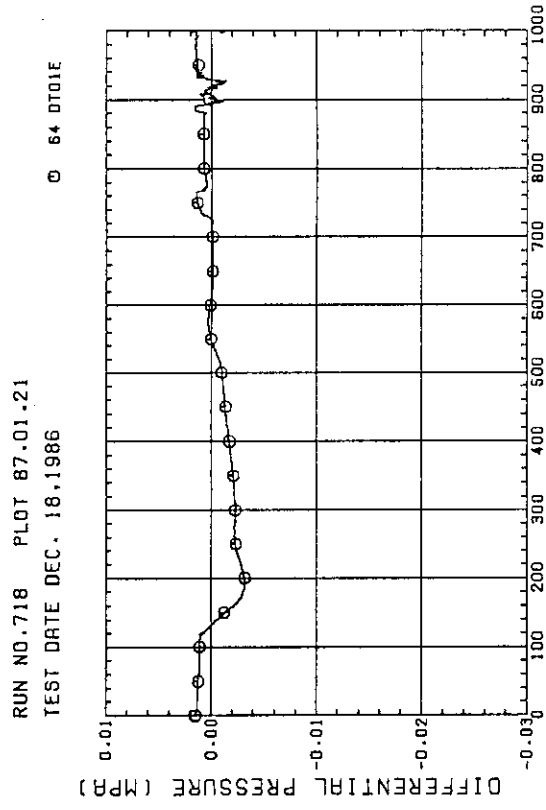

Fig. C-43 DIFFERENTIAL PRESSURE, CONTAINMENT TANK-II - CONTAINMENT TANK-I

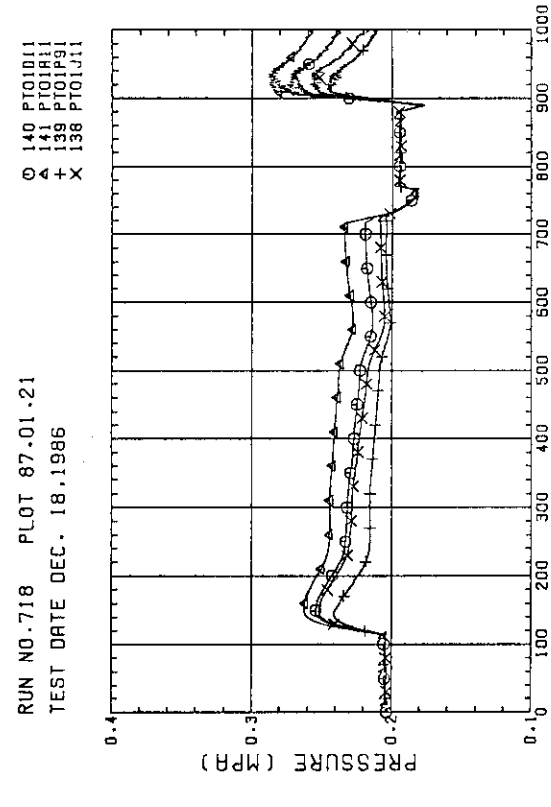

Fig. C-44 PRESSURE IN PV (J - TOP OF PV, D - CORE CENTER, A - CORE INLET, P - BELOW COLD LEG NOZZLE IN DOWNCOMER)

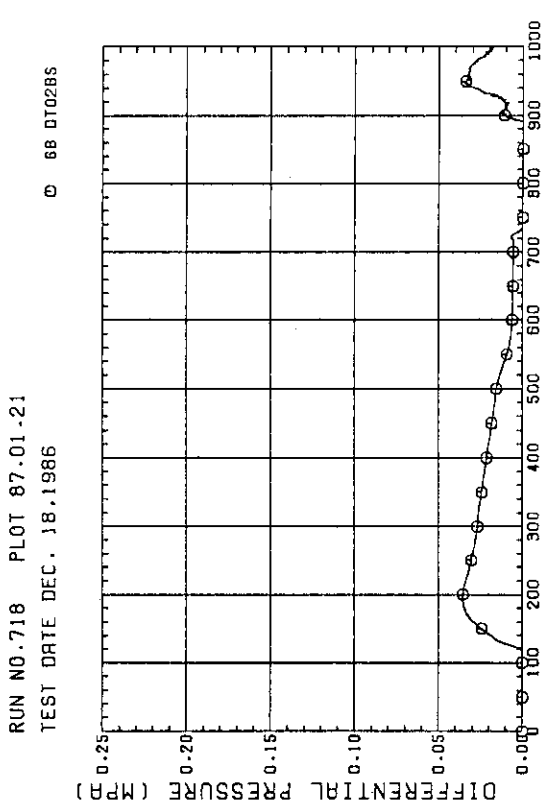

Fig. C-41 DIFFERENTIAL PRESSURE, STEAM/WATER SEPARATOR - CONTAINMENT TANK-II

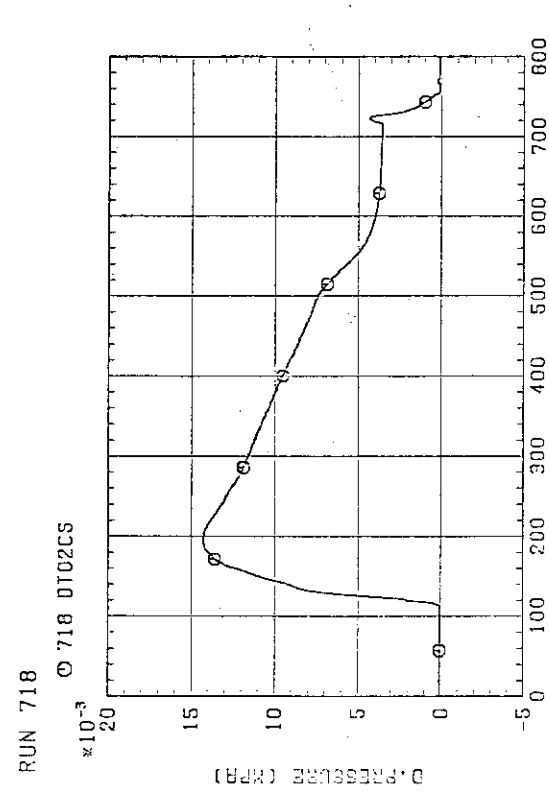

FIG. C-42 DIFFERENTIAL PRESSURE OF INTACT COLD LEG

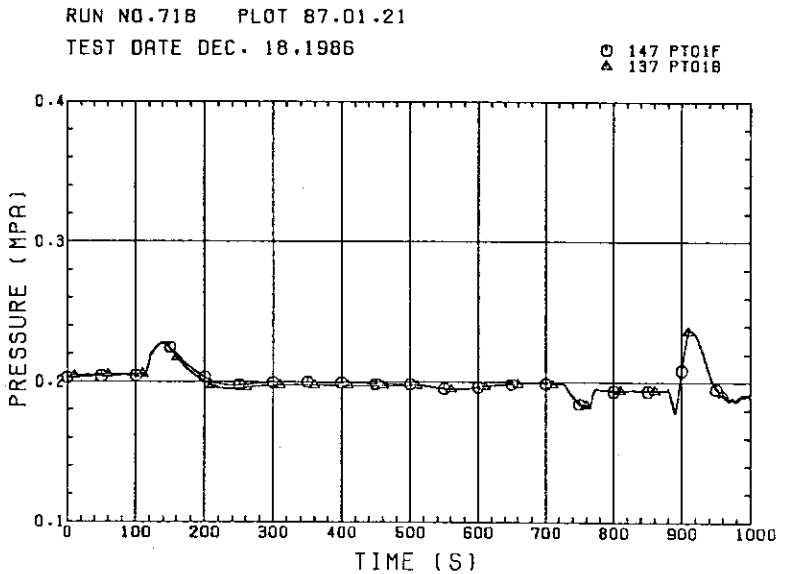

Fig. C-45 PRESSURE AT TOP OF CONTAINMENT TANK-I AND CONTAINMENT TANK-II (F-CONTAINMENT TANK-I, B-CONTAINMENT TANK-II)

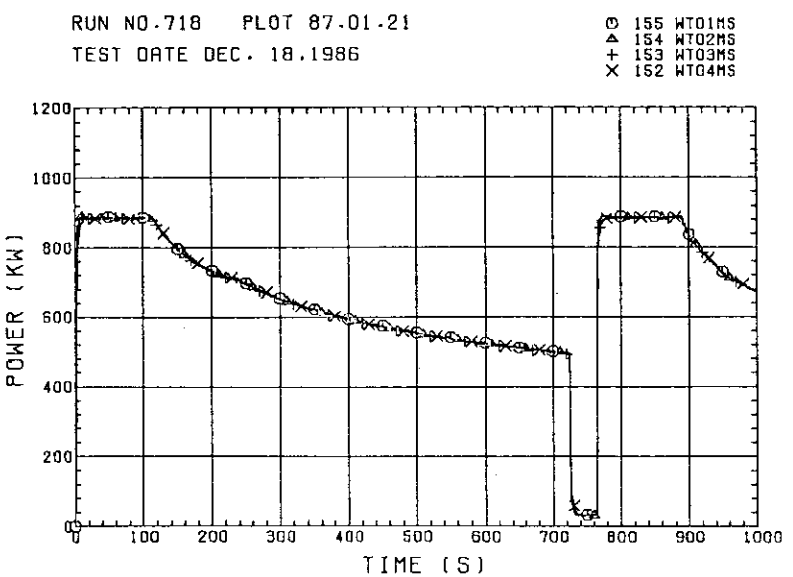

Fig. C-46 BUNDLE POWER (BUNDLE 1,2,3,4)

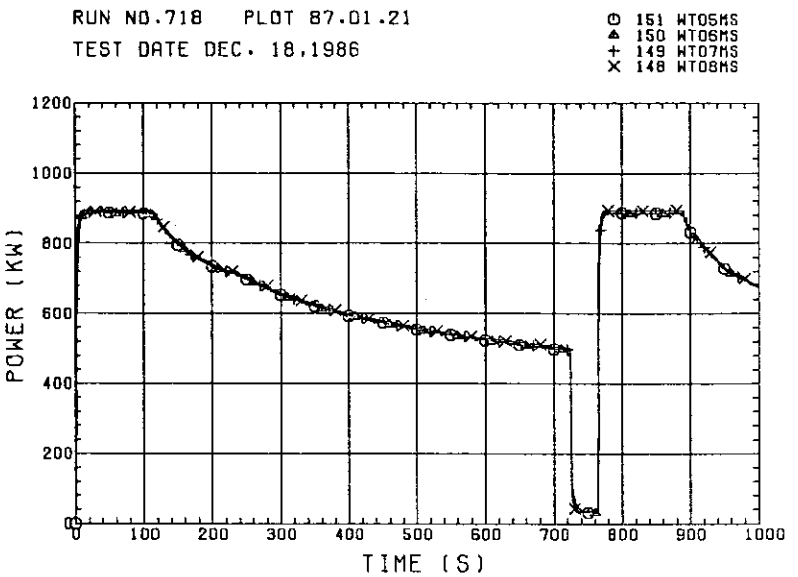

Fig. C-47 BUNDLE POWER (BUNDLE 5,6,7,8)

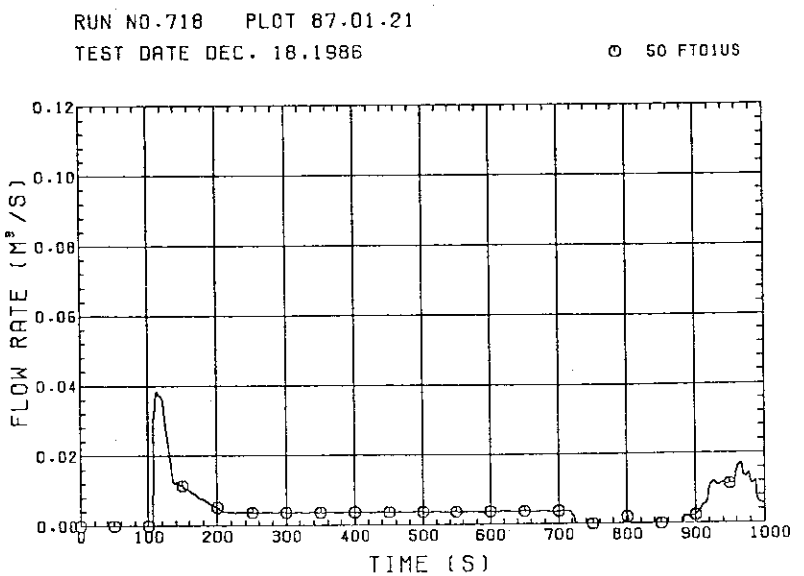

Fig. C-48 FLOW RATE OF LOWER PLENUM INJECTION WATER (ACC HEADER LINE)

Appendix D Selected Data of Test S3-15

Fig. D- 1 D- 8	Heater rod temperatures
Fig. D- 9 D-12	Non-heated rod temperatures
Fig. D-13 D-16	Steam temperatures
Fig. D-17 D-18	Fluid temperatures just above end box tie plate
Fig. D-19 D-20	Fluid temperatures above UCSP
Fig. D-21 D-24	Fluid temperatures in core
Fig. D-25 D-26	Liquid levels above end box tie plate
Fig. D-27 D-28	Liquid levels above UCSP
Fig. D-29	Liquid levels in downcomer
Fig. D-30	Liquid level in lower plenum
Fig. D-31	Liquid levels in hot leg
Fig. D-32 D-33	Differential pressures across core full height
Fig. D-34 D-35	Differential Pressures across end box tie plate
Fig. D-36 D-38	Horizontal differential pressures in core
Fig. D-39 D-43	Differential pressures in primary loops
Fig. D-44 D-45	Pressures in pressure vessel and containment tanks
Fig. D-46 D-47	Bundle powers
Fig. D-48	Ecc flow rate

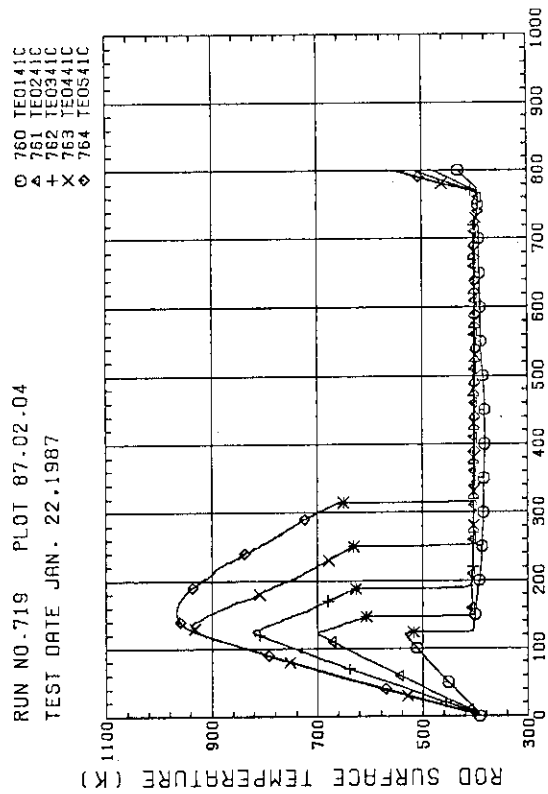

Fig. D-3 HEATER ROD TEMPERATURE (BUNDLE 4-1C, LOWER HALF)

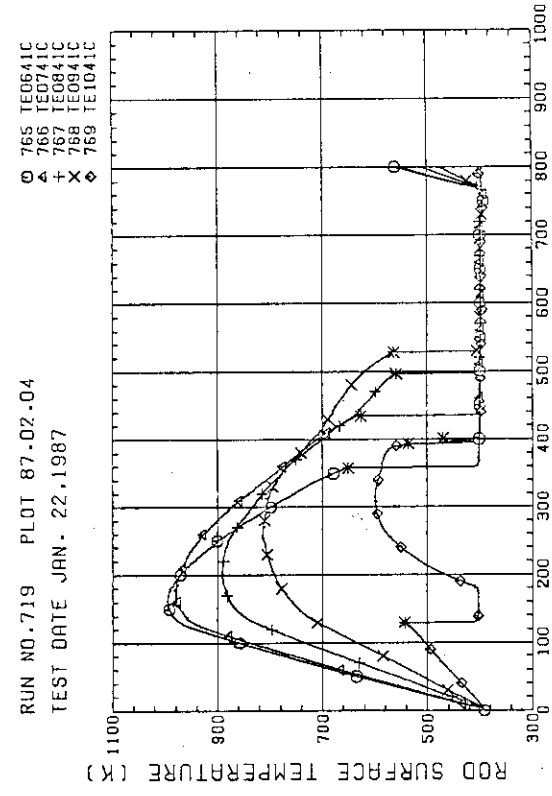

Fig. D-4 HEATER ROD TEMPERATURE (BUNDLE 4-1C, UPPER HALF)

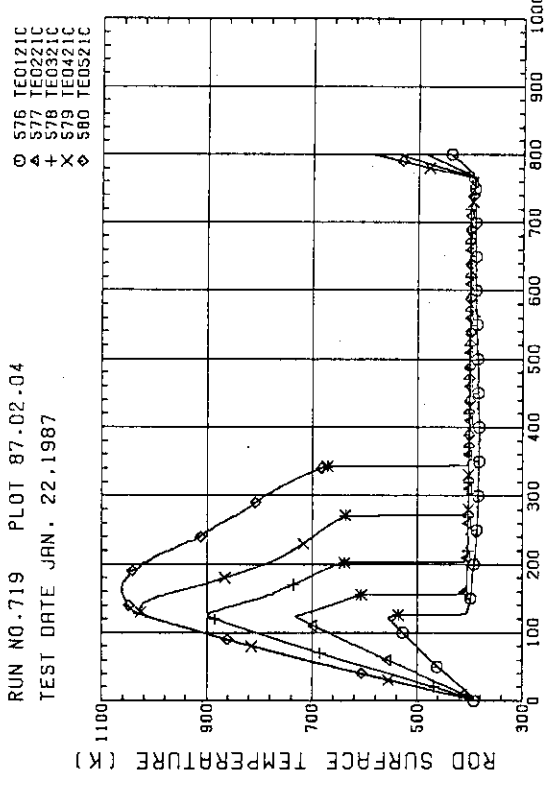

Fig. D-1 HEATER ROD TEMPERATURE (BUNDLE 2-1C, LOWER HALF)

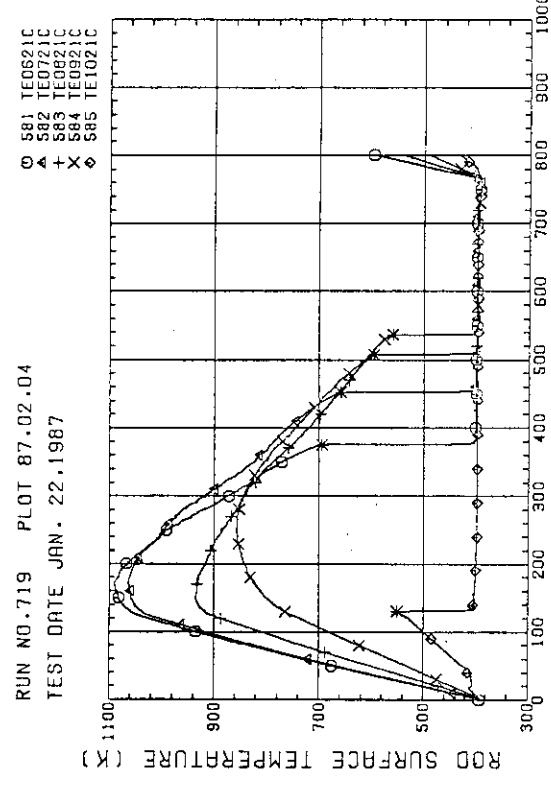

Fig. D-2 HEATER ROD TEMPERATURE (BUNDLE 2-1C, UPPER HALF)

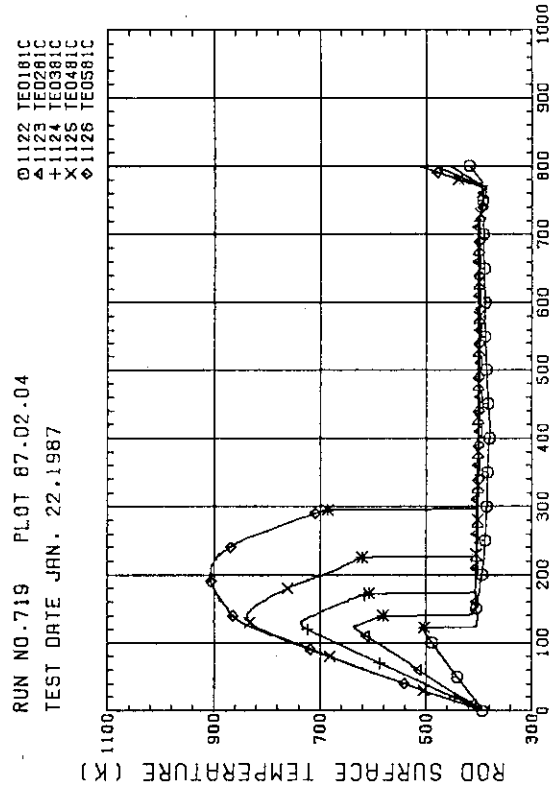

Fig. D-5 HEATER ROD TEMPERATURE (BUNDLE 6-1C, LOWER HALF)

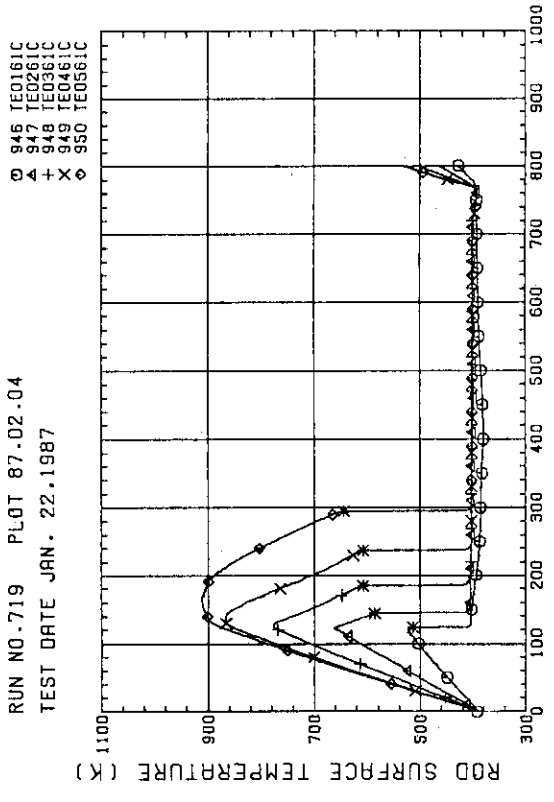

Fig. D-6 HEATER ROD TEMPERATURE (BUNDLE 6-1C, UPPER HALF)

Fig. D-7 HEATER ROD TEMPERATURE (BUNDLE 8-1C, LOWER HALF)

Fig. D-8 HEATER ROD TEMPERATURE (BUNDLE 8-1C, UPPER HALF)

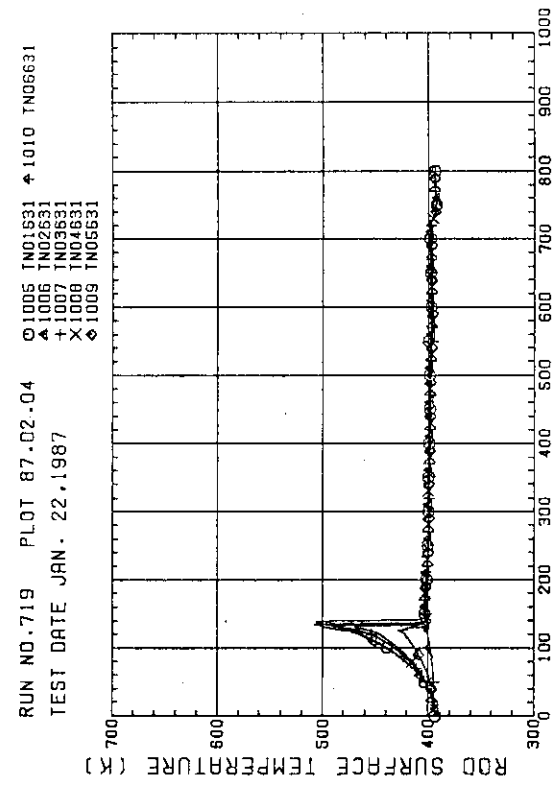

Fig. D-11 NON-HEATED ROD TEMPERATURE (BUNDLE 6-31)

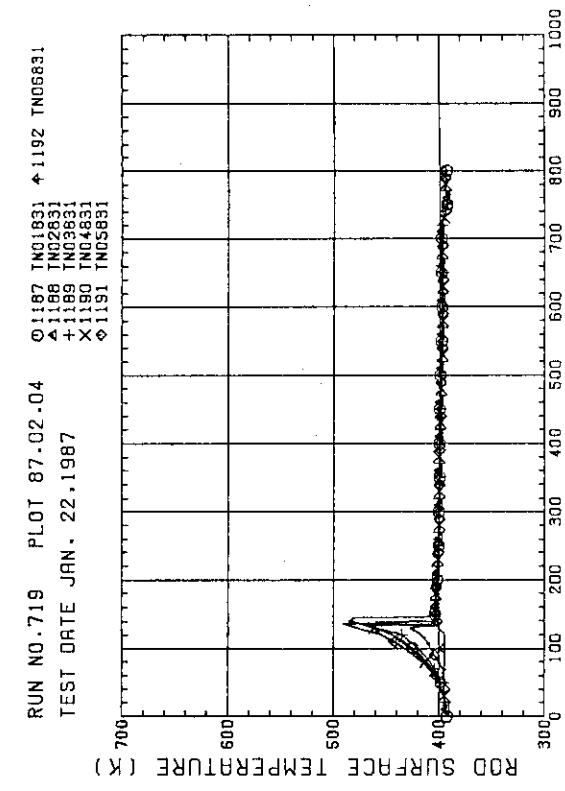

Fig. D-12 NON-HEATED ROD TEMPERATURE (BUNDLE 8-31)

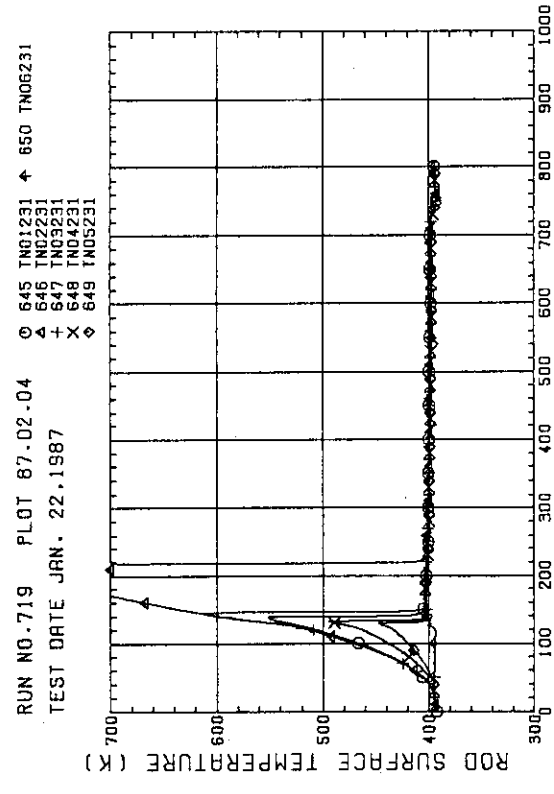

Fig. D-9 NON-HEATED ROD TEMPERATURE (BUNDLE 2-31)

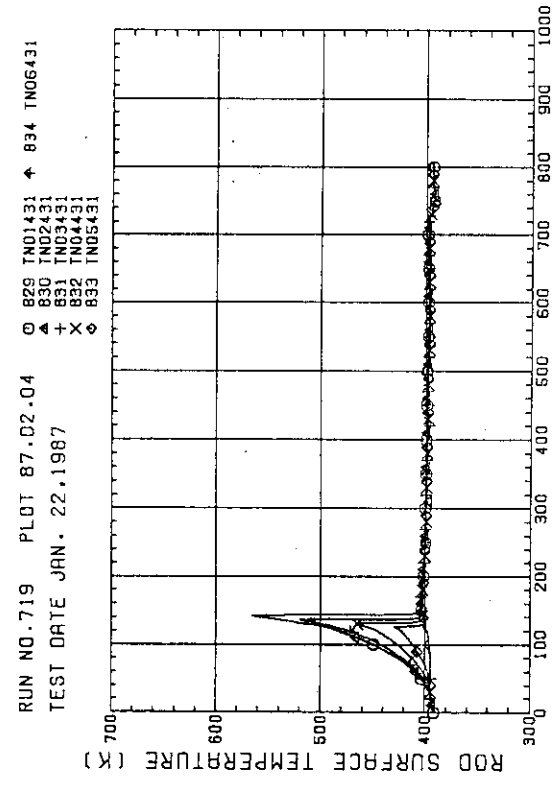

Fig. D-10 NON-HEATED ROD TEMPERATURE (BUNDLE 4-31)

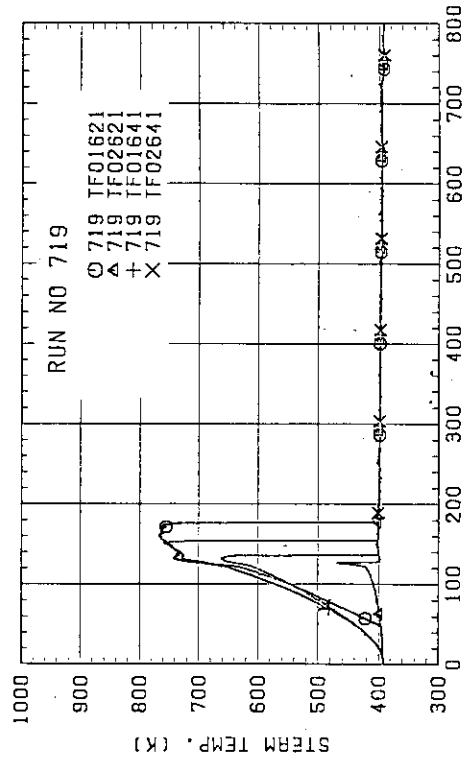

Fig. D-15 STEAM TEMPERATURE IN CORE, BUNDLE 6

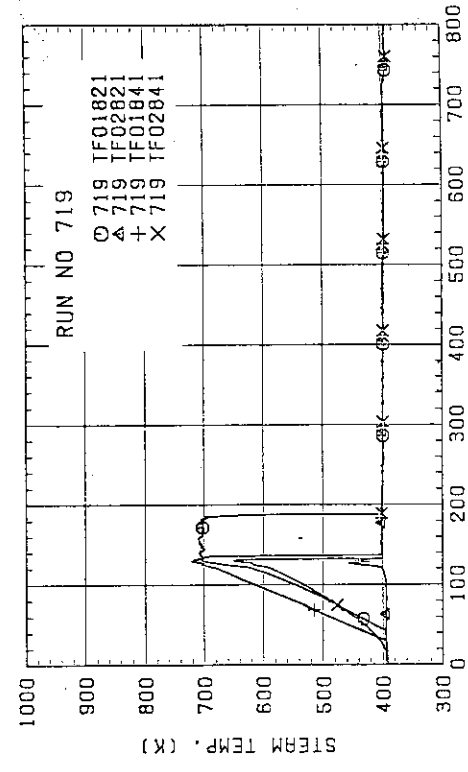

Fig. D-16 STEAM TEMPERATURE IN CORE, BUNDLE 8

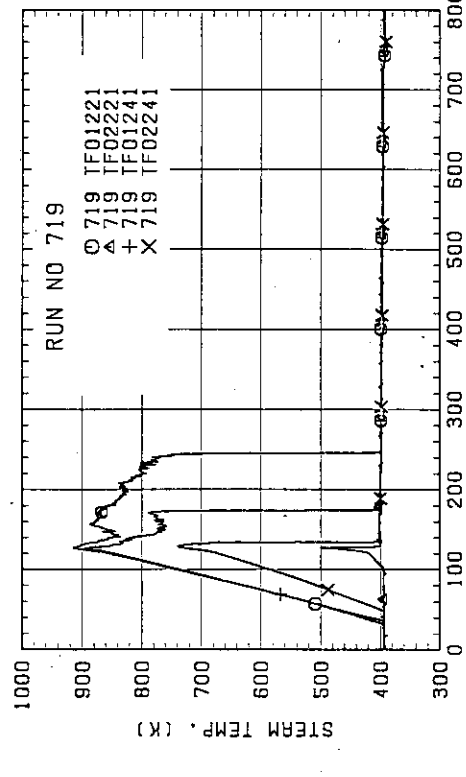

Fig. D-13 STEAM TEMPERATURE IN CORE, BUNDLE 2

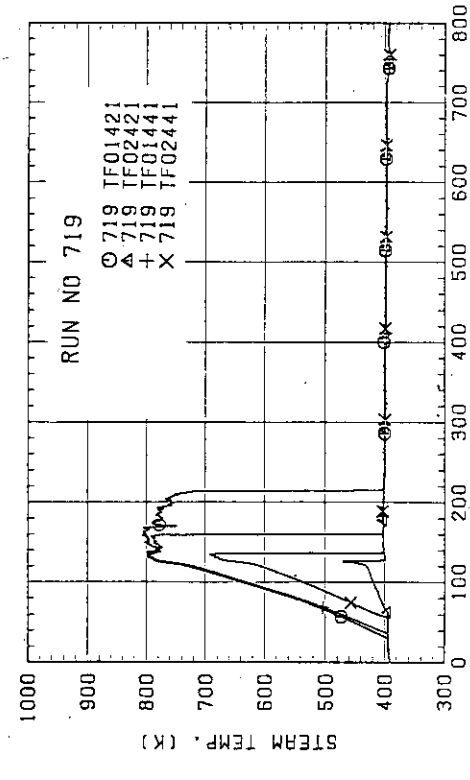

Fig. D-14 STEAM TEMPERATURE IN CORE, BUNDLE 4

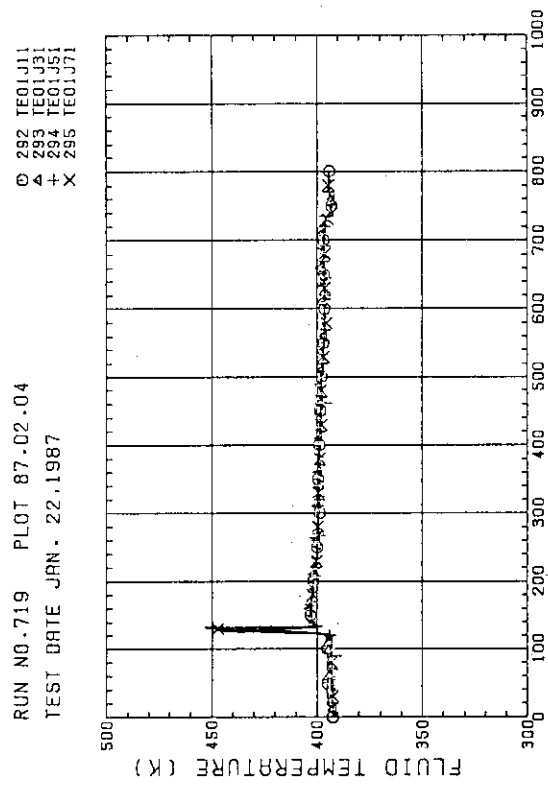

Fig. D-19 FLUID TEMPERATURE ABOVE UCSP
(BUNDLE 1,3,5,7, 100MM ABOVE UCSP)

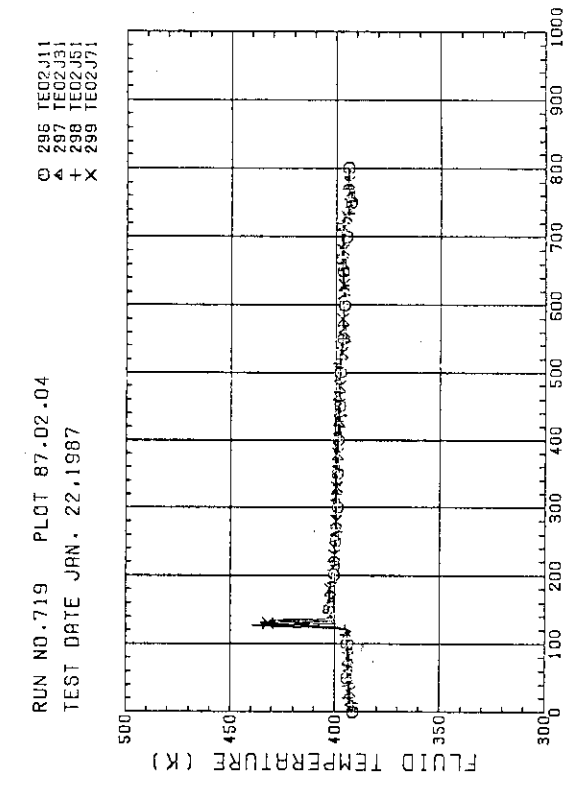

Fig. D-20 FLUID TEMPERATURE ABOVE UCSP
(BUNDLE 1,3,5,7, 250MM ABOVE UCSP)

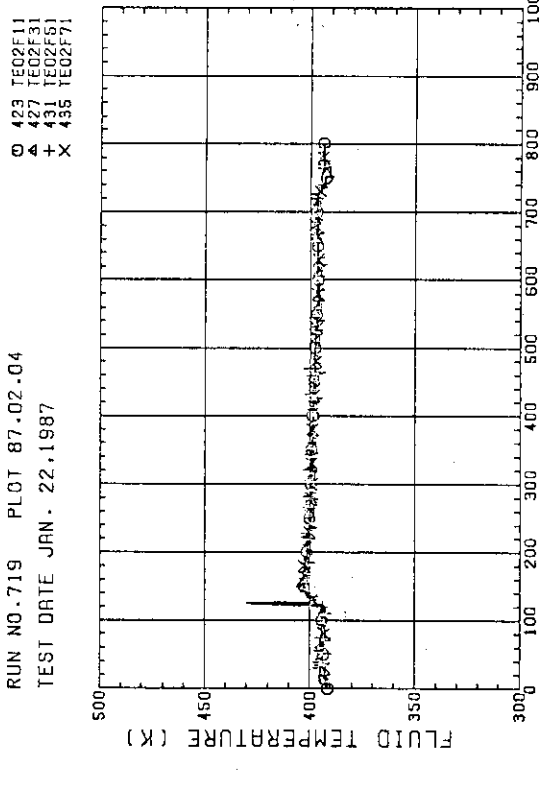

Fig. D-17 FLUID TEMPERATURE JUST ABOVE END BOX TIE PLATE
(BUNDLE 1,3,5,7, OPPOSITE SIDE OF COLD LEG, OUTER)

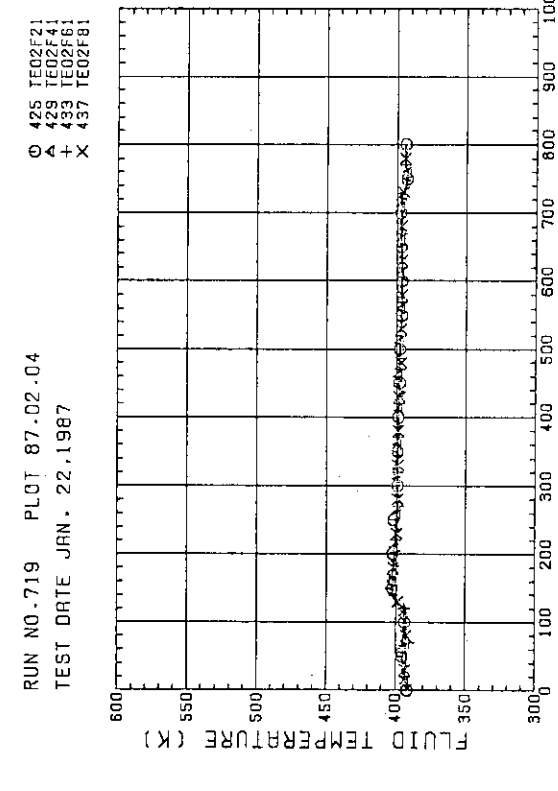

Fig. D-18 FLUID TEMPERATURE JUST ABOVE END BOX TIE PLATE
(BUNDLE 2,4,6,8, COLD LEG SIDE, OUTER)

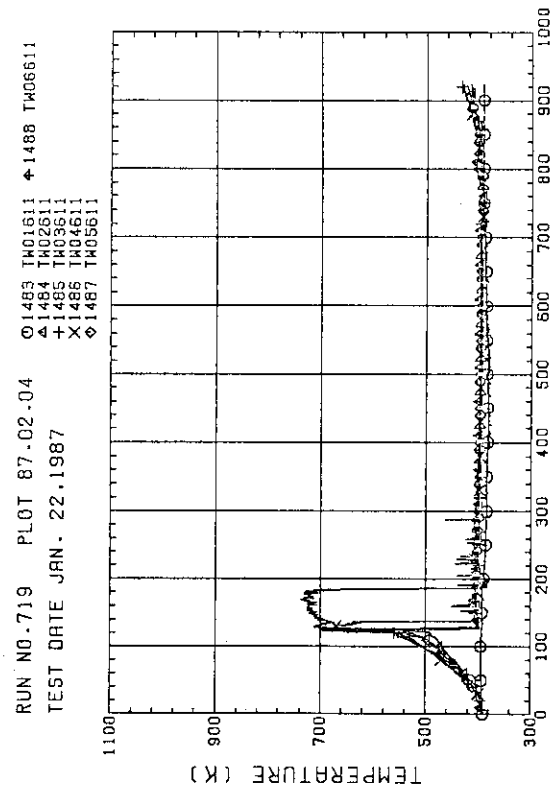

Fig. D-21 TEMPERATURE FOR SPUTTERING DETECTION BUNDLE 2 , REGION 1 , TYPE 3

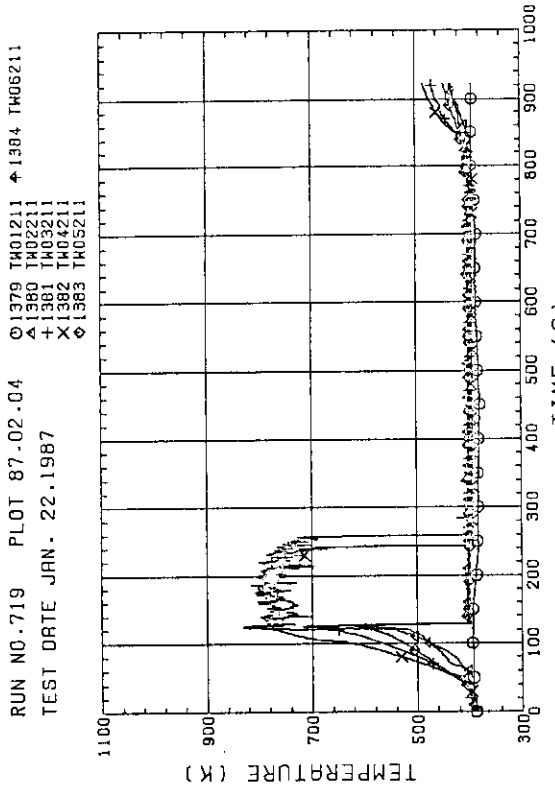

Fig. D-23 TEMPERATURE FOR SPUTTERING DETECTION BUNDLE 6 , REGION 1 , TYPE 1 3

Fig. D-22 TEMPERATURE FOR SPUTTERING DETECTION BUNDLE 4 , REGION 1 , TYPE 3

Fig. D-24 TEMPERATURE FOR SPUTTERING DETECTION BUNDLE 8 , REGION 1 , TYPE 3

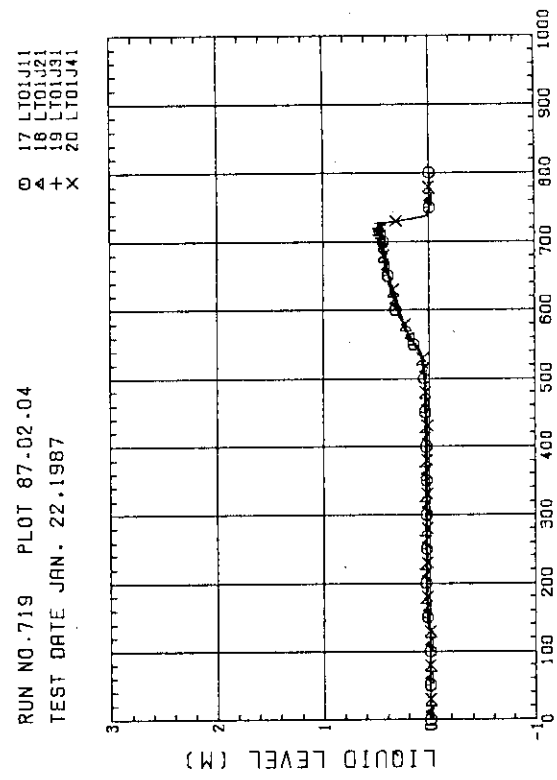

Fig. D-27 LIQUID LEVEL ABOVE UCSP (BUNDLE 1,2,3,4)

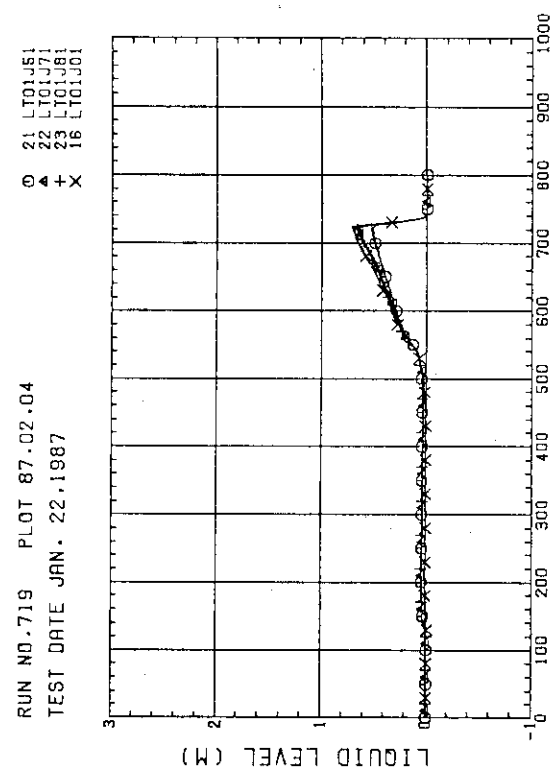

Fig. D-28 LIQUID LEVEL ABOVE UCSP (BUNDLE 5,6,7,8 AND CORE BAFFLE)

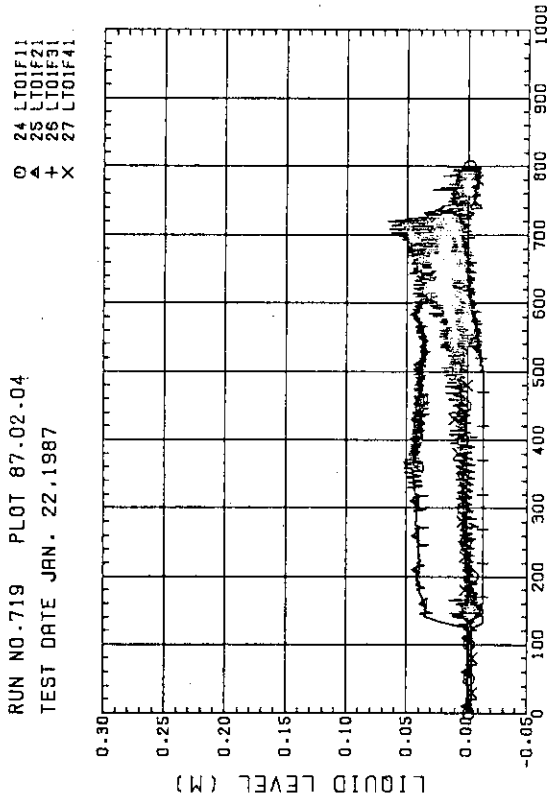

Fig. D-25 LIQUID LEVEL ABOVE END BOX TIE PLATE (BUNDLE 1,2,3,4)

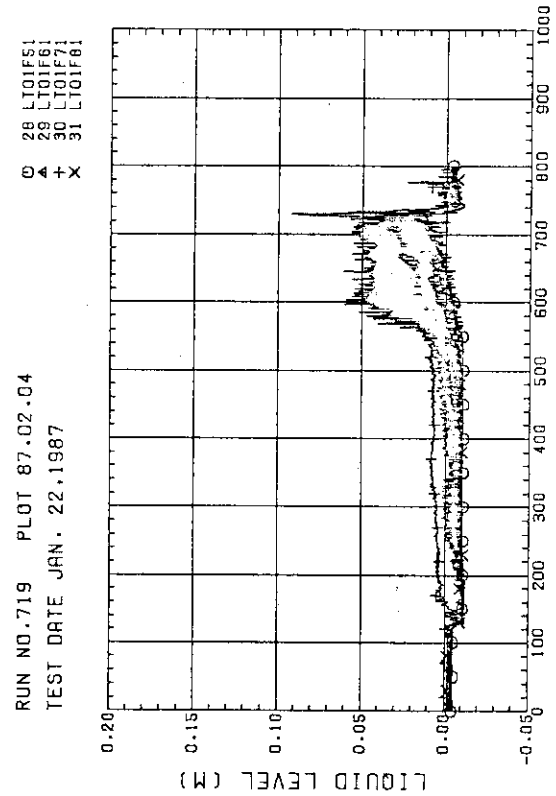

Fig. D-26 LIQUID LEVEL ABOVE END BOX TIE PLATE (BUNDLE 5,6,7,8)

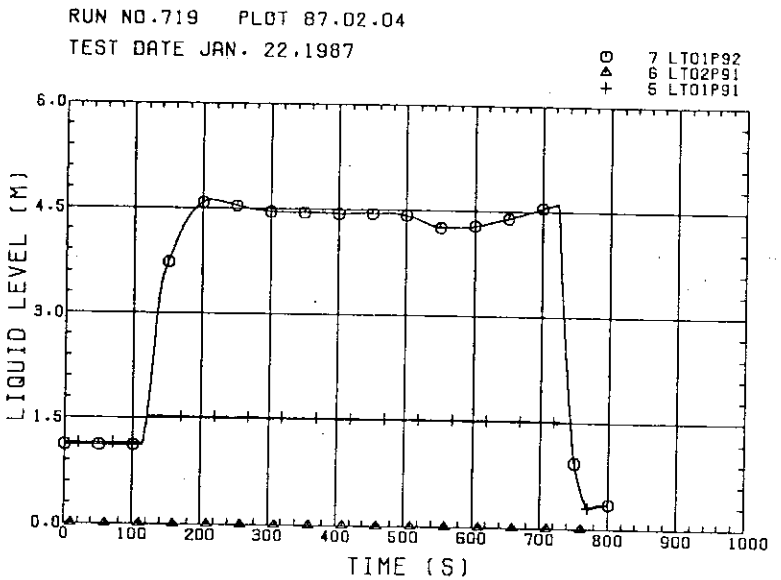

Fig. D-29 LIQUID LEVEL IN DOWNCOMER (01P91-ABOVE BLOCKING PLATE, 01P92-ACROSS BLOCKING PLATE, 02P91-C.L. TO TOP OF PV)

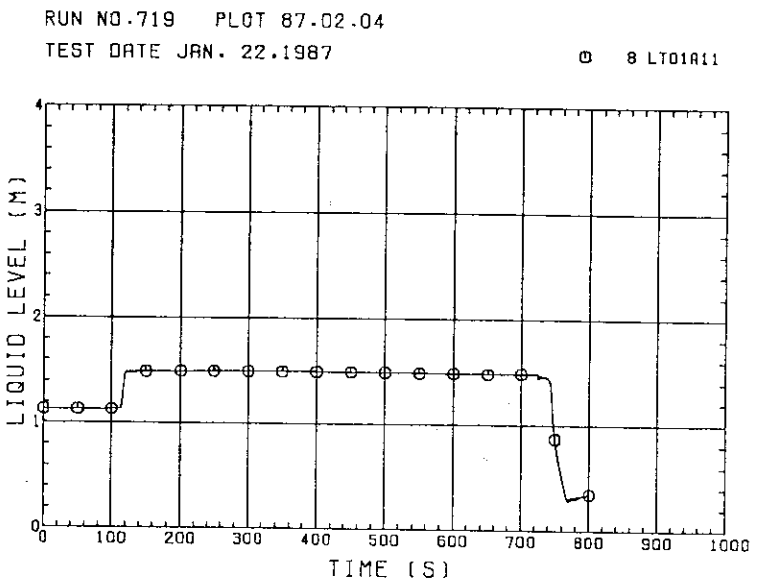

Fig. D-30 LIQUID LEVEL IN LOWER PLENUM

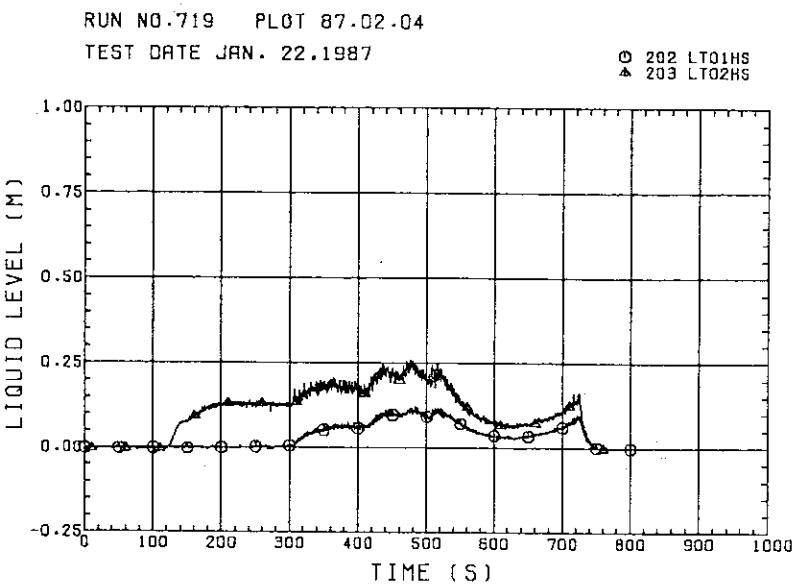

Fig. D-31 LIQUID LEVEL IN HOT LEG (01HS - PV SIDE, 02HS - STEAM/WATER SEPARATOR SIDE)

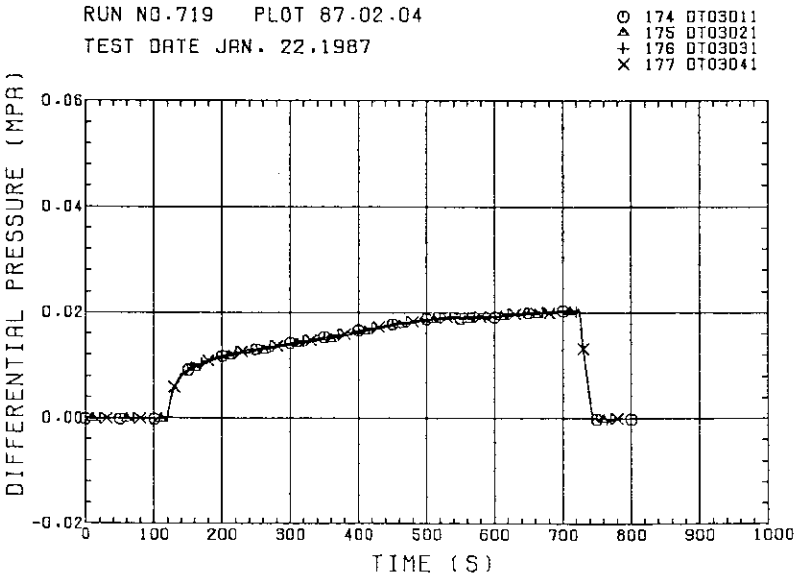

Fig. D-32 DIFFERENTIAL PRESSURE OF CORE FULL HIGHT (BUNDLE 1.2.3.4)

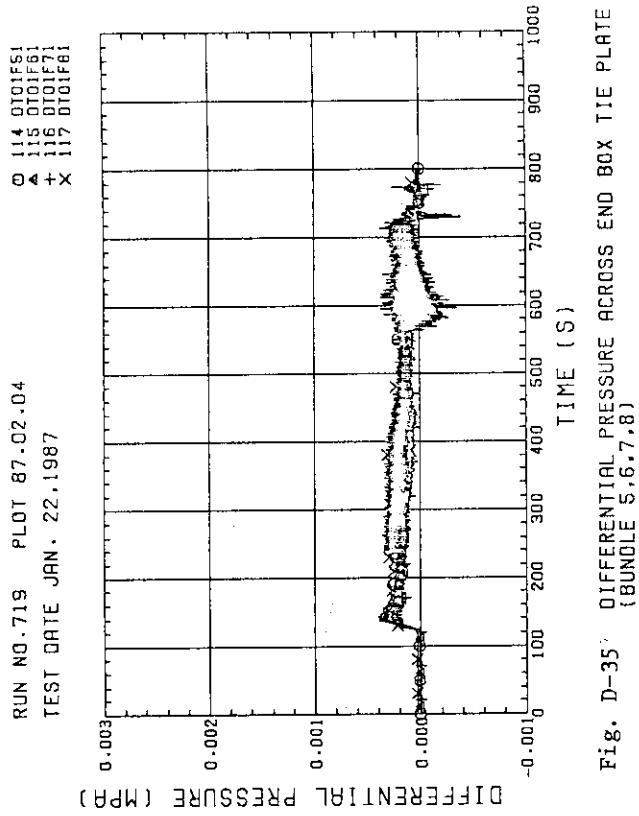

Fig. D-35 DIFFERENTIAL PRESSURE ACROSS END BOX TIE PLATE (BUNDLE 5,6,7,8)

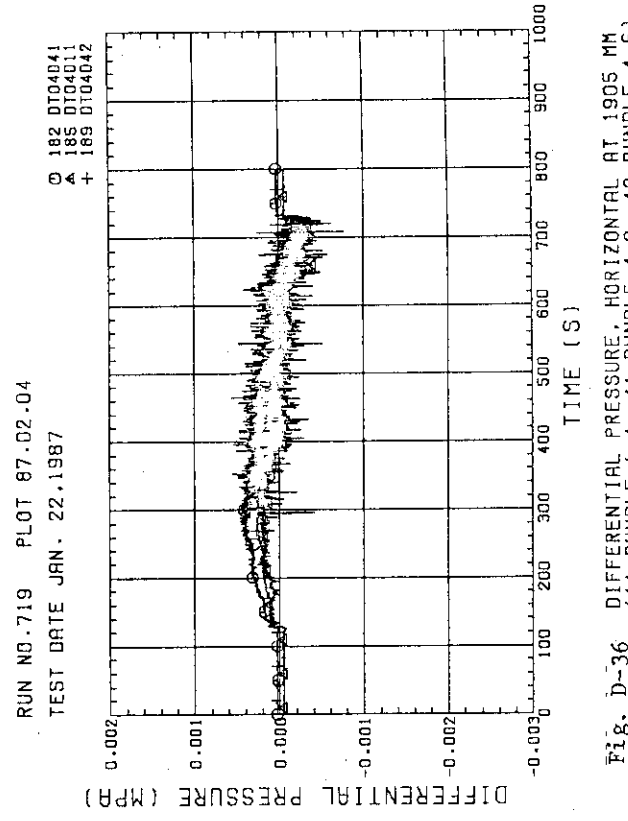

Fig. D-36 DIFFERENTIAL PRESSURE, HORIZONTAL AT 1905 MM (11-BUNDLE 1-4, 41-BUNDLE 4-8, 42-BUNDLE 4-6)

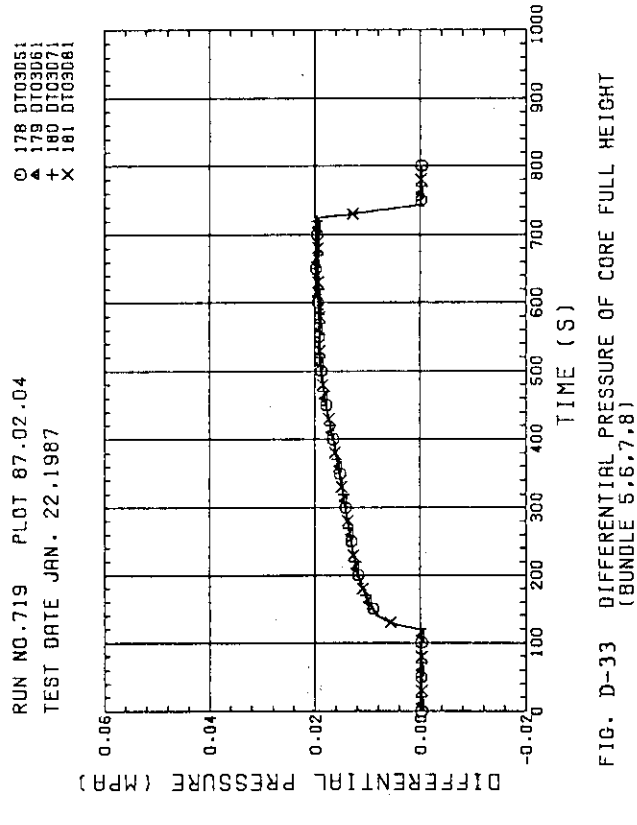

FIG. D-33 DIFFERENTIAL PRESSURE OF CORE FULL HEIGHT (BUNDLE 5,6,7,8)

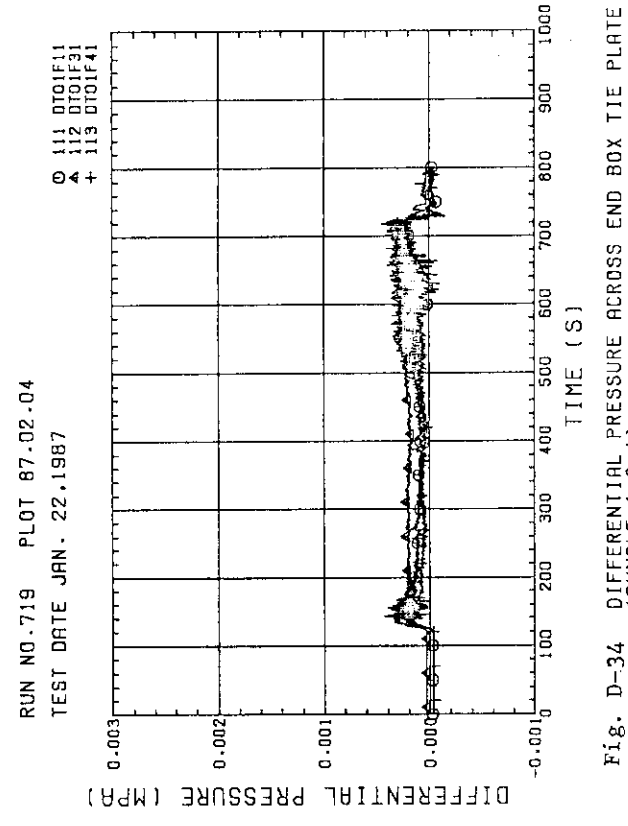

Fig. D-34 DIFFERENTIAL PRESSURE ACROSS END BOX TIE PLATE (BUNDLE 1,3,4)

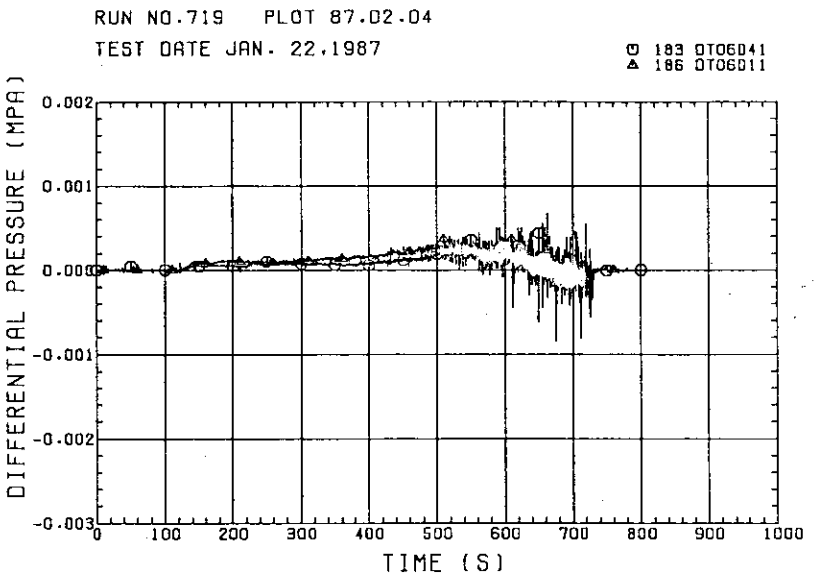

Fig. D-37 DIFFERENTIAL PRESSURE, HORIZONTAL AT 3235 MM (11-BUNDLE 1-4, 41-BUNDLE 4-8)

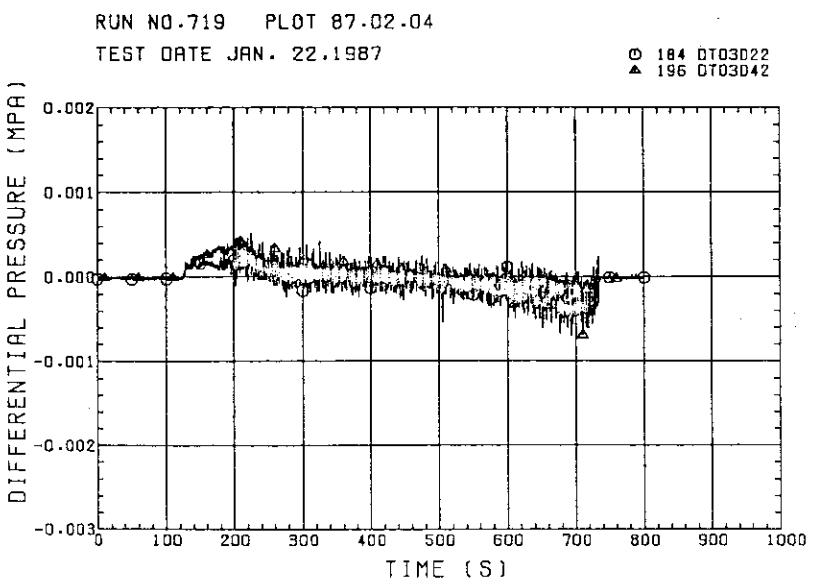

Fig. D-38 DIFFERENTIAL PREESURE, HORIZONTAL AT 1365 MM (22-BUNDLE 2-4, 42-BUNDLE 4-8)

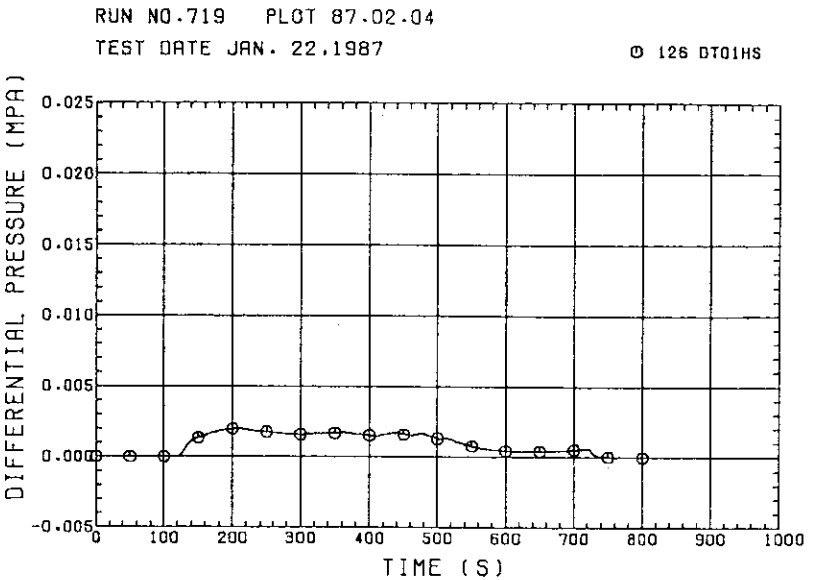

Fig. D-39 DIFFERENTIAL PRESSURE OF HOT LEG, HOT LEG INLET - STEAM/WATER SEPARATOR INLET

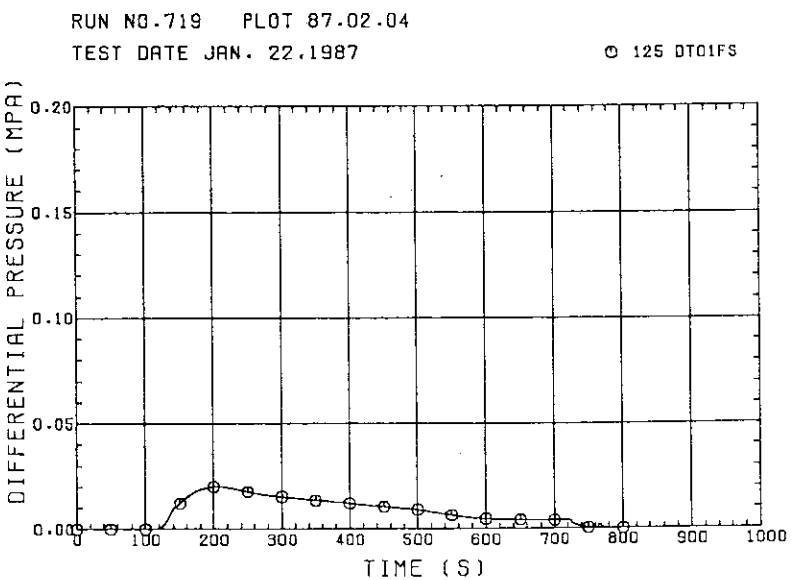

Fig. D-40 DIFFERENTIAL PRESSURE OF BROKEN COLD LEG - PV SIDE, DOWNCOMER - CONTAINMENT TANK-I

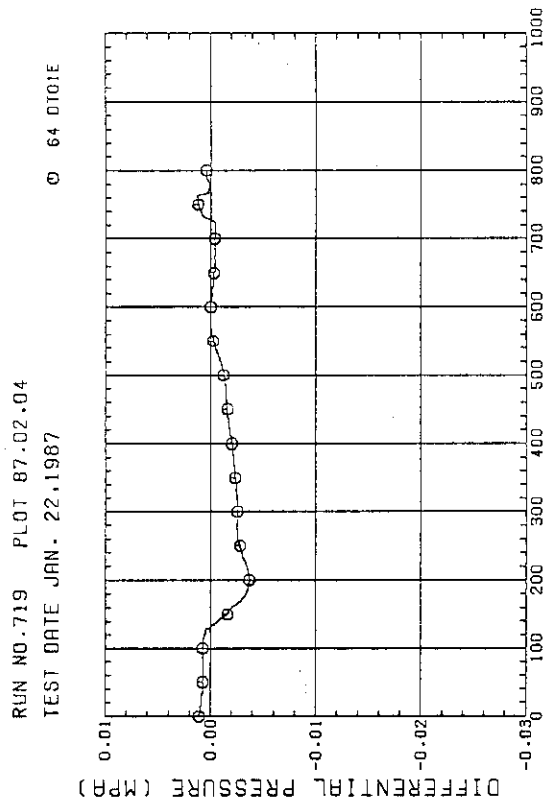

Fig. D-43 DIFFERENTIAL PRESSURE, CONTAINMENT TANK-II - CONTAINMENT TANK-I

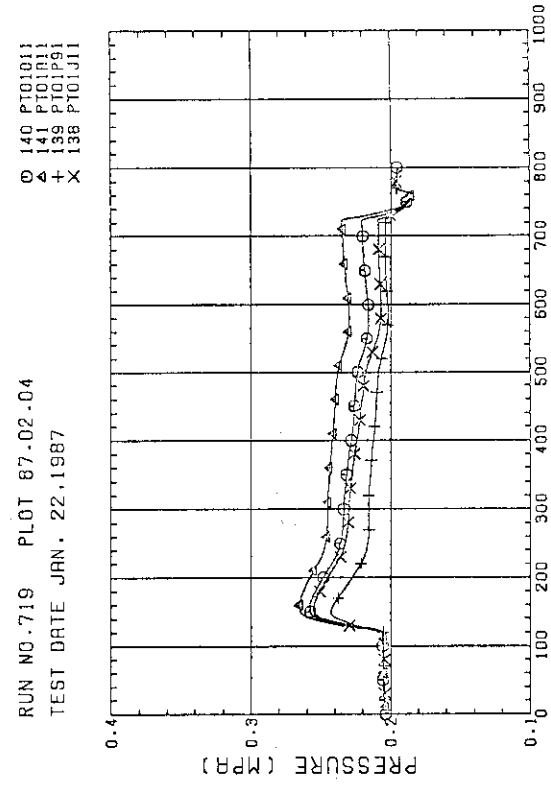

Fig. D-44 PRESSURE IN PV (J - TOP OF PV, D - CORE CENTER, A - CORE INLET, P - BELOW COLD LEG NOZZLE IN DOWNCOMER)

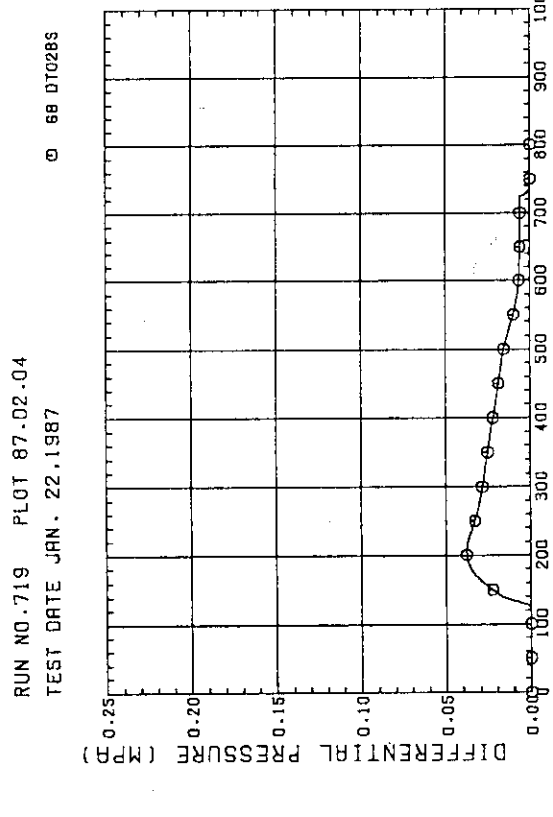

Fig. D-41 DIFFERENTIAL PRESSURE, STEAM/WATER SEPARATOR - CONTAINMENT TANK-II

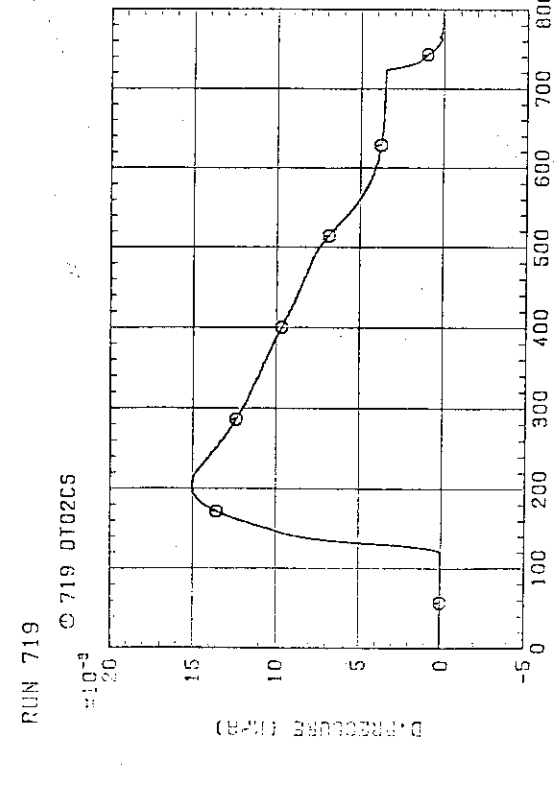

FIG. D-42 DIFFERENTIAL PRESSURE OF INTACT COLD LEG

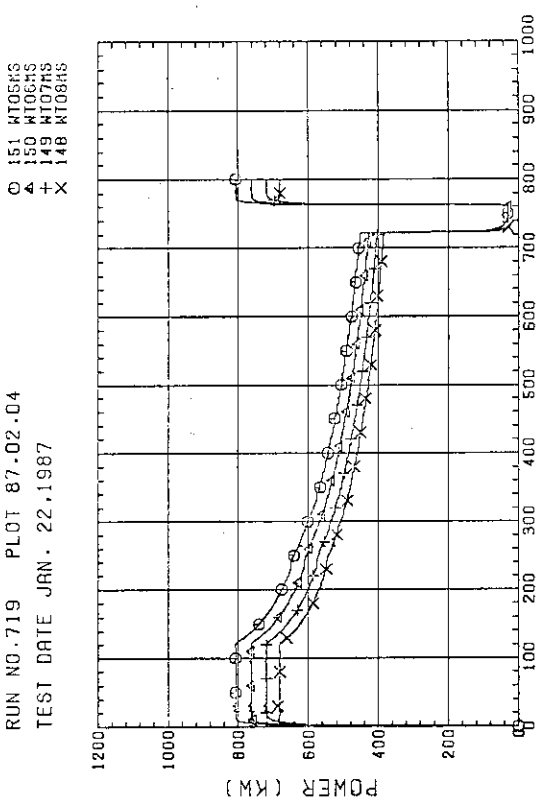

Fig. D-47 BUNDLE POWER (BUNDLE 5,6,7,8)

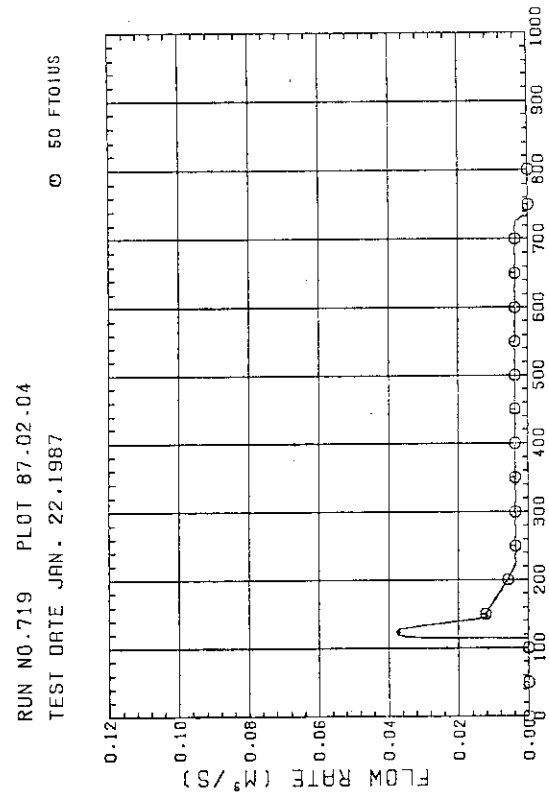

Fig. D-48 FLOW RATE OF LOWER PLENUM INJECTION WATER (ACC HEADER LINE)

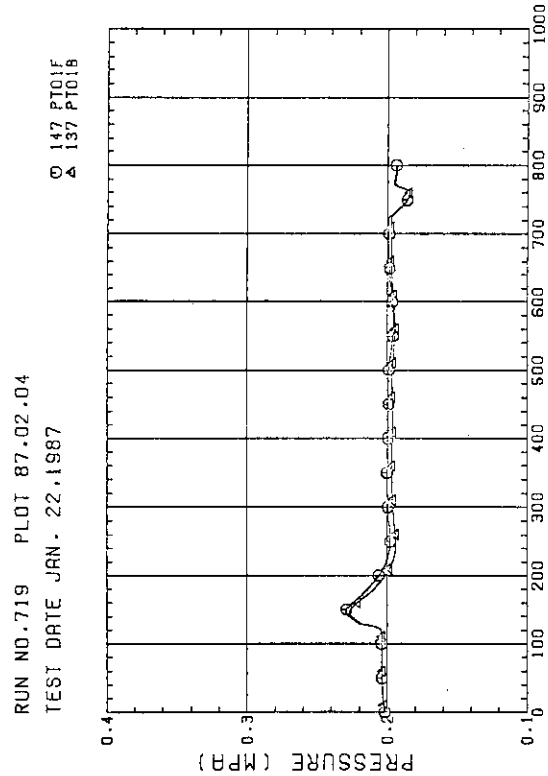

Fig. D-45 PRESSURE AT TOP OF CONTAINMENT TANK-I AND CONTAINMENT TANK-II (F-CONTAINMENT TANK-I, B-CONTAINMENT TANK-II)

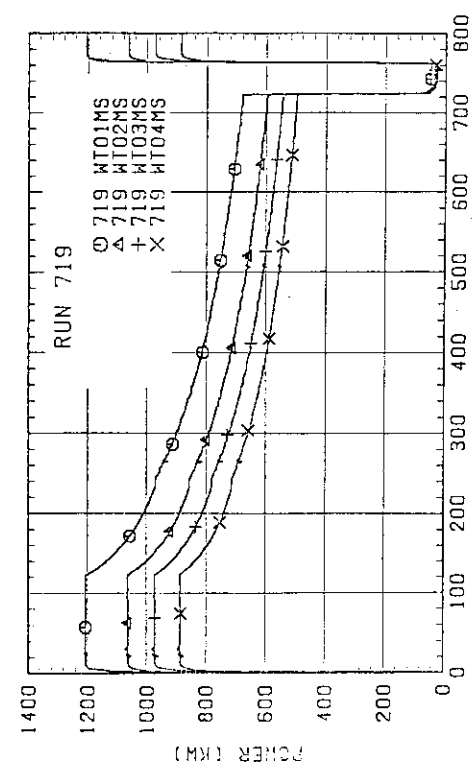

FIG. D-46 BUNDLE POWER (BUNDLE 1,2,3,4)

Appendix E Selected Data of Test S3-16

Fig. E- 1 E- 8	Heater rod temperatures
Fig. E- 9 E-12	Non-heated rod temperatures
Fig. E-13 E-16	Steam temperatures
Fig. E-17 E-18	Fluid temperatures just above end box tie plate
Fig. E-19 E-20	Fluid temperatures above UCSP
Fig. E-21 E-24	Fluid temperatures in core
Fig. E-25 E-26	Liquid levels above end box tie plate
Fig. E-27 E-28	Liquid levels above UCSP
Fig. E-29	Liquid levels in downcomer
Fig. E-30	Liquid level in lower plenum
Fig. E-31	Liquid levels in hot leg
Fig. E-32 E-33	Differential pressures across core full height
Fig. E-34 E-35	Differential Pressures across end box tie plate
Fig. E-36 E-38	Horizontal differential pressures in core
Fig. E-39 E-43	Differential pressures in primary loops
Fig. E-44 E-45	Pressures in pressure vessel and containment tanks
Fig. E-46 E-47	Bundle powers
Fig. E-48	Ecc flow rate

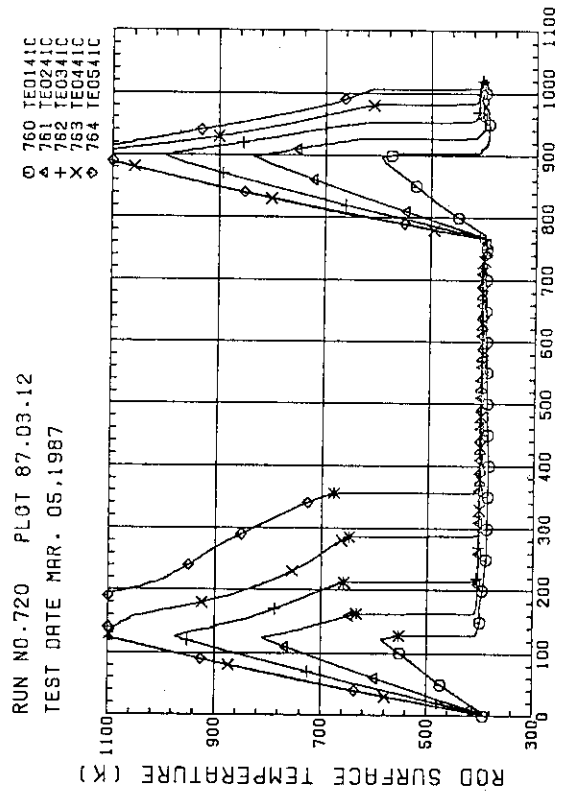

Fig. E-1 HEATER ROD TEMPERATURE (BUNDLE 2-1C, LOWER HALF)

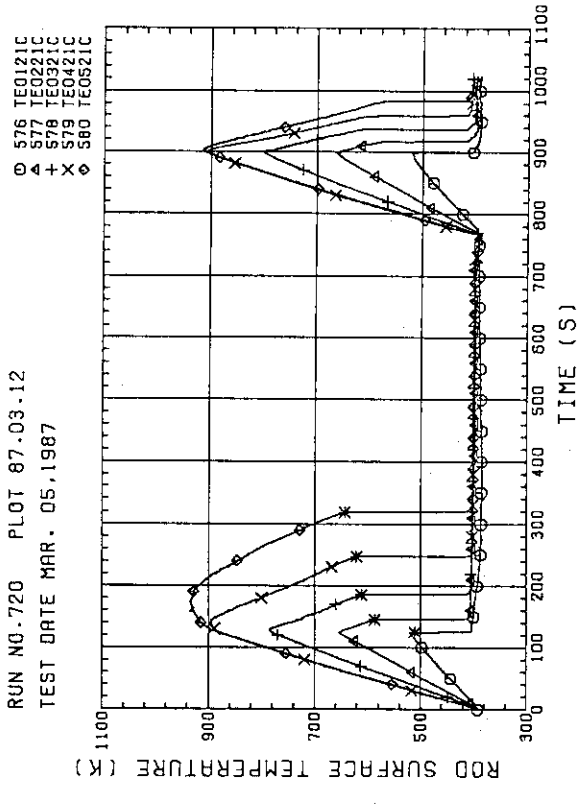

Fig. E-2 HEATER ROD TEMPERATURE (BUNDLE 2-1C, UPPER HALF)

Fig. E-3 HEATER ROD TEMPERATURE (BUNDLE 4-1C, LOWER HALF)

Fig. E-4 HEATER ROD TEMPERATURE (BUNDLE 4-1C, UPPER HALF)

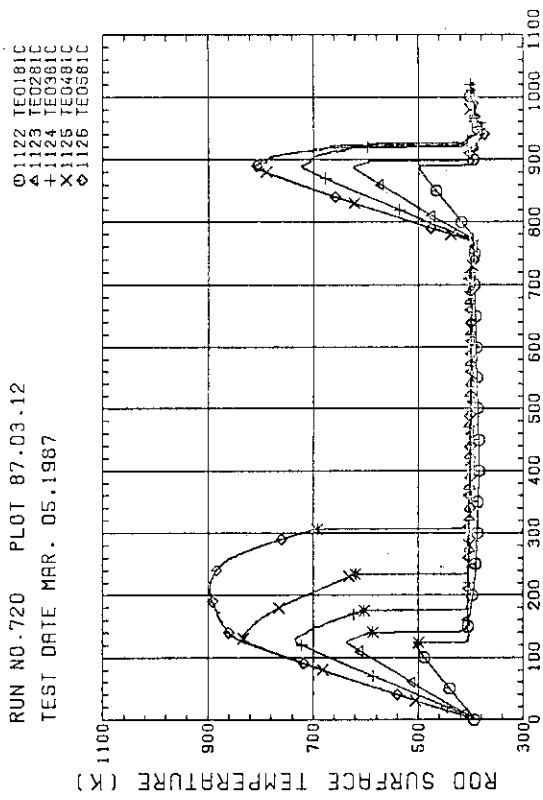

Fig. E-5 HEATER ROD TEMPERATURE (BUNDLE 6-1C, LOWER HALF)

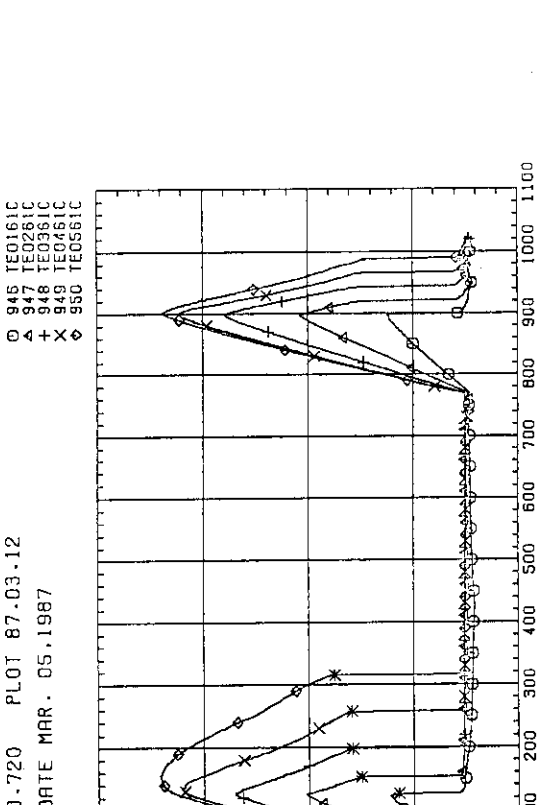

Fig. E-6 HEATER ROD TEMPERATURE (BUNDLE 6-1C, UPPER HALF)

Fig. E-7 HEATER ROD TEMPERATURE (BUNDLE 8-1C, LOWER HALF)

Fig. E-8 HEATER ROD TEMPERATURE (BUNDLE 8-1C, UPPER HALF)

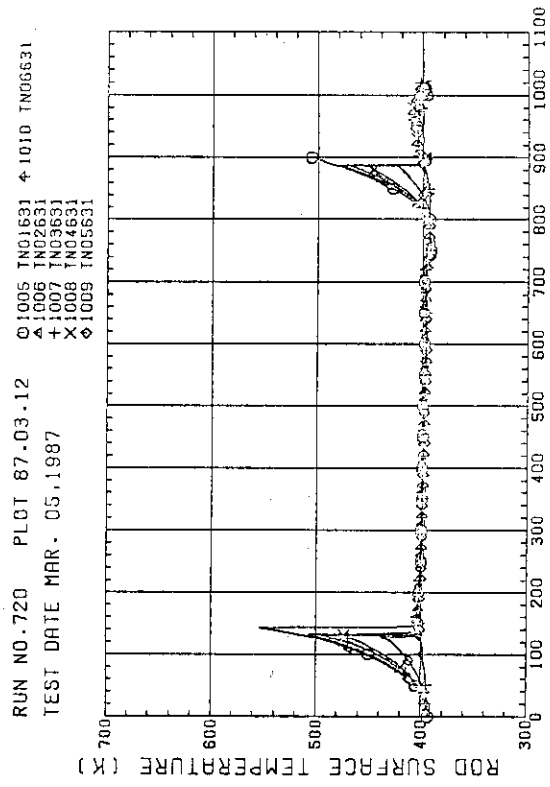

Fig. E-11 NON-HEATED ROD TEMPERATURE (BUNDLE 6-31)

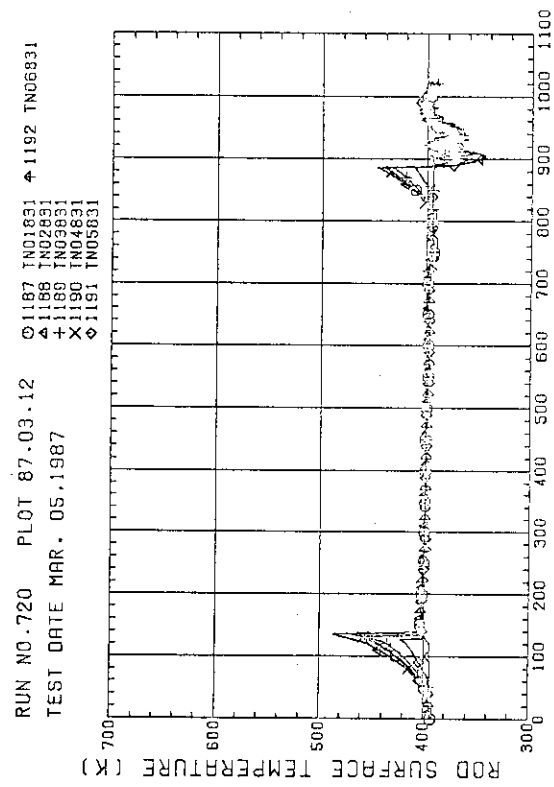

Fig. E-12 NON-HEATED ROD TEMPERATURE (BUNDLE 8-31)

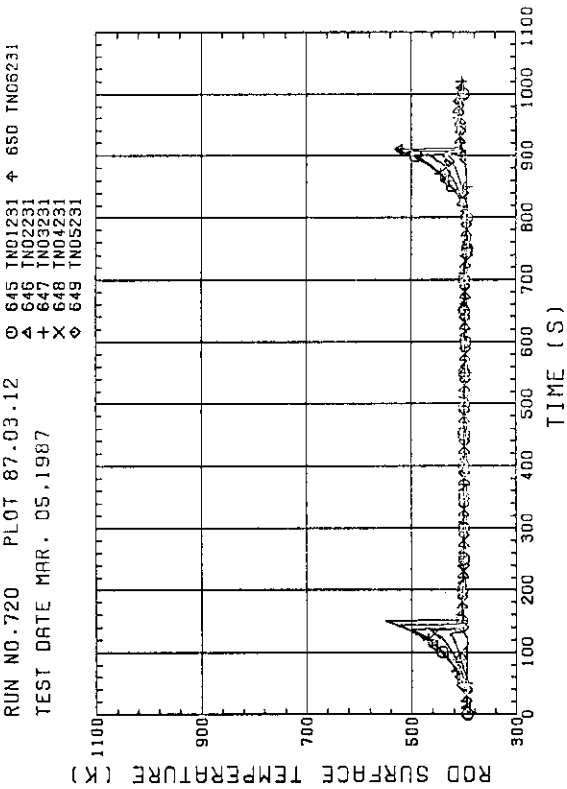

Fig. E-9 NON-HEATED ROD TEMPERATURE (BUNDLE 2-31)

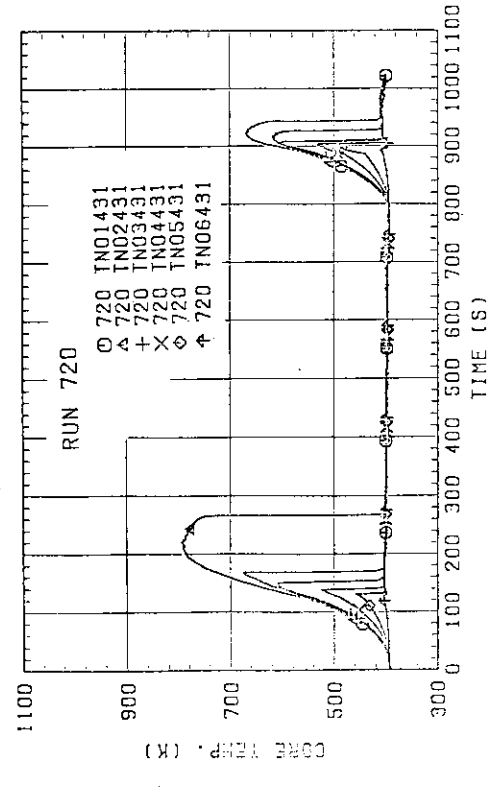

Fig. E-10 NON-HEATED ROD TEMPERATURE (BUNDLE 4-31)

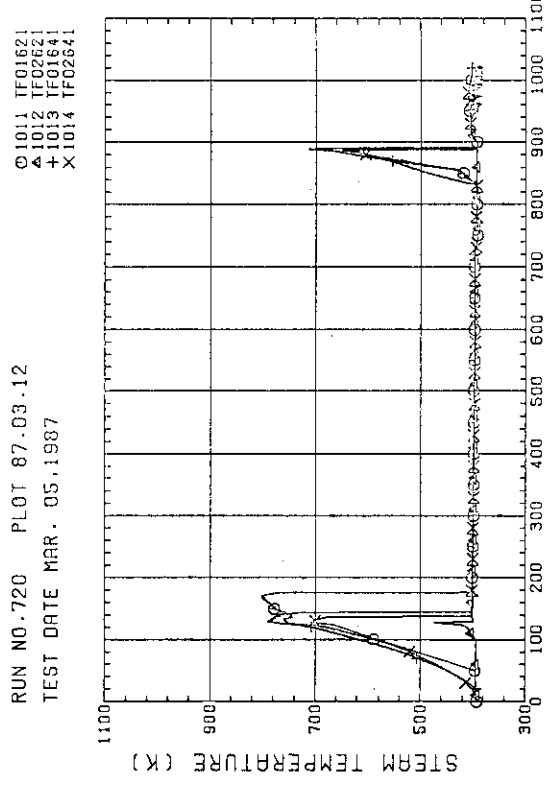

Fig. E-15 STEAM TEMPERATURE IN CORE, BUNDLE 6

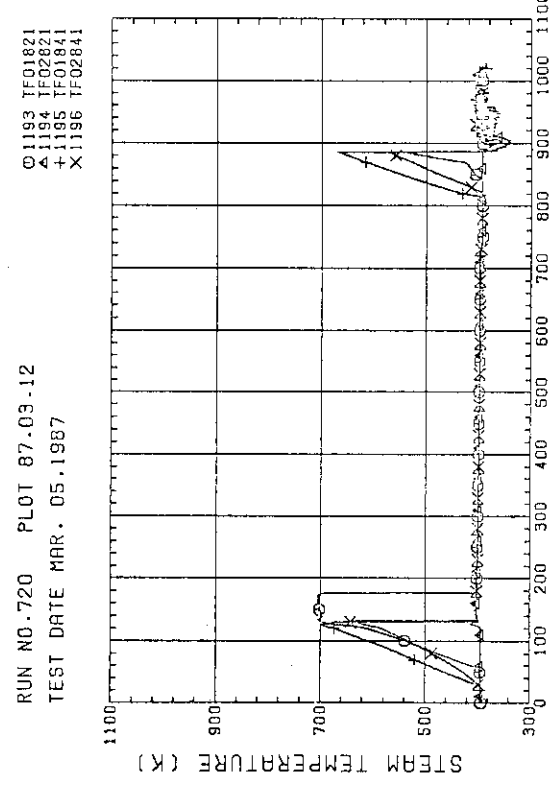

Fig. E-16 STEAM TEMPERATURE IN CORE, BUNDLE 8

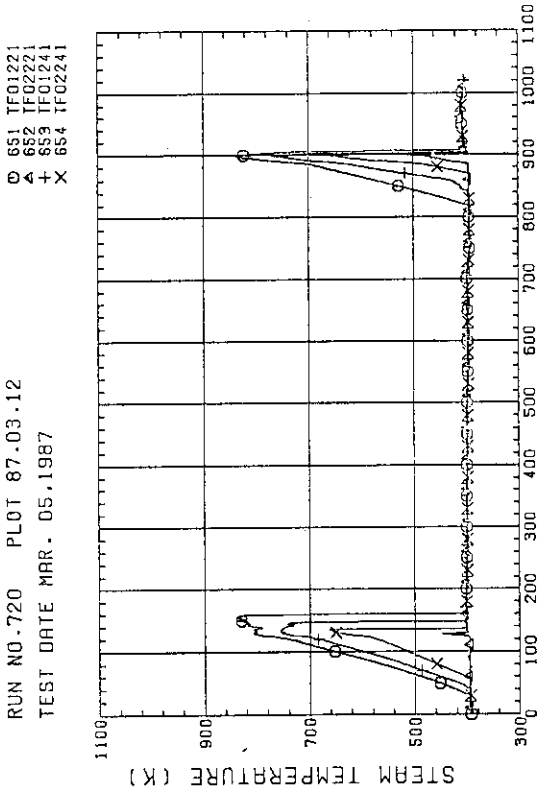

Fig. E-13 STEAM TEMPERATURE IN CORE, BUNDLE 2

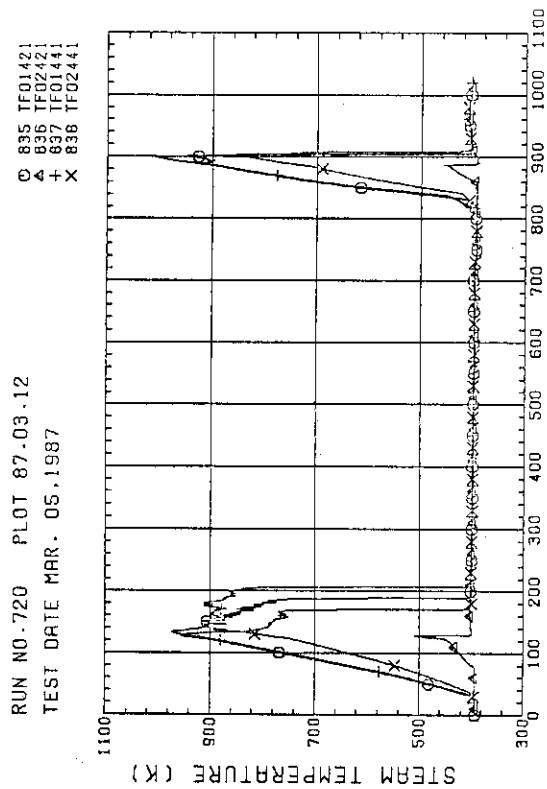

Fig. E-14 STEAM TEMPERATURE IN CORE, BUNDLE 4

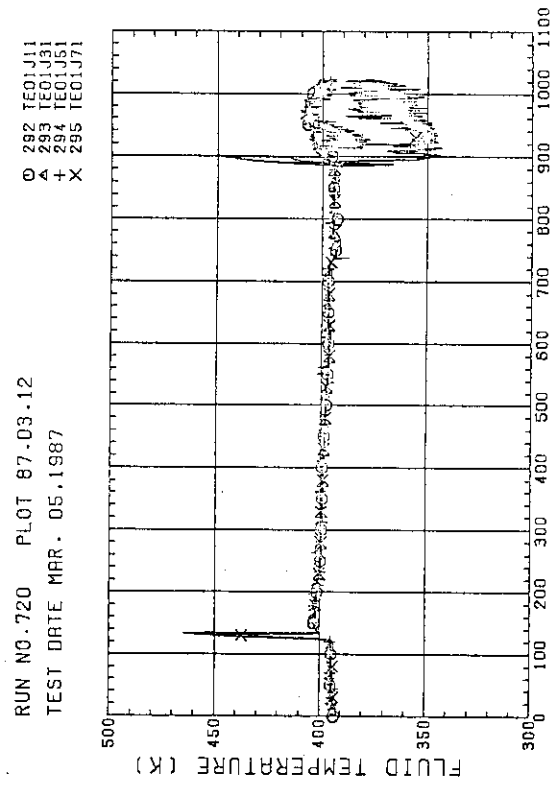

Fig. E-19 FLUID TEMPERATURE ABOVE UCSP (BUNDLE 1,3,5,7, 100MM ABOVE UCSP)

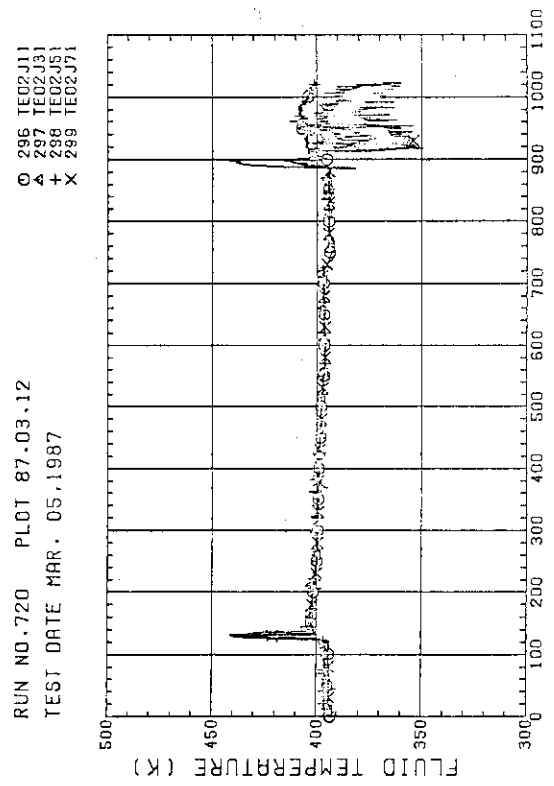

Fig. E-20 FLUID TEMPERATURE ABOVE UCSP (BUNDLE 1,3,5,7, 250MM ABOVE UCSP)

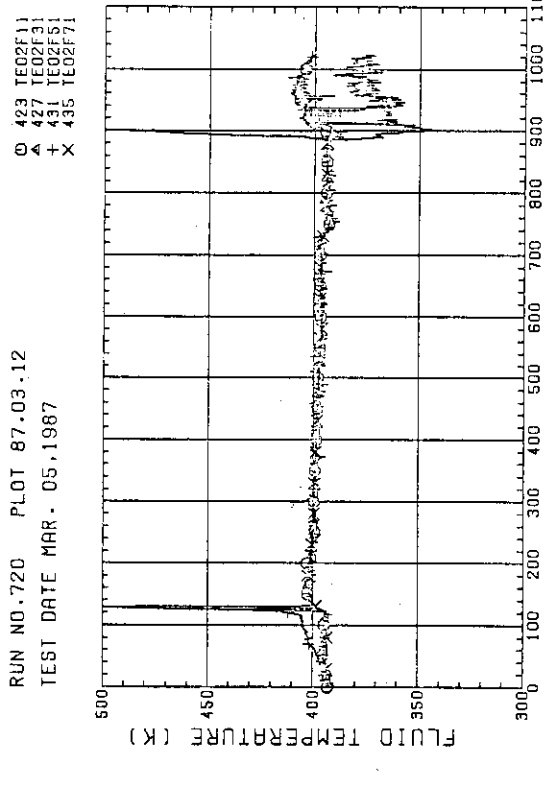

Fig. E-17 FLUID TEMPERATURE JUST ABOVE END BOX TIE PLATE (BUNDLE 1,3,5,7, OPPOSITE SIDE OF COLD LEG, OUTER)

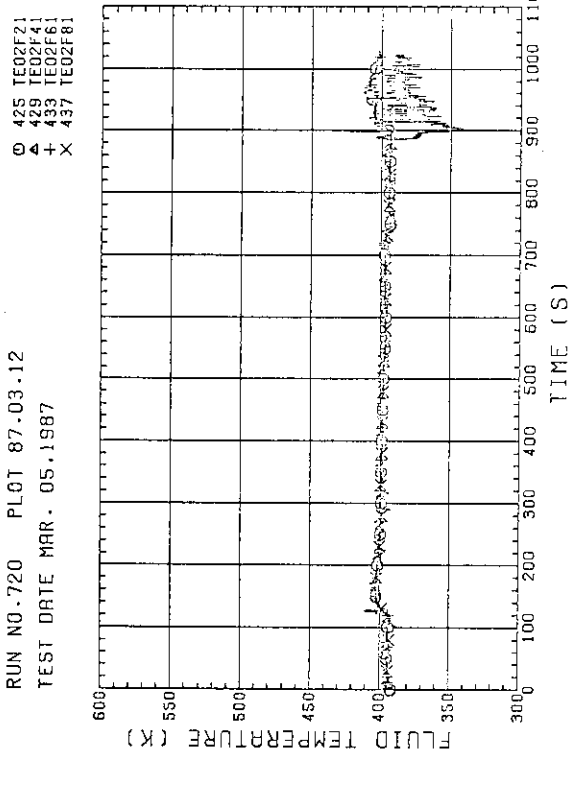

Fig. E-18 FLUID TEMPERATURE JUST ABOVE END BOX TIE PLATE (BUNDLE 2,4,6,8, COLD LEG SIDE, OUTER)

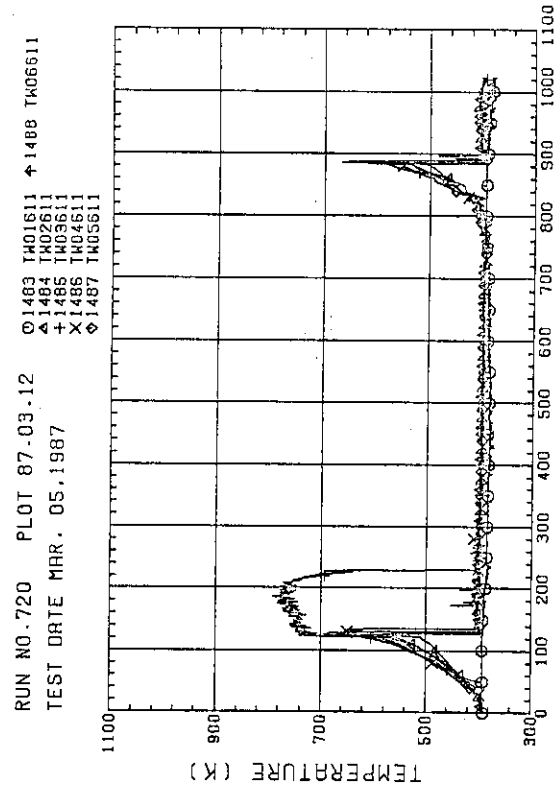

Fig. E-23 TEMPERATURE FOR SPUTTERING DETECTION BUNDLE 6 , REGION 1 , TYPE 1 3

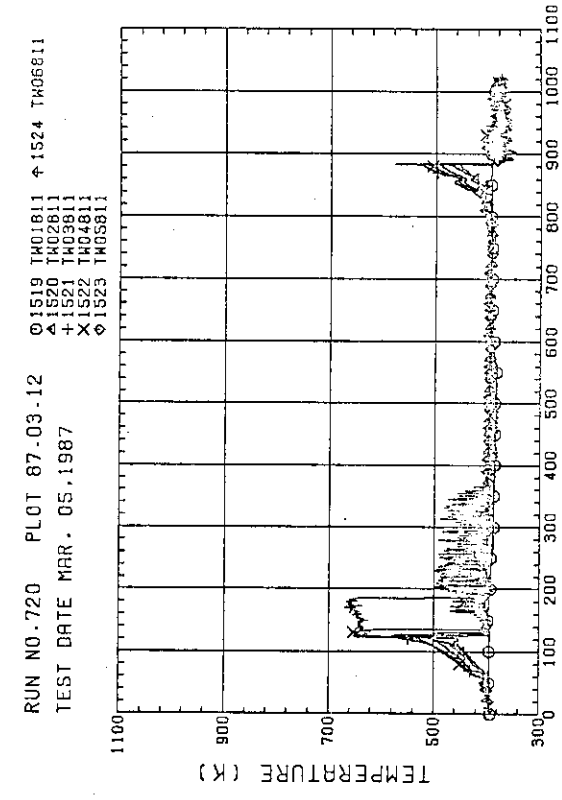

Fig. E-24 TEMPERATURE FOR SPUTTERING DETECTION BUNDLE 8 , REGION 1 , TYPE 3

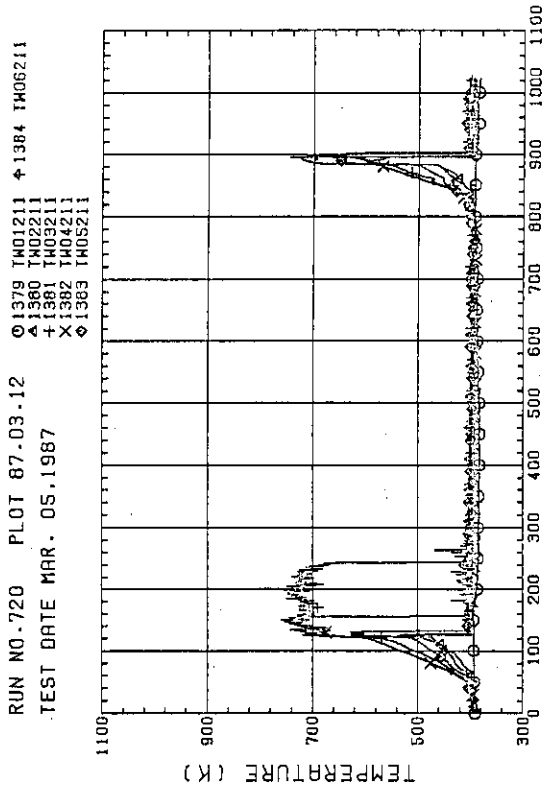

Fig. E-21 TEMPERATURE FOR SPUTTERING DETECTION BUNDLE 2 , REGION 1 , TYPE 3

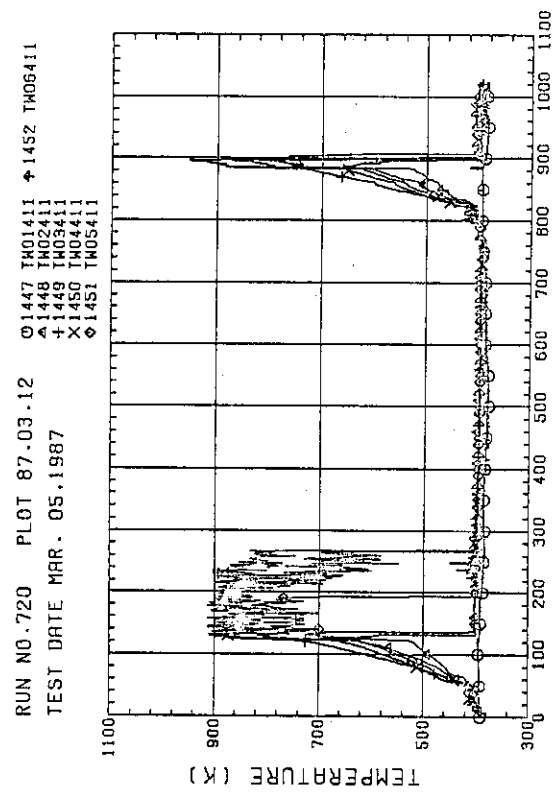

Fig. E-22 TEMPERATURE FOR SPUTTERING DETECTION BUNDLE 4 , REGION 1 , TYPE 3

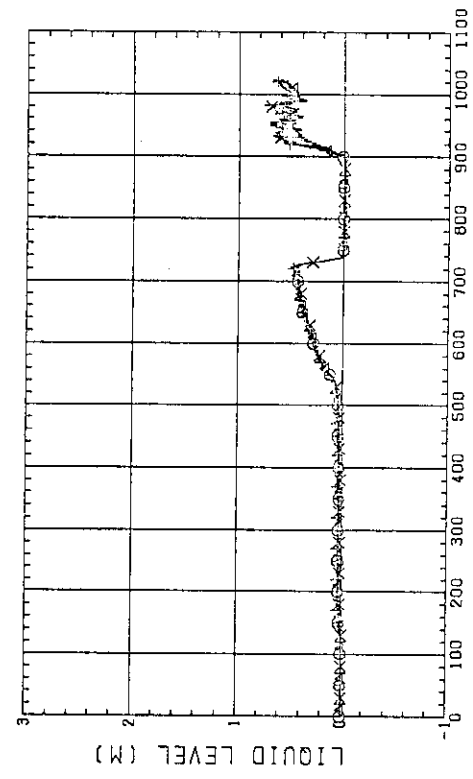

Fig. E-27 LIQUID LEVEL ABOVE UCSP (BUNDLE 1,2,3,4)

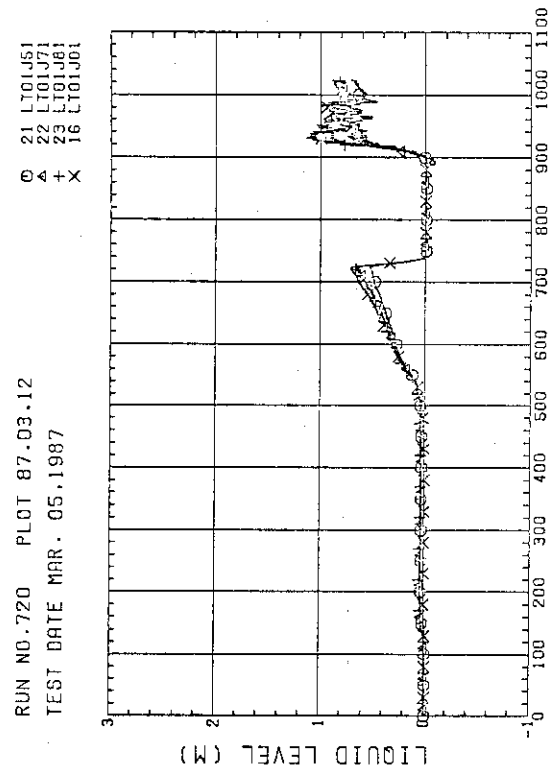

Fig. E-28 LIQUID LEVEL ABOVE UCSP (BUNDLE 5,6,7,8 AND CORE BAFFLE)

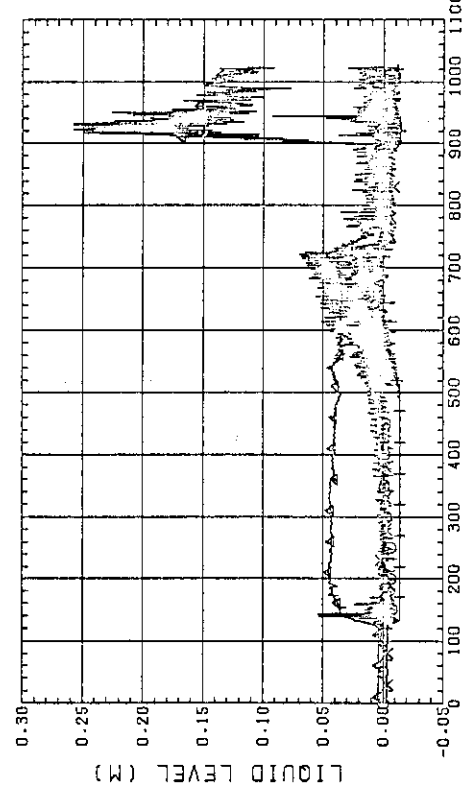

Fig. E-25 LIQUID LEVEL ABOVE END BOX TIE PLATE (BUNDLE 1,2,3,4)

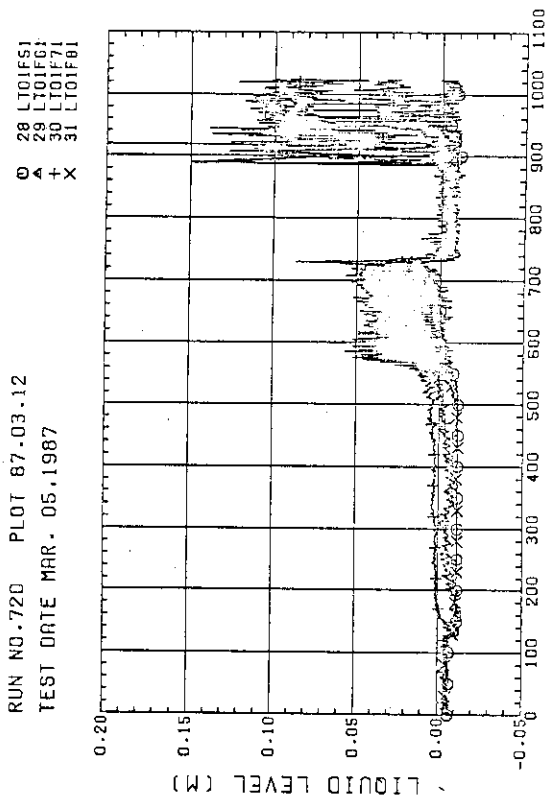

Fig. E-26 LIQUID LEVEL ABOVE END BOX TIE PLATE (BUNDLE 5,6,7,8)

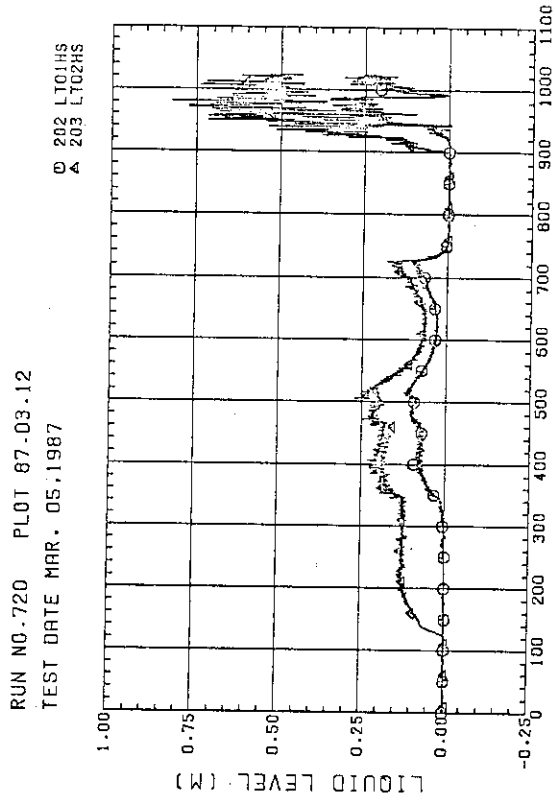

Fig. E-31 LIQUID LEVEL IN HOT LEG
(01HS - PV SIDE, 02HS - STEAM/WATER SEPARATOR SIDE)

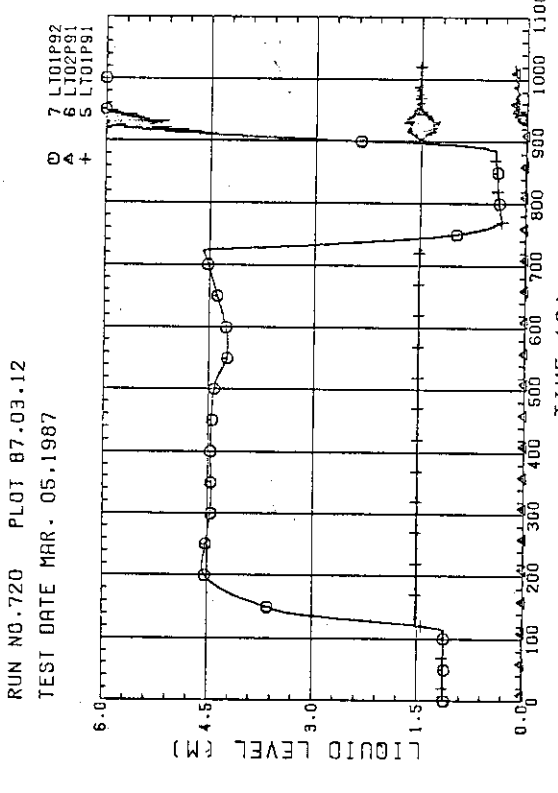

Fig. E-29 LIQUID LEVEL IN DOWNCOMER (01P91-ABOVE BLOCKING PLATE,
01P92-ACROSS BLOCKING PLATE, 02P91-C.L. TO TOP OF PV)

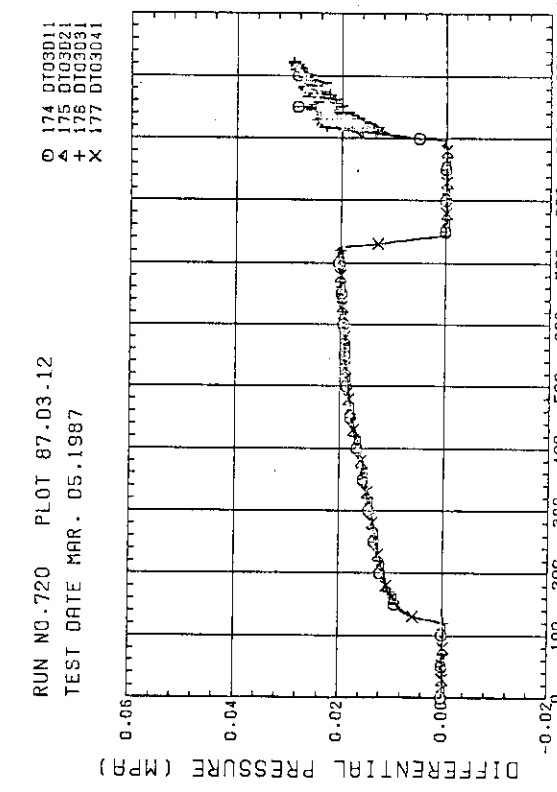

Fig. E-32 DIFFERENTIAL PRESSURE OF CORE FULL HIGHT
(BUNDLE 1,2,3,4)

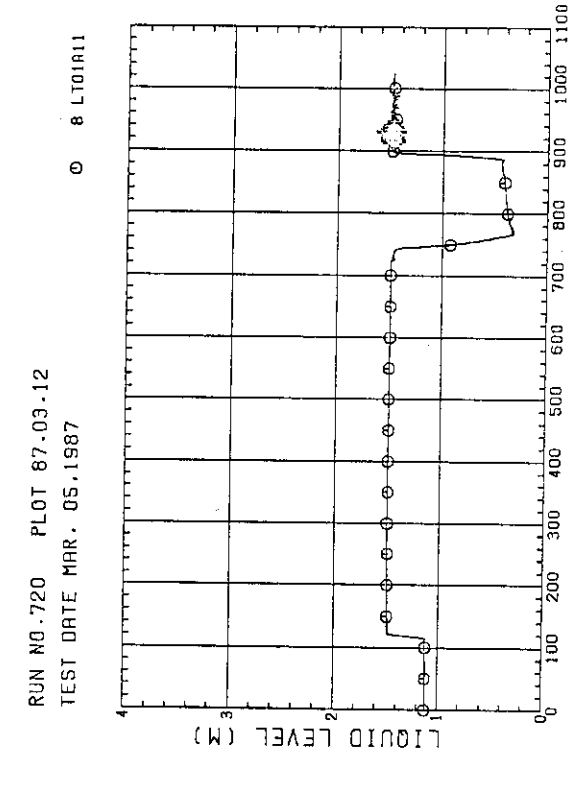

Fig. E-30 LIQUID LEVEL IN LOWER PLENUM

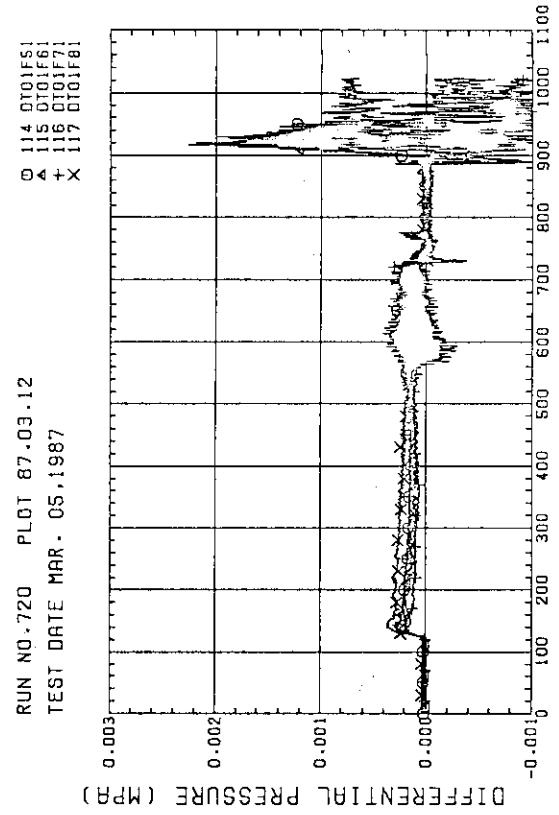

Fig. E-33 DIFFERENTIAL PRESSURE OF CORE FULL HEIGHT (BUNDLE 5,6,7,8)

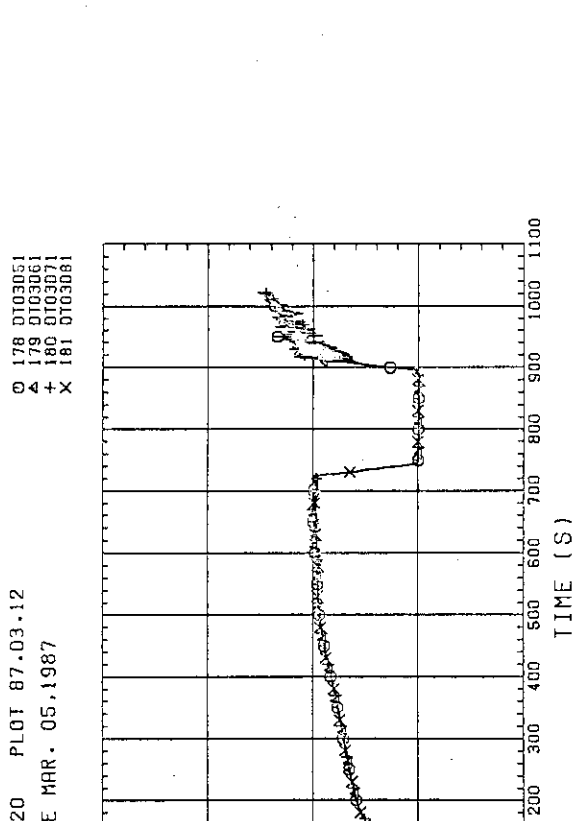

Fig. E-35 DIFFERENTIAL PRESSURE ACROSS END BOX TIE PLATE (BUNDLE 5,6,7,8)

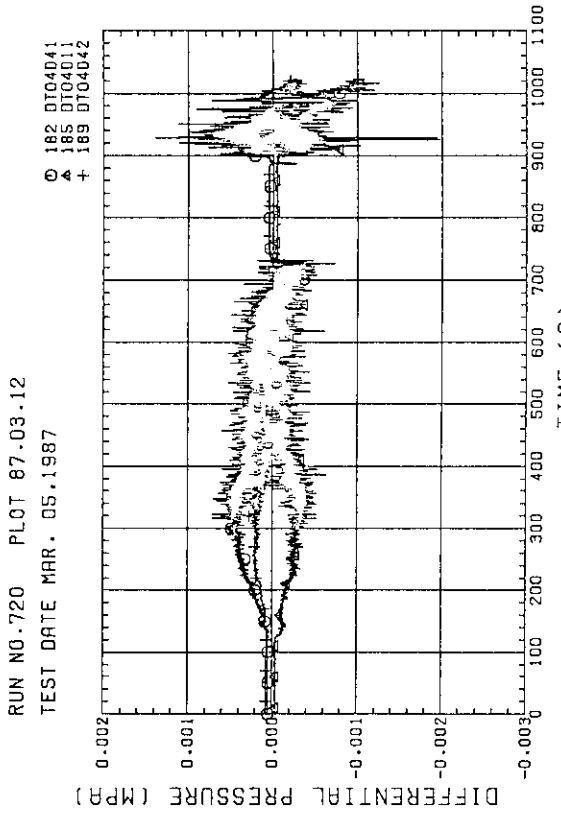

Fig. E-34 DIFFERENTIAL PRESSURE ACROSS END BOX TIE PLATE (BUNDLE 1,3,4)

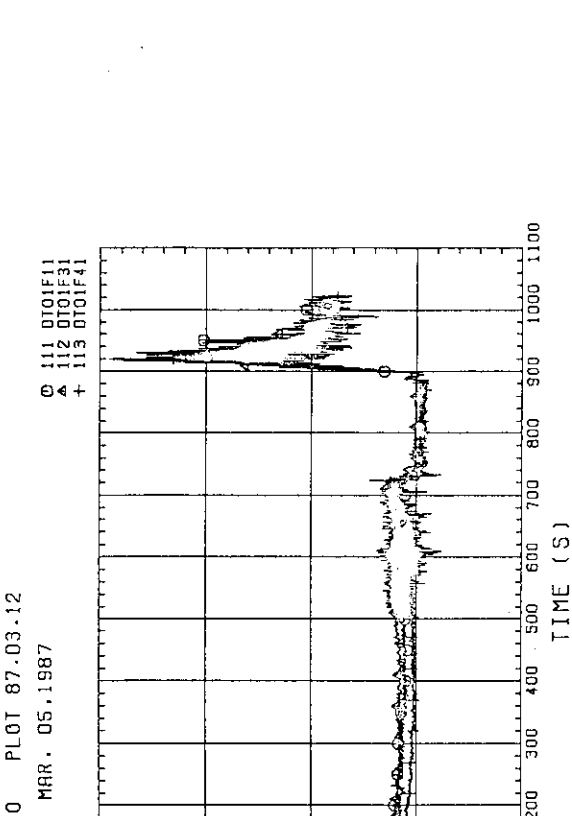

Fig. E-36 DIFFERENTIAL PRESSURE, HORIZONTAL AT 1905 MM (11-BUNDLE 1-4, 41-BUNDLE 4-8, 42-BUNDLE 4-6)

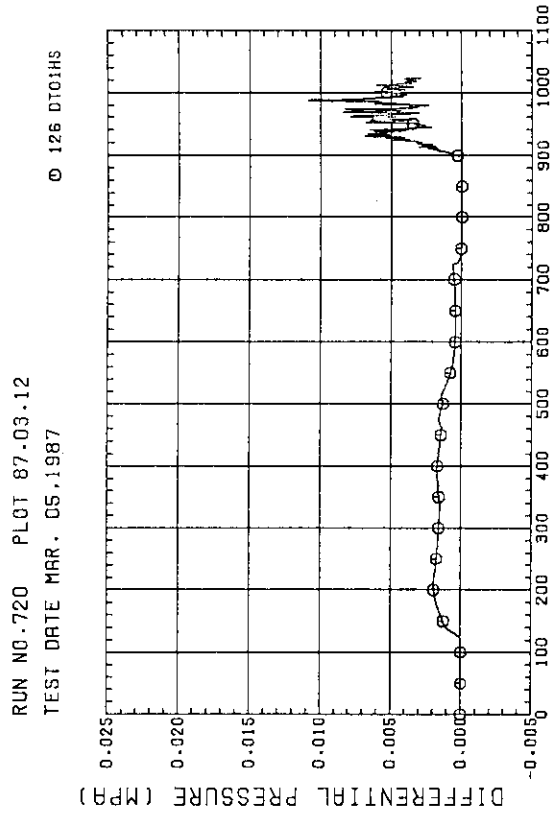

Fig. E-39 DIFFERENTIAL PRESSURE OF HOT LEG, HOT LEG INLET - STEAM/WATER SEPARATOR INLET

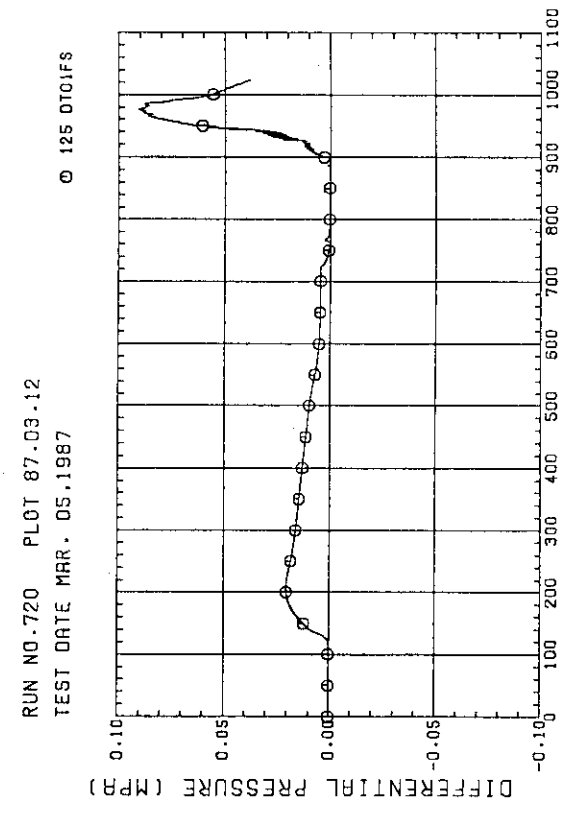

Fig. E-40 DIFFERENTIAL PRESSURE OF BROKEN COLD LEG - PV SIDE, DOWNCOMER - CONTAINMENT TANK-1

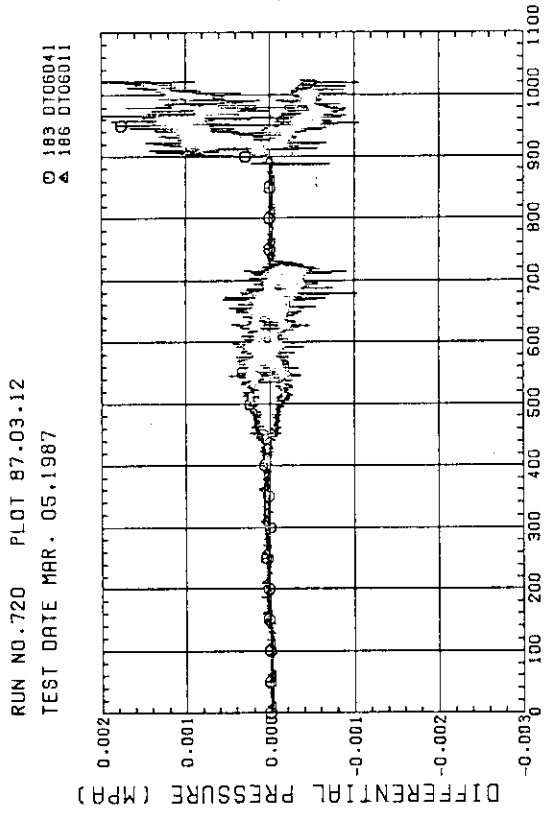

Fig. E-37 DIFFERENTIAL PRESSURE, HORIZONTAL AT 3235 MM (11-BUNDLE 1-4, 41-BUNDLE 4-8)

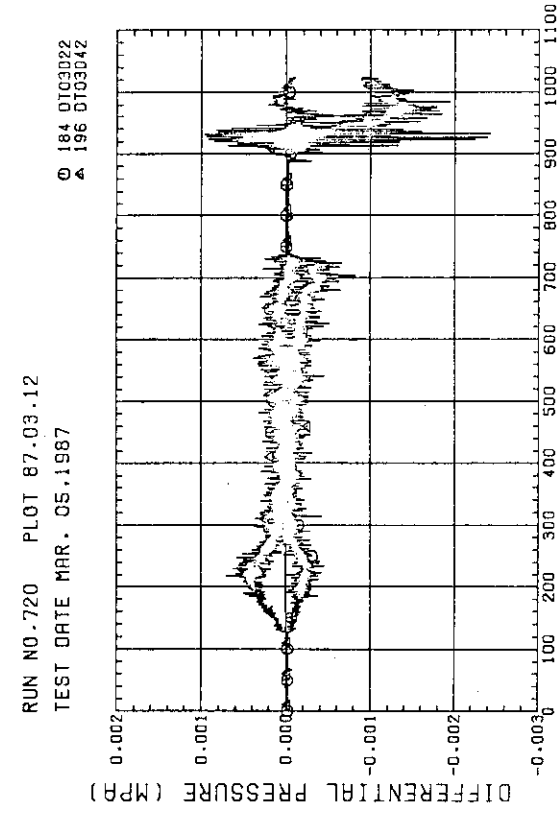

Fig. E-38 DIFFERENTIAL PREESURE, HORIZONTAL AT 1365 MM (22-BUNDLE 2-4, 42-BUNDLE 4-8)

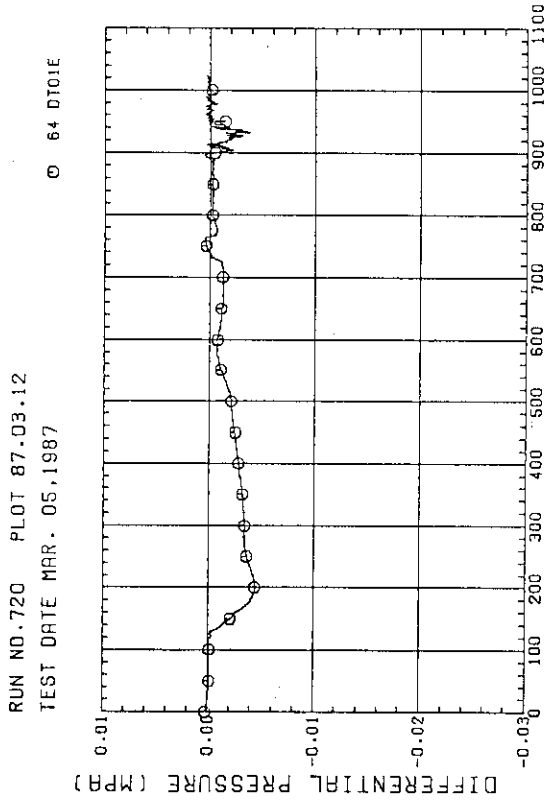

Fig. E-43 DIFFERENTIAL PRESSURE, CONTAINMENT TANK-II - CONTAINMENT TANK-1

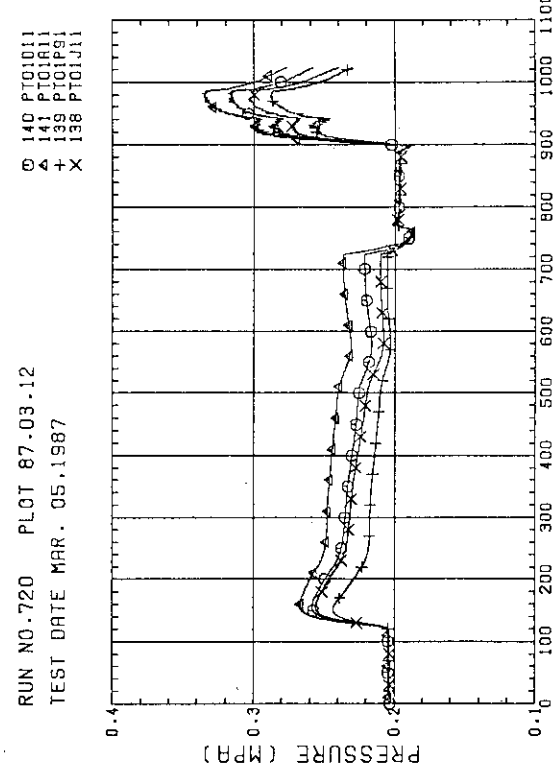

Fig. E-44 PRESSURE IN PV (J - TOP OF PV, D - CORE CENTER, A - CORE INLET, P - BELOW COLD LEG NOZZLE IN DOWNCOMER)

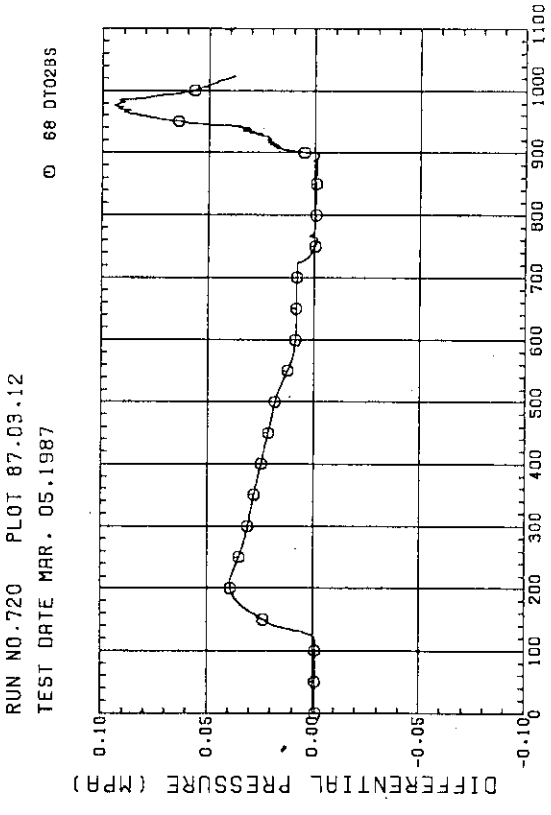

Fig. E-41 DIFFERENTIAL PRESSURE, STEAM/WATER SEPARATOR - CONTAINMENT TANK-II

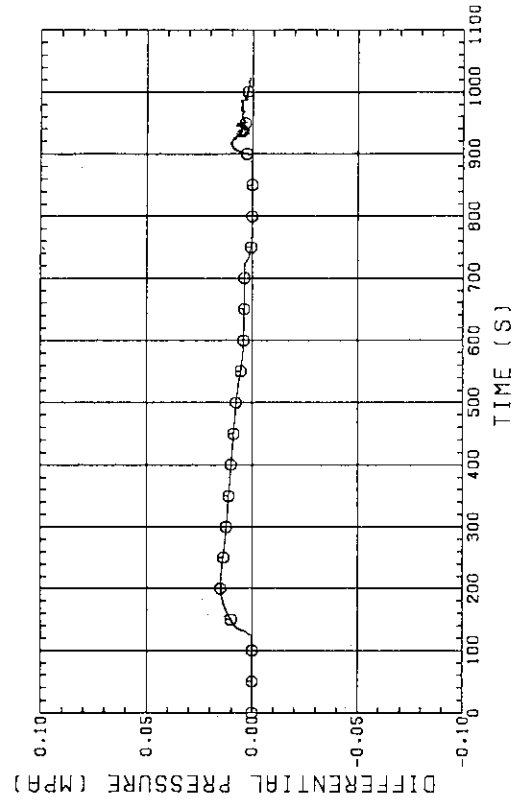

Fig. E-42 DIFFERENTIAL PRESSURE OF INTACT COLD LEG

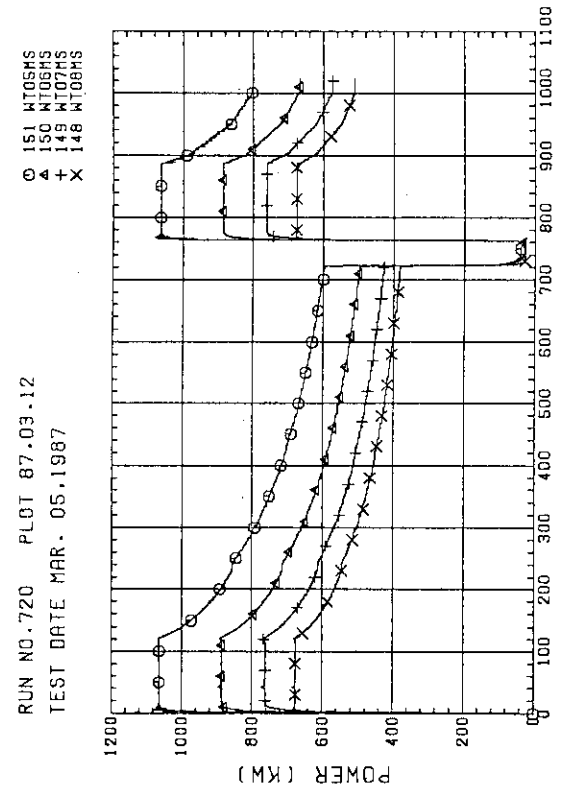

Fig. E-47 BUNDLE POWER (BUNDLE 5,6,7,8)

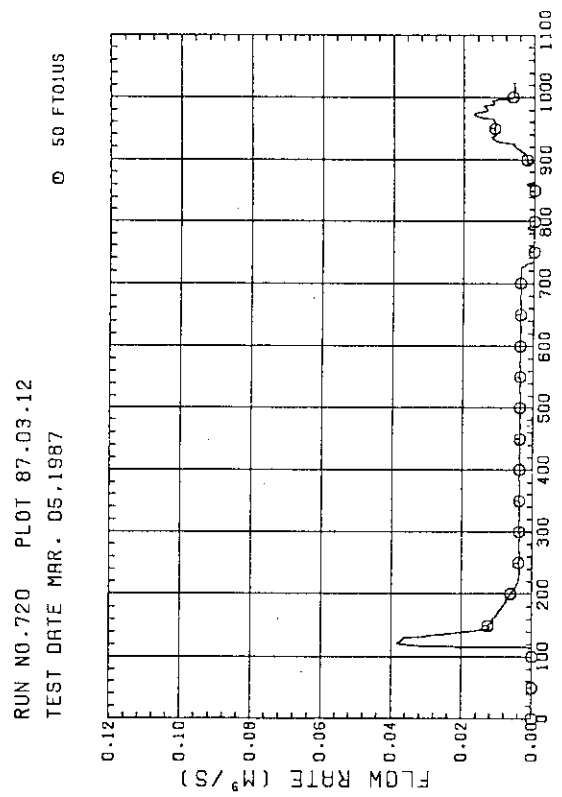

Fig. E-48 FLOW RATE OF LOWER PLENUM INJECTION WATER (ACC HEADER LINE)

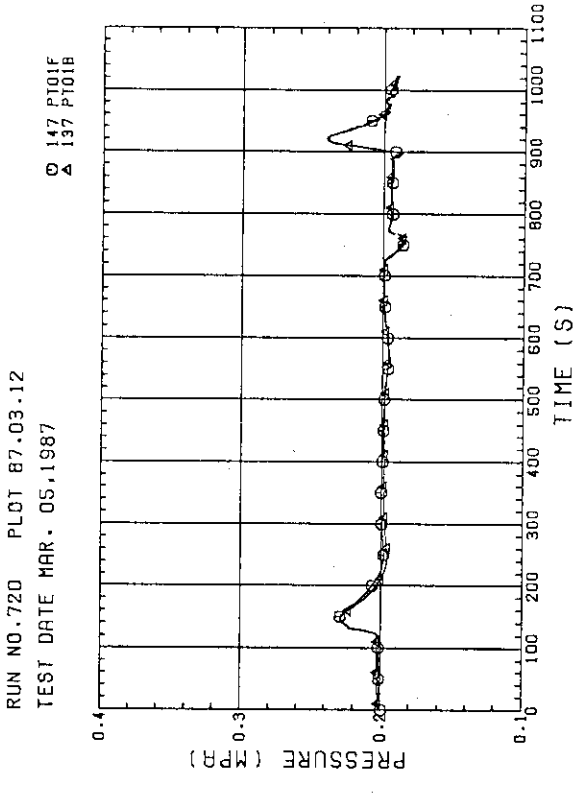

Fig. E-45 PRESSURE AT TOP OF CONTAINMENT TANK-I AND CONTAINMENT TANK-II (F-CONTAINMENT TANK-I, B-CONTAINMENT TANK-II)

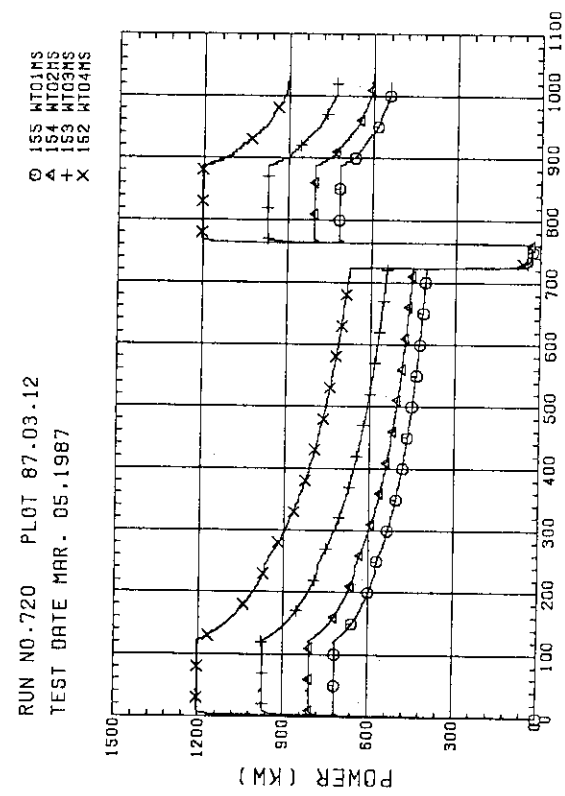

Fig. E-46 BUNDLE POWER (BUNDLE 1,2,3,4)